SPIM

Thèse de Doctorat

école doctorale **sciences pour l'ingénieur et microtechniques**

UNIVERSITÉ DE BOURGOGNE

THÈSE

Pour l'obtention du grade de

Docteur de l'Université de Bourgogne

Spécialité : Mécanique

Présenté par

Zul Hilmi CHE DAUD

17 Décembre 2014

Contribution à l'Etude du Comportement Thermique de la Batterie Lithium-ion pour Véhicules Electriques et Hybrides

Membres du Jury

Mr. François BADIN	Professeur, IFPEN	Rapporteur
Mr. Narayan KAR	Professeur, University of Windsor	Rapporteur
Mr. Luis LE MOYNE	Professeur, Université de Bourgogne	Directeur
Mme. Daniela CHRENKO	Maitre de Conférences, Université de Bourgogne	Co-Encadrant

RÉSUMÉ

Chapitre 1 Introduction

Au cours des dernières années, l'utilisation de véhicules terrestres a augmenté pour satisfaire les besoins de mobilité, qui comprennent le transport des personnes et des biens. Il existe plusieurs types de véhicules terrestres; les motos, les voitures, les autobus, les camions et les tracteurs. Conventionnellement, la plupart de ces véhicules sont alimentés par des moteurs à combustion interne (MCI) qui brûlent un combustible hydrocarboné liquide comme l'essence et le diesel. Le problème avec ce type de moteur est qu'il est basée sur la combustion, ce qui produit non seulement la puissance de propulsion du véhicule, mais constitue également une source de pollution, tels que les oxydes d'azote (NO_x), le monoxyde de carbone (CO), le dioxyde de carbone (CO_2) et les matières particulaires; il est donc difficile de répondre aux exigences futures sur le moteur de véhicule en ce qui concerne le bruit, les émissions et la consommation d'énergie. Le secteur des transports contribue à 14% des émissions de gaz à effet de serre dans le monde avec plus de deux tiers des émissions de gaz à effet de serre liées au transport provenant de véhicules terrestres. L'augmentation de la concentration de gaz à effet de serre conduit à un réchauffement considérable de la terre appelé le réchauffement climatique. La réserve de pétrole brut pour produire de l'essence et du carburant diesel s'épuise et est non renouvelable. Avec la technologie et l'usage courant, les réserves de pétrole brut devraient durer seulement entre 40 à 50 ans. La pénurie de l'approvisionnement en pétrole brut, la nécessité de respecter les normes d'émissions de plus en plus strictes, et la menace du réchauffement climatique ont stimulé le changement dans le mode de transport et inciter les constructeurs automobiles à la recherche de nouvelles technologies de véhicules à haut rendement et moins polluants.

Il ya plusieurs façons conventionnelles pour améliorer l'économie de carburant et réduire les émissions, par exemple on pourrait augmenter l'efficacité du MCI, diminuer le poids total du véhicule, et de réduire la traînée aérodynamique et la résistance au roulement. Une autre solution importante serait l'utilisation de transmissions alternatives, telles que les véhicules électriques (VE), les véhicules hybrides électriques (VHE) et les véhicules à pile à combustible. Afin de répondre aux exigences des clients en autonomie et au coût du véhicule, et en même temps pour réduire la consommation et les polluants, qui ne peuvent être satisfaite par les voitures de MCI ou VE, la solution la plus réalisable à l'heure actuelle est VHE.

Dans les véhicules électriques et les véhicules hybrides électriques, les batteries sont parmi les éléments clés les plus importants qui doivent continuellement accepter et fournir de l'énergie électrique par la transformation de l'énergie chimique en énergie électrique et vice versa. Les batteries doivent avoir une puissance et une énergie spécifique élevée, une longue durée de vie, un faible coût initial et de remplacement, une grande fiabilité et robustesse. Les batteries le plus souvent utilisées sont plomb-acide, nickel-cadmium, nickel-métal hydrure et lithium-ion. La batterie lithium-ion est un bon choix pour le VHE grâce à les propriétés supérieures telles la puissance spécifique élevée, l'énergie spécifique élevée, et la durée de vie élevée. En outre, les batteries lithium-ion n'ont pas le problème d'effet de mémoire et n'utilisent pas les métaux toxiques tels que le plomb, le mercure ou le cadmium. Cependant, ces batteries souffrent de certains problèmes liés à la gestion thermique de la batterie y compris la sécurité et la mauvaise performance à basse température et leur prix est encore élevé.

La température est un des paramètres d'une batterie lithium-ion qui doit être soigneusement contrôlée, car la température de fonctionnement de la batterie lithium-ion à une grande influence sur l'efficacité, la dégradation de capacité des cellules, la durée de vie et la sécurité. La température optimale de fonctionnement est normalement limitée entre 20°C et 65°C. Les cellules de batterie produisent de la chaleur pendant le processus de charge et de décharge. La génération de chaleur dans la batterie peut augmenter subitement et provoquer une surchauffe dans certaines conditions telles que le taux de décharge élevé et la température ambiante élevée et aussi une charge ou une décharge excessive au cours du cycle. Celle ci est la principale contribution à une défaillance prématurée dans des batteries sous forme d'emballement thermique ou d'accélération de perte de la capacité de la batterie. L'emballement thermique est l'un des modes de défaillance des batteries, ce qui se produit généralement quand une réaction exothermique va hors du contrôle. Ceci peut être expliqué par l'augmentation de la vitesse de réaction en raison d'une augmentation de la température et provoque une augmentation supplémentaire de la température ainsi donc une augmentation supplémentaire de la vitesse de réaction.

La modélisation est un outil très important dans le développement du VHE, en particulier pendant la phase de conception. Elle est utile dans l'optimisation de la conception du produit et réduit le coût et le temps utilisé dans le développement de VHE avant de procéder à la construction des prototypes ainsi. Pour assurer le succès de la modélisation, la précision de

chaque modèle est très importante. Cependant, les modèles de haute précision exigent normalement une structure complexe avec un immense effort de maillage et de temps de calcul. En outre, la plupart des logiciels sont coûteux, ce qui limite l'utilisation uniquement à un petit groupe d'utilisateurs. Le modèle de simulation ne peut pas être considéré comme complet sans être validé par des données expérimentées. Seul le modèle de simulation validée peut fournir un bon degré de précision et garantir la fiabilité des prévisions. Par conséquent, mettre en évidence l'importance d'un modèle simple mais fonctionnel de VHE qui peutt représenter précisément un modèle de véhicule réel et de leurs composants avec le temps de calcul raisonnable et accessible à un grand nombre d'utilisateurs.

L'objectif principal de cette étude est de fournir les informations essentielles sur le comportement thermique des cellules de batterie pour l'automobile en particulier pour les véhicules électriques et les véhicules hybrides électriques dans le cadre de travaux expérimentaux afin de développer une modèle électrothermique efficace en 3D pour les cellules de batterie lithium-ion. Cette étude expérimentale se concentre sur la distribution de température en différents endroits de la surface de la cellule de la batterie, de l'impact de différentes décharges de courant, et également de l'importance du système de refroidissement (convection forcée avec différent vitesses d'air) sur le comportement de la température de la batterie. Cette thèse met en évidence le comportement de température de la cellule de batterie dans des conditions de décharge d'abus (moins de 20% du SOC) et de l'impact de l'empilement des cellules de batterie à l'intérieur de la boite de batterie. L'effet de la température et l'état de charge (SOC) sur la résistance interne de la cellule de la batterie et une étude de cas sur le comportement thermique des cellules de batterie utiliseé dans une série VHE pour compléter les cycles de conduite en utilisant des stratégies de refroidissements différents sont également étudiés. En plus, l'étude expérimentale est étendue à la caractéristique du comportement du flux d'air de refroidissement à l'intérieur de la batterie, en particulier près de la surface de la cellule de batterie à travers le système de vélocimétrie par images de particules (PIV)

Avec le travail expérimental, l'étude se concentre sur le développement de la modèle électrothermique 3D CFD. Le modèle est développé dans un logiciel gratuit avec un code source ouvert, OpenFOAM. L'objectif est d'avoir un modèle relativement simple mais précis avec un temps de calcul raisonnable. De cette façon, ce modèle est facile d'accès, de manipulation et d'utilisation par d'autres chercheurs pour une analyse ultérieure des cellules de la batterie. Ce

modèle considère la génération de la chaleur par le courant et la résistance interne de la batterie qui est introduite dans la cellule par l'électrode positive et négative, le transfert de chaleur à l'intérieur de la cellule de batterie par conduction et le transfert de chaleur de cellules de batterie à l'environnement par convection forcée et rayonnement. Une attention importante est accordée à la résistance interne de la batterie parce que sa valeur varie avec la température. La valeur de résistance interne en fonction de la température qui est proposé et utilisé dans ce modèle est basé sur des résultats expérimentaux effectués dans cette étude. Le modèle est validé en comparant les résultats expérimentaux à deux aspects principaux; le comportement d'écoulement de l'air de refroidissement proche de la surface de cellule et la température de batterie à divers endroits sur la surface de la cellule de batterie sous différentes conditions de décharge de courant et de convection forcée. Ce modèle validé peut être utilisé comme un modèle de base pour une analyse plus approfondie des cellules de la batterie. L'utilisation de logiciel de code source ouvert crée une opportunité pour d'autres personnes fournissant un accès gratuit et facile à ce modèle. Dans l'avenir, elles pourront utiliser ce modèle et ajouter ou supprimer certaines fonctionnalités pour mieux satisfaire à l'exigence pour une analyse plus approfondie de la cellule de la batterie.

Chapitre 2 Etude bibliographique

Les véhicules hybrides électriques sont une combinaison de deux ou plusieurs sources d'énergie, normalement un conventionnel MCI et un moteur électrique permettant d'obtenir la puissance nécessaire pour propulser le véhicule. Ce système est considéré comme l'une des technologies les plus prometteuses qui peuvent fournir le meilleur compromis entre une bonne autonomie de conduite, à faible coût, et la réduction de la consommation de carburant et polluants. Ceci peut être réalisé par la possibilité de combiner les avantages de zéro émission de VE pur et de l'énergie et la densité de puissance élevée des véhicules MCI pure. On peut surmonter les désavantages comme une mauvaise économie de carburant et la pollution par les véhicules MCI pur aussi qu'une pauvre autonomie de conduite par charge de la batterie dans les VE purs. En règle générale, les VHE peuvent être classés en quatre différentes architectures de base qui sont l'hybride série, hybride parallèle, série-parallèle ou hybride combiné et complexe hybride. Il est prévoit que la popularité de VHE sera augmentée à l'avenir avec le développement de la technologie de la batterie, de la technique de commande, et le soutien du gouvernement aux propriétaires d'automobiles et les fabricants.

La batterie est un des éléments clés les plus importants dans les VHE qui doivent continuellement accepter et fournir de l'énergie électrique par la transformation de l'énergie chimique en énergie électrique et vice versa. Les batteries lithium-ion sont considérées comme un bon choix pour les VHE pour leurs propriétés supérieures comme forte puissance, haute densité d'énergie, et le cycle de vie élevée comparé au plomb-acide, nickel-cadmium, et la batterie nickel-hydrure métallique. La dégradation de capacité de la batterie est un phénomène de la perte de la capacité de décharge au cours du temps. Les principaux facteurs qui influent sur la diminution de la capacité de la batterie sont le taux de charge et de décharge, SOC, le nombre de cycles de charge-décharge et aussi la température de fonctionnement. Il existe une faible influence de la température sur la dégradation de capacité mais la température affecte la résistance interne de la batterie. La dégradation de capacité de la batterie augmente avec l'augmentation du taux de charge. Les résultats expérimentaux montrent également qu'à une température constante, la dégradation de capacité augmente avec l'augmentation du nombre de cycles de charge-décharge.

La température est un facteur important qui affecte les performances de la batterie et sa durée de vie. La température de chaque cellule de la batterie à l'intérieur du boitier de la batterie est différente en fonction de l'endroit où il se trouve. Cette différence de température peut alors conduire au déséquilibre des capacités des cellules qui provoque les cellules à être surchargées ou trop déchargées au cours du cycle qui est la contribution majeure à une défaillance prématurée des batteries sous forme d'accélération de la dégradation de capacité ou emballement thermique; un état dans lequel la cellule de batterie est en surchauffe et explose. Pour résoudre ces problèmes, un système de gestion thermique de batterie est nécessaire. Il est destiné à réguler les cellules de la batterie à fonctionner dans la plage de température souhaitée et à réduire la différence de la température entre les cellules. Pour assurer le succès de l'utilisation d'un système de gestion thermique, un bon modèle thermique des batteries et des cellules individuelles est très important. Il peut fournir des informations exactes qui illustrent l'état réel de la température de la batterie. C'est une information importante pourront être utilisé par le système de gestion thermique pour éviter tout risque d'abus.

En général, il existe quatre principales méthodes de modélisation de la batterie; des modèles mathématiques, des modèles électrochimiques, des modèles basés sur des polynômes et des modèles électriques. Les modèles électriques sont plus réalistes, intuitifs, faciles à manipuler

et sont considérés comme le meilleur compromis de complexité, de temps de calcul et de précision par rapport à d'autres modèles. En plus, ils peuvent être appliqués à n'importe quel type de batterie, indépendamment de sa composition chimique, sa configuration et le taux de décharge, en utilisant la combinaison appropriée des paramètres. Dans la modélisation de batterie lithium-ion, certaines recherches se concentrent sur la modélisation électrique de la batterie, y compris la tension de la batterie, du courant, et aussi le l'état de charge (SOC). Plusieurs différentes méthodes sont présentées dans l'estimation de la batterie SOC y compris la tension en circuit ouvert (OCV), Coulomb comptage (CC), et les méthodes de filtrage de Kalman. La tension de la batterie est calculée à partir de la batterie OCV, le courant et la résistance interne de la batterie. En outre, la résistance interne de la batterie peut être constante, ou une fonction de la température ou SOC, ou la combinaison de la température et SOC. En général, la valeur de la résistance diminue avec l'augmentation de la température. Cependant, un manque d'information existe sur le rapport de la résistance à la température pour des températures supérieures à 50ºC.

Plusieurs travaux ont été réalisés dans la modélisation du comportement thermique de la batterie. Certains travaux ont porté uniquement sur la modélisation des comportements thermiques, tandis que d'autres prennent en compte la combinaison des modèles thermiques et électriques qui simulent l'impact des changements de température de la batterie à la performance électrique de la batterie. En plus, le modèle développé peut être pour une seule cellule, plusieurs cellules ou des cellules dans la boite de batterie qui tiennent compte de l'impact de l'empilage de la batterie ou de l'arrangement de la batterie.

La génération de la chaleur est normalement modélisée sous la forme d'une combinaison de la génération de chaleur due à la perte de puissance due à la résistance interne et/ou la réaction électrochimique à l'intérieur de la cellule de batterie. La température de la batterie est modélisée en tant que soit une température uniforme ou à une température non uniforme. Pour une température non uniforme, la température est normalement plus élevée près de l'électrode positive et négative que d'autres endroits à cause de la densité de courant plus élevée près de l'électrode. Aussi, la température près de l'électrode positive est plus élevée que celle proche de l'électrode négative du fait de la conductivité électrique inférieure de l'électrode positive. Certains travaux se concentrent sur la production de chaleur à taux de décharge constants, tandis que d'autres calculent la production de chaleur pour la batterie utilisée dans un véhicule pour compléter les cycles de conduite tels que US06, NEDC, ou Artemis. Certains travaux utilisés

uniquement convection naturelle comme moyen de refroidissement de la batterie, tandis que l'autre considère convection forcé, un refroidissement par liquide, ou d'un système de refroidissement passif par l'intégration d'un matériau à changement de phase (PCM) dans le boitier de batteries. Le transfert de chaleur par rayonnement est généralement ignoré, en raison de sa complexité et de moindre importance par rapport à d'autres types de transfert de chaleur.

Chapitre 3 Analyse thermique de la batterie

Divers travaux expérimentaux concernant la température de la surface des cellules de la batterie peuvent être trouvés dans la littérature. Ces travaux peuvent être divisés en plusieurs groupes, selon les méthodes utilisées dans la mesure de la température, le nombre de cellules, la méthode de charge/décharge, et le type de système de refroidissement utilisés. Cependant, il a été constaté qu'il existe un manque de travaux expérimentaux qui mettent en évidence l'évolution de la température de la cellule à tous les endroits d'une seule cellule, ainsi que l'impact de l'emballage de plusieurs cellules dans une boite de batterie, en utilisant différents taux de décharge et différent vitesses de l'air de refroidissement. En plus, la plupart des travaux existants seulement analyse la température de la cellule à un niveau de l'état de charge (SOC) relativement élevé. Il n'y a pas de résultats qui montrent ce qui se passe pour le comportement thermique de la cellule de batterie lorsque la cellule est déchargée à petit SOC, moins de 20%. Toutes ces informations sont importantes pour comprendre le comportement de température de la cellule de batterie à diverses conditions. En outre, la plupart des résultats expérimentaux utilisés pour valider le modèle de simulation de la batterie uniquement considérés le taux de décharge constant pour une seule cellule, sans système de refroidissement. Ainsi, le résultat de la simulation pourrait ne pas être précis pour prédire le comportement thermique de la batterie avec l'effet de système de refroidissement et des cellules de la batterie dans le pack.

Cet article présente l'étude expérimentale sur le comportement thermique de la surface de la cellule de batterie lithium-ion utilisé dans des applications automobiles. Cette étude porte sur la distribution de température en différents points de la surface de la cellule de batterie, l'impact de l'empilement des cellules de batterie à l'intérieur de la batterie pack, de l'impact de différents constants taux de décharge, et également l'importance du système de refroidissement (convection forcée à l'aide des vitesses d'air de refroidissement) sur le comportement de la température de la batterie. Cette étude met également en évidence le comportement de la température des cellules

de la batterie dans des conditions de décharge abusée (de décharge au SOC moins de 20%), l'impact de différentes températures et SOC sur la résistance interne de la cellule de la batterie et une étude de cas sur le comportement thermique des cellules de batterie utilisée dans un VHE à compléter les cycles de conduite en utilisant des différents stratégies de refroidissement.

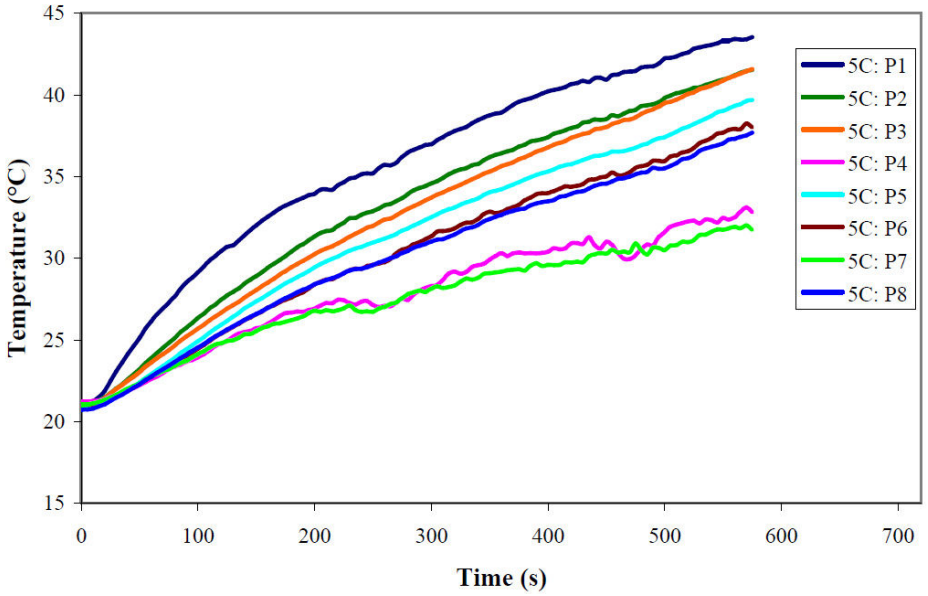

Figure 1. La température de surface de la cellule au taux de décharge de 5C avec une vitesse d'air de refroidissement de 2 m/s à 21℃.

Les résultats des expériences de décharge à courant constant et de refroidissement à vitesse d'air constante, indiquent que la température de la surface de la cellule est non homogène, avec une différence significative entre la température la plus haute et la plus basse, comme le montre la Figure 1. D'une manière générale, on observe que la température la plus élevée est à P1, suivi par P2 et P3. Ces trois points sont prés de l'électrode positive et négative. La température est élevée proche de ces deux électrodes en raison des densités de courant plus élevées à l'électrode positive et négative par rapport au reste de la cellule. En plus, la température à proximité de l'électrode positive est plus élevée que sur l'électrode négative, parce que la valeur de conductivité électrique de l'électrode positive est inférieure à celle de l'électrode négative. On peut observer que les deux températures les plus basses sont enregistrées à P4 et P7, même si ces deux points sont près de l'endroit le plus chaud, à côté de l'électrode positive. Il existe d'énormes différences de température entre P7 et P8. Température à P4 et P7 est plus faible que d'autres endroits en raison de l'effet de système de refroidissement. Ces emplacements sont à proximité

du bord de la cellule qui fait face à l'air de refroidissement d'entrée qui reçoit l'air de refroidissement à la température la plus basse. L'air de refroidissement prend la chaleur de la cellule, par conséquent la température de l'air augmente quand elle passe de la cellule de batterie.

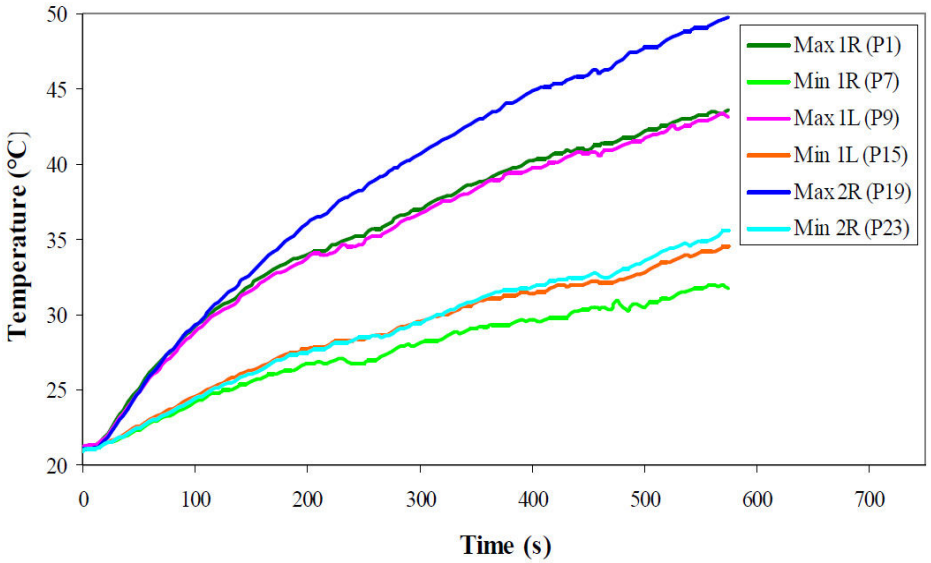

Figure 2. Comparaison de max et min température pour différentes surfaces de cellules au taux de décharge de 5C avec une vitesse d'air de refroidissement de 2 m/s.

La Figure 2 représente la température la plus élevée et la moins élevée à trois différentes surfaces de cellules; de la première et deuxième cellule (1R, 1L, et 2R) avec une vitesse d'air de refroidissement de 2 m/s au taux de décharge de 5C. En général, la température de la deuxième cellule est plus élevée que pour la première cellule, car la deuxième cellule se trouve au milieu du boîtier de la batterie, entre la première et la troisième cellule. Dans cette configuration, la seconde cellule a une efficacité de transfert de chaleur inférieure par rapport à d'autres cellules. Ainsi, le transfert de chaleur est moins élevé et l'augmentation de température est plus importante. En plus, l'électrode positive de la première et de la troisième cellule est proche de l'orifice d'entrée d'air de refroidissement, tandis que l'électrode positive de la seconde cellule est loin de cet orifice. Cela amplifie la différence de température entre la première et la deuxième cellule. La température maximale de la surface 1R et 1L est égale, tandis que la température minimale à 1L est supérieure à la surface 1R.

La comparaison de l'évolution de la température maximale et minimale pour le taux de décharge de 1C, 3C, et 5C sont résumés dans la Figure 3. Il montre qu'il existe un fort lien entre le taux de décharge et l'augmentation de la température. En général, les températures à P1 et P7

sont plus élevées pour une valeur de taux de décharge plus élevée. Le taux de décharge plus élevée signifie qu'une plus grande quantité de courant circule et génère plus de chaleur et augmente ainsi la température de la cellule. Les températures de surface de cellule à la fin de la décharge à P1 sont de 25°C, 33°C et 44°C pour le taux de décharge de 1C, 3C, et 5C respectivement. La différence de température entre P1 et P7 est plus grande quand le taux de décharge est élevé. A taux de décharge de 1C, seulement 2°C de différence de température est enregistrée, mais cette valeur augmente à 5°C pour 3C et 12°C pour 5C.

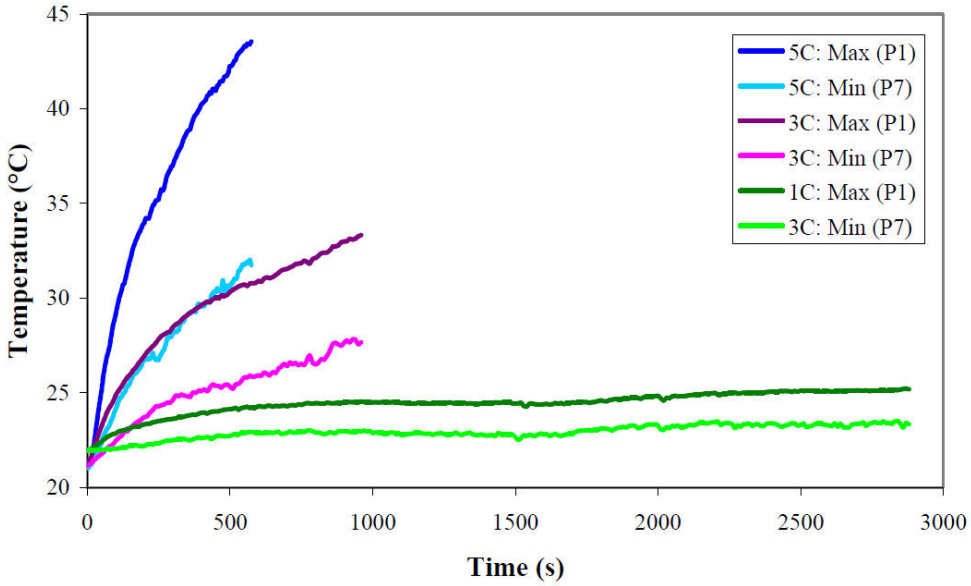

Figure 3. Comparaison de max et min température pour différentes taux de décharge avec une vitesse d'air de refroidissement de 2 m/s.

Le système de refroidissement est très important dans le contrôle de la température de la cellule de batterie; il réduit la température globale de la cellule et la différence de température entre la température maximale et la température minimale. La Figure 4 montre l'évolution de la température au point P1 et P7 à cinq vitesses de l'air de refroidissement différents, de 2 m/s à 10 m/s. A P1, la température de surface de la cellule est de 44°C à la fin de la décharge avec une vitesse d'air de refroidissement de 2 m/s. Cette valeur diminue à 38°C, 36°C, 33°C et 32°C à une vitesse d'air de 4 m/s, 6 m/s, 8 m/s et 10 m/s respectivement. La différence de température entre P1 et P7 diminue lorsque la vitesse de l'air de refroidissement augmente. A 2 m/s, 12°C de différence de température est enregistrée, cette valeur a diminué à 8°C pour 4 m/s, 7 °C pour 6 m/s et 5°C à la fois pour 8 m/s et 10 m/s de vitesse de l'air de refroidissement. À la petite vitesse de l'air de refroidissement, la température de la cellule continue d'augmenter du début

jusqu'à la fin de la décharge. Cependant, à la vitesse de l'air de refroidissement élevée de 10 m/s, la température de la cellule augmente jusqu'à 300 secondes de temps de décharge, après la température est pratiquement constante jusqu'à la fin de décharge.

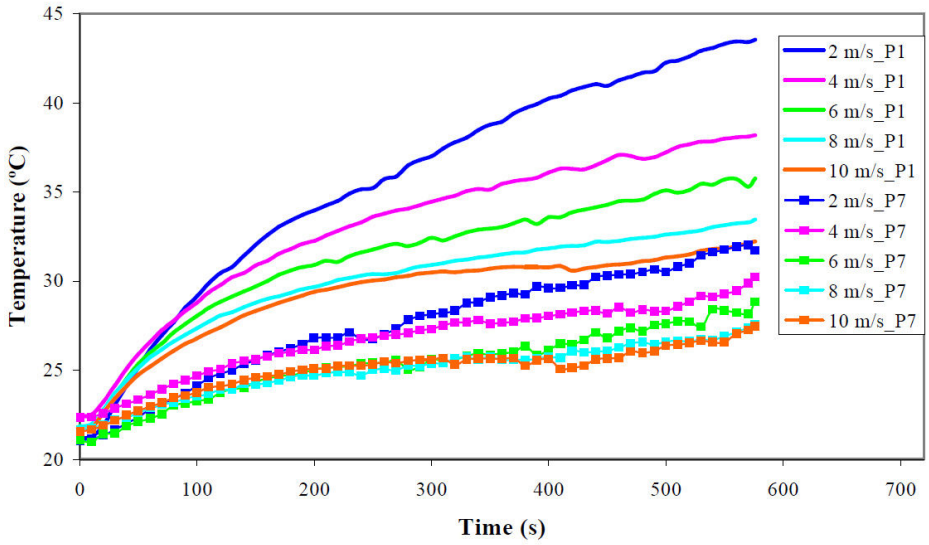

Figure 4. La température de la surface 1R (P1 et P7) à cinq vitesses d'air de refroidissement différent au taux de décharge de 5C.

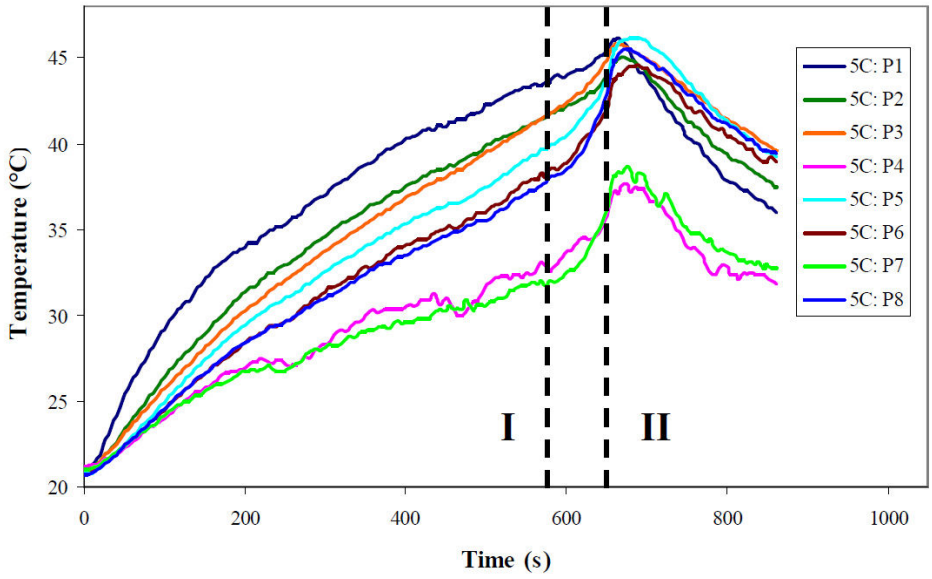

Figure 5. La température de surface de la première cellule au taux de décharge de 5C avec une vitesse d'air de refroidissement de 2 m/s sur la condition de décharge excessive.

Décharger la batterie au SOC inférieure à 20% contribue à une augmentation radicale de température à tous les endroits de cellules de la batterie, tel que représenté sur la Figure 5. Cette situation est directement influencée par une augmentation soudaine de la valeur de résistance interne inférieure à 20% SOC. Ceci explique pourquoi il est dangereux de décharger la batterie à SOC moins de 20%. En général, les températures pour SOC entre 20% à 10% augment à deux valeurs distinctes; une température supérieure à P1, P2, P3, P5, P8 et, et une température inférieure à P4 et P7. A cette condition, il n'y a plus d'effet de fortes densités de courant à des électrodes positives et négatives et également la différence de la conductivité électrique sur l'augmentation de la température.

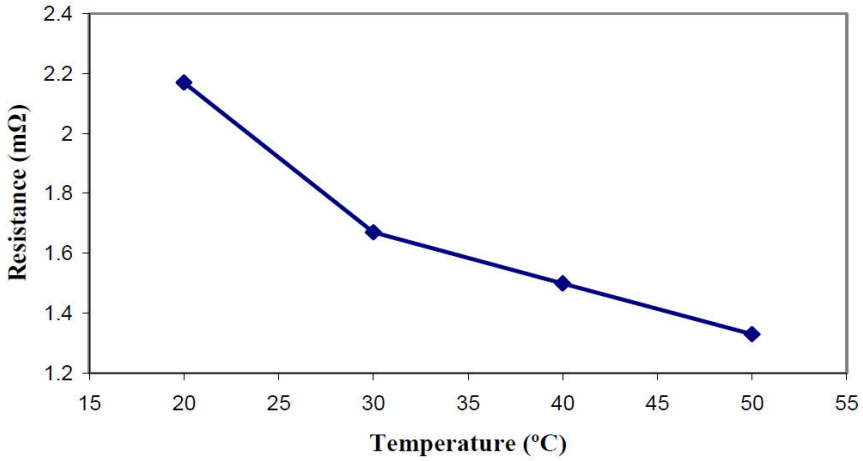

Figure 6. La résistance interne de la batterie en fonction de la température.

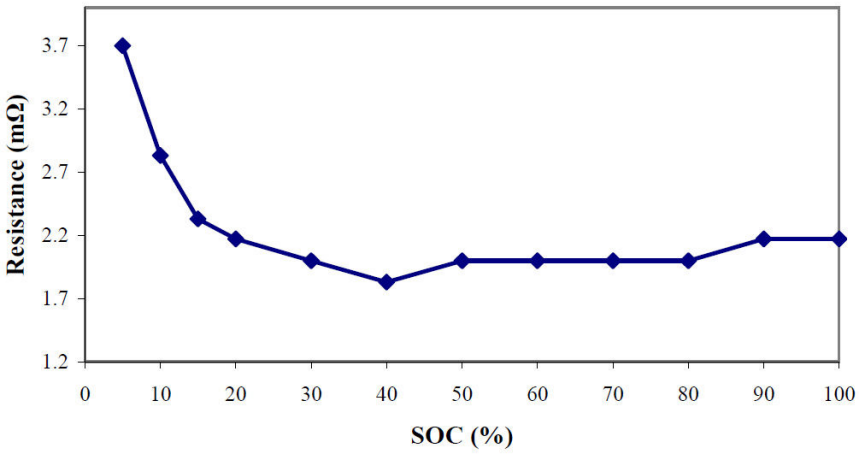

Figure 7. La résistance interne de la batterie en fonction de SOC.

La résistance interne de la batterie diminue avec l'augmentation de la température à une certaine limite, comme le montre la Figure 6. Dans la présente étude, la résistance diminue de près de la moitié de sa valeur initiale à 20°C lorsque la température augmente à 50°C. La valeur de la résistance interne est entre 2.17 mΩ à 1.33 mΩ. A température constante, la résistance interne est à peu près constante dans la plage de SOC de 100% à 20%, comme le montre la Figure 7. Dans cette plage, la valeur de la résistance interne varie entre 1.8 à 2.17 mΩ. Après 20% SOC, il ya un saut brusque de la valeur de la résistance interne de 2,83 mΩ à 10% SOC et 3,7 mΩ à 5% SOC.

Dans l'étude de cas des cellules de la batterie utilisée en condition réelle dans un véhicule hybride, il ya juste une petite augmentation de la température en utilisant la vitesse d'air de refroidissement constant et la vitesse d'air de refroidissement en fonction de la vitesse du véhicule pour le cycle de conduite NEDC et Artemis rural. Quoi qu'il en soit, de meilleures répartitions de chaleur sont obtenues lorsque la batterie est refroidie en utilisant la vitesse de l'air en fonction de la vitesse du véhicule. Les résultats suggèrent qu'il n'y a pas besoin de système de refroidissement auxiliaire dans ces cas.

Chapitre 4 Modélisation électrothermique

La température est un des paramètres d'une batterie lithium-ion qui doit être soigneusement contrôlée, car la température de fonctionnement de la batterie a une grande influence sur l'efficacité, la dégradation de la capacité, et la durée de vie de la batterie. La température de chaque cellule à l'intérieur de la batterie varie en fonction de la conception de la batterie. Les variations de température peuvent conduire à une surcharge ou une décharge excessive pendant le cycle qui contribue davantage à une défaillance prématurée des batteries sous la forme d'accélération de la dégradation de la capacité ou de l'emballement thermique. La modélisation électrothermique de batteries est importante, pour concevoir les systèmes de gestion de la batterie (BMS) plus performants, pour éviter la dégradation de la batterie et de prolonger la durée de vie de la batterie, et aussi de prévenir les risques de sécurité, tels que l'emballement thermique. En outre, un modèle thermique précis de batteries et des cellules individuelles est essentiel pour illustrer l'état réel de la température de la batterie et prévenir d'éventuels abus. En plus, la température à l'intérieur de la cellule est difficile à mesurer expérimentalement, mais ceci est tout à fait possible grâce à la modélisation.

Il existe un grand nombre d'articles sur le modèle thermique de la batterie, à un certain degré de complexité et de précision. Des modèles simples sont seulement capables d'illustrer le comportement thermique de batterie en 0D, tandis que d'autres sont étendus à 2D et 3D. Dans le modèle 0D, la température de cellule est considérée comme homogène. D'autre part, les modèles 2D sont capables d'illustrer la variation de température le long de la surface de la cellule, tandis que les modèles 3D peuvent prédire la variation de la température à tous les endroits de cellules. La plupart des travaux de modélisation sont uniquement concentrés sur la modélisation d'une seule cellule. Il existe cependant certains modèles qui prennent en compte de plusieurs cellules de batterie dans une batterie pack.

Normalement, les systèmes de refroidissement de batterie peuvent utiliser le refroidissement par air, refroidissement liquide (eau/huile/réfrigérant), matériaux à changement de phase (PCM), ou une combinaison de ces méthodes. Beaucoup de modèles existants considèrent le système de refroidissement de l'air, comme dans la réalité, c'est le moyen de refroidissement le plus simple et le plus efficace. L'inconvénient du système de refroidissement à air est l'insuffisante dissipation de chaleur de la batterie par convection, cela peut se produire dans des conditions de stress et d'abus. Malheureusement, la plupart de ces modèles ne sont validés qu'à l'aide de résultat de l'expérience avec la convection naturelle. Cependant, ils sont alors utilisés pour simuler le comportement thermique de la batterie soit par convection naturelle ou forcée, ou les deux. Ces pratiques peuvent ne pas être une bonne solution, car le modèle validé pourrait ne pas représenter correctement le comportement thermique réel de la cellule de batterie sous les processus de convection forcée.

Un modèle électrothermique d'une batterie au lithium-ion pour les applications automobiles est présenté et validé. Ce modèle est implémenté dans un logiciel d'OpenFOAM, offrant la possibilité de relier la production de chaleur à partir de pertes thermiques à l'intérieur des cellules de la batterie au rayonnement et convection forcée d'un flux d'air. La source de chaleur est calculée en fonction du courant de décharge et de la résistance interne de la batterie. Un facteur d'échelle qui tient en compte de la différence de conductivité électrique entre les électrodes positives et négatives est utilisé pour différencier la quantité de chaleur générée aux électrodes positives et négatives. La résistance interne de la batterie en fonction de la température est proposée et utilisée dans cette étude comme le montre la Figure 8. La source de chaleur calculée est introduite dans la cellule par deux plaques très fines situées sur la partie

haute des électrodes positives et négatives de la cellule de la batterie. Ensuite, la chaleur de ces plaques est transférée à l'autre endroit de la batterie par un processus de conduction, avant de se dissiper dans l'environnement par rayonnement et convection forcée. La validation du modèle est centré sur deux aspects importants, le comportement d'écoulement de l'air à proximité de la surface de cellule à différentes vitesses initiales d'air de refroidissement et les évolutions de la température de la batterie à diverses positions de la surface de la cellule de batterie sous différents taux de décharge et des différentes conditions de convection forcée.

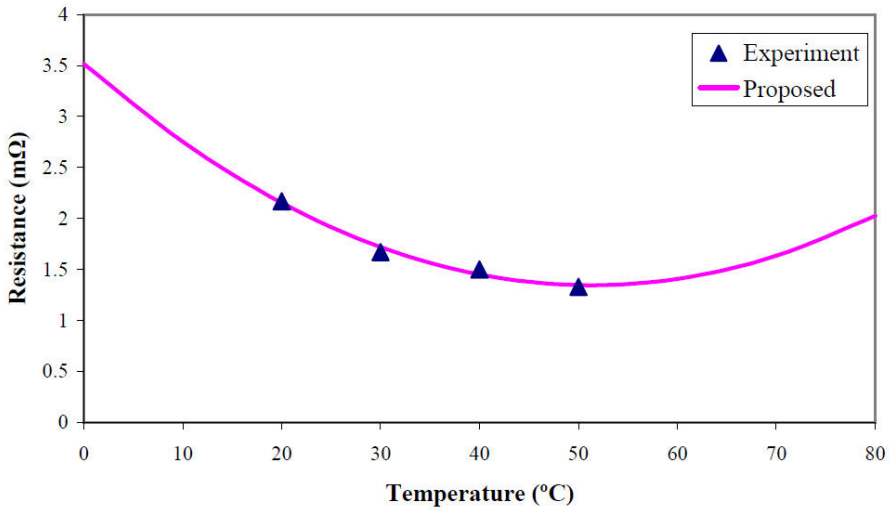

Figure 8. La résistance interne de la batterie en fonction de la température utilise dans la modélisation OpenFOAM.

Des expériences pour valider le comportement de l'écoulement de l'air à l'intérieur de la boîte de la batterie en particulier près de la surface de la cellule sont menées à l'aide de vélocimétrie par images de particules (PIV). La clé de ces expériences est de vérifier que le flux d'air produit par la simulation est correct, car il influe sur le processus de convection forcée et donc la température prédite de la surface de la cellule de batterie. PIV est une technique de champ d'écoulement entier utilisé pour obtenir des mesures de la vitesse instantanée et des propriétés connexes des fluides dans une section transversale d'un écoulement. L'écoulement d'air est ensemencé avec de petites particules de traceur, et éclairé par une nappe de lumière laser, de sorte que les particules sont visibles. Le mouvement des particules d'ensemencement est utilisé pour calculer les dimensions fondamentales du champ de vitesse (vitesse et direction) de l'écoulement à l'étude.

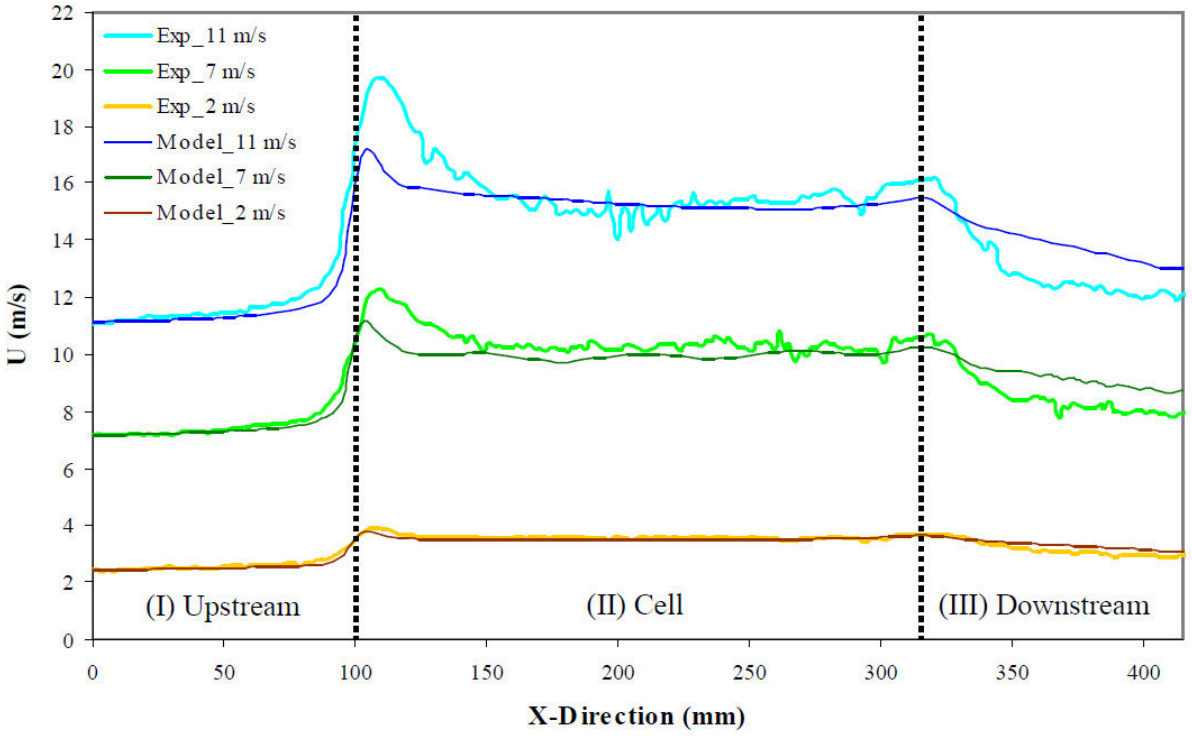

Figure 9. La vitesse d'écoulement de l'air dans le plan b (près de la surface 1R) pour faible, moyenne, et grande vitesse.

La comparaison entre la simulation et résultats expérimentaux de PIV de la vitesse d'écoulement de l'air dans le plan b (près de la surface 1R) sont présentées dans la Figure 9, à différentes vitesses d'initiale d'air de 2 m/s, 7 m/s et 11 m/s, qui représentent la ***faible vitesse***, ***vitesse moyenne*** et ***grande vitesse*** de la gamme des vitesses de refroidissement de l'air produite dans l'expérience. Un bon accord existe entre la simulation et les résultats expérimentaux. En général, les résultats ont révélé que l'écoulement d'air au début de la section d'amont est à une vitesse à peu près constante. La vitesse augmente à son entrée dans la section de la cellule, où la surface d'écoulement diminue, occupée par les trois cellules de la batterie. La vitesse de l'air se stabilise le long de la section de la cellule. Lorsque l'air passe de la section de cellule à la section d'aval, la vitesse de l'air diminue jusqu'à ce qu'elle atteigne sa vitesse initiale. Le modèle d'OpenFOAM est capable de prédire le comportement de la vitesse d'écoulement de l'air avec une bonne conformité par rapport aux résultats expérimentaux de PIV ; le pourcentage d'erreur est inférieur à 5,0%. Néanmoins, il existe des différences principalement la valeur de crête au début de la section de la cellule et la diminution de vitesse au section aval. Ces différences sont dues à la différence de géométrie de l'arête de la batterie réelle et à la modèle utilisé dans

l'expérience. Dans le modèle, les bords de la pile sont parfaitement perpendiculaires tandis que dans la réalité ils sont légèrement incurvés. Un autre facteur est que le canal d'écoulement d'air utilisé dans l'expérience n'est pas pris en compte dans le modèle. L'utilisation du canal d'écoulement d'air provoque des chutes de pression et donc une réduction de vitesse d'air plus importante en section aval.

La température de surface de la cellule prédite par le modèle électrothermique d'OpenFoam est comparée aux résultats expérimentaux présentés dans le chapitre 3. Les principaux objectifs sont de valider le modèle en termes de comportement thermique de la batterie à différents endroits de la surface de cellule, la réactivité du modèle pour prédire la température lorsque le taux de décharge change, et la capacité de simuler l'effet d'un système de refroidissement par convection forcée à différentes vitesses de l'air de refroidissement. Pour atteindre ces objectifs, l'analyse portera sur trois principaux endroits; P1, P7, P19 et, trois taux de décharge; 1C, 3C, 5C, et trois différentes vitesses de l'air de refroidissement; 2 m/s, 4 m/s, et de 6 m/s. P1 et P7 sont choisies pour représenter les endroits le plus chaud et le moins chaud de la première cellule respectivement, tandis que P19 représente l'endroit le plus chaud de la deuxième cellule. En comparant la température de P1 et P19, on peut valider le modèle électrothermique d'OpenFAOM pour prédire la différence de température pour différentes cellules, qui sont rangées à différents endroits dans le boîtier de la batterie.

La Figure 10 illustre la température de la surface de batterie et le champ d'écoulement de l'air pour (a) la première cellule et (b) la seconde cellule à la fin du processus de décharge sous le taux de décharge de 5C. Elle montre que la température à proximité de l'électrode positive et négative de la batterie est supérieure à d'autres endroits sur la surface de la cellule due à différentes densités de courant aux électrodes de la cellule. La température à proximité de l'électrode positive est également plus élevée qu'à l'électrode négative du fait de la différence de conductivité électrique. Ces résultats de simulation sont en bonne conformité avec les résultats obtenus par l'expérience. La Figure 11 montre que les résultats de simulation confirment les observations de résultats expérimentaux qu'il y a un lien étroit entre le taux de décharge et l'augmentation de la température.

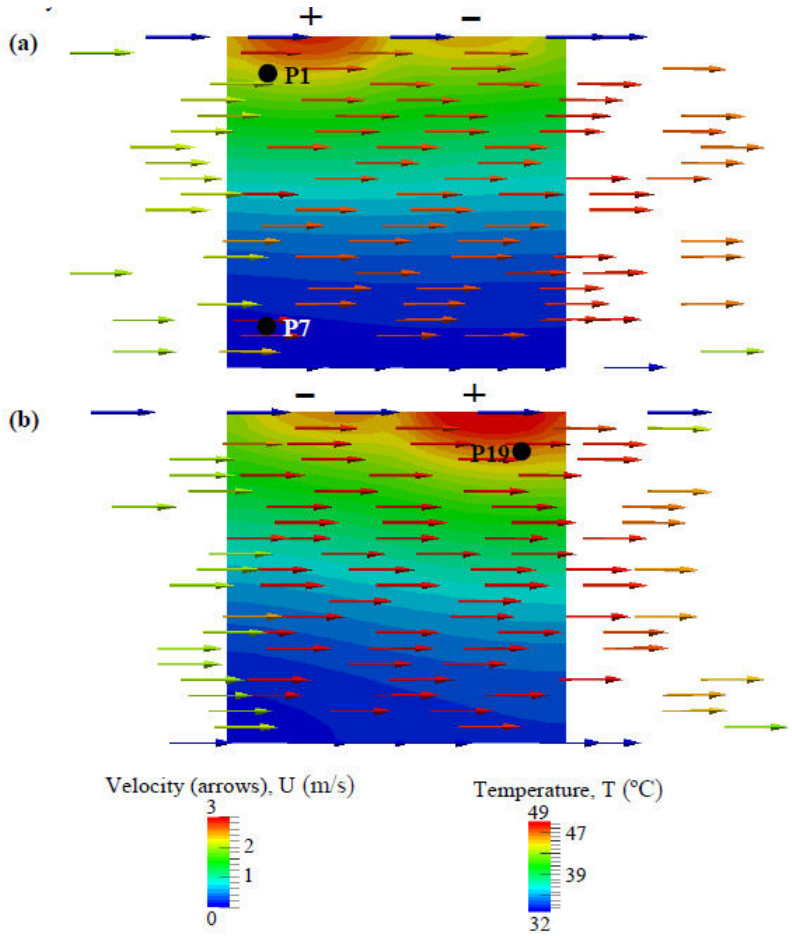

Figure 10. La température de la surface de batterie et le champ d'écoulement de l'air pour (a) la première cellule et (b) la seconde cellule.

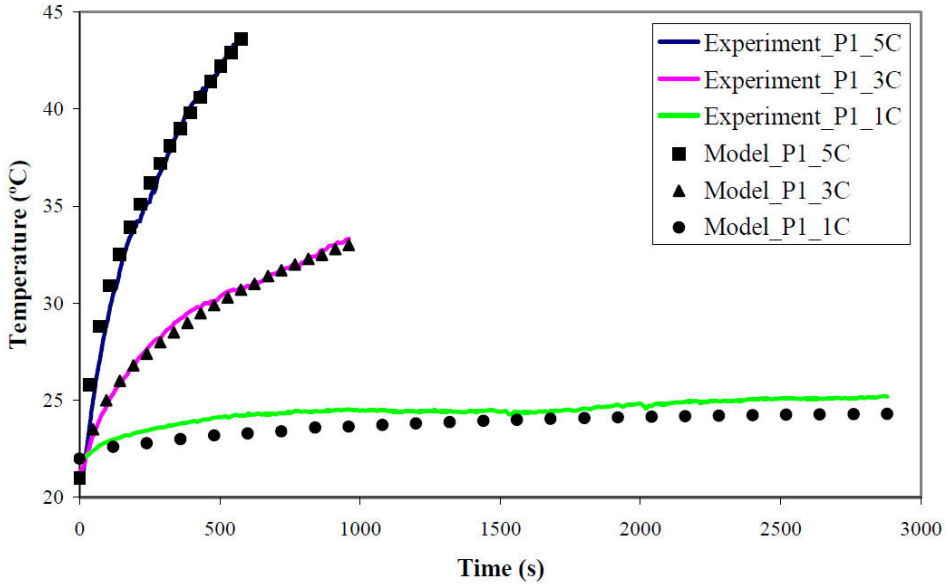

Figure 11. La comparaison de la température de P1 entre les résultats de simulation et expérimentaux au taux de décharge de 1C, 3C, et 5C avec une vitesse d'air de refroidissement de 2 m/s

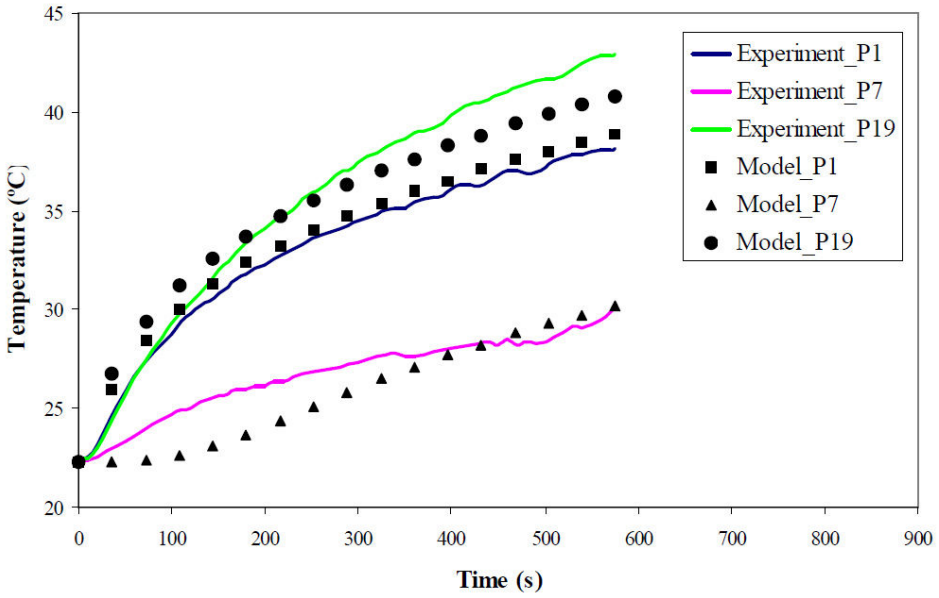

Figure 12. La comparaison de la température entre les résultats de simulation et expérimentaux au taux de décharge de 5C avec une vitesse d'air de refroidissement de 4 m/s pour P1, P7, et P19

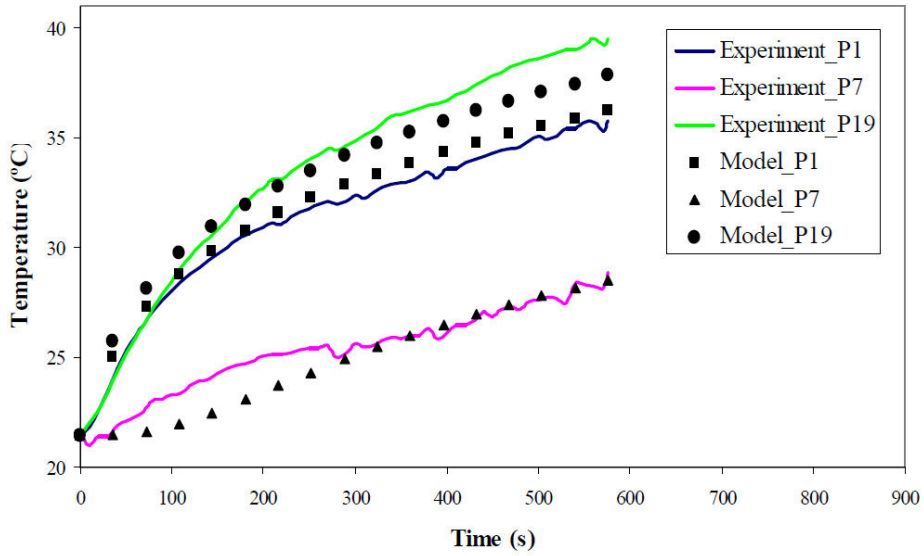

Figure 13. La comparaison de la température entre les résultats de simulation et expérimentaux au taux de décharge de 5C avec une vitesse d'air de refroidissement de 6 m/s pour P1, P7, et P19.

Le modèle électrothermique est capable de prédire la température à des endroits différents sur la surface de la cellule, et pour différentes cellules, en particulier la différence de température de la première et deuxième cellule comme le montre la Figure 12. Ce modèle est

capable de prédire l'effet d'empilement de la cellule de la batterie à l'intérieur de la boite de batterie. Néanmoins, il existe certaines différences entre l'expérience et la simulation pour la température de la cellule dans le milieu de la boite (seconde cellule), le modèle prédit une température légèrement inférieure à celle obtenue par l'expérience. La Figure 12 et la Figure 13 montrent que le modèle proposé est également capable de simuler l'effet de différentes vitesses de l'air de refroidissement sur les températures de surface de la cellule. En général, de bonnes précisions de résultats sont obtenues de la température de la surface de la cellule près des électrodes positives et négatives. Une légère différence entre le résultat calculé et expérimental peut être observée à la température de la surface de la cellule de batterie à l'endroit éloigné des électrodes de la cellule; à proximité de l'endroit avec la plus basse température, au début du processus de décharge, puis une bonne synchronisation de résultat est atteint vers la fin du processus de décharge.

En général, la différence entre les résultats prédits par le modèle et les résultats acquis par l'expérience est due à la différence de la valeur initiale de la vitesse de l'air de refroidissement et de la température imposée par le modèle et la valeur réelle au cours de l'expérience. Dans le modèle, la valeur de la vitesse de l'air de refroidissement et la température est considérée comme une constante, alors que dans la réalité, au cours de l'expérience ces valeurs varient légèrement par rapport à leurs valeurs fixes indiquées. D'autres facteurs qui contribuent à la différence des résultats proviennent de la manière dont les sources de chaleur sont introduites par deux plaques fines dans la partie supérieure de la cellule dans le modèle proposé et également de l'utilisation de thermocouples dans l'expérience qui légèrement interrompu la vitesse d'écoulement de l'air près de la surface de la cellule. Les thermocouples ne sont pas pris en compte dans le modèle.

Chapitre 5 Conclusion et perspectives

L'objectif principal de l'étude présentée dans cette thèse est d'étudier le comportement thermique des cellules de batterie au lithium-ion dans le pack de batterie par le travail expérimental. Avec le travail expérimental, l'étude se concentre sur le développement et la validation de modèles électrothermique 3D de cellules de batterie au lithium-ion et le pack. L'étude expérimentale est axée sur la distribution de température en différents endroits de la surface de la cellule de batterie, l'impact de l'état de décharge de l'abus, l'impact de différents taux de décharges constants, et également l'importance du système de refroidissement (différentes vitesses de l'air de

refroidissement) sur la température de la surface de la cellule de batterie. En outre, une étude de cas est menée afin d'évaluer le comportement thermique de la batterie utilisée dans le véhicule électrique pour compléter les cycles de conduite.

D'après les résultats expérimentaux, on peut conclure que la température de la surface de la cellule est non-homogène, avec une différence significative entre l'endroit avec la plus haute et la plus basse température. En plus, la température est plus élevée à proximité des électrodes positives et négatives, avec une température un peu plus élevée à proximité de l'électrode positive observée par rapport à l'électrode négative. Il a été constaté que le taux de décharge de la batterie a une énorme influence sur le comportement thermique de la batterie; les taux de décharge plus élevés signifient qu'une plus grande quantité de courant circule à l'intérieur de la cellule, donc plus de chaleur est générée et par conséquent l'augmentation de température est plus élevée. Par exemple, à une vitesse de l'air de refroidissement constante à 2 m/s, la température maximale de la première cellule à P1 augmente de 25,2°C à taux de décharge de 1C à 33,3°C et 43,6°C à 3C et 5C respectivement.

Le système de refroidissement joue un rôle important dans le contrôle de la température de la cellule de batterie. Dans la présente étude, la température maximale de surface de la cellule est réduite de 12°C en utilisant la vitesse d'air de 10 m/s au lieu de 2 m/s. En outre, la vitesse de l'air de refroidissement plus élevée permet également de diminuer la variation de température de la surface de la cellule. A 2 m/s, la différence entre la maximum température à P1 et P7 de la première cellule est de 11,8°C, et cette valeur diminue à 4,8°C en utilisant la vitesse de l'air de refroidissement de 10 m/s.

La décharge de la batterie au SOC inférieure à 20% révèle une augmentation soudaine de la température à tous les endroits de cellules de la batterie. Cette situation est directement influencée par la variation de la valeur de la résistance interne à différent SOC. Les expériences montrent qu'à une température constante, la variation de la résistance interne au SOC entre 100% à 20% est faible. Cependant, après 20% du SOC il y a un saut brusque de la valeur de la résistance interne. D'autre part, la résistance interne de la batterie est fortement influencée par la température. Dans la présente étude, la résistance diminue de près de la moitié de sa valeur initiale quand la température augment de 20ºC à 50ºC. La valeur de la résistance interne est entre 2.17 mΩ and 1.33 mΩ. Dans l'étude de cas, il y a juste une petite augmentation de la température de surface de la cellule de la batterie dans les deux cas, qui utilise la vitesse de l'air de

refroidissement constant et la vitesse de l'air refroidissement en fonction de la vitesse du véhicule pour le cycle de conduite NEDC et Artemis rural. Néanmoins, une meilleure répartition de chaleur est obtenu lorsque la vitesse de l'air de refroidissement en fonction de la vitesse du véhicule est utilisée.

La deuxième partie du travail présenté dans cette thèse consiste la modélisation électrothermique de batterie grâce à logiciel OpenFOAM. Le modèle considère la génération de chaleur par le courant et la résistance interne de la batterie, le transfert de chaleur à l'intérieur de la cellule de batterie par conduction et le transfert de chaleur des cellules de batterie à l'environnement par convection forcée et rayonnement. Le modèle proposé utilise la résistance interne de la batterie en fonction de la température comme le résultat acquis dans l'expérience. La source de chaleur calculée est introduite dans la cellule par deux plaques minces situées au niveau des électrodes positives et négatives dans la partie supérieure de la cellule de batterie. Ensuite, la chaleur de ces plaques est transférée à la cellule entière par le processus de conduction, avant de se dissiper dans l'environnement par le rayonnement et le transfert de chaleur par convection forcée.

Le modèle est validé en comparant les résultats expérimentaux à travers deux aspects principaux; comportement d'écoulement d'air à proximité de la surface de cellule à différentes vitesses initiales d'air de refroidissement et les évolutions de la température de la batterie à diverses endroits de la surface de la cellule de batterie sous différentes taux de décharge et des différentes conditions de convection forcée. La comparaison du modèle de OpenFOAM et résultats expérimentaux de PIV dans la présente étude montre que le modèle est capable de produire de bons résultats des caractéristiques de champ d'écoulement de l'air à l'intérieur du boîtier de batterie; à proximité de la surface de la cellule de batterie, pour différentes vitesses initiales de l'air. En termes de comportement thermique, une bonne concordance entre les résultats prédit par la simulation et les résultats expérimentaux acquis est obtenue. Les résultats des simulations confirment les observations à partir des résultats expérimentaux que la température est plus élevée près des connecteurs et il existe un lien fort entre le taux de décharge et l'augmentation de la température. Le modèle permet de prédire la température à des endroits différents sur une surface de la cellule, et pour les différentes cellules. En plus, le modèle proposé est capable de simuler l'effet de différentes vitesses de l'air de refroidissement sur les températures de surface de la cellule. De bons résultats sont obtenus de la température de la

surface de la cellule près des électrodes positives et négatives. Une légère différence entre les résultats calculés par le modèle et les résultats expérimentaux peut être observée pour la température de la surface de la cellule de batterie à l'endroit éloigné des électrodes de la cellule; près de l'endroit la plus bas température de la cellule, principalement au début du processus de décharge, puis de bons résultats synchronisation sont atteints vers la fin du processus de décharge. Le modèle est capable de prédire l'effet de l'empilage de la cellule de batterie à l'intérieur de la boîte de la batterie. Malgré cela, il existe certaines différences entre l'expérience et la simulation pour la cellule au milieu (seconde cellule), le modèle prédit une température légèrement inférieure à celle obtenue par l'expérience.

En général, la différence entre le résultat prédit par le modèle et le résultat d'expérience peut être décrite comme étant la différence des conditions aux limites entre le modèle et l'expérience. Dans le modèle, la valeur de la vitesse de l'air de refroidissement et la température au début de la section d'amont (X=0 mm) est constant, alors que dans l'expérience ces valeurs varient légèrement par rapport à leur valeur fixe indiquée. D'autres facteurs qui contribuent à la différence de résultats sont la manière dont les sources de chaleur sont introduites dans la cellule du modèle proposé, l'utilisation de thermocouples dans l'expérience interrompent légèrement l'écoulement d'air à proximité de la surface de la cellule et l'utilisation du canal d'air dans le travail expérimental qui ne sont pas pris en compte dans la modélisation.

En conclusion, le modèle électrothermique proposé dans cette étude est capable de prédire le comportement de température de surface de la cellule et les caractéristiques de débit d'air à proximité de la surface des cellules avec une bonne précision. En outre, ce modèle qui est relativement simple utilise une source de calcul raisonnable pour obtenir des bons résultats. Ce modèle électrothermique qui est développé dans un logiciel gratuit avec code source ouvert (OpenFOAM) est facile d'accès, manipulé et utilisé par d'autres chercheurs pour une analyse plus approfondie de la cellule de la batterie.

Dans la continuité des travaux présentés dans cette thèse, il est d'abord suggéré que l'étude expérimentale sont effectuée en utilisant un plus grand nombre de cellules de batterie et à différents espaces entre les cellules. Ceci permet de mieux comprendre l'effet de l'empilage des cellules, la différente sur les distances entre les cellules dans le boîtier de la batterie sur le comportement thermique de la batterie. Ces résultats peuvent ensuite être utilisés pour valider le modèle d'OpenFOAM électrothermique. De cette façon, la capacité du modèle pour prédire le

comportement thermique des cellules de la batterie à divers aspects; les différentes taux de décharge, les différentes vitesses de l'air de refroidissement, les différents endroits sur la surface de cellule, le différent nombre de cellules, et les différentes distances entre les cellules seront confirmés. L'objectif est que, dans l'avenir, le modèle proposé puisse être utilisé pour prédire le comportement thermique de la cellule de batterie pour toutes les configurations possibles de la batterie, comme l'exige les véhicules hybrides et électriques.

Pour l'avenir, il sera important d'améliorer la production de chaleur à l'intérieur de la cellule de la batterie dans le modèle électrothermique. La première approche utilisée dans cette étude a été de se servir de plaques minces attachées au sommet de la cellule à électrodes positives et négatives pour introduit la source de chaleur. Cette approche présente des faiblesses, notamment pour l'endroit de la cellule de batterie loin de cette source de chaleur. Quand la distance de cette source de chaleur augmente, le résultat calculé par le modèle devient moins précis, en particulier au début du processus de décharge. En plus du procédé actuel, il est proposé de créer une surface mince à l'intérieur de la cellule de batterie à utiliser comme source de chaleur. Cette surface mince doit être placée au milieu de la cellule, et couvrir toute la longueur et la hauteur de la cellule. En utilisant ce procédé, une meilleure répartition de la chaleur à tous les endroits de cellules sera obtenue.

En continuité avec les travaux en cours, il est suggéré d'améliorer la valeur de la résistance interne utilisée dans le modèle électrothermique, pour des résultats plus précis. Dans la présente étude, la résistance interne de la batterie utilisée est basée sur le résultat expérimental. C'est une courbe polynomiale qui correspond le mieux au résultat expérimental. En utilisant cette résistance, le modèle a tendance à prédire une température légèrement supérieure (aux endroits proches de la source de chaleur), en particulier au début du processus de décharge, où la température est relativement faible, donc valeur de la résistance interne élevée. Dans le futur, l'amélioration de la valeur de la résistance interne peut être réalisée en utilisant les résultats de températures acquises par l'expérience pour calculer la résistance interne. L'application de la résistance interne calculée par cette méthode peut conduire à une meilleure prédiction de température de la surface cellulaire.

SPIM

Thèse de Doctorat

école doctorale **sciences pour l'ingénieur et microtechniques**

UNIVERSITÉ DE BOURGOGNE

THESIS

for obtaining the degree of

DOCTOR OF PHILOSOPHY OF UNIVERSITÉ DE BOURGOGNE

Specialisation : Mechanical

by

Zul Hilmi CHE DAUD

17 December 2014

Contribution to Thermal Behaviour Study of Lithium-ion Battery for Electric and Hybrid Electric Vehicle

Members of Jury

Mr. François BADIN	PROFESSOR, IFPEN	Reviewer
Mr. Narayan KAR	PROFESSOR, University of Windsor	Reviewer
Mr. Luis LE MOYNE	PROFESSOR, Université de Bourgogne	Director
Ms. Daniela CHRENKO	ASS. PROFESSOR, Université de Bourgogne	Co-Encadrant

Acknowledgment

First of all, I would like to thank my PhD supervisors, Dr Daniela Chrenko and Professor Luis Le-Moyne, whose guidance and support throughout these three years have made it possible for the completion of this degree. Dr Alan Keromnes and Dr El-Hassan Aglzim, for their expertise in the field of science and engineering. Also, to all lecturers and postgraduate students in ISAT. Special thanks to Mr. Christian Mathieu, project manager Danielson Engineering, whose assistance ensured the successful of experiments conducted at Danielson Engineering.

I would also like to thank my family, especially my wife, Zainab Asus, and my daughter, Auji Batrisyia, who have been patient and supportive with me throughout these trying three years. Not forgetting my parents and siblings in Malaysia, although they are far away in distance, but close at heart.

Lastly, I would also like to take the chance to thank the University of Technology Malaysia and the Ministry of Higher Education, Malaysia for their sponsorship throughout my postgraduate studies.

Table of Contents

CHAPTER 1: INTRODUCTION

1.1 MOTIVATION

In recent years, the use of land vehicles has increased to satisfy the needs for mobility, which includes the transportation of people and goods. In the year 2010, there were more than 1 billion vehicles in use worldwide, increased from 980 million units in 2009 [1, 2]. This value continues to increase with the production of a total of 80 million vehicles in 2011 [3]. There are several types of land vehicles; i.e. motorcycles, cars, buses, trucks, and tractors. Conventionally, most of these vehicles are powered by internal combustion engines (ICE) which burning liquid hydrocarbon fuel like gasoline and diesel. The problem with this type of engine is that it is based on combustion, which produces not only power to propel the vehicle but is also a source of pollution such as nitrogen oxides (NO_x), carbon monoxide (CO), carbon dioxide (CO_2) and particulate matter; thus it is difficult to meet future requirements on vehicle's engine regarding noise, emission and energy consumption [4, 5, 6].

The transportation sector contributes 14% of worldwide greenhouse gas emissions as shown in Figure 1, with more than two thirds of transport-related greenhouse gas emission originating from land vehicles [1, 7, 8, 9]. The greenhouse gases are the gaseous that trap heat in the atmosphere by absorbing and emit radiation within thermal infrared radiation range. Water vapour (H_2O), carbon dioxide (CO_2), nitrous oxide (N_2O), methane (CH_4) and ozone (O_3) are the primary greenhouse gases [10]. The greenhouse gases act like a mirror and reflected a part of the heat radiation back to the earth. The higher the concentration of green house gases in the atmosphere, the more heat energy is being reflected back to the earth. The increase of green house gas concentration leads to a substantial warming of the earth called global warming [9, 11, 12]. In 2013, the Intergovernmental Panel on Climate Change (IPPC) reported a global average temperature increase of approximately 1ºC between 1880 and 2012 [12], as shown in Figure 2. The main effects of global warming include melting of polar ice in the Arctic and Antarctic region, the rise of sae level, extinction of animal and plant species, natural catastrophe, and climate changes [9, 11, 13, 14].

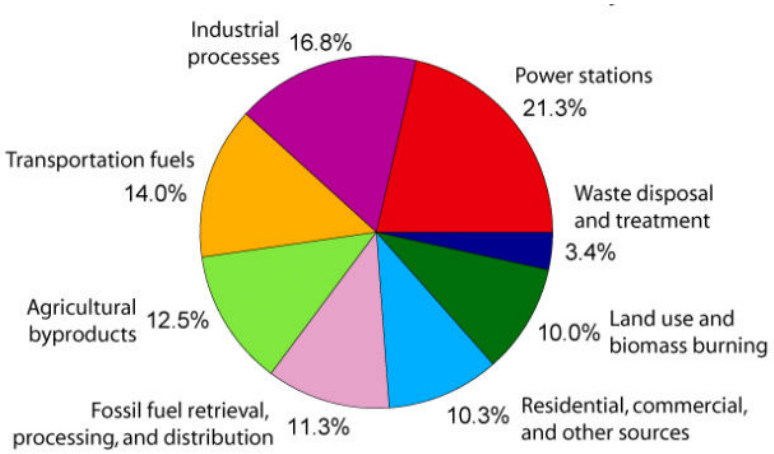

Figure 1. Annual greenhouse gas emission by sector [9]

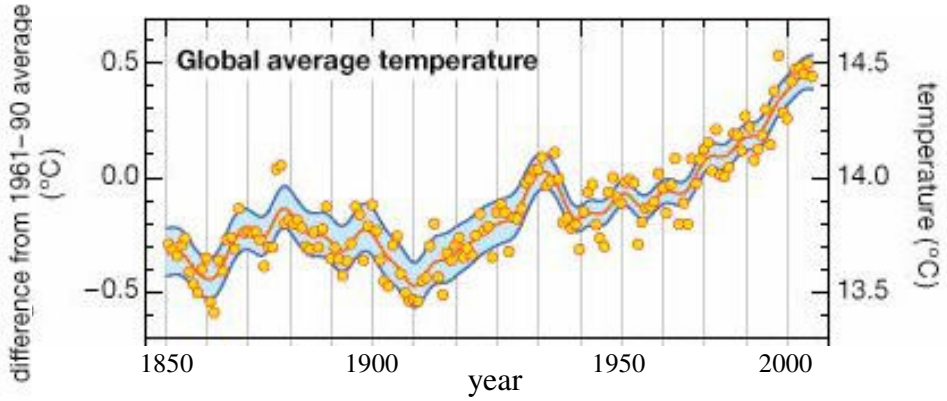

Figure 2. Changes in global average temperature [12].

The reserve of crude oil to produce gasoline and diesel fuel is depleting and not renewable. With current technology and usage, crude oil reserves are projected to last only another 40 to 50 years [1, 15, 16]. Figure 3 shows the comparison of new crude oil discoveries, actual production and prediction of the crude oil production [15]. It shows that in most of the 20th century, prospectors discovered far more oil than industrial societies could consume. By the 1970s, however a major slowdown in discoveries was observed while the oil production continues to increase until reaching the peak value around 2010. The crude oil reserve is predicted to deplete by the late 2050s. This argument is supported by Energy Watch Group (EWG) [16] in their report released in 2013 as summarize in Figure 4. Based on close

examination of data from all over the world, EWG concludes that the world reached its maximum level of oil production in 2012, and they expect a 40% decline in production by 2030. The shortage of crude oil supply, the need to meet increasingly stringent emission standards, and the threat of global warming have stimulated the change in the mode of transportation and urge carmakers to search for new, fuel efficient and lower emission vehicle technology [17, 18, 19].

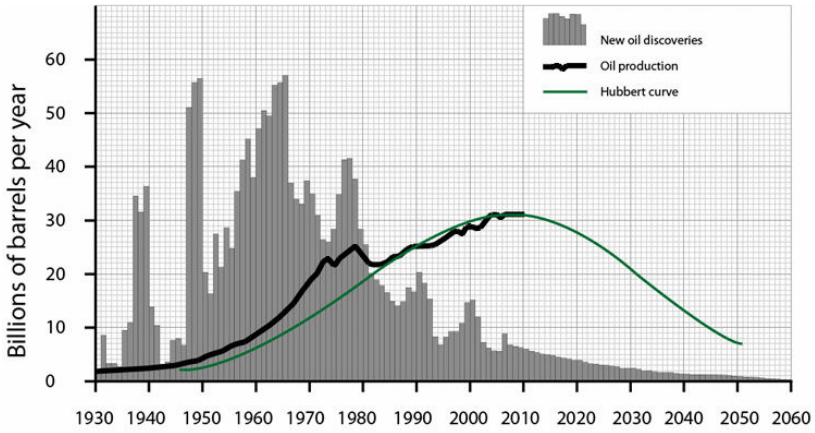

Figure 3. Global oil discoveries and production, 1930-2060 [15].

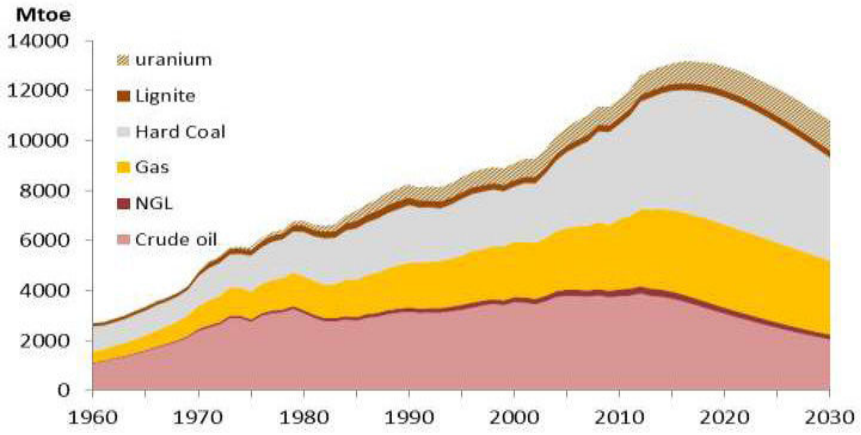

Figure 4. Scenario of world supply of fossil fuels and uranium measured in energy units (1Mtoe=1 million tons of oil equivalent) [16].

There are several conventional ways to increase fuel economy and reduce emissions, some examples would be to increase ICE efficiency, lower the overall vehicle weight, and reduce air drag and rolling resistance [20, 21, 22]. Another important solution would be the use of alternative drivetrains, such as battery electric vehicles (BEVs), hybrid electric vehicles (HEVs)

and fuel cell vehicles (FCVs) [20, 23]. Numerous researches have been done to explore their advantages and weaknesses and to ensure that they can comply with the legal restrictions on fuel economy and emissions [23]. In order to meet customer requirements regarding driving range and cost, and at the same time reduce consumption and pollutants, which both cannot be fulfilled by conventional ICE cars or EVs, the most feasible solution at present is HEVs [4, 6, 19, 24, 25]. The demand and popularity of HEVs is expected to increase in the future with the development of battery technology, control technique, and government support to the automobile owners and manufacturers, including tax rebates for purchase of these vehicles, sponsoring research conducted at universities, and by becoming an early adopter of HEVs [18, 26, 27, 28, 29]

In EVs and HEVs, batteries are among the most important key components which must continually accept and provide electrical energy by transforming chemical energy into electrical energy and vice versa [20, 22]. Batteries are desired to have high specific power, high specific energy, long calendar and cycle life, low initial and replacement cost, high reliability and high robustness. Most commonly used batteries are lead-acid, nickel-cadmium, nickel-metal hydride and lithium-ion battery [30]. Lithium-ion battery is a good choice for electric and hybrid vehicles thanks to their superior properties such as high power rating, high energy density, and high cycle life [20, 22, 31, 32, 33]. In addition, lithium-ion batteries have no memory effect and do not use poisonous metals, such as lead, mercury or cadmium. However, these batteries suffer from some problems related to battery thermal management including safety and poor low temperature performance and their price is still high [34].

Temperature is one of the parameters of a lithium-ion battery that has to be controlled carefully, because, the working temperature of the lithium ion battery has a big influence on efficiency, cell degradation, life time and safety [35]. The optimum working region is normally limited between 20°C and 65°C [36, 37, 38]. Battery cells generate heat during charge and discharge process [31]. The heat generation in the battery can increase sharply leading to over heating under certain conditions such as high discharge rate and high ambient temperature [31] and also over-charge or over-discharge during cycling [36, 37]. This is the major contribution to premature failure in battery packs in form of thermal runaway or accelerating capacity fading [36, 37]. The thermal runaway is one of the failure modes in batteries, which generally occurs when an exothermic reaction goes out of control. This can be explained by the increase of reaction rate due to an increase in temperature causing a further increase in temperature and hence a further

increase in the reaction rate [34]. The BMS (battery management system) is intended to provide a supervision of the individual cells and the battery pack in order to improve the battery performance and decrease risks. The supervision provided by the BMS might include the cell voltage, charging and discharging current, temperature and also an interface to the cooling system [35, 39, 40].

Computer modelling and simulation is a very important tool in the development of HEVs, especially during the design stage. It is useful in optimizing the product design and thus reduces cost and time used in developing HEVs before proceeding to prototype construction [41, 42]. To ensure the success of modelling and simulation, the precision of each model is very important [43]. However, high accuracy models normally require a complex structure with an immense effort on meshing and computation time. Moreover, most of existing software packages are expensive, thus limiting the utilisation only to a small fortunate group of people. The simulation model cannot be considered as complete without being validated against measured data. Only the validated simulation model can provide a good degree of accuracy and ensure the reliability of the predictions [44]. Therefore, emphasize is put on the importance of a simple but functional virtual model of HEVs that can precisely represent a real vehicle model and their components at reasonable computational time and accessible to a large number of users.

1.2 OBJECTIVES AND SCOPES

The main objective of this study are to provide the essential information on the thermal behaviour of the battery cells for automotive purpose especially for EVs and HEVs through experimental work in order to develop an effective 3D electro-thermal model for lithium-ion battery cells and pack. This experimental study is focusing on the distribution of temperature at various points of the battery cell surface, impact of different constant discharge rates, and also the importance of cooling system (forced convection with cooling air velocities) on the battery temperature behaviour. This thesis highlights the battery cell temperature behaviour under abuse discharge condition (less than 20% SOC) and the impact of stacking the battery cells inside the battery pack. Impact of different temperature and SOC on the battery cell internal resistance and a case study on the battery cell thermal behaviour used in a series HEV to complete driving cycles using different cooling strategies are also studied. Furthermore, the experimental study is extended to the characteristic of the cooling air flow behaviour inside the battery pack, especially

near the battery cell surface through particulate image velocimetry (PIV) system. The experimental study covers low, median, and high cooling air flow velocity.

Along with the experimental work, the current study focuses on the development of 3D electro-thermal CFD model. The model is implemented in a free, open source CFD software package called OpenFOAM. The target is to have a relatively simple but accurate model with reasonable computation time. In this way, this model is easy to access, manipulate and use by other researchers for further battery cell analysis. This proposed model considers the heat generation from battery current and internal resistance which is introduced to the cell through patches attached to the positive and negative electrode, heat transfer inside the battery cell through conduction and heat transfer from battery cells to environment through forced convection and radiation. Important attention is given to the battery internal resistance as its value varies with temperature. The value of internal resistance as a function of temperature is proposed and used in this model is based on the experimental results conducted in this study. The model is validated by comparing to experimental results in two main aspects; air flow behaviour close to cell surface at different initial cooling air velocities and battery cell temperature at various locations on the battery cell surface under different discharge rates and forced convection conditions. This validated model can be used as the base model for further battery cell analysis. The used of open source software creates an opportunity for other people providing free and easy access to this proposed model. In the future, they can use this model and adding or remove some features to best suit the requirement for further battery cell analysis.

1.3 ORGANISATION OF THESIS

Other than the general introduction in Chapter 1, this thesis is structured around five chapters of which the following is a brief summary.

Chapter 2 starts with a review of hybrid electric vehicles (HEVs), in terms of advantages, architectures and modelling. The chapter continues with reviews on battery use in HEVs, with focus on lithium-ion battery. This includes an introduction to battery capacity fading, battery thermal behaviour, and selected works that have been done related to the battery in both modelling and experimental works. In the modelling work, the review is focused on the battery thermal modelling at cell level and also several cells in battery packs.

Chapter 3 discusses in detail the experimental works conducted in this study. First, the experimental set-up is described, followed by the experimental results and discussions. Experiments include the battery cell surface thermal behaviour at various cell surface locations, for different discharge rates and different cooling air velocities from 2m/s to 10 m/s. The current study underlines the effect of stacking the battery cells inside the battery box from thermal behaviour point of view. Furthermore, the effect of abuse discharge condition on the cell temperature is analysed and discussed. This brings to the discussion of the effect of temperature and state of charge (SOC) on the battery internal resistance, obtained through experiment at temperatures between 20ºC to 50ºC and SOC from 100% to 5%. Generally, analysis and discussions are focused on the temperature of the hottest location near positive and negative electrodes and the coolest location on the first and second cell. At the end of the chapter, the thermal behaviour of lithium-ion battery used in HEVs to complete NEDC and Artemis driving cycle using different cooling strategies are presented.

Chapter 4 describes the electro-thermal CFD model construction and validation. This includes the introduction and description to modelling software used in this study; called OpenFOAM. The model considers heat generation inside the battery cell from internal resistance and discharge current, heat transfer inside the cell through conduction and heat dissipation to environment through radiation and forced convection with the help of cooling air flow. The battery internal resistance is modelled as a function of cell temperature. Thereafter, the model is validated using experimental results. The validation is separated into two main domains, cooling air flow behaviour near cell surface and the cell surface thermal behaviour. The air flow behaviour validation includes the air flow behaviour close to the first and second cell at air initial temperature of 2 m/s, 7 m/s and 11 m/s comparing predicted results and PIV experimental results. Furthermore, the thermal behaviour validation includes the cell surface temperature at various cell locations, for different discharge rates, under different cooling air velocities, for first and second cell.

This thesis is ended by conclusions of the study and some recommendations for future works, which are listed in chapter 5.

CHAPTER 2: LITERATURE REVIEW

2.1 HYBRID ELECTRIC VEHICLE

2.1.1 Introduction

Hybrid electric vehicles (HEVs) are a combination of two or more prime movers and/or power sources, normally conventional internal combustion engine (ICE) and electric motor (EM) [1, 6, 8, 20, 30, 45]. In general the ICE is used to convert fuel into mechanical movement and/or generate electricity in combination with an electrical generator. Other power sources can be used to replace ICE such as fuel cells, or the Stirling engine [46, 30]. Different types of electric motors can be used as electric prime movers such as standard DC, induction AC, brushless DC [30], reluctance motor, and permanent magnet synchronous motor (PMSM) [24]. An electrochemical battery is usually used as electric energy storage system and super capacitor may be used in some systems [30].

HEVs can offer the possibility of combining both zero local emissions advantages of pure electric vehicle and high energy and power density from pure ICE vehicles [30], and overcome disadvantages such as poor fuel economy and environmental pollution of pure ICE vehicles and poor operation range per battery charge in pure electric vehicles [19, 20, 25, 47]. Thomas [48] stated in his review that if all vehicles in U.S were replaced by BEVs and plug–in HEVs, then the greenhouse gas (GHG) emissions would be reduced by 25% and oil consumption by 67 %. A current study conducted by Hutchinson et al. [18] for 44 hybrid passenger cars available in U.S also agreed that hybrid electric vehicles have the capacity to substantially reduce GHG and oil consumption. This shows the importance of HEVs as a solution for the shortage of crude oil and global environment issues. Other possibilities that HEVs can offer to lower fuel consumption and emissions are engine downsizing, optimizing the energy distribution, energy recovery during deceleration/braking using “regenerative braking” system, and the elimination of idle fuel consumption using “stop-and-start” system [30]. Depending on powertrain arrangement, HEVs can be classified in general into three basic architectures which is series hybrid, parallel hybrid, and series-parallel or combined hybrid, and complex hybrid [1, 6, 30, 45, 49].

2.1.2 Hybrid architectures

2.1.2.1 Series hybrid

Series hybrid, as shown in Figure 5, is more like an electric vehicle with an internal combustion engine as an auxiliary power unit for range extender. Engine output is converted into electricity by a generator. This energy can either be used directly by the electric motor or charge the battery. Engine operation is not directly proportional to the power needed by the vehicle, so the engine can be fixed at a working point with optimal efficiency and/or emissions. With this arrangement, the transmission does not require a clutch because there is no mechanical connection between the internal combustion engine and drive axle [1, 6, 30, 49, 50]. The disadvantage of this system is it must be equipped with big-size battery pack and generator [6]. Chevrolet Volt is one example of series hybrid vehicle [1].

2.1.2.2 Parallel hybrid

On the other hand, a parallel hybrid layout is rather considered as ICE based vehicle with an additional electric component. Both ICE and electric motor are connected to a mechanical transmission and they can supply the traction power either alone or in combination. Typically, the engine can be turned off at idle and the electric motor can be used to assist acceleration. Parallel layout does not need a generator, so that fewer components compared to the series hybrid are used, but it needs a clutch since the engine is mechanically linked to the drive train [1, 6, 30, 49, 50]. As a comparison to the series hybrid, a parallel hybrid requires a smaller internal combustion engine and electric motor to provide similar performance [6, 50], but the internal combustion engine works in variant cycles as in conventional vehicles; therefore, consumed higher fuel [6]. An example of parallel hybrid would be the Honda Insight [1]. Basic parallel hybrid configuration is shown in the Figure 6.

2.1.2.3 Combined hybrid

Combined hybrid is mostly a parallel hybrid with some features of a series hybrid. Both a mechanical and an electric link exist. As in a parallel hybrid, the electric motor is used as a prime mover (along with engine) or as a generator during regenerative braking. There is also a generator to charge the battery via engine as in series hybrid [30]. Even though it possesses the

advantage of series and parallel HEVs, it is relatively more complicated and costly [49, 50]. An example of combined hybrid configuration is shown in Figure 7.

2.1.2.4 Complex hybrid

Complex hybrid features a complex configuration which cannot be classified into previous three types. Complex hybrid seems to be similar to combined hybrid, with the big difference is on the addition of the power converter to the generator and electric motor [49, 50]. Similar to combined hybrid, the draw back of the complex hybrid is its complexity and cost. Complex hybrid configuration can be found in Toyota Prius [1]. Example of complex hybrid configuration is shown in the Figure 8.

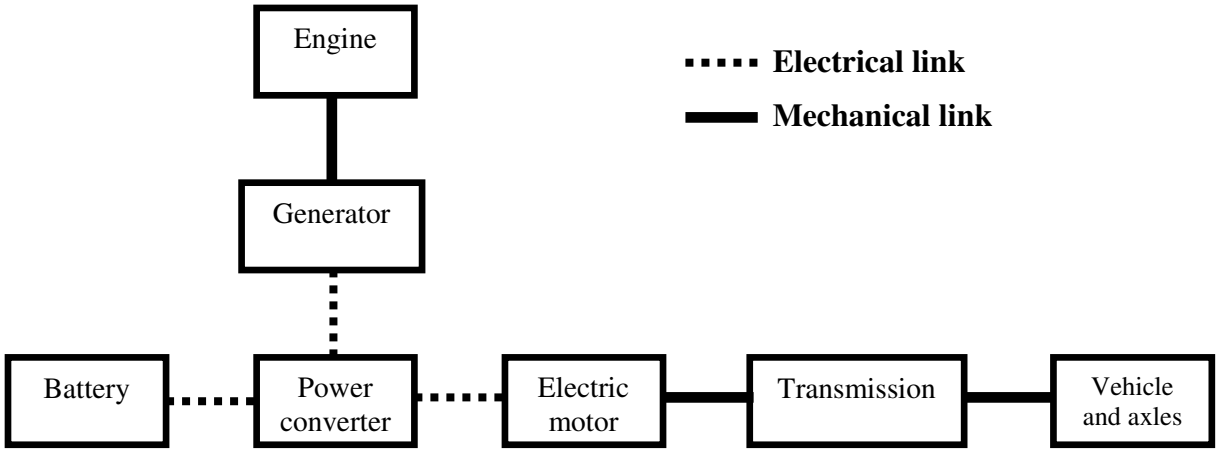

Figure 5. Series hybrid configuration.

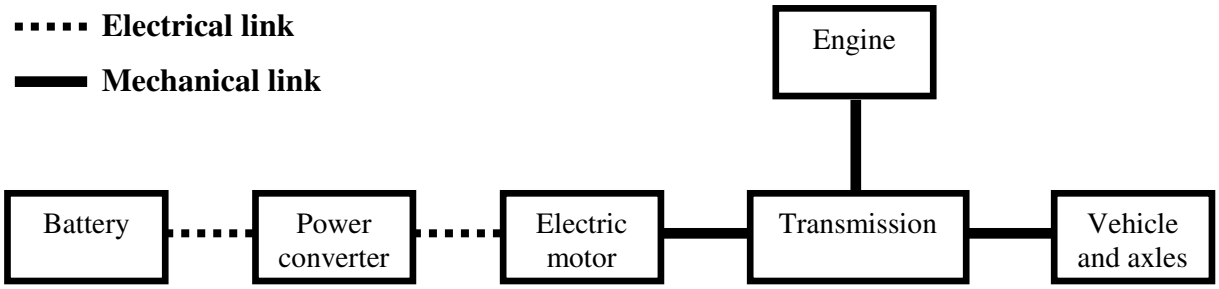

Figure 6. Parallel hybrid configuration.

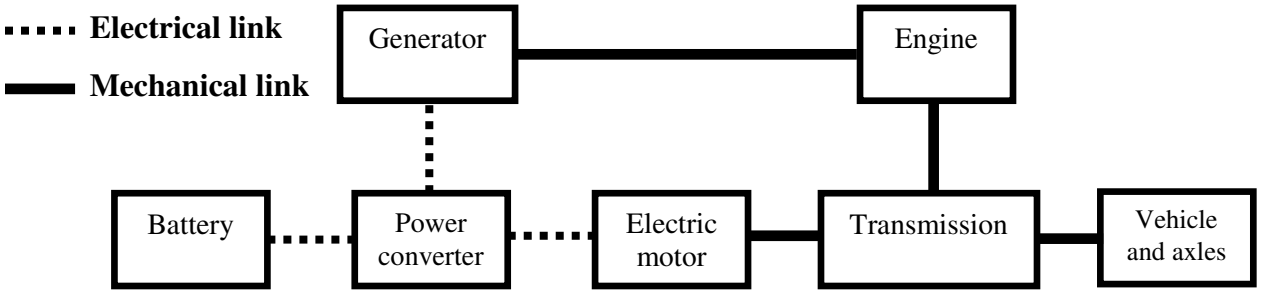

Figure 7. Combined hybrid configuration.

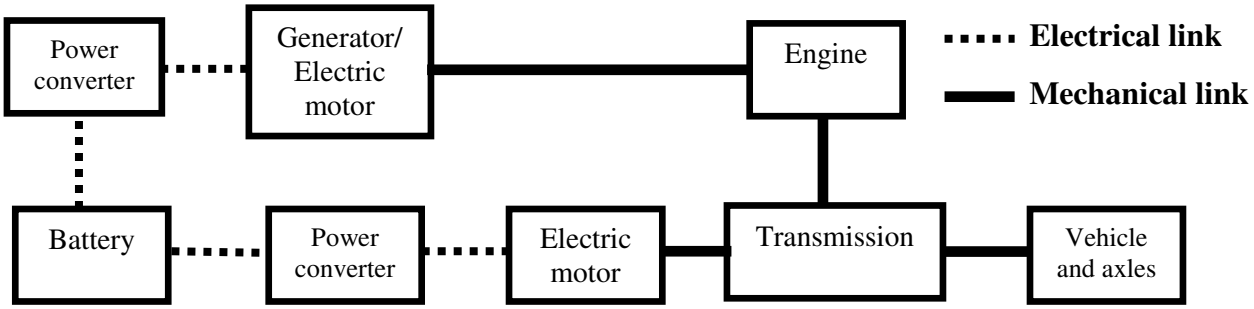

Figure 8. Complex hybrid configuration.

2.1.3 Reviews on HEVs

Emadi et al. [46] discusse the operational characteristics of the topologies for hybrid electric vehicles (HEVs), fuel cell vehicles (FCVs), and more electric vehicles (MEVs). FCVs are still considered in the stage of demonstration and are too expensive for commercialization. On the other hand, HEVs will continue to be more widely used in the future, in order to meet requirements on fuel economy, efficiency, and emissions. Ehsani et al. [24], in their review on architecture and motor drives of HEVs, have concluded that series, parallel, and series-parallel are the most commonly used architecture for HEVs. Series hybrid HEVs are mostly used in heavy vehicles, military vehicles, and buses while parallel and series–parallel are mostly used in small automobiles HEVs. The most promising way to meet the energy and power demands in HEVs utilisation is by the combination of chemical batteries and ultracapacitors as well as integrated compact and lightweight vehicle structure.

Amjad et al. [26] suggest that in the development of future HEVs in order to achieve the expected efficiency and performance, some important parameters should be considered including weight, volume and cost reduction combined with optimized control strategy. It is also very important to improve the performance of the energy storage system. Mainly improve battery life, number of deep discharge cycles, and charge-discharge efficiency. Reviews from [24, 26, 27, 46] show that the battery is a key component in the success of the development of HEVs. It is important to improve the performance of the battery in terms of life span, number of charge – discharge cycle, charge-discharge efficiency, safety, temperature, cost, and size and weight of battery pack; which are considered as the major challenges in the development of automotive batteries nowadays [1].

Then, Bayindir et al. [27] stated in their overview of hybrid electric vehicle, that the popularity of HEVs is expected to increase in the future with the development of battery technology, control technique, and government support to the automobile owners and manufacturers. Hutchinson et al. [18] analyse the data gathered from 44 hybrid passenger cars available in US, and they agree that the hybrid vehicle market share is on the rise because of advance in technology and government incentives.

2.1.4 HEV modelling and simulation

In terms of HEV modelling, Powell et al. [51] develop a vehicle model for a parallel hybrid electric vehicle (PHEV) that includes vehicle components such as internal combustion engine, engine clutch, CVT, electric motor, lead-acid battery, vehicle driveline, hydraulic brakes, and vehicle longitudinal and tire dynamics. This model offers the potential to evaluate the effects of using different components (engines, motors, etc.) on the behaviour of the vehicle without the need to redesign the entire model. Kuchita et al. [52] develop a virtual powertrain model for prediction of fuel consumption, exhaust emission and driving comfort of a vehicle. Each vehicle component, such as engine, transmission, vehicle dynamic, and control system, is developed as a separate computational model, and can be combined to create a virtual vehicle.

A lot of models available [4, 20, 28, 30, 42], including calculation of traction power to propel the vehicle, electric motor model, energy storage model, ICE fuel consumption model, generator, and control strategy or controller model. The tractive effort which is the force propelling the vehicle forward, transmitted to the ground through the drive wheel is explained in

detail in [20, 22, 30]. To propel a vehicle with a mass m_v, at a velocity V and up a slope of angle θ, the tractive effort has to overcome the aerodynamic drag, overcome rolling resistance, provide the force needed to overcome the component of vehicle's weight over a slope, and accelerate the vehicle, if the velocity is not constant [22] as shown in Figure 9. The equations of tractive effort that will be used later in section 3.7 as explained in [20, 22, 30] are as follows:

a) Aerodynamic drag force, F_a

This is the force due to the friction of vehicle body moving through the air. The aerodynamic drag force is calculated using this equation:

$$F_a = \frac{1}{2} \cdot \rho \cdot A \cdot C_d \cdot V^2 \quad (1)$$

where ρ stands for air density [kg.m^{-3}], A is the vehicle frontal area [m^2], C_d represents the drag coefficient constant, and V is the velocity of the vehicle [m.s^{-1}]. The value of the drag coefficient C_d depends on the vehicle shape. The typical value of C_d for a saloon car is around 0.3 and 0.7 for buses. The value of air density varies with temperature, altitude and humidity. However, 1.25 kg.m^{-3} is a reasonable value to use in most cases.

b) Rolling resistance force, F_r

The rolling resistance is primarily due to friction of the vehicle tyre and the road. It is proportional to vehicle weight. It is often modelled as:

$$F_r = \mu_r \cdot m_v \cdot g \quad (2)$$

with μ_r representing the coefficient of rolling resistance, m_v the mass of the vehicle [kg], and g the acceleration due to gravity [m.s^{-2}]. The coefficient of rolling resistance μ_r depends mostly on vehicle speed, type of tyre, tyre pressure, and road surface condition. For many applications, particularly when the vehicle speed remains moderate, the rolling resistance coefficient may be assumed to be constant [30]. Typical value of μ_r is around 0.015 for a radial ply tyre.

c) Hill climbing force, F_g

This is the force needed to drive the vehicle up a slope as a function of the component of the vehicle weight. The equation for modeling this force is as follow:

$$F_g = m_v \cdot g \cdot \sin(\theta) \quad (3)$$

d) Acceleration force, F_{acc}

This is the force needed to accelerate the vehicle in order to change the velocity of the vehicle. It can be divided into 2 types; linear acceleration force (F_{la}) and rotational acceleration force ($F_{\omega a}$) which is the force needed to make the rotating parts turn faster. Linear acceleration force is calculated using this equation, $F_{la} = m_v.a$; where a is acceleration in $m.s^{-2}$. Rotational acceleration force can be calculated as, $F_{\omega a} = m_{\omega}.a$; where m_{ω} is mass of rotating parts. So the total acceleration force for the vehicle is:

$$F_{acc} = F_{la} + F_{wa}$$
$$= (m_v + m_{\omega}).a \quad (4)$$

Rotational acceleration force is much smaller than the linear acceleration force, but cannot be neglected. It is a reasonable approximation to take into consideration that the rotational mass is about 5% of the mass of vehicle [22].

e) Total Tractive effort, F_t

The total tractive effort is the sum of all these forces:

$$F_t = F_a + F_r + F_g + F_{acc} \quad (5)$$

where F_a is the aerodynamic drag force, F_r the rolling resistance force, F_g the hill climbing force, and F_{acc} the acceleration force, This is the force needed at the tyres to move the vehicle with mass m_v, velocity V and acceleration a, at slope angle of θ. Force is in unit Newtons. The tractive power needed (power demand) at the tyres in unit Watt is, P_t:

$$P_t = F_t \cdot V \quad (6)$$

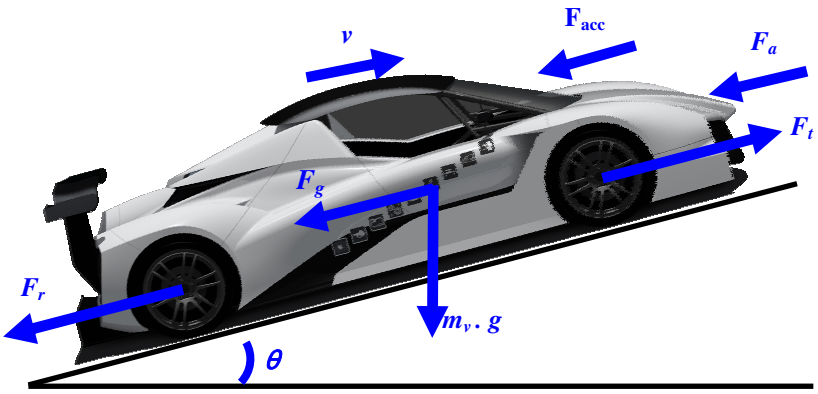

Figure 9. Schematic representation of the forces acting on a vehicle in motion.

2.2 INTRODUCTION TO BATTERY

2.2.1 Types of battery

In hybrid electric vehicles (HEVs), battery is the most important key component which must continually accept and give out electrical energy by transforming chemical energy into electrical energy and vice versa [22]. Batteries are electrochemical devices. During charging process, it converts electrical energy into potential chemical energy, and converts chemical energy into electric energy during discharging [20].

A battery is composed of several cells joined together [20, 22]. A cell is an independent and complete unit that consists of positive and negative electrode joined by an electrolyte [20, 22], as shown in Figure 10. The conversion of chemical energy to electrical energy occurs at these two electrodes, also called as cathode and anode [53]. The cathode is the electrode where reduction (gain of electrons) takes place. The anode is the electrode where oxidation (loss of electrons) takes place. The cathode becomes the positive electrode when discharging, and negative electrode when charging. On the other hand, the anode becomes negative electrode when discharging, and positive electrode when charging [30]. The chemistry of these two electrodes will determine the nature of the electrochemical reaction [53].

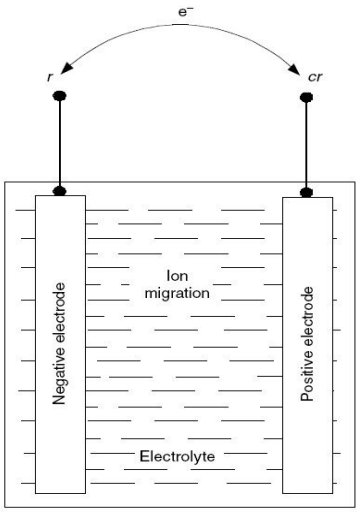

Figure 10. A typical electro chemical battery cell [20, 22].

In HEVs, the battery is desired to have high specific power, high specific energy, long calendar and cycle life, low initial and replacement cost, high reliability and high robustness.

Most commonly used batteries are lead-acid, nickel-cadmium, nickel-metal hydride and lithium-ion battery [30, 53]. Figure 11 shows the volumetric energy density against gravimetric energy density for common batteries [1, 26, 53], and Figure 12 shows the Ragone plot of specific power density vs. specific energy density of various electrochemical energy storage and conversion devices [1].

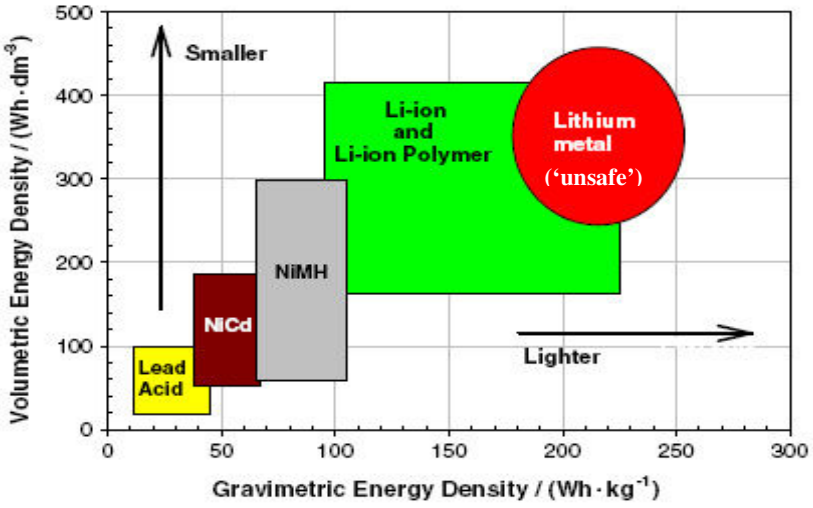

Figure 11. Plot of volumetric energy density against gravimetric energy density for common batteries [1, 26, 53].

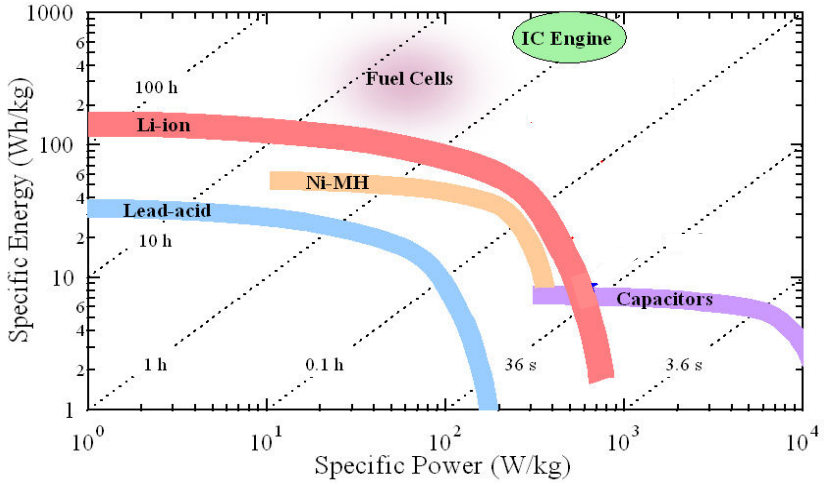

Figure 12. Ragone plot of specific power density vs. specific energy density of various electrochemical energy storage and conversion devices [1].

a) Lead-acid battery

Lead-acid battery is the oldest type of rechargeable batteries with relatively high power-to-weight ratio, capable of supplying high surge currents. However, its energy-to-weight and energy-to-volume ratios are very low such that this type of battery cannot provide enough energy and power in the limited space of the HEV.

Lead–acid batteries used a sponge metallic lead as anode, a lead dioxide as cathode, and sulfuric acid as electrolyte [30]. In the process of producing electrical energy, the sulfuric acid will combine with the lead and the lead oxide to produce lead sulphate and water. The overall chemical reaction is shown in equation 7 [22]. With the advantage of low cost, robustness, and reliability, it has been a successful commercial product for over a century and is still widely used as electrical energy storage in conventional vehicles, and also in some HEV applications [20, 30]. Their main disadvantages are the low cycle life and the low energy density [20, 22, 30].

$$Pb + PbO_2 + 2h_2SO_4 \longleftrightarrow 2PbSO_4 + 2H_2O \quad (7)$$

b) Nickel-cadmium battery

Nickel-cadmium batteries use cadmium as anode, nickel oxyhydroxide as cathode, and potassium hydroxide as electrolyte [30]. The chemical reaction to obtain the electrical energy is shown in equation 8 [22]. Compared to lead-acid battery, a nickel-cadmium battery has a longer life cycle and higher specific energy [30], nearly twice the value of specific energy of lead acid battery [22]. However, it has several disadvantages such as high initial cost, relatively low cell voltage, environmental hazard of cadmium [20, 30] and a well-known limitation so-called "memory effect" [30]. This term refers to a temporary loss of cell capacity, which occurs when a cell is recharged without being fully discharged; this may lead to shorten the battery life [30].

$$Cd + 2NiOOH + 2H_2O \longleftrightarrow Cd(OH)_2 + 2Ni(OH)_2 \quad (8)$$

c) Nickel-metal hydride battery

Nickel-metal hydride used alloys with metals that can store hydrogen atoms as anode, nickel oxyhydroxide as cathode, and potassium hydroxide as electrolyte [30]. The chemical reaction for this battery is presented in equation 9 [22]. Nickel-metal hydride battery has a higher cost and lower life cycle compared to nickel-cadmium battery, but the life cycle is still higher than lead-

acid battery [30]. On the other hand, it has advantages over nickel-cadmium battery as higher energy density and power density with less memory effect [30]. Its energy density is equivalent to Li-ion battery, but the drawback is that it has much higher self-discharge rate. In addition, the current that a nickel-metal hydride battery can provide is very limited so it may better fit some little digital devices like cameras and cell phones instead of a HEV [54].

$$MH + NiOOH \longleftrightarrow M + Ni(OH)_2 \tag{9}$$

d) Lithium-ion battery

Lithium-ion battery same as other types of batteries is an electrochemical device composed of two electrodes separated by a separator and an electrolyte. Electrodes (positive and negative) are electronic conductors that contain the active material, while the electrolyte ensures the ionic conduction between both electrodes [33]. A conventional lithium-ion cell uses carbon as anode, metal oxide as cathode and lithium salt in an organic solvent as electrolyte [34]. A separator, which is a very thin sheet of micro-perforated plastic, is located between the anode and the cathode to separate the positive and negative electrodes while allowing ions to pass through [34]. Equation 10 gives the overall chemical reaction [22], while Figure 13 shows the schematic of the principle lithium-ion battery [34].

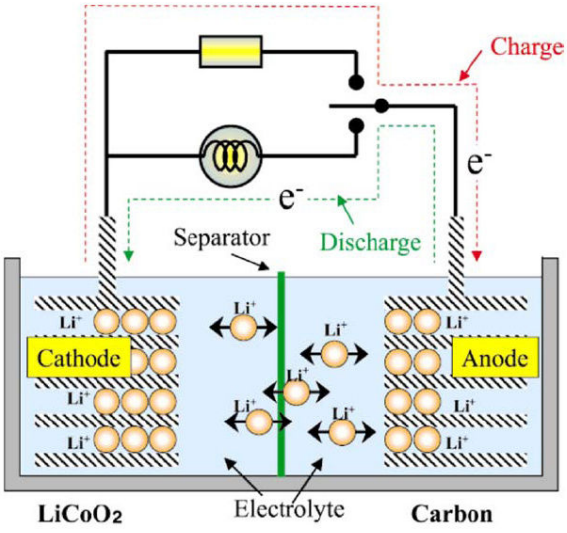

Figure 13. The schematic of the principle lithium-ion battery [34].

The lithium-ion battery is likely a good choice for HEVs for its superior properties such as high power rating, high energy density, and high cycle life [20, 22, 31, 33, 40] and it is considered as the most promising technology in the next decades [7]. The price of lithium-ion batteries is projected to decline rapidly in line with the impressive technology progress and high volume battery production, and in 10 years time they will likely be the cheapest rechargeable batteries [1, 7]. By the year 2020 the market for lithium-ion batteries in the automotive sector is projected to reach over $50 billion [1].

$$xLi + M_y O_z \longleftrightarrow Li_x M_y O_z \tag{10}$$

2.2.2 Battery modelling methods

There are basically four main methods in battery modelling [54, 55]: mathematical models, electrochemical models, polynomial-based models and electrical models. Mathematical models are the easiest but the least accurate model [56]. In these models, an empirical or mathematical method like stochastic approach is used to predict system-level behaviour such as battery runtime, efficiency, or capacity [55]. It cannot provide any I-V information and most of them only work for specific applications and provide inaccurate results [55]. An example of the simplest and oldest mathematical methods would be the Peukert's equation that integrates the battery capacity as a function of the discharge rate of the battery [35].

Electrochemical models which are based on chemical reaction occurring inside the battery cells [35] are complex and time consuming but able to produce more accurate result. Normally electrochemical models are suitable to be used in physical design optimization of batteries, characterize the fundamental mechanisms of power generation, and relate battery design parameters with macroscopic information such as battery voltage and current and microscopic information including the concentration distribution inside the battery. These models require long simulation time, complex numerical algorithms, and battery-specific information that is difficult to obtain. Hence, the electrochemical models are not suitable for vehicular applications, since, the control systems usually need real time data [35].

Polynomial-based models used a simplistic expression containing state of charge (SOC) to represent a battery. Battery parameters such as the open circuit voltage are a function of a fixed quantity; mostly state of charge. These models have limited capacity in presenting the I-V

information [55]. Electrical models are based on a combination of electrical components such as voltage sources, resistors, and capacitors to capture the electrochemical processes and dynamics of a battery [35, 56]. Electrical models are more realistic, intuitive, and easy to handle as compared to other models. Furthermore, it can be applied to any battery model irrespective of its chemistry, configuration and rate of discharge; by using suitable combination of parameters [54]. Some electrical battery models are explained in section 2.3.4 and will be used later in section 3.7.

2.2.3 Battery capacity fading

Spotnitz [57] refers to a battery capacity fade as a phenomenon of the loss in discharge capacity over time. These losses are called "calendar life losses" and concern to the discharge capacity loss when the battery is inactive or stored and "cycle life losses" when the battery is in use [57, 58]. The capacity loss can be further divided into two categories: irreversible and reversible capacity loss. Reversible capacity loss (self-discharge) can be easily recovered by charging the battery. On the other hand, the irreversible capacity loss which is associated with degradation of battery; cannot be recovered. The amount of these losses varies with the battery applications [57].

Over the years, researchers have conducted experiments and analysis in order to better understand the main factors that influence the battery capacity fading and their impact on the battery performance. There are several factors that influence the battery capacity fading: temperature [59, 60, 61, 62, 63, 64], current discharge rate [58, 59, 61, 62, 65], state of charge [59, 60, 62], and the cycle number [65, 64]. The capacity fades increase when the cycle number increases. Excessive discharge rate can accelerate the battery capacity degradation. Other factors that can shorten the battery life are over-discharge and over-charge of the battery [61]. In comparison, over-charge will lead to more significant damage to the lithium-ion battery compared to over-discharge [61].

Ramadass et al. [63] develop a mathematical model for capacity fading of lithium-ion battery cells based on semi-empirical approach. The developed model is based on the performance analysis of 18, 650 cells for the battery state of charge and resistance as a function of cycle number. This mathematical model is capable to predict the battery capacity fading as a function of charge-discharge cycle number and battery temperature. Hoke at al. [60] present a method for charging the battery of electric vehicle (EV) in order to minimize the charging cost

by taking into consideration the electricity cost and estimated costs of battery degradation using a simplified lithium-ion battery lifetime model.

2.3 BATTERY THERMAL BEHAVIOUR

2.3.1 Introduction

The temperature of each battery cell is different throughout the battery pack depending on where it is located. The difference in temperature between the individual cells in a battery packs might be the result of the difference of ambient temperature at the various points of the battery pack surface, non-uniform impedance distribution among cells, and difference in heat transfer efficiency among cells [37].

Non-uniform impedance may result from defects in quality control and also difference in local heat transfer rate, while the differences in heat transfer efficiency depend on where the cell is positioned in the battery pack. Cells at the edge are normally cooler than cells at the centre due to a better heat transfer to the environment. This temperature difference may then lead to the capacity imbalance among the cells that further causes the cells to be over-charged or over-discharged during cycling [36, 37]. This is the major contribution to premature failure in the battery packs in form of thermal runaway or accelerating capacity fading [36, 37].

The thermal runaway is a condition where the battery cell is overheating and igniting. It starts with a cell that is thermally unstable due to over-charge or over-discharge, and the high temperature produced by this cell leads to electrical and thermal transient in the neighbouring cells which results in a chain reaction where the entire pack explodes [66]. It also can be described as a failure mode that occurs when the exothermic reaction goes out of control. This is explained as an increase of reaction rate due to the increase in temperature, causing a further increase in temperature, and thus a further increase in the reaction rate, etc. [34].

Lithium-ion batteries optimal operation temperature is in the range of 20°C to 65°C [36, 37, 38]. In this range, they can achieve a good compromise between the battery performance and life span. The temperature difference between cells inside pack is desired to be as small as possible; less than 5°C [36]. In order to achieve this, a battery thermal management system is necessary. It is meant to regulate the batteries to operate in the desired temperature range and to reduce uneven temperature distribution between cells [36]. A thermal management system may use air or liquid for heating, cooling, and ventilation/insulation, or thermal storage such as phase

change materials (PCM), or a combination of these methods. It can be classified then as passive when only the ambient environment is used or active if it implements special component/system to provide heating or cooling at cold or hot temperature [36]. Liquid cooling offers higher cooling capacity than air cooling at similar parasitic pump/fan power, but this system is more complex, heavier, consume more volume, and costlier due to the use of pump, tank, and heat exchanger. Maintenance and repair of liquid cooling systems are also complicated and costly [67, 68, 69]. On the other hand, PCM systems have high thermal energy storage capacity with the use of latent heat, thus can maintain the battery temperature relatively constant during operation [69, 70]. However, the weak point that has limited widespread use of PCM system is because of its insufficient long term thermal stability, lack of cost effectiveness and complexity of structures [67, 69]. The air cooling system is the simplest and most efficient way of cooling. Anyhow, the drawback of air cooling system is that the insufficient convection heat dissipation from battery might occur under stressful and abuse conditions [69].

2.3.2 Battery safety issues

Wang et al. [34] review the state of art of lithium-ion battery safety and related thermal runaway prevention techniques. Authors have listed the problems of fires and explosions in lithium-ion battery, reported from all over the world for both small batteries like in mobile phone and laptop, and larger battery size used in EVs, HEVs, and cargo plane. Even though the probability of fires and explosions of lithium-ion batteries is small, but these widely-publicized incidents have arise concerns among consumers, and this gives a bad image on safety issue in lithium-ion technology.

Wang et al. [34] in their review also discuss the methods for battery safety which can be divided into two main categories; inherent safety method and safety device. Inherent safety method is done by modification of materials of cathode, anode, and electrolyte and also by using flame retardant additive in order to suppress the activity of the materials. As for the safety device, the idea is to find a way to release high pressure and heat before thermal runaway occurs. Among other techniques proposed are the use of safety vents, thermal fuses, positive temperature coefficient (PTC), shutdown separators and also battery management system (BMS).

Overall battery cost, safety factor, battery lifetime, reducing the size and weight of the battery pack, operating temperature, shortening the charging time and providing better charging facilities are considered as the major challenges in the development of battery technology [1, 53].

Furthermore, Ritchie and Howard [71] in the review on recent developments and likely advances in lithium-ion batteries concluded that cost and safety are still among the main factors that limit the use of lithium-ion battery in HEVs.

Controlling battery operational temperature is very important in order to extend the lifetime of the battery, while controlling voltage from exceeding the allowed range which is within 2.5 V to 3.65 V [53] is important to avoid premature ageing which can lead to safety risks [53]. Thermal modelling of the battery packs is very important, helping in designing battery management systems for better performance such as to prevent battery degradation and extend battery lifetime [39] and also preventing safety risks such as thermal runaway [35].

2.3.3 Battery experimental works

Recently, several experimental works regarding battery cell surface temperature have been reported. Some works consider a homogeneous temperature throughout the cell surface for a single cell [72, 73] and also cells in the pack [74]. The battery cell is tested under different discharge rates with natural convection cooling system. The test set-up conducted by Shadman Rad et al. [73] is shown in Figure 14. Temperature profile for different discharge rates and the effect of different air ambient temperatures are shown in Figure 15.

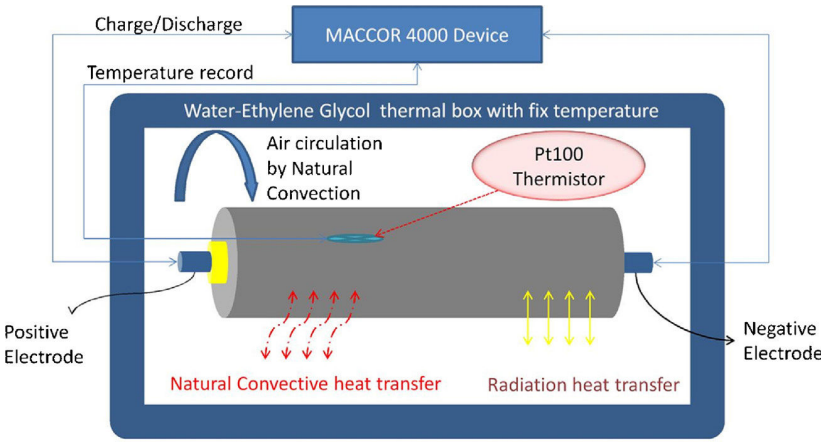

Figure 14. Experiment set-up [73].

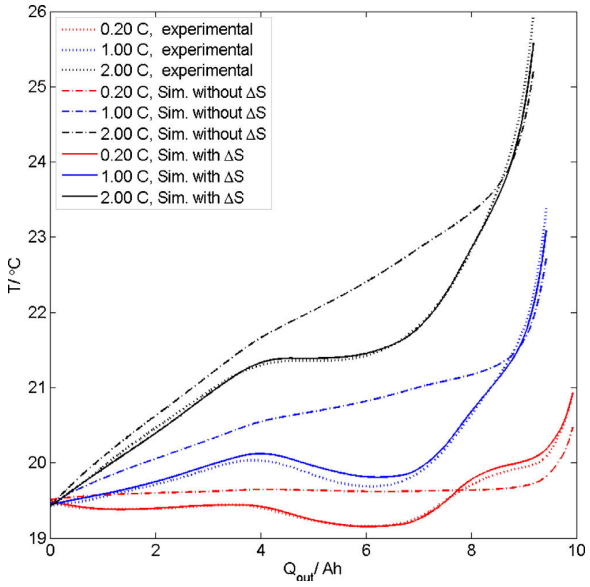

Figure 15. Temperature profile during discharge ambient temperature of 20ºC [73].

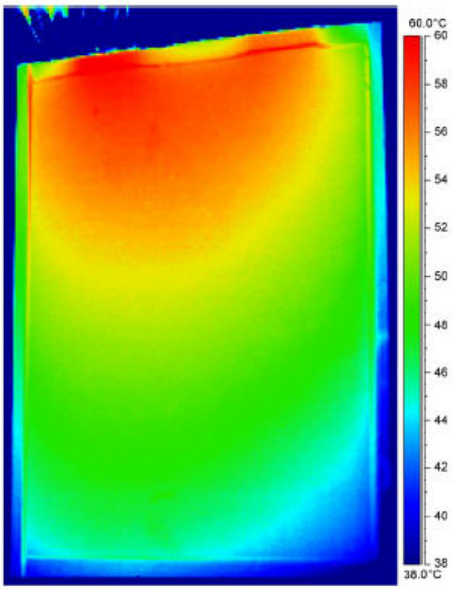

Figure 16. Temperature distribution at 5C discharge rate [75].

Experiments that point out the difference of temperature throughout the cell surface can be found in [31, 75, 76, 77, 78, 79, 80]. Results for a single cell are presented in [31, 75, 78, 79] while the result for battery cells in pack are presented in [76, 77, 80]. In [75, 78, 79], infrared

image is used to represent the cell surface temperature at the end of discharge processes. Experiments are conducted for a single cell at different discharge rates, but only natural convection is considered. Figure 16 shows the temperature distribution on the battery cell surface at 5C discharge rate.

=

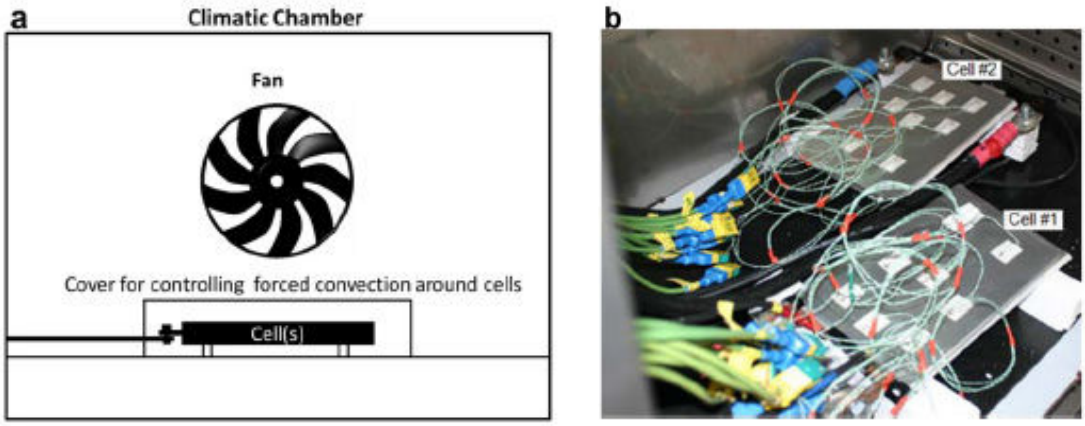

Figure 17. a) Schematic of Li-ion cell test set up, b) instrumented cell in climatic chamber [31].

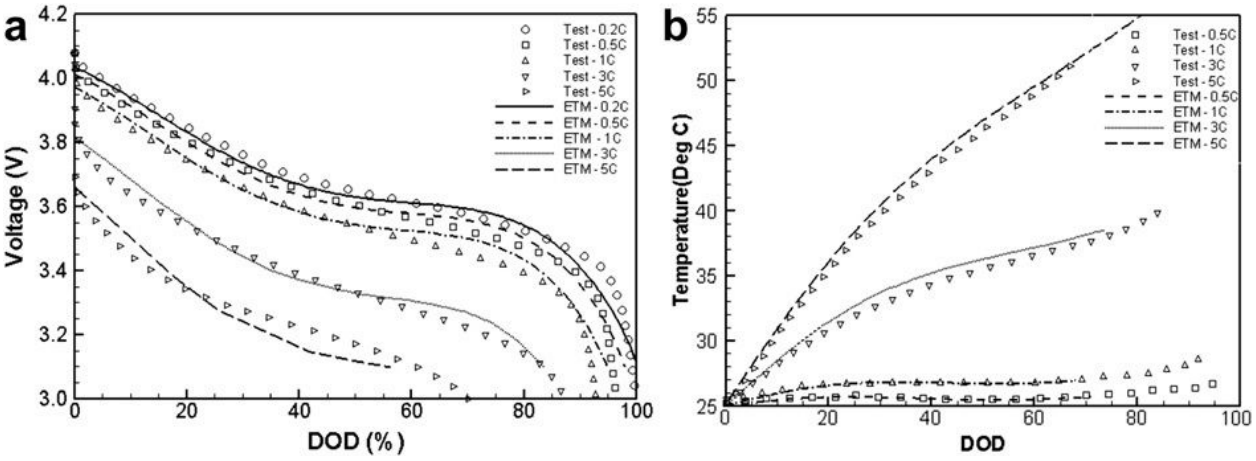

Figure 18. a) Average voltage, and b) average temperature versus DOD at various discharge rates [31].

Chacko and Chung [31] have conducted the experiment in a climatic chamber as shown in Figure 17. This test condition is to ensure well-defined free convective cooling and protect the cell from forced convection. The battery cell is tested under several constant current charge-

discharges rates at constant reference temperatures. Result for average voltage and average temperature versus depth of discharge (DOD) at various discharge rates are shown in Figure 18 (a) and (b) respectively.

Awarke et al. [76] measure cell surface temperature at various locations during a constant current discharge under natural convection for 7 battery cell in a battery module. Pesaran and Keyser [80] have presented their study on thermal characteristic of selected EV and HEV batteries; Lead acid, Nickel zinc, and Lithium-ion battery. In this study, they have used a calorimeter to measure the heat capacity and heat generation from batteries, and infrared equipment to obtain thermal images of battery modules under load. Thermal imaging shows that the temperature distribution in modules/cells depends on their design. Normally, the temperature is higher at the centre cell and where the cells meet each other, as shown in Figure 19. This is justified by the smaller surface area exposed to the ambient air. With a better design, a more uniform temperature distribution can be achieved [80].

Guiliano et al. [77] use thermochromic liquid crystal (TLC) thermography for cell surface temperature measurement of five battery cells in a pack. In this work, cooling plates, inserted between adjacent cells that are connected to water, are used as cooling system. Figure 20 shows five TLC strips attached to the surface of the cell. The TLC strips have the temperature ranges of 5ºC. Figure 21 shows the cell surface temperature at 6C discharge with and without cooling system. The activation of the cooling system causes the temperature profile invert. Red colour indicates lower temperature while blue colour indicates higher temperature.

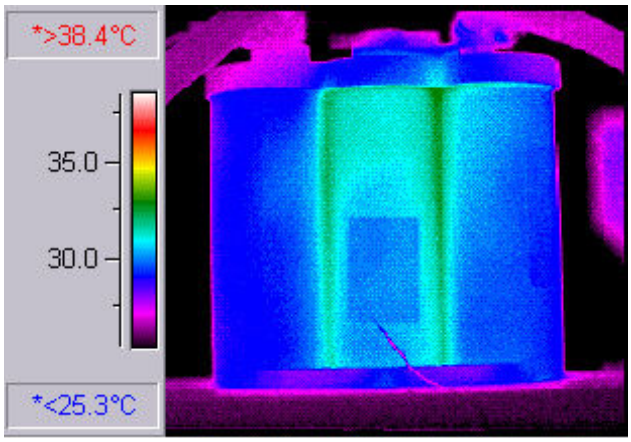

Figure 19. Temperature distributions in modules [80].

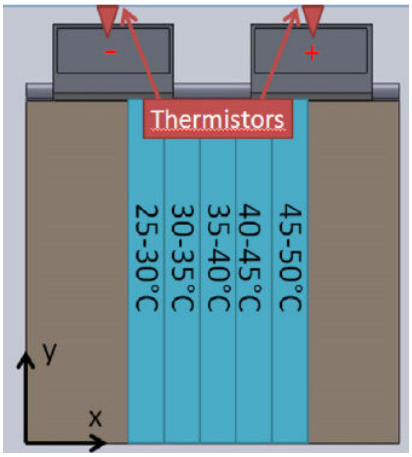

Figure 20. Schematic view of the front cell of the stack with five TLC strips attached to the surface of the cell [77].

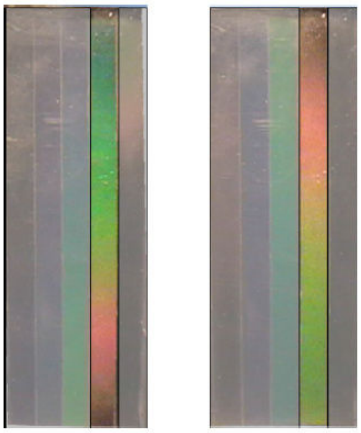

Figure 21. Left: temperature visualization 18 min at 6C test without cooling. Right: the same image 34 min into the test with cooling [77].

Sato [81] has conducted thermodynamic studies and experiments on lithium-ion batteries. The heat generation factors are divided into three main categories: reaction heat, polarization heat, and Joule heat. The reaction heat during charging is the heat absorbed by the battery through the process of intercalation of lithium ions by the negative electrode. During discharge process, the same amount of heat is generated. The polarization heat exists because energy is required for the diffusion and movement of atoms in the battery reaction process. The Joule heat is the heat generation that is dependent on the battery's internal resistance. The electrolyte that is commonly used in lithium-ion batteries has an electric conductivity that varies with temperature. The temperature decrease will result in an increase of the battery's internal resistance. The

temperature rise due to Joule heat is larger than the temperature rise due to reaction heat and polarization heat.

Okamoto et al. [82] investigate the heat characteristics of a lithium-ion secondary battery. The heat produced in the battery is noted as the combination of ohmic loss due to internal resistance and chemical loss due to an internal chemical reaction. Heat is then released to the environment through convection process. The losses and the degree of heat release depend on the cell active material, battery structure and shape. In this project, the internal resistance of the battery is measured in two ways; from I-V relation and direct measurement using a battery tester. Results show that the value of internal resistance is different during operation and at rest and the temperature rise in the lithium-ion battery depends on the magnitude of discharge current.

Patten et al. [83] present their acquired data of the performance of a PHEV through one year period monitoring. The main objective is to create a better understanding of how temperature affects PHEV battery performance and overall efficiency. Two main aspects are analysed: fuel economy and electrical efficiency due to different ambient temperatures. Results show that lower ambient operation temperature (lower than 2ºC) will drastically reduce the capacity and overall efficiency of PHEV. This is marked by the drop in fuel economy when the vehicle is operated in low temperature as shown in Figure 22. The highest fuel economy is obtained when it is operated in the temperature range of 9ºC to 20ºC. In the full electric mode, the electrical performance increases with the increase of ambient temperature as summarised in Figure 23, which means that the vehicle can travel a longer distance during summer in comparison to distance travelled in cold winter.

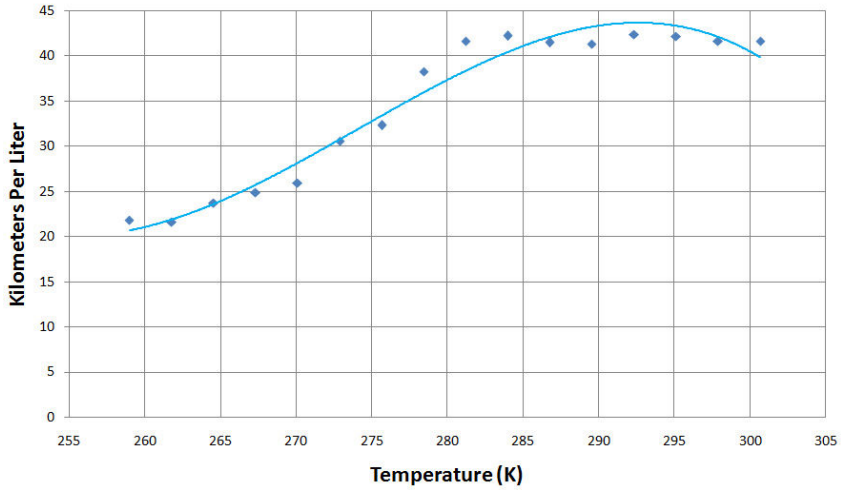

Figure 22. Impact of temperature on fuel economy.

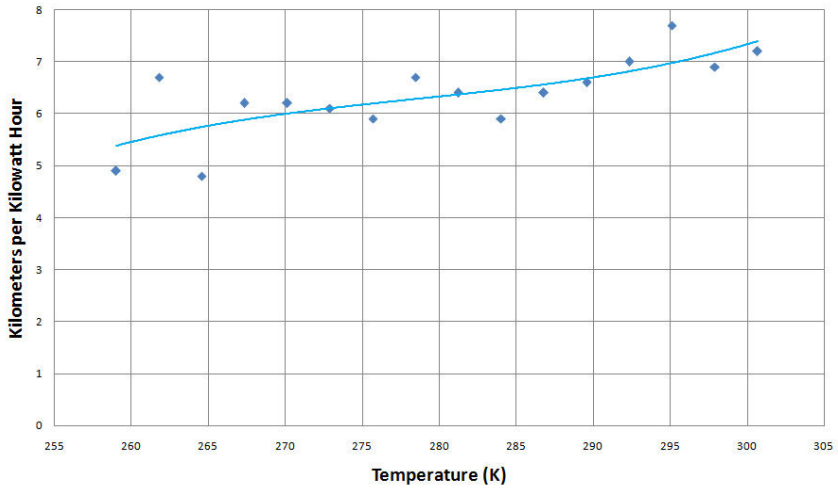

Figure 23. Impact of temperature on electrical performance.

XU et al. [84] use a special integrated circuit (IC) to measure the battery temperature, battery voltage and battery current. Szente-Varga et al. [85] propose an experimental methodology to measure the battery discharge voltage at different constant ambient temperatures. The experiment is conducted in a thermal test chamber with streaming air and regulated temperature. A constant current discharge test is conducted, and the discharge temperature is regulated to a constant temperature regardless of the cell voltage. Figure 24 shows that the voltage curves shift lower when a lower discharge temperature is set. In other words, the voltage decrease with temperature and the discharging time period becomes shorter.

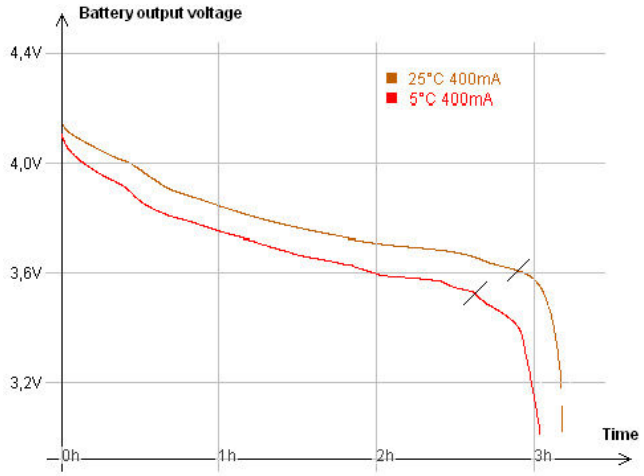

Figure 24. Battery output voltage under different temperature conditions.

2.3.4 Battery modelling works

2.3.4.1 Electrical battery model

Yatsui and Bai [86] use the combination of open circuit voltage (OCV), Coulomb counting (CC), and Kalman filter methods to accurately estimate the state of charge (SOC) of Lithium-ion battery cells under various factors. This combination is used because the direct relation OCV method which is the most common method to measure the SOC is only suitable for offline measurement, when there is no current transfer in the battery. On the other hand CC method which is traditionally used for online measurement, works by measure of the battery current, integrated over time, and determines an estimated battery SOC, might accumulate errors in long run integration [86].

Cho et al. [87] propose a battery model for lithium-ion batteries which includes a SOC estimation method that takes into consideration various battery operation conditions such as battery temperature and driving mode. This battery model operates on least sum square error estimation for parameters mapping from experimental results. A precise model to predict SOC is very important, as the battery SOC can be considered as a fuel level in the vehicle [87]. Failing to predict battery SOC will cause overcharge or over discharge during cycles. This may lead to permanent damage to the battery which reduces performance and cycle life. The battery voltage is calculated using equation 18. The SOC estimation is a combination of SOC estimated from current integration (Coulomb counting) and battery model: SOCi and SOCv, respectively as shown in equation 19 and 20.

$$\hat{V}_k = V_{o,k} + I_k R_o + \frac{1}{c} I_k \Delta t + \{\exp(-\frac{\Delta t}{RC})\}[V_{k-1} V_{o,k-1} - I_{k-1} R_o] \tag{18}$$

$$SOC_{i,k} = SOC_{c,k-1} + \frac{\Delta t}{Q_{\max}} I_k \tag{19}$$

$$SOC_{v,k} = SOC_{v,k}(V_{o,k}, T_k) = SOC_{v,k}(V_k, I_k, T_k) \tag{20}$$

where C represents the electric double layer capacitor (F), I the current (A), k the discrete-time increment, $Q_{\max}$ the battery capacity (Ah), R the lumped interfacial resistances (Ω) R_0 the lumped series resistances (Ω), SOC_c the final estimated value of SOC by SOC estimation methodology, SOC_i the state-of-charge estimated by current integration, SOC_v the state-of-

charge estimated by battery model, t the time (s), V the experimentally measured battery voltage (V), $\hat{V}_k$ the model-estimated battery voltage (V), V_0 the open circuit voltage (V).

Chen and Mora [88] propose an electrical battery model to predict battery runtime and *I-V* performance (*I* stands for current and *V* for voltage) of a battery by combining the transient behaviours of battery, internal resistance and open circuit voltage that depend on battery SOC. Later, Erdinc et al. [89] improve the model of Chen and Mora [88] by adding the thermal and capacity fading effect on battery dynamics. In this model, the capacity fading is a function of storage time, temperature, and cycle number and a potential correction term is added to the battery voltage calculation to compensate for the variation of equilibrium potential that is induced by temperature changes. The same trends of battery model developments which integrate battery dynamic model with thermal and capacity fading effect are reported in [90, 91]. In the battery model presented by [89, 90, 91], the temperature is considered as a constant which is independent from battery charge-discharge process. The equations for the battery model as proposed by Chen and Mora [88] and improved by Erdinc et al. [89] are as follow:

a) Battery output voltage, V_{bat} [V]

Battery output voltage, V_{bat} is calculated by:

$$V_{bat} = V_{oc}\left(SOC\right) - I_{bat} \cdot R + \Delta E\left(T\right) \tag{11}$$

with $V_{oc(SOC)}$ represents the battery open circuit voltage [V] in function of SOC, I_{bat} the battery current [A], R the battery resistance, and $\Delta E(T)$ the temperature correction of potential [V]

b) Battery open circuit voltage, $V_{oc(SOC)}$ [V]

Battery open circuit voltage is calculated using an equation as a function of battery SOC. This equation is as follows:

$$V_{oc(SOC)} = -1.031.exp\,(-35.SOC) + 3.685 + 0.2156.SOC - 0.1178.SOC^2 + 0.3201.SOC^3 \tag{12}$$

SOC is depending on the battery initial SOC condition (SOC_{init}), current (I_{batt}) and battery capacity (C). So SOC is calculated by:

$$SOC = SOC_{init} \cdot \int \left(\frac{I_{bat}}{C_{usable}} \right) dt \tag{13}$$

With C_{usable} is the usable battery capacity [Ah], and SOC_{init} is the initial state of charge.

c) Usable battery capacity, C_{usable} [Ah]

The value of the battery usable capacity decreases with increasing charge-discharge cycle number, discharge current, and storage time (self-discharge) and when the battery temperature decreases [88]. This is known as the effect of capacity fading. The remaining usable battery capacity is:

$$C_{usable} = 3600 \cdot C_{init} \cdot CCF \tag{14}$$

with *CCF* is the capacity correction factor that takes into consideration the capacity fading effect.

d) Capacity fading effect

Capacity fading effect is the reduction of usable battery capacity in function of time, temperature, and cycle number. This is an irreversible loss in capacity and affecting the remaining life of the battery. Reduction in battery capacity occurs when the battery is not in use (stored) and when used repeatedly (charge-discharge). These losses are called calendar life losses and cycle life losses respectively, which increase with time and increasing temperature. Capacity correction factor is calculated using equation from Erdinc et al [89]:

$$\text{CCF} = 1 - (\text{Calendar life losses} + \text{Cycle life losses}) \tag{15}$$

Calendar life losses are calculated using expression of percentage storage losses:

$$\text{Storage losses}(\%) = 1.544 \text{ x } 10^{7} \cdot \exp\left(\frac{-40498}{8.3143T} \right) \cdot t_s \tag{16}$$

where *T* stands for temperature [K], and t_s the storage time [month].

Cycle life losses are related to the negative electrode SOC. The rate of change in negative electrode SOC depends on cycle number and temperature and can be expressed as:

$$\frac{d\theta_n}{dN} = k_1 \cdot N + k_2 \tag{17}$$

where N is cycle number and the value of coefficient k_1 and k_2 is given in the Table 1 as a function of cycling temperature.

Table 1. Coefficient k_1 and k_2

Cycling temperature (ºC)	k_1(cycle^{-2})	k_2(cycle^{-1})
25	8.5 x 10^{-8}	2.5 x 10^{-4}
50	1.6 x 10^{-6}	2.9 x 10^{-4}

e) Temperature correction of potential, ΔE(T) [Volt]

Potential correction of temperature is used to compensate for the variation of equilibrium potential that is induced by temperature changes. Figure 25 describing this ΔE (T) as proposed by Gao et al. [90] is as follows:

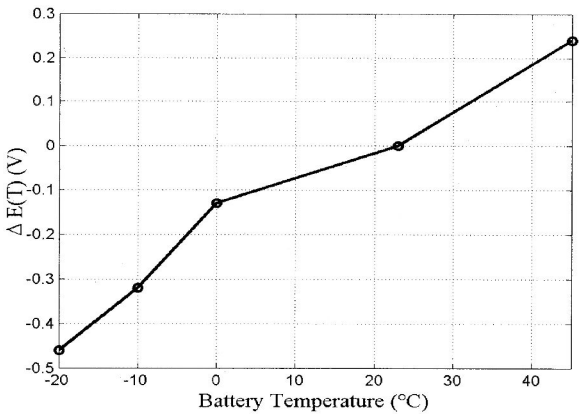

Figure 25. Temperature-dependent potential-correction term. Reference temperature is at 23ºC.

f) Battery resistance, R [Ω]

Generally, the battery internal resistance R can be described either as a constant [54, 78, 92, 93] or as a function of battery state of charge (SOC) [72, 88, 91, 94] or temperature [31, 40, 64, 74, 76, 95, 96] or both [97]. Figure 26 shows the battery internal resistance as a function of temperature presented by Sen and Kar [40]. It shows that the battery cell resistance slightly changes with the change of the battery temperature. The battery internal resistance cell decreases from 0 ºC to the limit of efficient operating range, at 45 ºC. After 45 ºC, the internal resistance increases drastically. The change of battery internal resistance with the temperature as reported

in [31, 64, 74, 76, 95] is summarised in Figure 27. It shows that the battery cell internal resistance decreases when the temperature increases. This variation is due to the electrolyte that is commonly used in lithium-ion batteries that has an electric conductivity that varies with temperature [81].

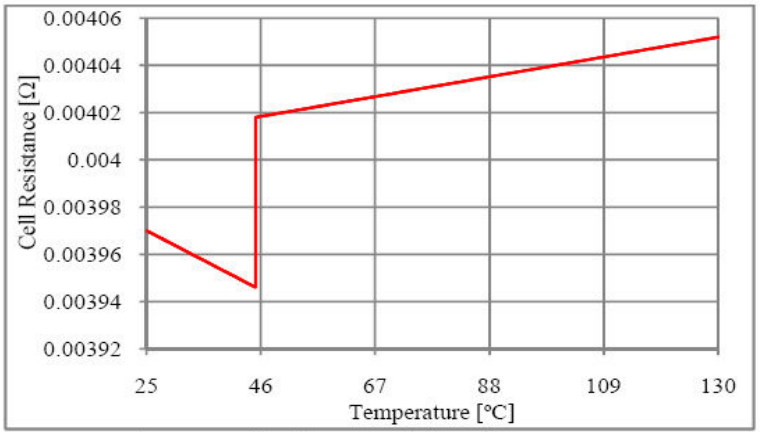

Figure 26. Cell resistance variations with temperature from Sen and Kar[40] .

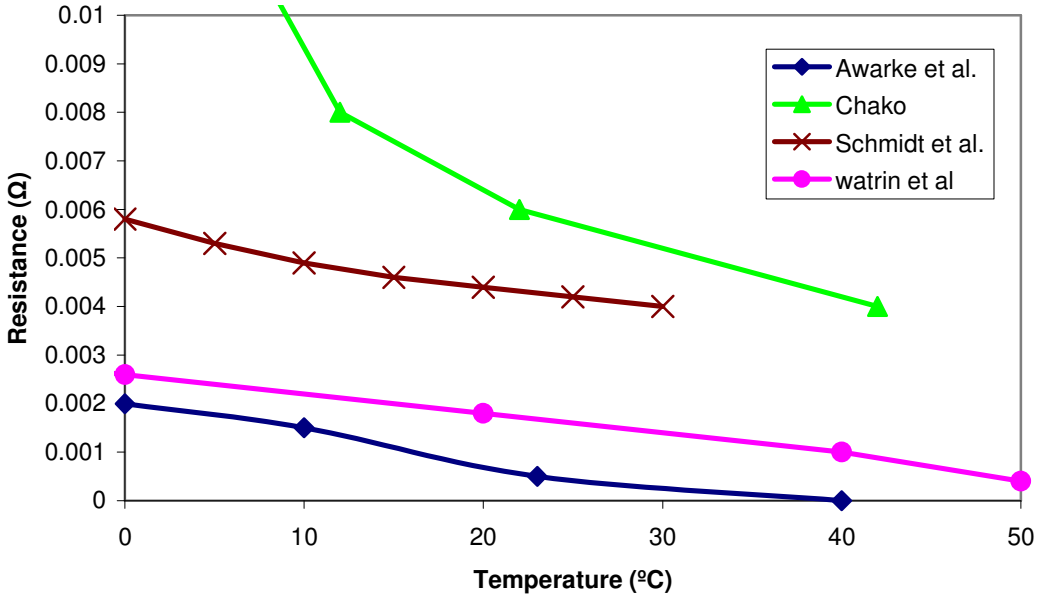

Figure 27. Cell resistance in function of temperature by Chacko and Chung [31], Awarke et al. [76], Schmidt et al. [95], and Watrin et al. [74].

Lin et al. [72] presented battery resistance in function of SOC as shown in Figure 28. It shows that the battery internal resistance rises significantly when SOC drops from 0.2 to 0.1. At SOC 0.2 to 0.8, the value of internal resistance is nearly constant. Figure 29 shows the different

values of resistance as a function of SOC during charge and discharge processes as presented by Sun et al. [94]. Baronti et al. [97] combined the effect of temperature and SOC on the battery resistance as shown in Figure 30.

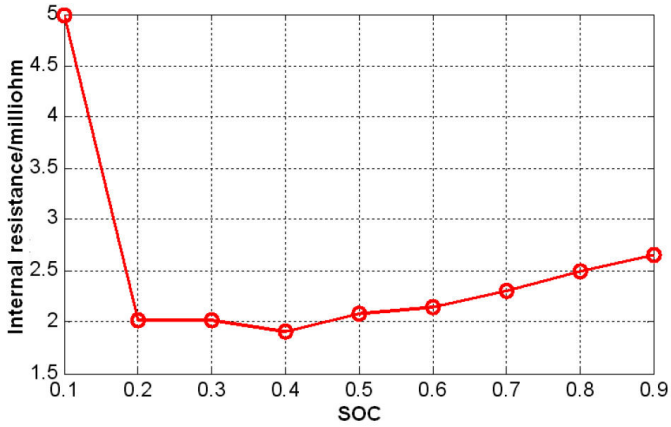

Figure 28. Relation of internal resistance and SOC [72].

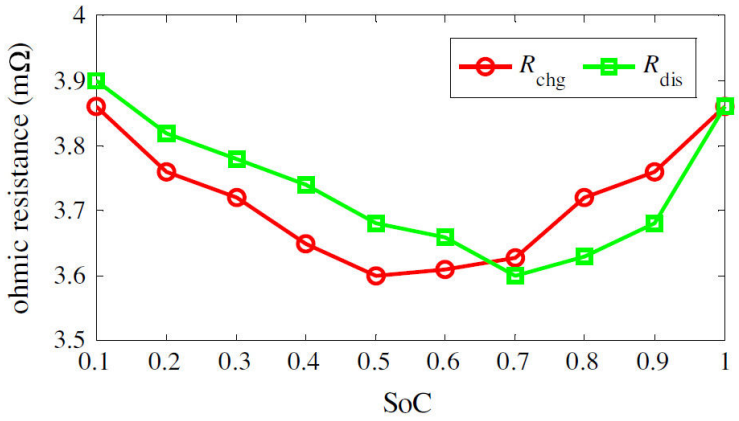

Figure 29. Resistance characteristic in function of SOC during charge (chg) and discharge (dis) [94].

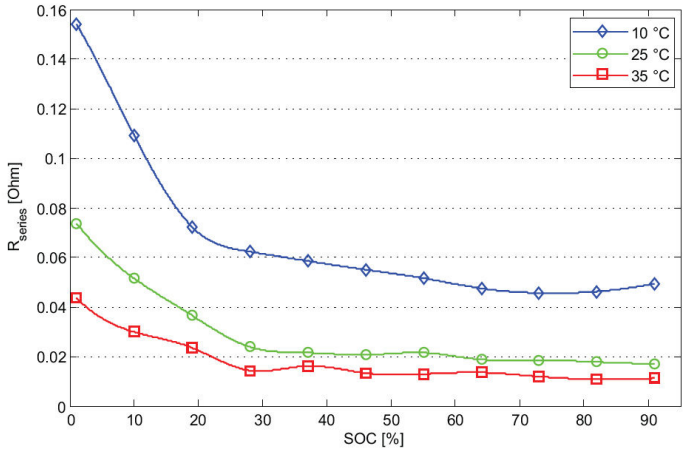

Figure 30. Cell resistance in function of SOC and temperature [97].

2.3.4.2 Thermal battery model

In the modelling and simulation of the battery thermal behavior, some works focus only on the model of thermal behaviours, while others take into account the combination of thermal and electrical models that simulate the impact of temperature changes in the battery to the electrical performance of the battery. Furthermore, the developed model can be for a single cell, several cells or cells in battery pack that takes into account the impact of stacking the battery or battery arrangement in the packs. These models can be further divided into zero dimensional (0D), two dimensional (2D), and three dimensional (3D). 0D models are the less complex models and can provide results at fastest calculation time but also the less accurate models. 3D models on the other hand are complex, need huge computation source and time to predict the battery thermal behaviour but they can give accurate results at different cell locations.

I) Single cell

a) Zero dimensional model (0D)

Shadman Rad et al. [73] present a thermal model to predict the thermal behaviour of battery cell. Overpotential and entropic heat generation inside the battery cell is transferred to environment through radiation and forced convection heat transfer. The temperature of the cell is assumed as uniform. This model is capable to predict the cell temperature evolution for different discharge rates, ambient temperatures, and different convective heat transfer coefficients as shown in Figure 31.

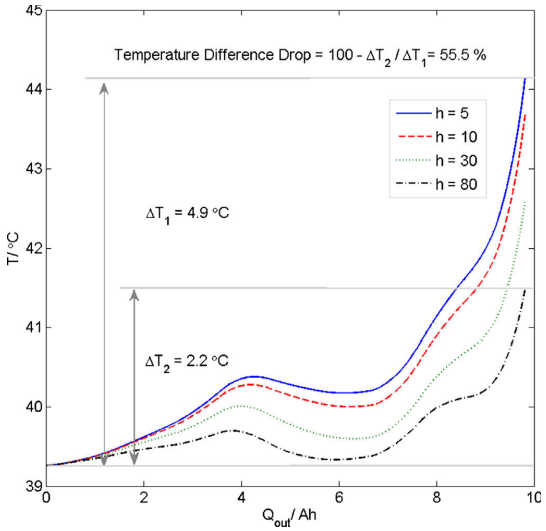

Figure 31. Battery cell temperature at different convection heat transfer coefficients for 2C discharge at 40ºC ambient temperature [73].

b) Two dimensional model (2D)

Kim et al. [79] use the finite element based method to model the thermal behaviour of a lithium-ion battery. The heat generated is the combination of the heat generated due to the electrochemical reactions and electrical resistance within the cell as a function of the electric current and SOC, as explained in section 2.3.3. The heat generation rate, q is given in equation 21.

$$q = aJ\left[E_{oc} - E - T\frac{dE_{oc}}{dT}\right] + a_p r_p i_p^2 + a_n r_n i_n^2 \qquad (21)$$

where a is the specific area of the battery (m^{-1}), J the current density (Am^{-2}), Eoc the open-circuit potential of the cell (V), E the cell voltage (V), a_p and a_n the specific area of the positive and negative electrodes (m^{-1}), respectively, and i_p and i_n are the magnitudes of the linear current density vectors, respectively. The first term of the right-hand side of equation 21 is the heat generated due to charge transfer at the electrode/electrolyte interfaces. This involves an irreversible part, representing the energy loss by the deviation of the cell potential from the open-circuit potential due to electrochemical polarization, and a reversible part, representing the heat proportional to dE_{oc}/dT due to entropy change. The third and fourth terms arise from ohmic heating in the positive and negative electrodes, respectively. Figure 32 shows the temperature distribution on the battery cell surface. It shows that the temperature is higher near the current collecting tab. Figure 33 shows the effect of different discharge rates on the temperature rise. Results of battery temperature during charging process are discussed in [75] while the effect of different electrode configuration is discussed in [78].

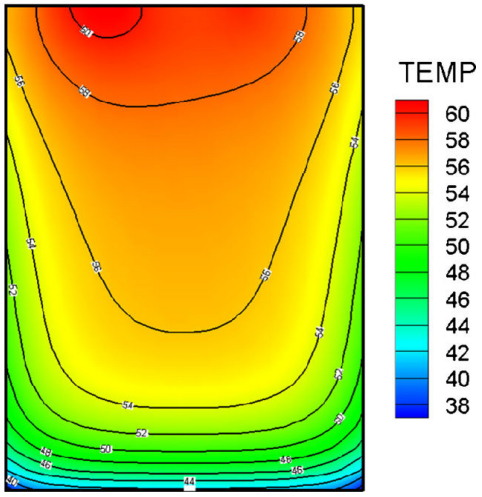

Figure 32. Temperature distribution at 5C discharge rate [79].

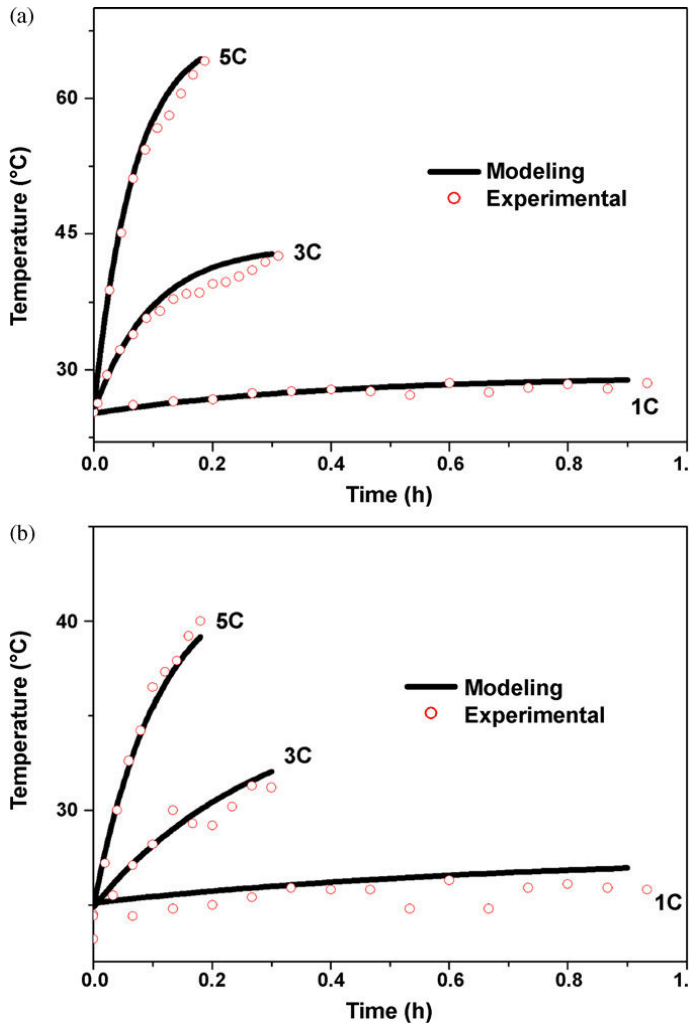

Figure 33. Maximum temperature (a) and minimum temperature (b) at discharge rates of 1C, 3C and 5C [79].

c) Three dimensional model (3D)

Lin et al. [72] present Finite Element Method (FEM) for thermal battery model. Equation 22 is used for modelling the heat transfer process in Lithium-ion battery.

$$\rho c \frac{\partial t}{\partial \tau} = \frac{\partial}{\partial x}\left(\lambda_x \frac{\partial t}{\partial x}\right) + \frac{\partial}{\partial y}\left(\lambda_y \frac{\partial t}{\partial y}\right) + \frac{\partial}{\partial z}\left(\lambda_z \frac{\partial t}{\partial z}\right) + \dot{\Phi} \tag{22}$$

$$q = \frac{I_L}{V_B}\left[\left(E_o - V_{oc}\right) - T\frac{dE_o}{dT}\right] \tag{23}$$

where, $\dot{\Phi}$ represents the heat generation rate per unit volume (W/m^3), λ the thermal conductivity (W/m.K), c the specific heat capacity (J/kg.K) and ρ the battery average density (kg/m^3). The heat generation rate, q is calculated based on Bernardi model as shown in equation 23. Here I_L is the working current (A), E_o the electromotive force (V), V_{oc} the open circuit voltage (V), V_B the battery volume (m^3), and T the battery temperature (K). In this model, it is considered that the heat generation rate and the battery material are symmetrical, the thickness of battery electrode tab is much smaller than the battery case, so the heat generation of the tab is ignored, the radiation heat transfer is ignored, and the thermo-physical parameters of each part are considered as constant. Results show that the battery temperature rise higher when higher discharge rates are applied as shown in Figure 34 (a), and the temperature of the battery is higher at the centre of the battery compared to the battery surface, shows by Figure 34 (b).

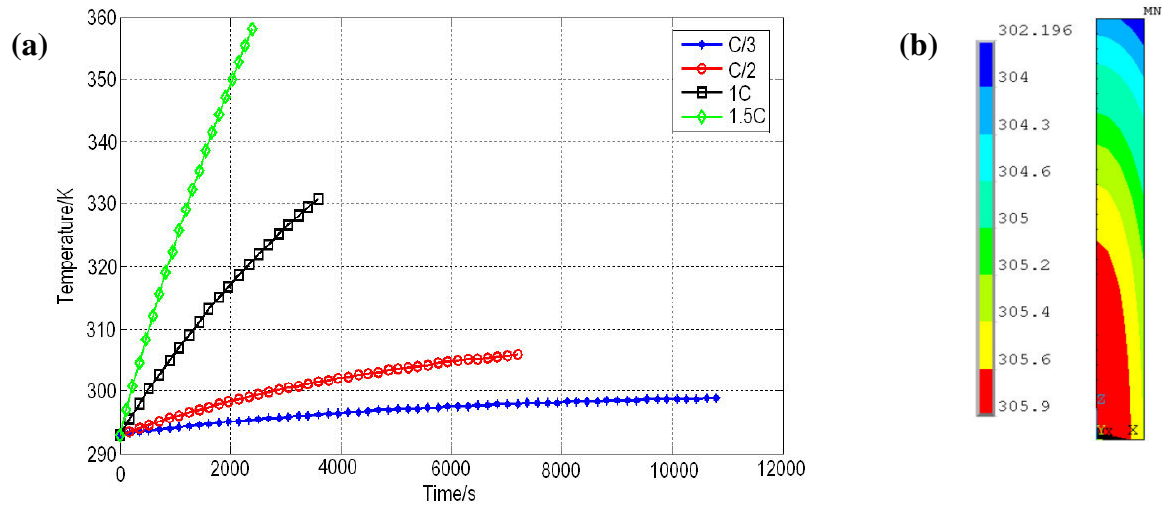

Figure 34. a) Battery inner temperature rise at different discharge rates, b) temperature field [72].

II) Cells in the pack

a) zero dimensional model (0D)

Hallaj and Selman [37] propose a thermal mathematical model with lumped parameters. In this model, the thermophysical properties and heat generation data for specific lithium-ion cells and the material used are determined through experimental work. This model is capable of simulating the temperature profiles under various operating conditions and cooling rates. Here a passive cooling system is used, by integrating a phase change material (PCM) in the battery pack. Other

work that uses PCM thermal management can be found in [98]. The PCM is used as a heat dissipation method that has the advantage of avoiding the problem of bulky, complex, and expensive conventional methods; such as force air-cooling and liquid-cooling. Authors show the possibility of using a well-designed phase change material system as a simple, cost effective thermal management solution for lithium-ion batteries in all applications including hybrid electric vehicle.

Hu et al. [99] present a battery thermal model using Foster network. Authors have used CFD to calculate the parameters needed in the Foster network. In this work the result for a single battery cell as well as cells in the battery pack with cooling system is shown. The thermal model using Foster network can provide a comparable result with regard to CFD calculation, as shown in Figure 35, but in shorter time spending. Furthermore, this Foster network model can be readily coupled with temperature dependant battery electrical model to replace the traditional network model to give a more accurate result and reasonable time consumption. However, CFD model or testing is still needed to generate the step responses for the battery system, to be used as the parameters in the Foster network model.

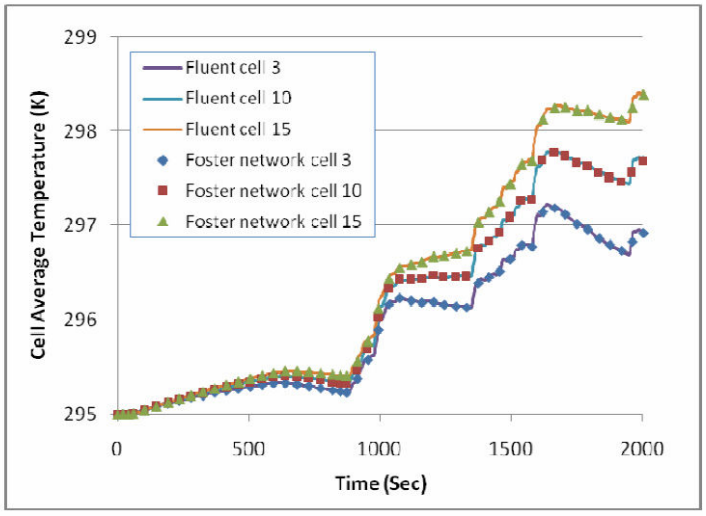

Figure 35. Comparison of CFD results with Foster network results [99].

b) Two dimensional model (2D)

Mi et al. [100] present the thermal modelling of a lithium-ion battery pack for HEVs application. Two groups of 24 cells are stacked together in the battery pack with aluminium cooling fins placed in between the cells. It is assumed that there is no direct heat exchange between the

battery and the ambient air. The heat from the battery is carried through the cooling fin to finally be evecuated by the cooling air. The battery pack is modelled using 2D finite element model. This model is capable of modelling the temperature gradients of the battery cell and the battery pack under different operating conditions as shown in Figure 36.

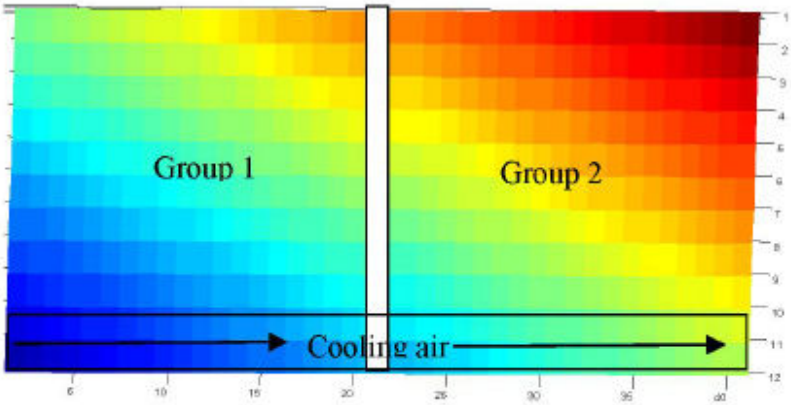

Figure 36. Battery temperature rise. X-axis: length direction of the battery; y-axis: heigh of battery (in cm). Lower left corner has inlet air temperature at 9ºC, top right corner has temperature of 40ºC [100].

Smyshlyaev et al. [66] develop a thermal dynamics model for a large battery pack in the form of two-dimensional partial differential equations (2D PDEs); a simplification from full CFD/FEM model. In reality, the thermal dynamics in a cell, as well as in a battery pack, are three dimensional. In this work, it is considered as 2D because the transient activity in the direction parallel to the axes of the cell is relatively small compared to the plane perpendicular to the axes. By using this method, authors manage to produce a result that can reasonably match the result from full CFD model as shown in Figure 37; with much less time used to compute. These PDE equations are as follow:

$$\frac{\partial \Theta}{\partial t} = kR\nabla^2\Theta + \frac{3}{2}(\alpha_1 + \alpha_2)(T - \Theta) + \frac{\gamma_1}{2}(T_\omega - \Theta) \tag{24}$$

$$\frac{\partial T}{\partial t} = 3(\alpha_3 + \alpha_4)(\Theta - T) + \frac{1}{\rho_c c_c}\Pi(x, y, t) \tag{25}$$

$$\frac{\partial T_\omega}{\partial t} = \gamma_2(\Theta - T_\omega) - \frac{1}{\rho_w c_w}Q(x, y, t) \tag{26}$$

here, Θ is the temperature of the pack material (K), T represent the temperature of the cell (K), and T_{ω} is the temperature of the cooling pipe (K). Information about parameters, constants, and assumption used in these equations is explained in detail by Smyshlyaev et al. [66].

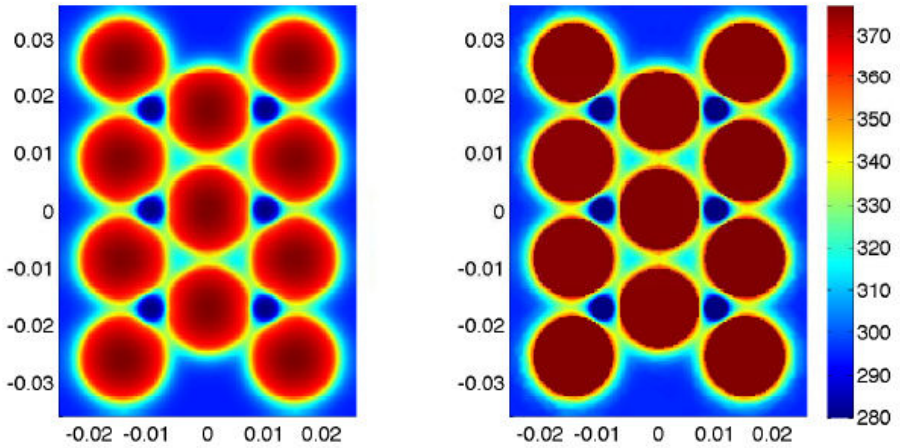

Figure 37. Temperature distribution in 3x4 battery pack at t=20 seconds.Left: Full CFD model. Right: Reduced model [66].

c) Three dimensional model (3D)

Pesaran [101] discusses his work on battery thermal modelling capabilities using an advance vehicle simulator (ADVISOR) and finite element battery module and pack thermal design. The battery thermal model in ADVISOR is modelled as two separate isothermal units; battery core and battery case. The battery cells in the core are assumed as one isothermal unit with no temperature variation among cells. The heat generation in the core is due to electrochemical reactions and resistive heating. Then, the heat is conducted through the case material and then convected to the air or fluid surrounding the battery. This model is then validated by comparing with result from a finite element battery model. The finite element model is extended to study the temperature distribution in a battery cell and in a battery pack with different cooling methods.

Abdul-Quadir et al. [36] investigate the thermal behavior of a 7 cells Lithium-ion battery through experiment and CFD model simulation, and suggest design modification for better battery cooling characteristics. In the simulation model, the heat generation in the battery is calculated using measurement data of dynamic impedance given by battery manufacturer. It is considered as uniform heat sources. Results from the experiment and simulation show that the cooling system is not effective due to the compactness of the cell assembly, and the time to cool

down the battery to desired temperature after utilization is too long. A better cooling is achieved by using the new proposed design, including the use of aluminium plates inserted in between cells together with liquid cold plates attached to it.

Awarke et al. [76] use a combination of vehicle dynamics model, equivalent electric circuit battery model and a 3D finite-element thermal model to analyse the thermal behaviour of a Lithium-ion battery module under ARTEMIS driving cycle (urban, road, and motorway) without cooling system (natural convection). A vehicle dynamics model is used to calculate the cell power profiles, an equivalent electric circuit battery model to estimate the cell electric currents, and 3D finite-element (FE) thermal model to predict the temperature distribution in the module. The battery resistance is presented as a function of temperature and SOC, but in the calculation, the temperature feedback is not coupled to the battery resistance, and only the parameters associated with 23ºC are used. The temperature increase corresponding to urban cycle is tolerable, but more significant temperature rise is recorded through road and highway cycle as shown in Figure 38, where suitable cooling system is needed.

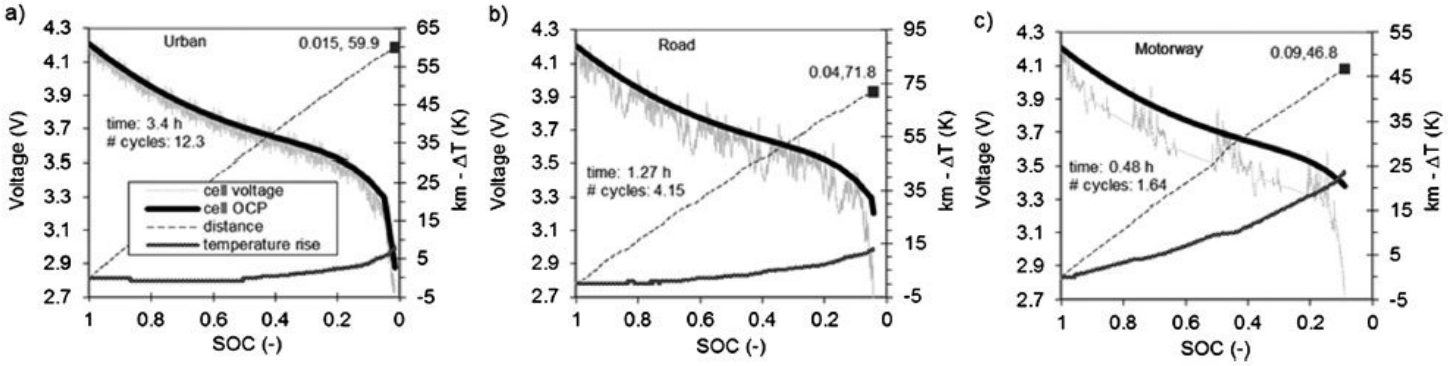

Figure 38. Evolution of cell OCP, cell voltage, temperature rise at the hottest location, and covered range during each driving cycle [76].

Fan et al. [102] present a 3D CFD simulation thermal study of Lithium-ion battery module used in PHEV. In this work, the effects of gap spacing between 8 battery cells and air flow rate on the temperature distribution are studied. The heat generation is simulated for the US06 driving cycle. Different constant air flow rates are used for cooling system. The radiation heat transfer is ignored. In general the maximum temperature rise is observed at the top of fourth cell (cell in the middle of module) as shown in Figure 39. The temperature rise can be lowered

by reducing gap spacing between neighbouring cells. Temperature uniformity can be improved using high flow rates at moderate gap spacing.

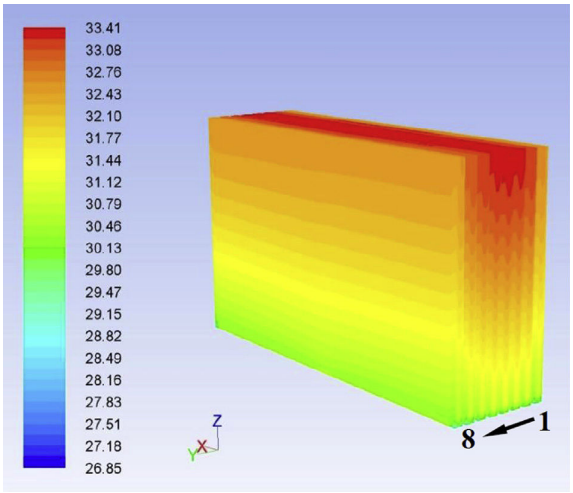

Figure 39. Temperature distribution (unit: ℃) of the cells after 600 s for the case of gap spacing of 3 mm and at air flow rate of 20.4 m^3 h^{-1} [102].

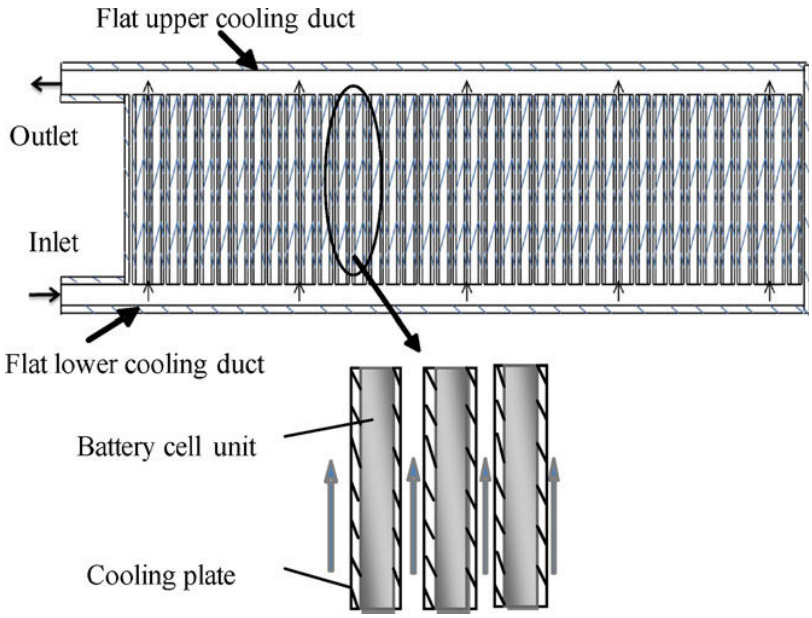

Figure 40. Scematic of a baseline “U-type” flow battery pack [96].

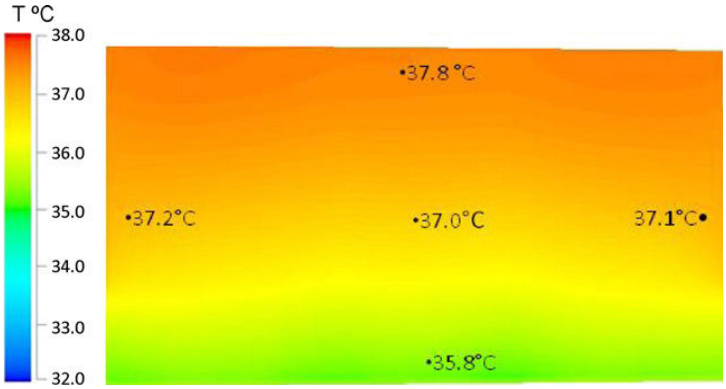

Figure 41. Temperature contour of battery cell surface [96].

Sun et al. [96] develop a 3D thermal model to analyse the thermal behaviour of battery cells in a pack under US06 driving cycle. The battery pack includes 40 battery cells and cooling plates and lower and upper ducts as shown in Figure 40. The thermal model includes convection heat transfer from battery cell to cooling plates, and forced convection at cooling plate's surface by cooling air. The radiation heat transfer is ignored. Figure 41 shows the temperature contour of the hottest battery cell in the battery pack with inlet cooling air flow rate of 60 CFM. It shows that the hottest spot occurs at the top edge of the battery cell while the bottom edge of the battery cell has the lowest temperature.

2.3.4.3 Electro-thermal battery model

I) Single cell

a) Zero dimensional model (0D)

Baronti et al. [38] propose a model of a lithium polymer cell including thermal effects by adopting the electrical battery model from Chen and Mora [88] and adding the battery thermal model into it. The cell temperature is calculated by the combination of ambient temperature, heat generation from power losses due to internal resistance, and heat dissipating to environment. The model is capable of predicting the battery cell performance including the temperature dependence on the cell parameters. Thanheiser et al. [103] proposed a battery electrical model considering thermal behaviour. The temperature change in the battery is due to ohmic losses from internal resistance and the electrochemical reaction inside the battery. Authors stated that the heat is transferred from the battery by conduction, convection, and radiation; but no detailed description or discussion is given. The information from the electrical model is used as input to

the thermal model to calculate the temperature change in the battery and then used as a feedback in the electrical model. These models are validated through experiments [38, 103]. In these works, only a single cell is considered, there is no discussion on the impact of battery packaging on the battery's electrical and thermal behaviour.

Smith and Wang [104] use a mathematical equation based modelling to represent the 1D electrochemical and lumped thermal model of a lithium-ion battery. In the thermal model, the sum of heat generated comes from reaction and joule heats, and then the heat is dissipated by means of convective heat transfer. Reversible heat is neglected due to lack of empirical data on the SOC-temperature relationship of the two electrodes, and presumed insignificant in HEVs application. The battery pack modelling assumes the cell construction, SOC, and temperature to be uniform throughout the pack. The battery model is then integrated in the vehicle model of a midsize passenger car to simulate the heat generation rates for a range of driving cycles and operating temperature. The heat generation is higher when the vehicle operates at lower temperature, and this value depends on the type of driving cycle. In an aggressive driving cycle, more heat is generated compared to less aggressive driving cycle.

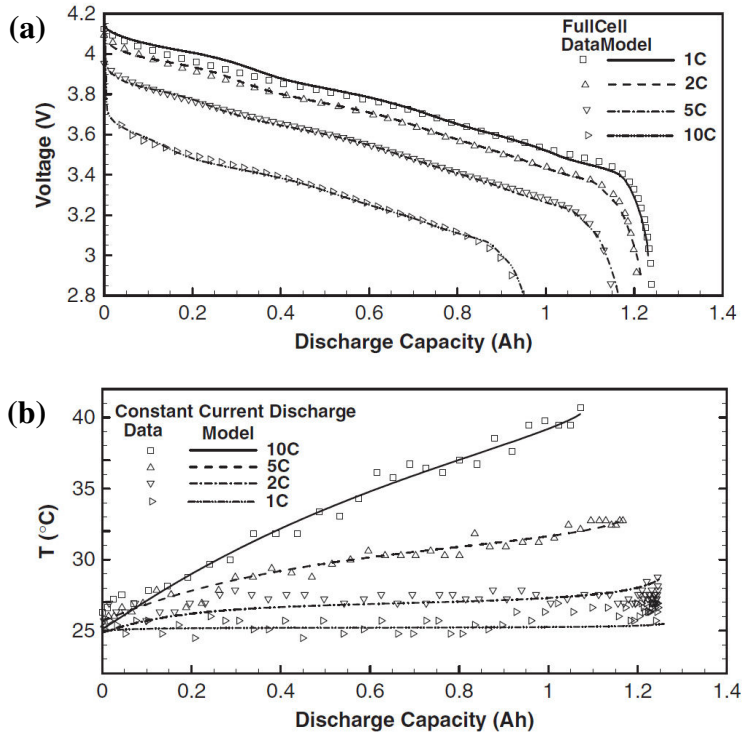

Figure 42. Experiment and simulation result of (a) cell voltage and (b) cell temperature for different discharge rates [105].

Fang et al. [105] develop an electrochemical-thermal model of lithium-ion battery that has the capability of predicting the performance of individual electrodes of lithium-ion cells under HEV condition and wide range of ambient temperature. In this work the cell temperature is assumed to be uniform. The temperature rise in the battery is due to joule heating of ohmic resistance in the solid active materials and the electrolyte. The reversible entropic heat is neglected due to lack of experimental data and their value is relatively small. Figure 42 shows the battery temperature and voltage at different discharge rates. This model is validated using experimental result. The experiment is conducted at room temperature (25ºC) with natural convection.

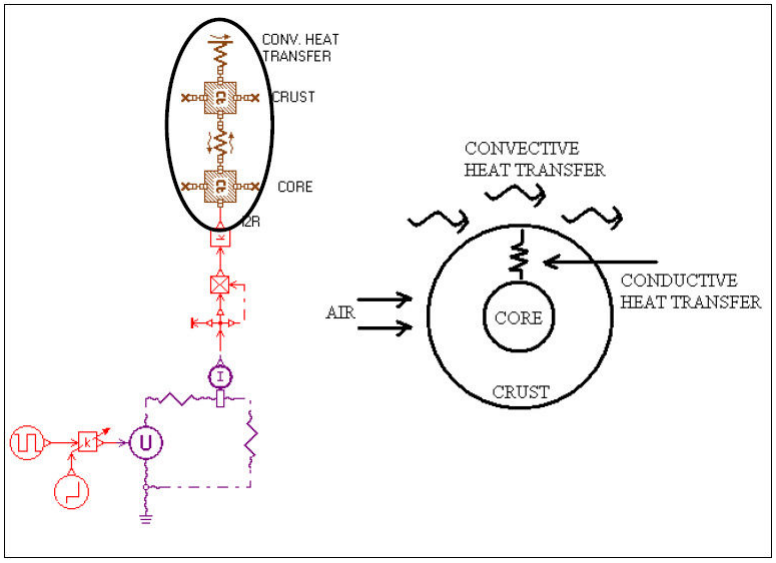

Figure 43. Thermal model of the cell [106].

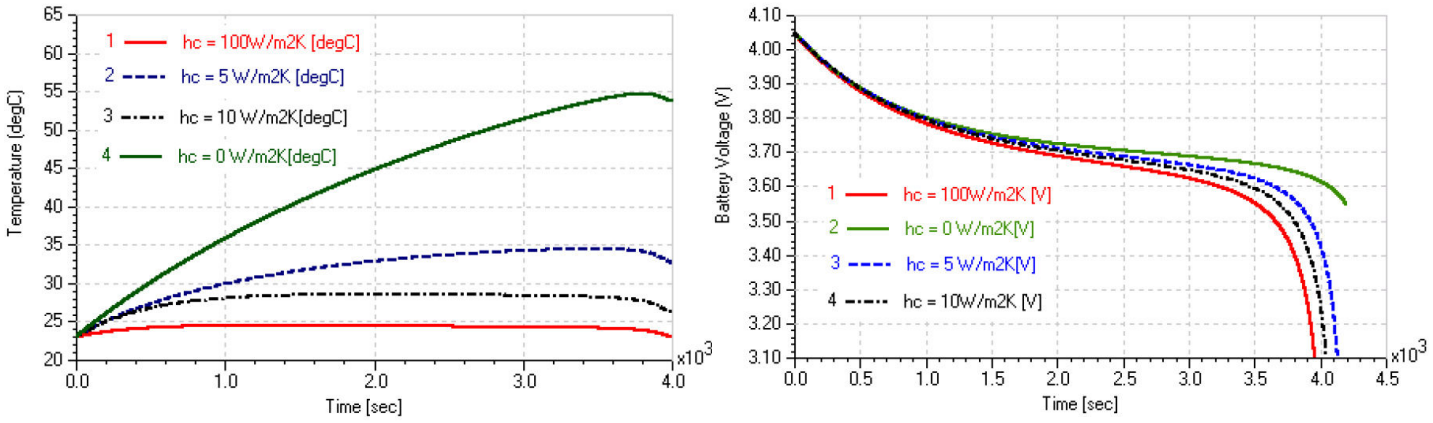

Figure 44. Battery temperature and voltage for different cooling rate [106].

Bhide and Shim [106] present an electrical based lithium-ion battery model incorporating thermal and rate factor effects. In this model a cylindrical shape battery cell is used. For the thermal model, the cell is modelled by two main components; core and crust as shown in Figure 43. The power losses due to battery internal resistance are converted into heat in the cell core. Then the heat is transferred to the crust through conductive heat transfer process. At the end, this heat is dissipating to the surrounding through convective heat transfer from crust. The convective heat transfer coefficient from the battery cell crust to the surrounding depends on the cooling methods and conditions. The radiation heat transfer effect is ignored. It is considered that the temperature within each cell is maintained uniform, and there is no temperature variation in axial direction. With the coupling of electrical and thermal model, this battery model is capable to predict the battery parameters such as voltage at a different constant temperature, and also the effect of different cooling methods and conditions on the temperature rise and voltage evolution as shown in Figure 44. However in this work, the performance of battery cells in pack is not discussed. Similar type of modelling works can be found in [54].

Watrin et al. [74] present a multiphysical model for high energy density battery. The equivalent circuit for this model is presented in Figure 45. It includes a resistance depending on temperature and another resistance depending on SOC and two *RC* branches. I is the current, V_{bat} is the battery measured voltage, and OCV is the open-circuit voltage.

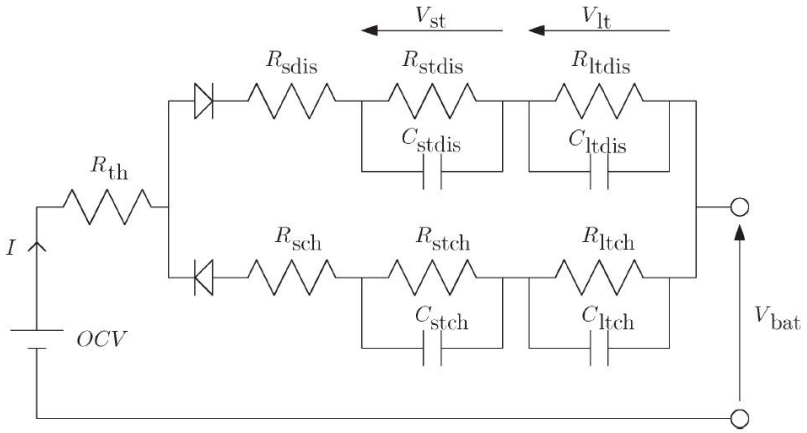

Figure 45. Electrical equivalent circuit model of a battery cell. The *dis* index is used for charge, and *ch* is used for discharge [74].

In this model, the temperature is calculated from the internal energy balance. This energy balance takes into consideration all losses, where most of it comes from battery current and internal resistance. Heat from battery is then dissipated to the environment by the process of convection and radiation. Equation 27 summarizes this energy balance. The first three positive components represent the thermal sources and the last two negative parts represent the thermal dissipation to the environment by convection and radiation respectively. Results from experiment and simulation in Figure 46 show that the battery temperature increases considerably during battery test cycle.

$$m \cdot C_p \frac{dT(t)}{dt} = \frac{1}{R_{stch}}\left[OCV(t) - V_{bat}(t) - V_{ltch} - R_{th} \cdot I(t)\right]^2 + \frac{1}{R_{ltch}}\left[OCV(t) - V_{bat}(t) - V_{stch} - R_{th} \cdot I(t)\right]^2 + R_{th} \cdot I(t)^2 - h_c.A.(T_a - T) - \sigma.\varepsilon.(T_a^4 - T^4) \quad (27)$$

with m stands for the cell mass (kg), C_p the specific heat (J/kg K), T the cell temperature (K), T_a the ambient temperature (K), R_{th} the series resistance, R_{stch} the short transient resistance, R_{ltch} the long transient resistance, h_c the cell heat transfer coefficient (W/m^2 K), A the external cell surface area (m^2), σ the Stefan Boltzman constant (W m^{-2} K^{-4}), ε the cell emissivity.

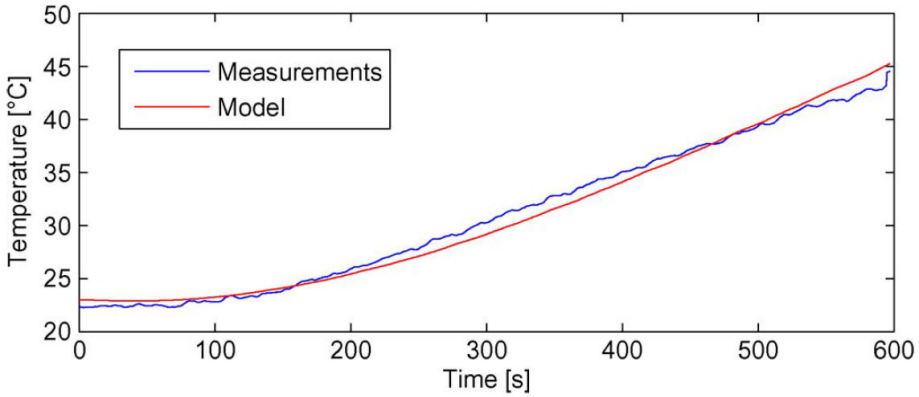

Figure 46. Battery temperature during test cycle [74]

Ye et al. [92] propose an electro-thermal model to study the effect of temperature on the performance of the battery. A significant temperature change occurs during high rate charge-discharge operation, as shown in Figure 47. This condition shows that the battery needs a proper cooling system to evacuate heat from battery and maintain the battery temperature in the desired range.

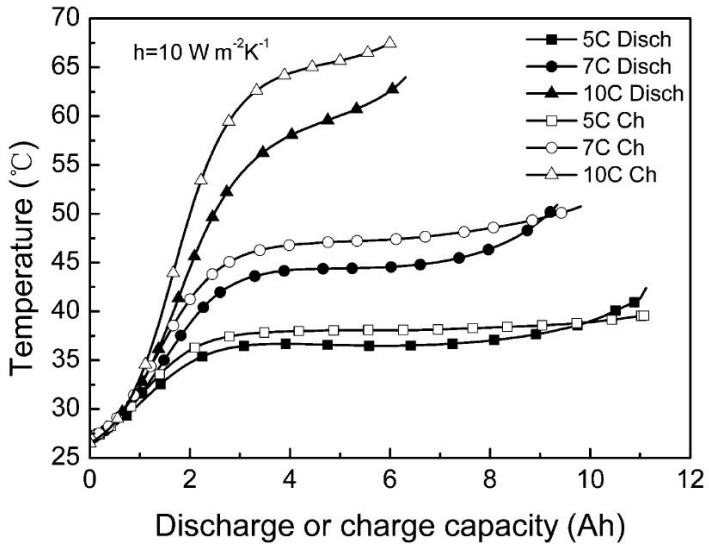

Figure 47. Simulation results on temperature changes during high rate charge and discharge [92].

b) Two dimensional model (2D)

Simic [107] proposed a thermal and electrical model of an automotive high power battery. In this model, the electrical loss is converted to heat sources that heat the battery cell. The thermal model is based on 2D discrete volume element. The simulation result is then validated by experimental work. For the electrical model, algebraic and ordinary differential equations are used based on resistance-capacitor model. Battery state of charge (SOC) is calculated from current integration. The discrete volume thermal model used geometrical and thermal measurement data to parameterize the model including thermal conductivity, specific thermal capacity, and density as well as thickness of each layer of material. Heat transfer from battery cell surface to environment is modelled using convection process.

c) Three dimensional model (3D)

Chacko and Chung [31] have developed a three dimensional electro-thermal model of a lithium-ion battery cell based on finite volume method. The developed model is then validated using experimental data. The three dimensional thermal model is built by taking into consideration the thermal behaviour during both charge and discharge process. Anode, cathode and separator are represented by a homogeneous layer that forms a battery cell. Local internal resistance and current densities are used to characterize the heat generation in the battery cell due to the

electrochemical reactions and the mass transfer of ion in the electrolyte. A convection heat transfer is considered between cell surface and the environment. The density, thermal conductivity, and heat capacity of the cell components are assumed to be uniform throughout the battery and remain constant within a known rage of temperature. The electro-thermal model is then used to predict the lithium-ion battery cell behaviour for several vehicle operating conditions such as the driving cycle during a hot environment and a repeated acceleration-deceleration driving cycle test. Figure 48 shows the model prediction of temperature contour on the cell surface during test cycle.

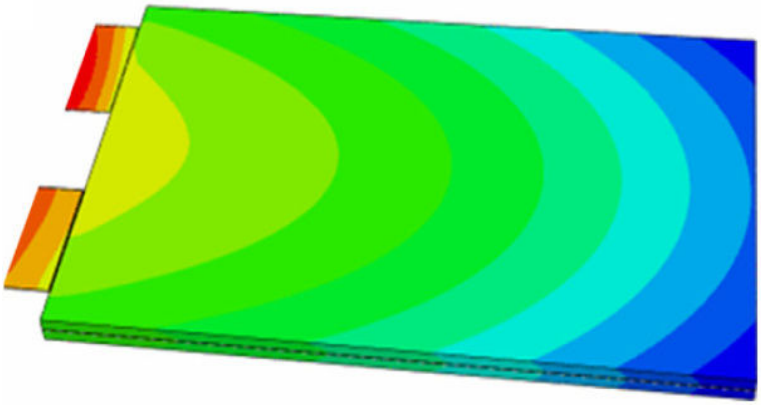

Figure 48. Electro-thermal model temperature contour on cell surface [31].

II) Cells in the pack

a) Zero dimensional model (0D)

Recently, Bhide and Shim [55] have improved their previous model [106] introduced in section 2.3.4.3 (I) by adding the effect of stacking the battery cells in a battery pack on battery performance. It is known that stacking causes different cooling of cells and thus causes the different temperature variations among different cells which then lead to the difference in output voltage of each cell. Here, a model with several cells stack is proposed with different cooling methods, such as series and parallel cooling configurations. In the parallel flow configuration, 9 battery cells are stacked, in which the space between the cells makes a form of a four-lobed star, and the fluid flows through this space. In the series configuration, a single pass of fluid with each cell interacting with the fluid flowing through the pipe is considered. The fluid progressively gets warmer and the cell temperature rises from the first cell to the last cell as shown in Figure 49.

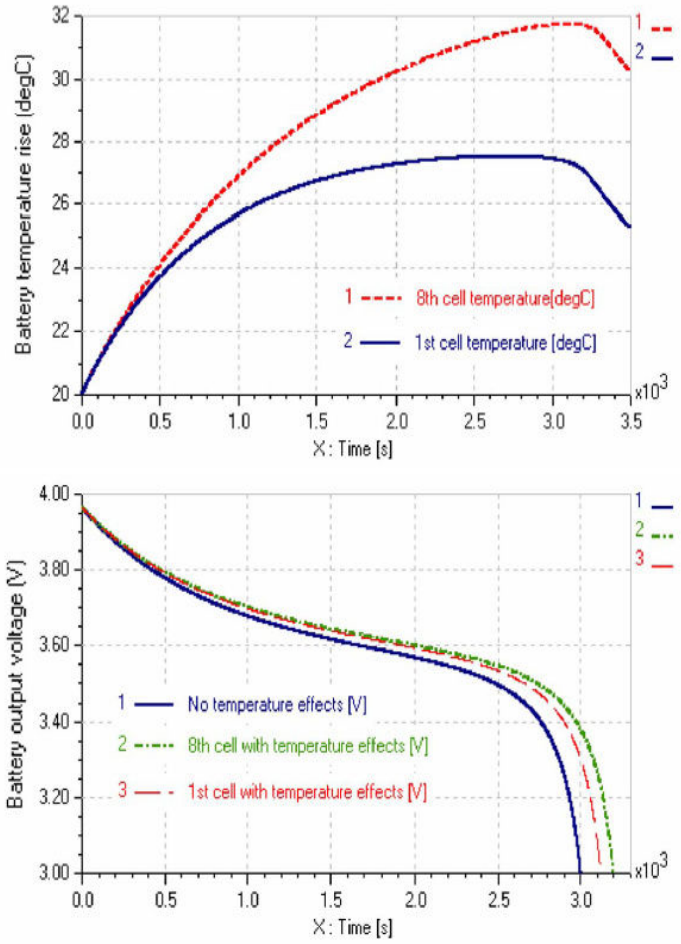

Figure 49. Temperature rise and voltage evolution for the first and eight cells in series configuration [55].

b) Three dimensional model (3D)

Guo et al. [108] presented 3D multi-physics model to predict the electrical potentials and temperature for Lithium-ion battery under constant current discharge. In this study three battery cells are connected in series by two electrical busbars in a battery module. The current is set to enter the battery module during discharge process from the negative electrode tab terminal of the cell 1 and exit through the positive electrode tab terminal of cell 3. Only natural convection is considered and radiation is ignored in thermal model. Figure 50 shows the temperature profiles across the module and individual cell for 5C discharge. The temperature of cell 2, which is located in the middle of the module, is hotter than the other two cells. For each cell, the temperature is higher near the positive electrode than other locations because of higher current density near the electrode and low electrical conductivity of positive electrode.

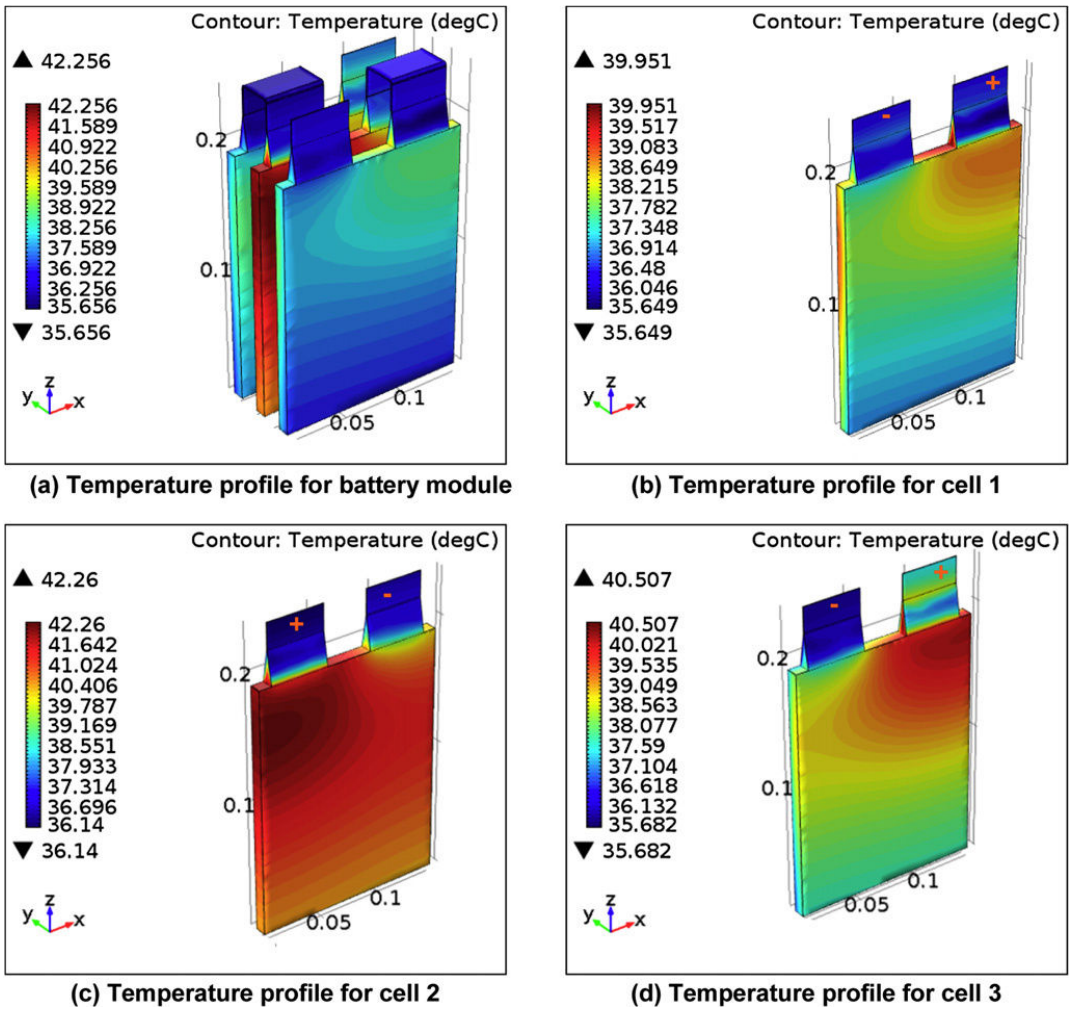

Figure 50. Profiles of temperature across the module and the individual cells at the end of 5C discharge [108].

2.4 CONCLUSION

Hybrid electric vehicles (HEVs) are a combination of two or more prime movers and/or power sources, normally conventional ICE and electric motor to obtain the required power to propel the vehicle. This system is viewed as one of the most promising technologies that can provide the best compromise between good driving range, low cost, and reduction of fuel consumption and pollutants. This can be achieved by the possibility of combining both zero local emissions advantages of pure electric vehicle and high energy and power density from pure ICE vehicles, and overcome their disadvantages such as poor fuel economy and environmental pollution from pure ICE vehicles and poor operation range per battery charge in pure electric vehicles.

Generally, HEVs can be classified into four basic architectures which are series hybrid, parallel hybrid, series-parallel or combined hybrid and complex hybrid. The popularity of HEVs is expected to increase in the future with the development of battery technology, control technique, and government support to the automobile owners and manufacturers.

Battery is one of the most important key components in HEVs which must continually accept and provide electrical energy by transforming chemical energy into electrical energy and vice versa. Lithium-ion batteries are considered as a good choice for HEVs for their superior properties such as high power rating, high energy density, and high cycle life compared to lead-acid, nickel-cadmium, and nickel-metal hydride battery. The battery capacity fade is a phenomenon of the loss in discharge capacity over time. The main factors that influence the battery capacity fading are charge and discharge rate, state of charge, charge-discharge cycle number and also operating temperature. There is a weak influence of temperature on capacity fade but the temperature affects the battery internal resistance. The battery capacity fading increases with the increase of charge and discharge rate. Experimental results also show that at a constant temperature, the capacity fade increases with the increase of charge-discharge cycle number.

Temperature is an important factor that affects the battery pack performance and life span. Temperature of each battery cell is different throughout the battery pack depending on where it is located. This temperature difference may then lead to the capacity imbalance among the cells that further causes the cells to be over-charged or over-discharged during cycling which is the major contribution to premature failure in the battery packs in form of accelerating capacity fading or thermal runaway; a condition where the battery cell is overheating and igniting. To solve these problems, a battery thermal management system is necessary. It is meant to regulate the batteries to operate in the desired temperature range and to reduce uneven temperature distribution between cells. To assure the success of the utilization of a thermal management system, a good thermal model of battery packs and the individual cells is very important. It can provide accurate information that illustrates the real condition of the battery temperature, which is important information to be used by thermal management system to prevent any potential abuse.

There are basically four main methods in battery modelling; mathematical models, electrochemical models, polynomial-based models and electrical models. Electrical models are

more realistic, intuitive, easy to handle and are considered as the best compromise of complexity, time consuming and accuracy as compared to other models. Furthermore, they can be applied to any battery model irrespective of its chemistry, configuration and rate of discharge, by using suitable combination of parameters. In the modelling and simulation of lithium ion battery, some works focus only on modelling the electrical battery dynamic; including the battery voltage, current, and also SOC. Several methods are reported in estimating battery SOC including open circuit voltage (OCV), Coulomb counting (CC), and Kalman filter methods. The battery voltage is calculated from battery OCV, current, and battery internal resistance. Furthermore, the battery internal resistance can be constant, or a function of temperature or SOC, or the combination of temperature and SOC. Generally the value of resistance decreases with the increase of temperature. Anyhow, a lack of information exists, though, on the relation of resistance to temperature for temperatures above 50ºC.

Several works have been conducted in modelling the thermal behaviour of the battery. Some works focused only on modelling of thermal behaviours, while others take into account the combination of thermal and electrical models that simulate the impact of temperature change in the battery to the electrical performance of the battery. Furthermore, the developed model can be for a single cell, several cells or cells in battery pack that take into consideration the impact of stacking the battery or battery arrangement in the packs.

The heat generation is normally modelled as a combination of the heat generation due to the power loss due to internal resistance and/or electrochemical reaction inside the battery cell. The battery temperature is modelled either as a uniform temperature or non-uniform temperature. For non-uniform temperature, the temperature is normally higher near the positive and negative electrode than other locations because of higher current density near the electrode. Furthermore, the temperature near the positive terminal is also higher than at the negative terminal because of lower electrical conductivity of positive electrode. Some works focus on heat generation at different constant discharge rates, while others calculate the heat generation for battery used in vehicle to completing driving cycles such as US06, NEDC, or Artemis. Some works only used natural convection for battery cooling, while other considered forced convection, liquid cooling, or passive cooling system by integrating a phase change material (PCM) in the battery pack. Radiation heat transfer is usually ignored, because of its complexity and lower importance compared to other types of heat transfer.

CHAPTER 3: BATTERY THERMAL ANALYSIS

3.1 INTRODUCTION

Various experimental works regarding battery cell surface temperature can be found in literature. These works can be divided into several groups, depending on the methods used in temperature measurement, number of cells, charge/discharge methods, and type of cooling system used. Some works only consider a homogeneous temperature, but most recent works consider non-homogeneous temperature throughout the cell surface. For non-homogeneous temperature, normally, cell temperature near the positive and negative terminal is higher than in other locations, with temperature differences varying from one work to another. The number of cells used in experiment can vary from a single cell to several cells combined in a battery pack. It is a common practice to discharge the battery with several constant discharge rates, without the helps of any special cooling system, in other words the heat transfer from battery to atmosphere occur through natural convection.

From literature, it was found that there is lack of experimental works that put into evidence the cell temperature evolution at all cell locations for a single cell as well as the impact of packaging several cells in a battery pack, using different discharge rates and different cooling air velocities as cooling system. Furthermore, most of the existing works only discuss the cell temperature at a relatively high SOC. There are no results that show what happens to the battery cell thermal behaviour when the cell is discharged to small SOC, less than 20%. All these information are important to understand the real battery cell temperature behaviour at various conditions. Moreover, most of the experimental results used to validate the battery simulation model only considered constant discharge rate for a single cell without cooling system. So the simulation result might not be accurate for predicting the battery thermal behaviour with the effect of cooling system and battery cells in the pack.

The aim of this study is to provide the essential information on the thermal behaviour of the battery cells inside the pack experimentally. This study focuses on the distribution of temperature at various points of the battery cell surface, impact of stacking the battery cells inside the battery pack, impact of different constant discharge rates, and also the importance of cooling system (forced convection using different cooling air velocities) on the battery

temperature behaviour. Section 3.5 highlights the battery cell temperature behaviour under abuse discharge condition (discharge at SOC less than 20%). Impact of different temperatures and SOC on the battery cell internal resistance and a case study on the battery cell thermal behaviour used in an electric vehicle to complete driving cycles using different cooling strategies are also presented in section 3.6 and section 3.7 respectively.

3.2 EXPERIMENTAL DETAIL

3.2.1 Experimental set-up

This section presents the experimental study of the cell surface thermal behaviour of lithium-ion battery use in EVs and HEVs. The experiment is conducted for three lithium-ion battery cells placed inside a battery box. The cells are connected in series electrically and arranged in parallel inside a battery, as shown in Figure 51.

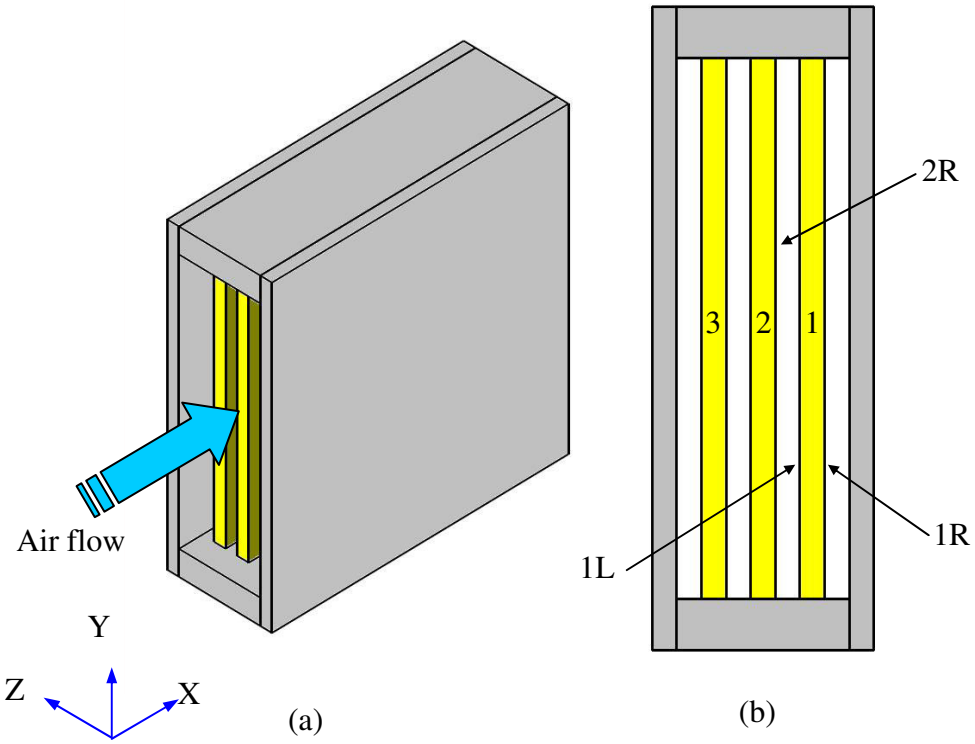

Figure 51. Battery cells arrangement in the box with (a) represent the isometric view and (b) the front view

In Figure 51, the arrow indicates air flow direction. An 18 mm space between each cell enables air to circulate and create a forced convection cooling system that takes heat from the cell surface into the surrounding environment. Figure 52 shows the experimental setup. “A” is the battery box that contains the 3 battery cells, “B” the air flow channel, “C” the cooling fans that control the cooling air velocity, both are powered by 24 V DC, “D” is the dynaload that controls the cell discharge current, “E” the anemometer to measure the cooling air velocity and temperature and “F” is the system control and data acquisition which is synchronised using cRIO 9074 from National Instrument

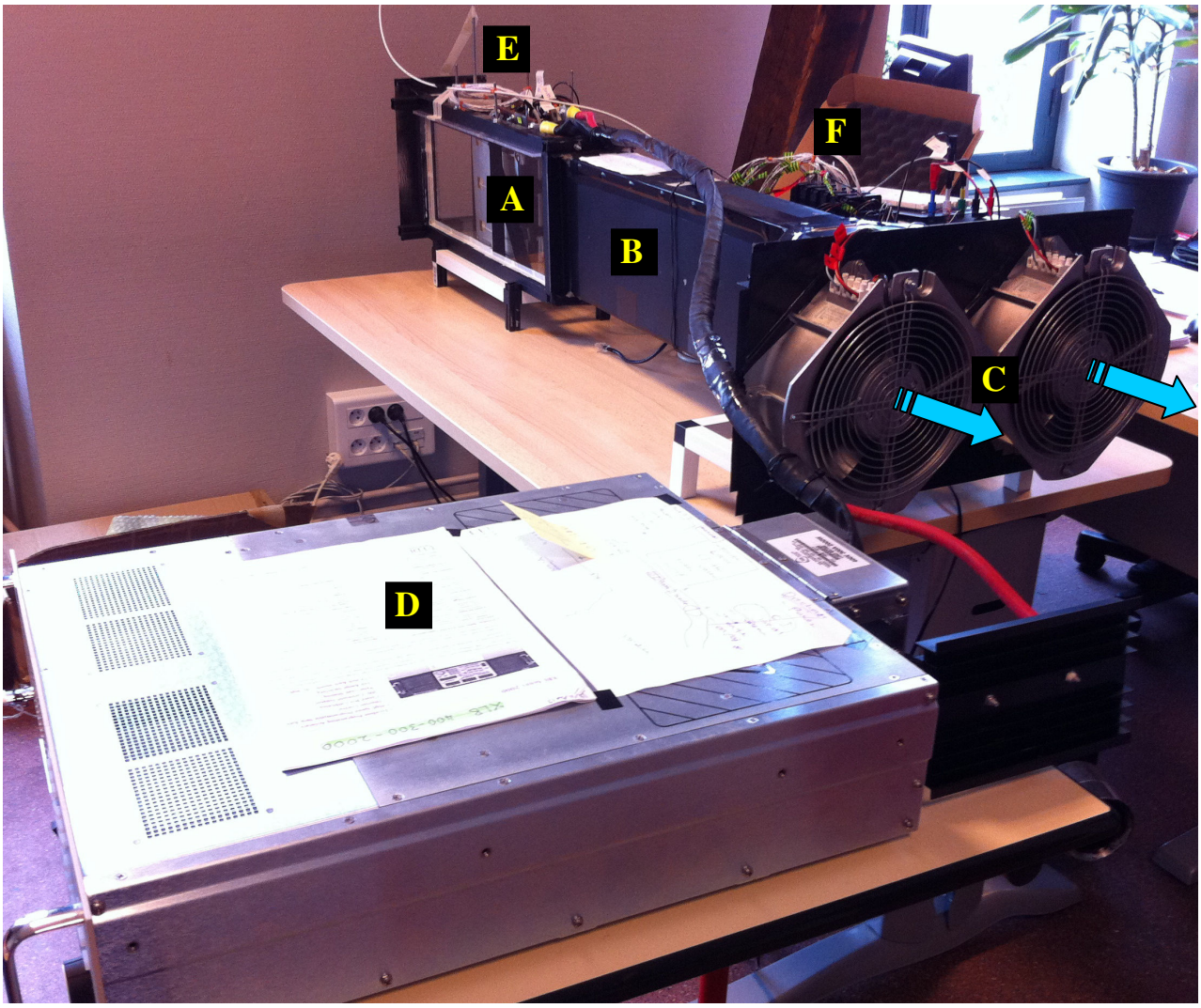

Figure 52. Experimental setup (A: battery box, B: air flow channel, C: cooling fans, D: dynaload, E: anemometer, and F: cRIO 9074)

a) Lithium-ion battery cell

Kokam SLPB 100216216H cells that have a typical capacity of 40 Ah are used in the present study. The maximum current allowed is 200 A during discharge and 80 A during charge. These cells use carbon at anode and Lithium Cobalt Manganese Nickel Oxide ($LiMnNiCoO_2$) at cathode. Each cell has a weight of 1.1 kg measuring 10 mm thickness, 215 mm width, and 210 mm length, as shown in Figure 53. The battery cell optimum operating temperature is between 0ºC to 40ºC during charging and -20ºC to 60ºC during discharge. Each cell has a nominal voltage of 3.7 V. The choice of this type of cell is based on the consideration that the cell's specifications are suitable to be used in both EVs and HEVs. The charge and discharge current of a battery is measured in C-rate. In this case, the battery which is rated 40 Ah provides 40 A for one hour if discharged at 1C rate. The same battery discharged at 0.5C provides 20 A for two hours. At 2C, the same battery delivers 80 A for 30 minutes. The typical cell capacity is expected to be achieved at room temperature (25ºC) using 0.5C discharge current from 4.2 V to 2.7 V.

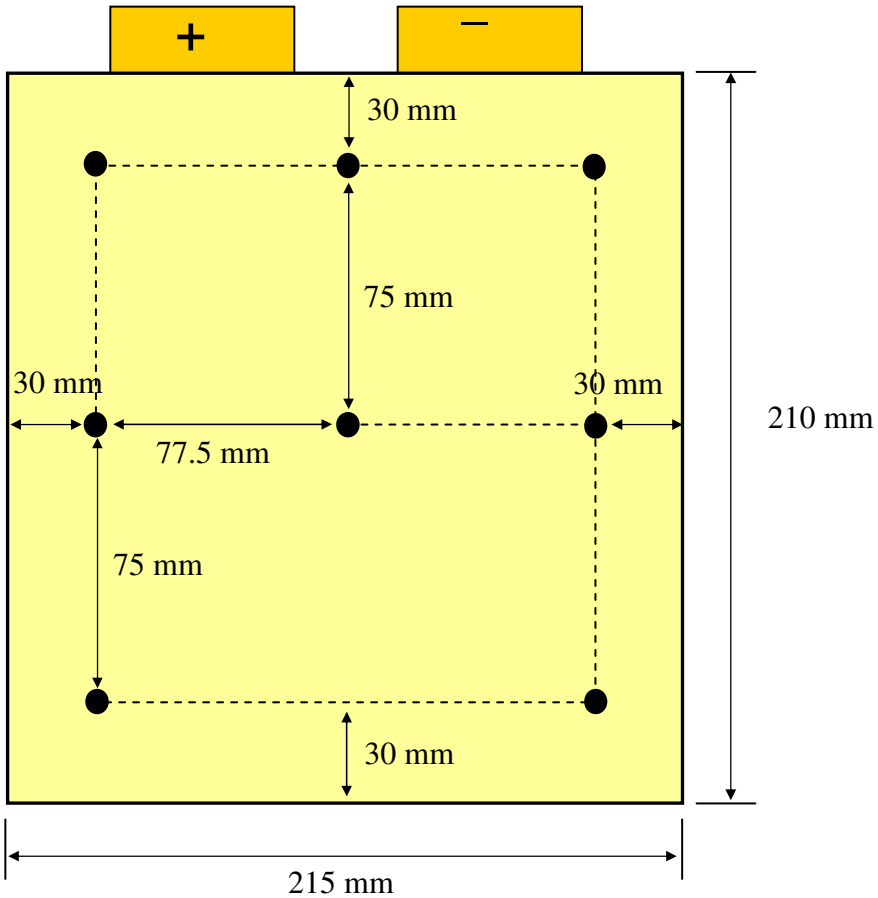

Figure 53. Battery cell parameters and the position of thermocouples

b) Thermocouple

Three cell surfaces are chosen to be monitored, marked as 1R, 1L, and 2R. Surface 1R and 1L are for the first cell on the right and left side of the cell respectively, while 2R is at the right side of the second cell. Author assumed that the thermal behaviour of the third cell is the same as the first cell due to symmetric arrangement of the cells in the battery box. That is why no temperature monitoring is planned for the third cell. Eight thermocouples are placed on each monitored cell surface at various locations as shown in Figure 53. In general, three thermocouples are placed at 30 mm from top edge of the cell near the positive and negative electrode terminal, three in the middle of the cell, and two at 30 mm from bottom edge of the cell. This arrangement is important in order to capture the cell surface temperature at the whole surface area with minimum amount of thermocouples used. A total of 24 thermocouples are used for the three surfaces.

The thermocouples at different positions of the cell surface are marked by P1 to P24, see Figure 54. Thermocouple P1-P8 and P9-P16 are on the first cell at surface 1R and 1L respectively, while P17-P24 are on the second cell at surface 2R. The arrow indicates air flow direction. The thermocouples are of type RTD PT100 with the class A precision (±0.06Ω at 0ºC). They have the capacity to capture the surface temperature from -73ºC to 260ºC with 1 second response time. Figure 55 shows the battery cells in the box with thermocouples attached to the cell surface. The thermocouples are attached to the cell surfaces thank to auto-adhesive head of 25x19 mm The wires of the thermocouples with a diameter of 2 mm are arranged in a way to minimise their influence on the movement of the cooling air.

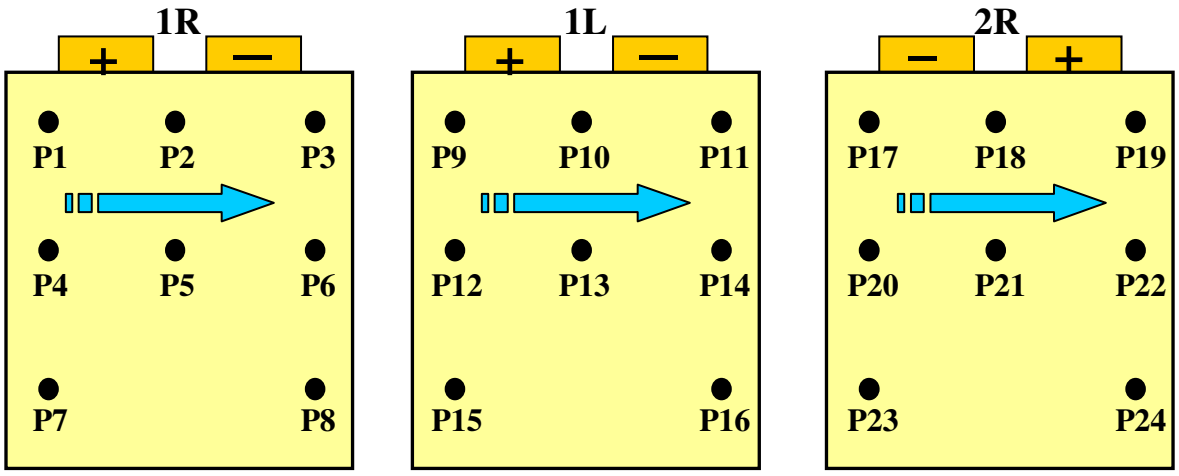

Figure 54. Position of thermocouples and air flow direction at surface 1R, 1L, and 2R.

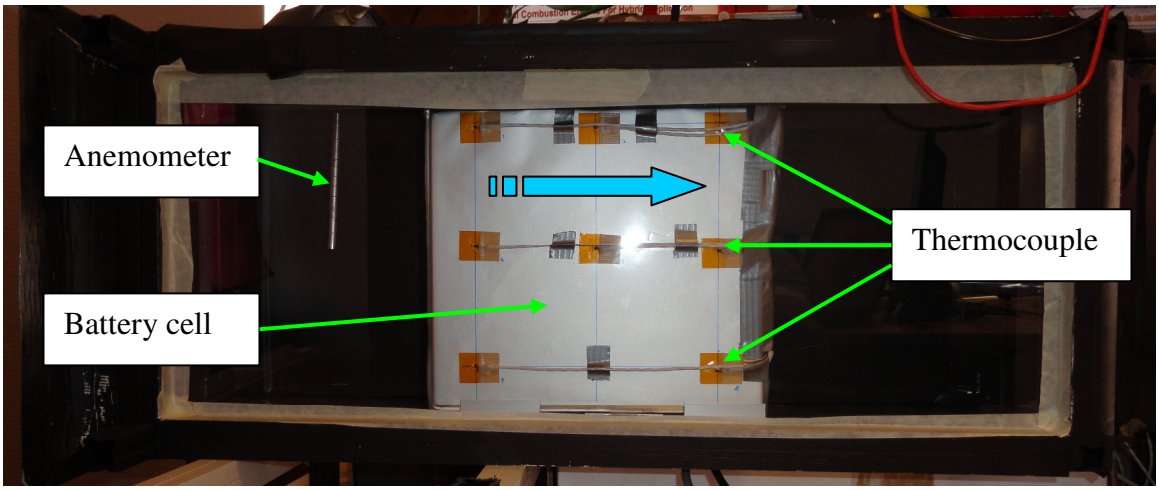

Figure 55. Battery cells in the box with thermocouples and anemometer.

c) Anemometer

The FMA1000 series *industrial air velocity/temperature transmitter/indicator* is used to measure and display cooling air velocity and temperature. This anemometer measures air velocities up to 61 m/s and air temperatures up to 121ºC. The accuracy of this anemometer is 1.5% of full scale air velocity and 0.5% of full scale air temperature. Its response time is programmable from 250 msec to 2 seconds. Air velocity and temperature are measured at 10 cm in front of battery cells at half the cell's height as shown in Figure 55. The measurement results are recorded directly through Labview software, and at the same time displayed by backlit LCD for supervision.

d) Cooling fan

Two axial compact fans, as shown in figure 2, are used to control the cooling air velocity inside the battery box. Each fan is powered by 24 V DC, and capable to produce maximum air flow rate of 1095 m^3/h. In theory, combining these two fans can produce maximum air velocity of 28 m/s in the given configuration, but in reality because of the actual experimental conditions, the system is only capable to produce air velocity up to 11 m/s measured at 10 cm in front of battery cells. This is due to the use of a 0.6 meter air flow channel (see Figure 56) that creates pressure drop inside the battery box, thus reduces the maximum cooling air velocity.

e) Dynaload

Current is discharged from the battery cells using a dynaload XLB Series 2000. The dynaloads standard operation modes include constant current mode, constant resistance mode, constant voltage mode, constant power mode, and pulse mode. It is capable to extract current up to 300 Amps, with accuracy of ±5 mA, voltage up to 400 Volts at accuracy of ±250 mV, and power up to 2000 Watts at accuracy of ±250 mW. The dynaload operating temperature is between 0ºC to 40ºC. The discharge current can be set either manually using direct control buttons from the dynaload control panel or control using external setting, through Labview software.

f) Air flow channel

Figure 56 shows (a) the top view (plane X-Z) and (b) the side view (plane Y-X) of the experimental set-up with the air flow channel highlighted. The airflow channel has the same height (210 mm) and width (102 mm) as the battery box with the length of 600 mm long. This length is chosen in the way that the distance from the cell to the cooling fan is more than 3 times the length of the battery cells. It is important to keep the electric fan far from battery cells to ensure that the fans rotation does not disturb the air flow inside the battery box. On the other hand, the air flow channel should not be too long as this will lead to a pressure drop inside the battery box and thus the decrease of the maximum cooling air velocity generated by the fan. In this study, it is targeted to have the cooling air velocity up to 10 m/s.

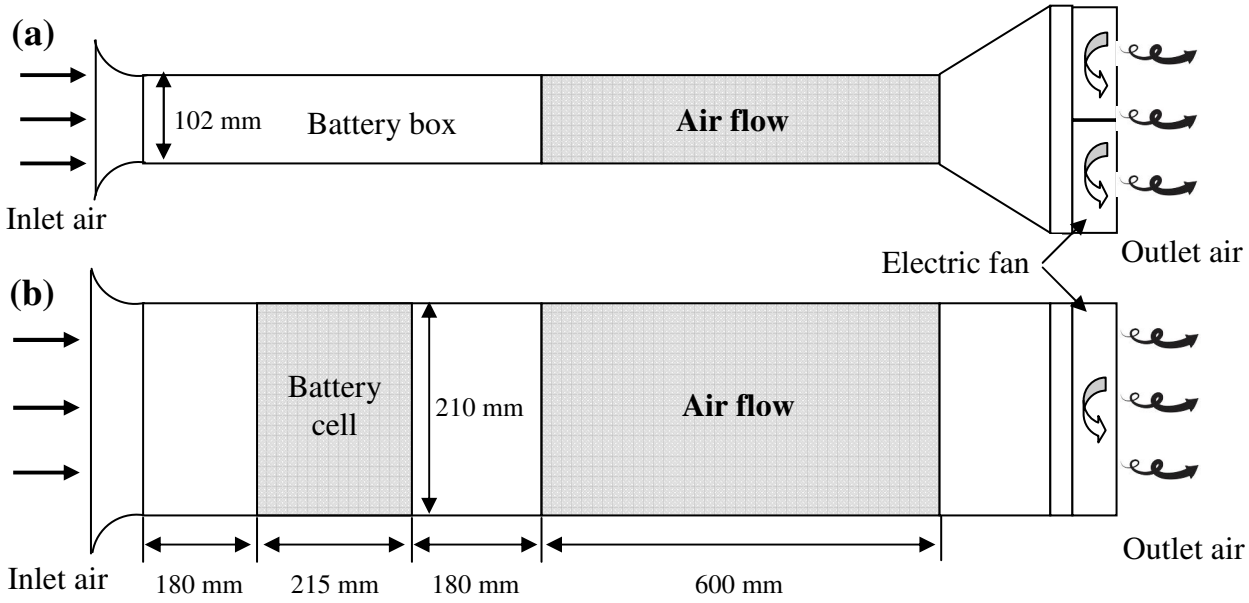

Figure 56. Experimental set-up with (a) the top view and (b) the side view.

g) System control

The system control and data acquisition is synchronised using cRIO 9074 from National Instrument. It is equipped by one *NI 9263 4-channel ±10V analog output* card to control the cooling fan speed and discharge current from dynaload, six *NI 9217 4-channel 100 ohm RTD analog input* cards to acquire the temperature from the 24 thermocouples and one *NI 9201 8-channel ±10V analog input* to acquire the cooling air velocity from anemometer, battery cell voltage, and dynaload discharge current. This information is summarised in Table 2. Data acquisition frequency of 10 Hz is used. The cRIO 9074 is linked to user interface in computer through Labview software.

Table 2. System control and data acquisition.

Card name	Device name	System control/data acquisition	Input/output
NI 9263	Electric fan	Control: Fan speed	±10V analog output
	Dynaload	Control: Discharge Current	±10V analog output
NI 9217	RTD thermocouple	Data acquisition: cell surface temperature	RTD analog input
NI 9201	Anemometer	Data acquisition: Cooling air velocity	±10V analog input
	Battery cell	Data acquisition: Cell voltage	±10V analog input
	Dynaload	Data acquisition: Discharge current	±10V analog input

3.2.2 Experimental procedure

To determine the temperature evolution of the battery cell surface, a series of experiments is conducted with different discharge rates and cooling air velocities. The battery is discharged at 1C (40 Amps), 3C (120 Amps), and 5C (200 Amps) discharge rate from 100% SOC to 10% SOC with a constant cooling air velocity of 2 m/s, 4 m/s, 6 m/s, 8 m/s and 10 m/s. The cooling air temperature is at room temperature, which happens to be between 20°C to 22°C during experiments. The experimental procedure is as follows:

1. The experiment is conducted only when the battery cells are full charge. It is considered that the battery cells are fully charged or 100 % SOC when the battery total voltage is equal to 12 Volts or 4 Volts per cell.
2. The charging process is stopped one hour before starting the experiment and the cells are left to cool down naturally to make sure that the temperature increase during charging does not affect the temperature measurement during discharge.
3. Example here is for 1C discharge rate at cooling air velocity of 2 m/s.
4. The experiment is started by setting the fan speed in order to obtain the desired constant cooling air velocity, 2 m/s.
5. At this stage the essential information is recorded; air velocity, air temperature, and battery cell voltage.
6. The battery cells are then discharged at a constant discharge rate, 1C discharge rate (40 Amps).
7. The discharge process is continued until the battery SOC reaches a limit of 10% SOC. The battery cell SOC is calculated using battery model as stated in section 2; equation 11 to 17. The discharge times to reach desired battery SOC are shown in Table 3.
8. The cooling air velocity is maintained constant at 2 m/s from t=0s until 100 seconds after the end of discharge process, in order to reduce the battery cell temperature rapidly after the end of discharge.
9. During discharge process, several parameters are monitored to ensure the validity of experiment result and for safety reasons. These include the constant cooling air velocity at 2 m/s, cooling air temperature, maximum cell surface temperature which has to stay below 60ºC, and the battery voltage above 2.7 Volts.
10. The experimental results including cell temperatures, battery voltage and current and cooling air velocity and temperature are recorded automatically through Labview software at the frequency of 10 Hz.

The experimental procedure is than repeated for 3C and 5C discharge rate at air velocity of 2 m/s, 4 m/s, 6 m/s, 8 m/s, and 10 m/s; leading to a total of 15 experiments. Normally only one experiment can be conducted every day due to long time needed to fully charge the battery cells. During charging process, the battery is charged with a charger that uses a typical charging profile

starting from a constant current charge and then converting into constant voltage charge at 4.2 Volts. A battery cell controller (BMS) is used for each cell to avoid over charge or over discharge that may lead to irreversible damage. During charge, the BMS disconnects the battery cell from the charger if the cell voltage exceeds the critical level of 4.25 Volts. During discharge, the load disconnects, as soon as the cell voltage drops below 2.5 Volts.

Table 3. Time to reach 20% and 10% SOC for different discharge rate.

Discharge rate	**Discharge time (s)**	
	20% SOC	**10% SOC**
1C	2880	3240
3C	960	1080
5C	576	648

3.3 TEMPERATURE EVOLUTION AT DIFFERENT DISCHARGE RATE

In this section the influence of different discharge rates on the temperature evolution is analysed. Figure 57-Figure 59 show the cell surface temperatures at P1-P8 (first cell, 1R) for discharge rates of 1C, 3C, and 5C respectively. The cooling air velocity is fixed at 2 m/s at air temperature is between 21ºC-22ºC. Results show the cell surface temperature for discharge process from 100% SOC until 20% SOC.

In general, cell surface temperatures are different at all locations where the highest temperature is observed at P1, followed by P2 and P3. These three points are near the positive and negative electrode. Temperature is higher near these two electrodes because of higher current densities at positive and negative terminal compared to the rest of the cell. At 1C discharge rate, only a small quantity of temperature increase is observed for all eight locations, less than 3ºC. At 3C and 5C discharge rate, a much more significant temperature increase is obtained, especially at P1; 12ºC and 23ºC respectively. It is clear that temperature near the positive electrode is higher than at the negative electrode, due to lower electrical conductivity of

the positive electrode. The value of electrical conductivity (Siemens/metre) at positive electrode is in the order of $38x10^6$ $S.m^{-1}$ and $60x10^6$ $S.m^{-1}$ at negative electrode [31, 108]. It can be observed that the two lowest temperatures are recorded at P4 and P7 even though these two points are near the hottest location, at positive electrode side. There are huge differences of temperature between P7 and P8. Temperature at P4 and P7 is lower than at other locations because of the effect of cooling system. These locations are close to the cell edge that faces the inlet cooling air that received the cooling air at lowest temperature. The cooling air takes heat from the cell, consequently the air temperature increases as it is passing the battery cell. At 1C discharge rate, the cell surface temperature is more sensitive than at 3C and 5C. This is because at a small discharge rate, only a small value of heat is generated inside the battery. Any small change of the cooling air velocity and temperature will have a big influence on the heat transfer and thus on the temperature increase.

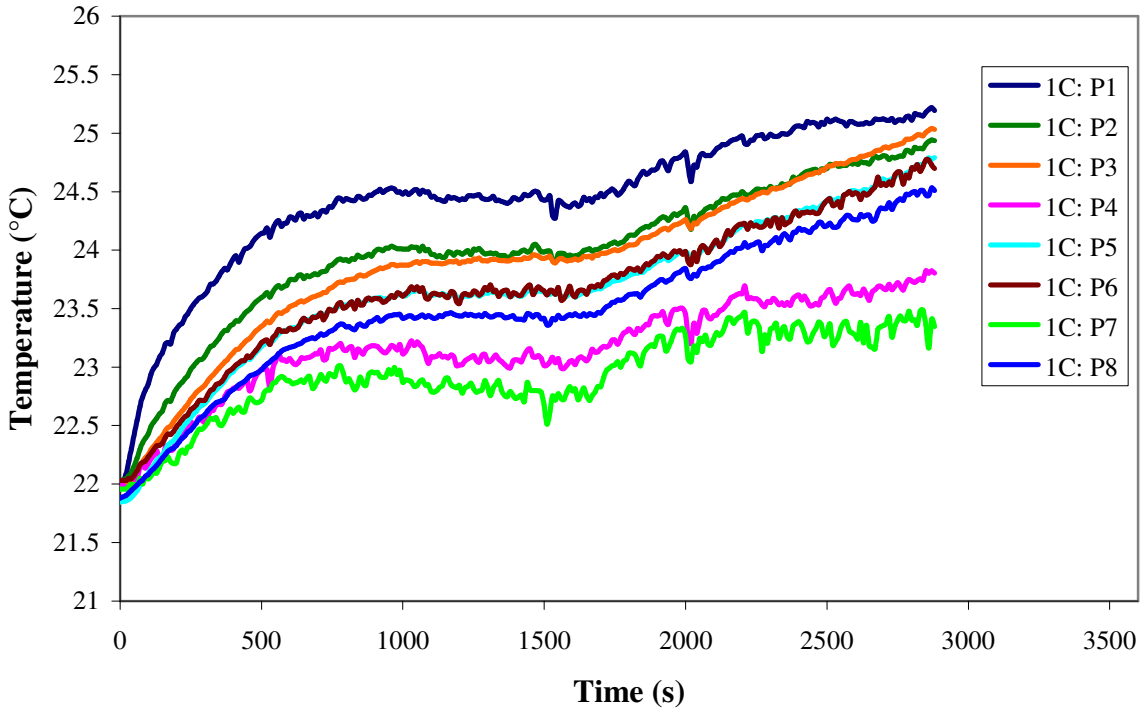

Figure 57. Cell surface temperature at 1C discharge rate with cooling air velocity of 2 m/s at air temperature of 22ºC.

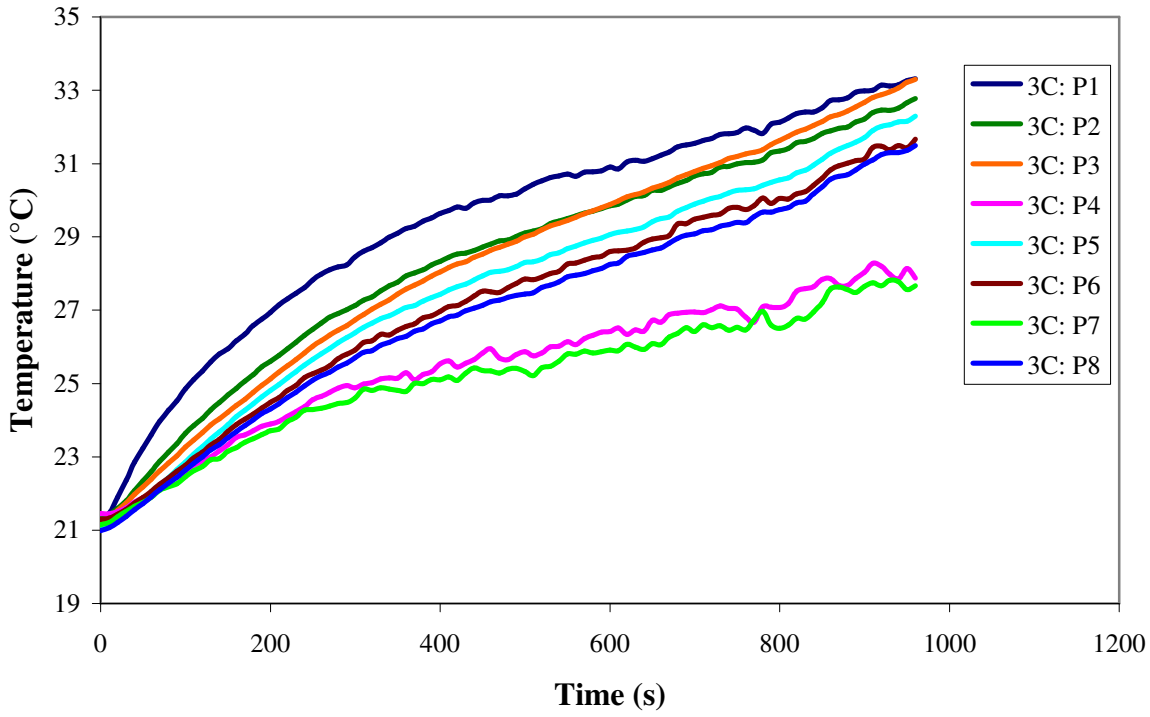

Figure 58. Cell surface temperature at 3C discharge rate with cooling air velocity of 2 m/s at air temperature of 21ºC.

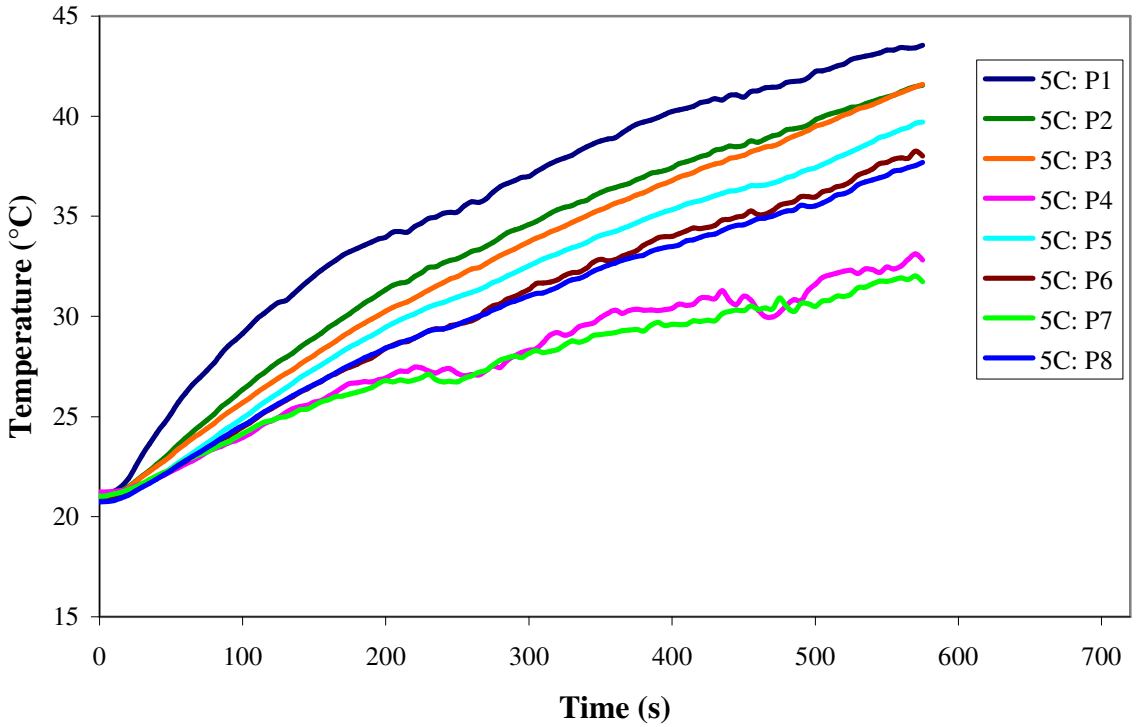

Figure 59. Cell surface temperature at 5C discharge rate with cooling air velocity of 2 m/s at air temperature of 21ºC.

The comparison of the maximum and minimum temperature evolution for 1C, 3C, and 5C discharge rates are summarised in Figure 60. In general, temperatures at P1 and P7 are higher for a higher value of discharge rate. This finding indicates that the battery temperature is affected by the amount of discharge rate. Higher discharge rate means that a higher amount of current circulates and generates more heat and thus increases the cell temperature. The cell surface temperatures at the end of discharge at P1 are 25°C, 33°C, and 44°C for the discharge rate of 1C, 3C, and 5C respectively. The temperature difference between P1 and P7 is greater for higher discharge rates. At 1C discharge rate, only 2°C of temperature difference is recorded, however this value increases to 5°C for 3C and 12°C for 5C discharge rate.

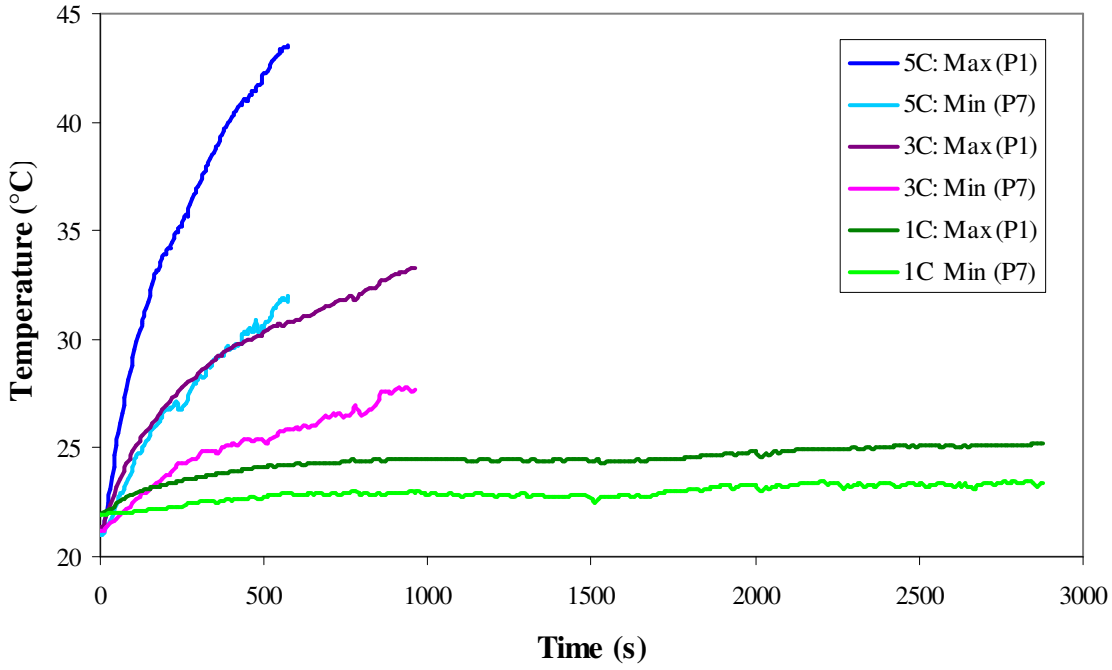

Figure 60. Comparison of max and min temperature for different discharge rate at cooling air velocity of 2 m/s.

Figure 61-Figure 63 show the maximum and minimum temperature at three different cell surfaces of the first and second cell (surface 1R, 1L, and 2R) with cooling air velocity of 2 m/s at discharge rate of 1C, 3C, and 5C respectively. In general, the maximum temperature for the second cell surface (surface 2R) is much higher compared to cell surface temperature of both surfaces of the first cell (1R and 1L). The minimum temperature at surface 2R is also higher than

the minimum temperature at surface 1R and 1L. The maximum temperature of surface 1R (P1) and 1L (P9) is same from the beginning until the end of discharge process for all three discharge rates. At 5C discharge, the temperature increases at the same rate at the beginning of discharge process until t=100 s, then the temperature of second cell increases at higher rate than the first cell. In contrast, at 1C and 3C discharge, the temperatures increase at different rates from the beginning of the discharge process, except for P1 and P9.

In general, for all three discharge rate, the temperature of second cell is higher than for the first cell because the second cell is in the middle of battery box, between first and third cell. In this configuration, the second cell has lower heat transfer efficiency compared to other cells. Thus, less heat transfer, and higher temperature increase. Furthermore, the positive electrode of the first and third cell is close to inlet cooling air, while the positive electrode of the second cell is far from this inlet cooling air. This amplified the difference of temperature between the first and second cell. The maximum temperature of the surface 1R and 1L is equal, while the minimum temperature at 1L is higher than at surface 1R.

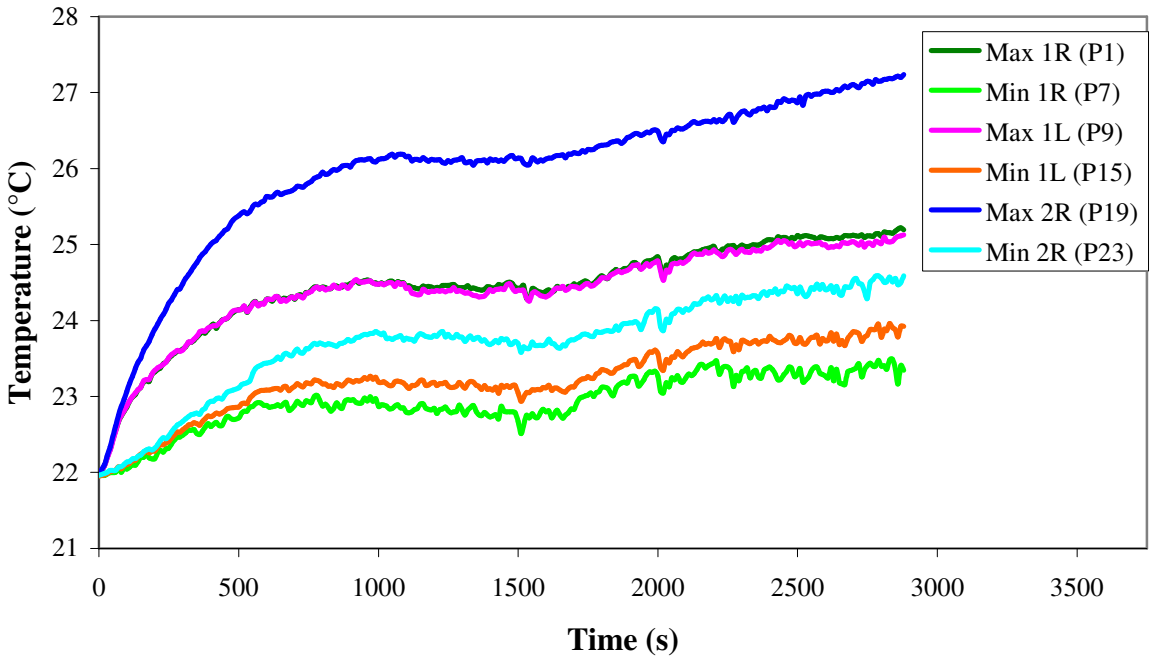

Figure 61. Comparison of max and min temperature for different cell surface at 1C discharge rate at cooling air velocity of 2 m/s.

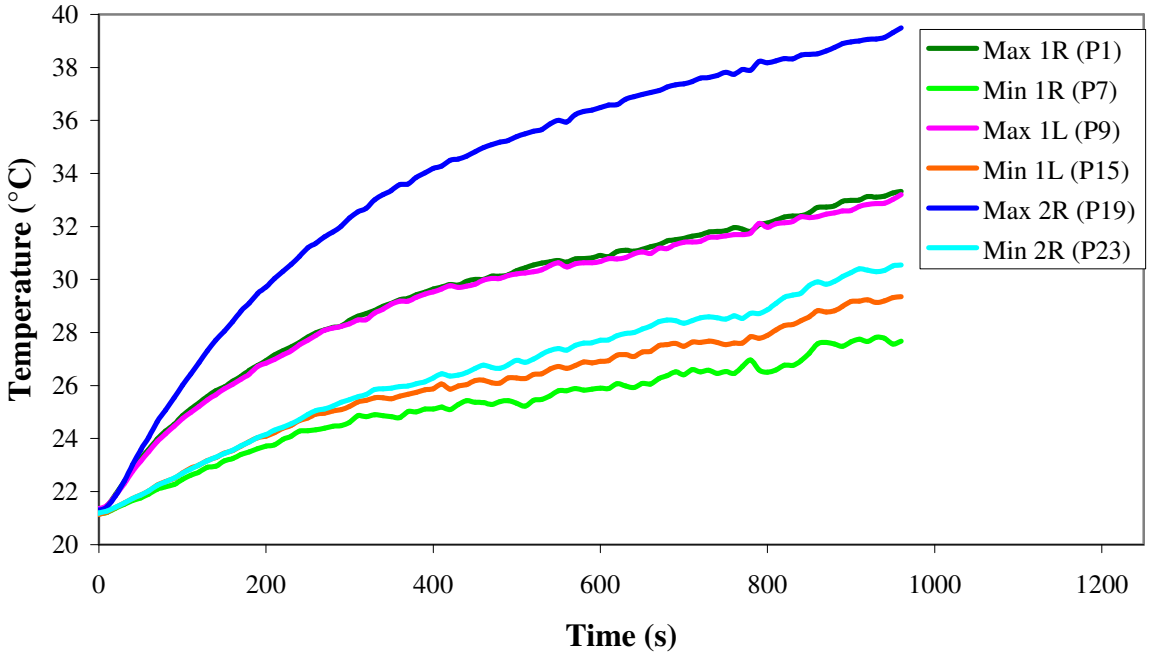

Figure 62. Comparison of max and min temperature for different cell surface at 3C discharge rate at cooling air velocity of 2 m/s.

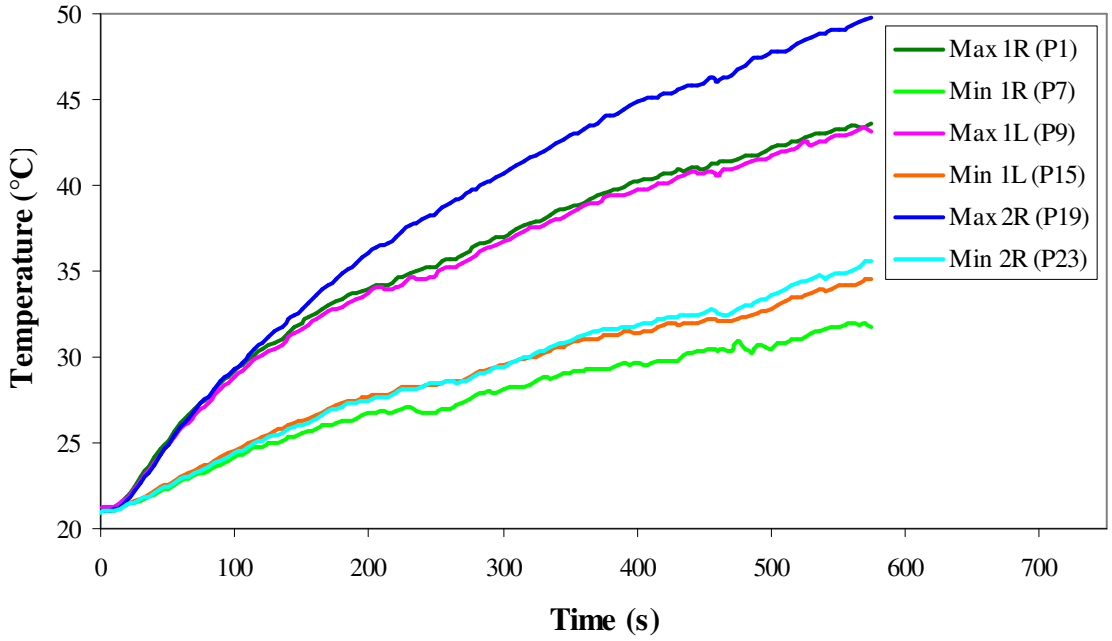

Figure 63. Comparison of max and min temperature for different cell surface at 5C discharge rate at cooling air velocity of 2 m/s.

3.4 INFLUENCE OF COOLING AIR VELOCITY ON CELL TEMPERATURE

To observe the impact of different cooling air velocities on the cell temperature, 5 different air velocities are used; 2 m/s, 4 m/s, 6 m/s, 8 m/s, and 10 m/s. The discharge rate is fixed at 5C. The temperature evolution for two most important points at first and second cell is observed, P1 and P7 for highest and lowest temperature point at the first cell (surface 1R) and P19 and P23 for the highest and lowest temperature point at the second cell (surface 2R). During experiment, cooling air temperature may vary between 21°C to 22°C.

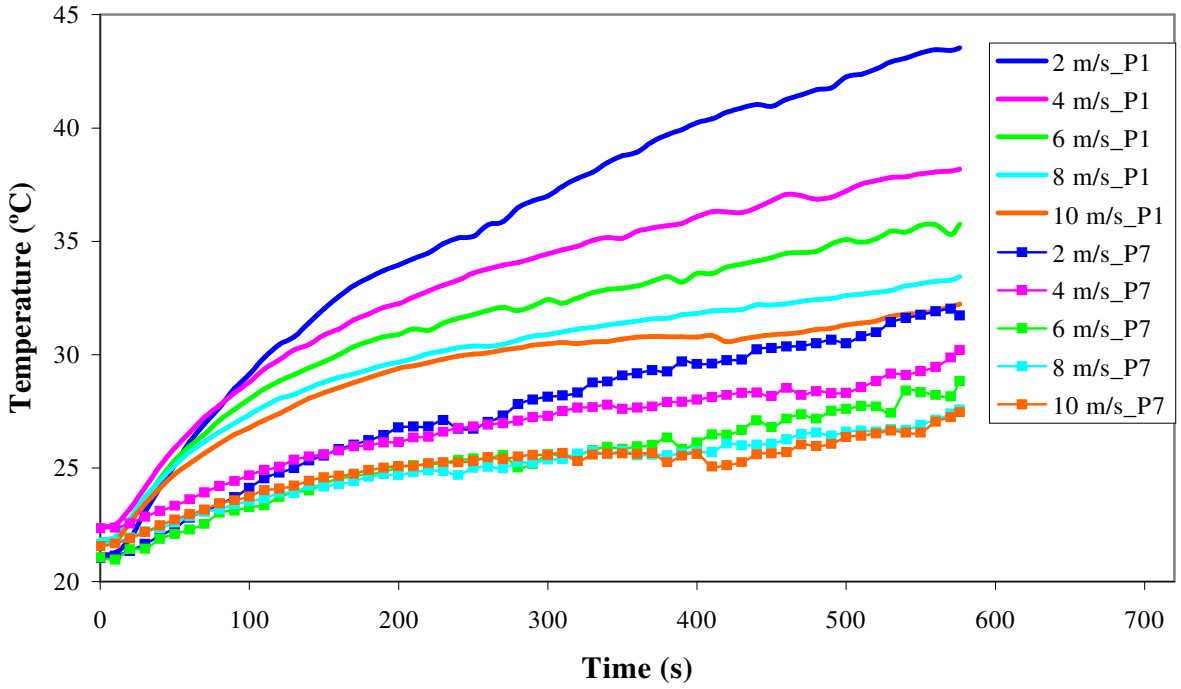

Figure 64. Cell surface temperature of surface 1R (P1 and P7) at different cooling air velocity for 5C discharge rate.

Figure 64 shows the temperature evolution at P1, and P7 for five different cooling air velocities. At P1, the cell surface temperature is 44°C at the end of discharge with cooling air velocity of 2 m/s. This value decreases to 38°C, 36°C, 33°C and 32°C at air velocity of 4 m/s, 6 m/s, 8 m/s and 10 m/s respectively. The difference of temperature between P1 and P7 decreases as the cooling air velocity increases. At 2 m/s, 12°C of temperature difference is recorded, this value decreased to 8°C for 4 m/s , 7°C for 6 m/s and 5°C for both 8 m/s and 10 m/s of cooling air velocity. At the beginning of discharge process, the temperature increases at the

same rate for all different cooling air velocities until 50 seconds discharge time. After 50 seconds, the temperature increases at different rates, higher rate at lower cooling air velocity, and the rate decreases as air velocity increases. At small cooling air velocity, cell temperature continues to increase until the end of discharge. At high cooling air velocity of 10 m/s, the cell temperature increases until 300 second discharge time, after that the temperature is nearly constant until end of discharge.

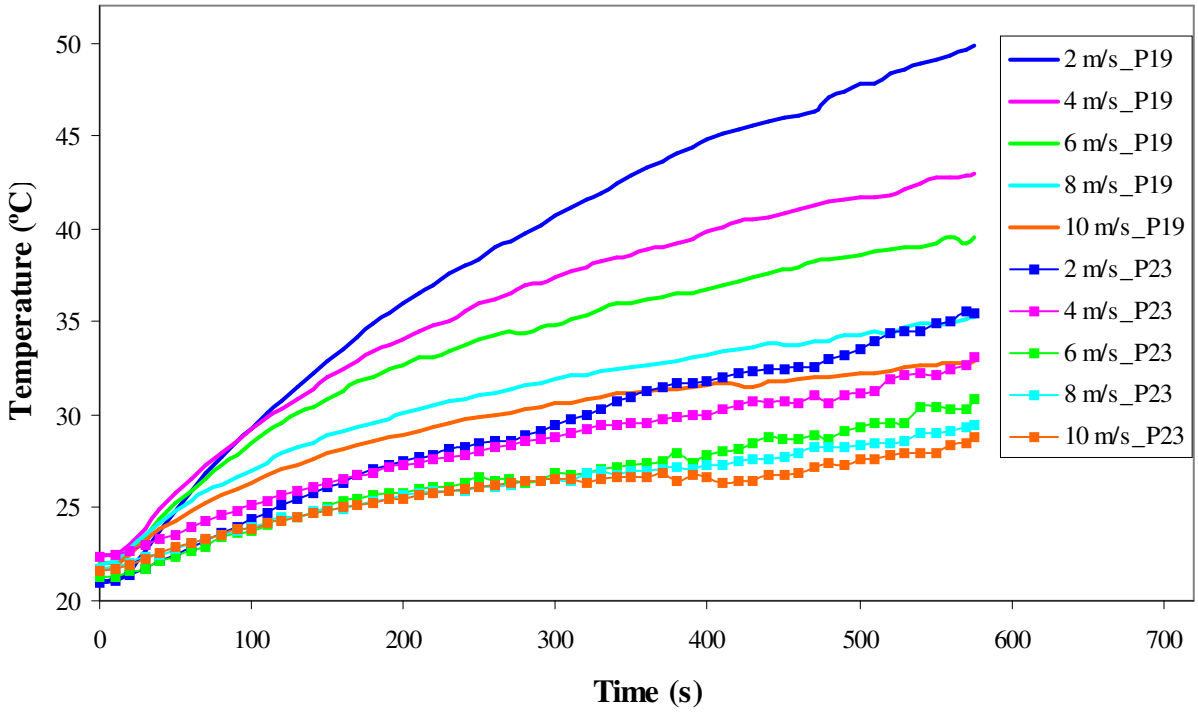

Figure 65. Cell surface temperature of surface 2R (P19 and P23) at different cooling air velocity for 5C discharge rate.

Figure 65 shows the temperature evolution of the second (surface 2R), at P19, and P23 for five different cooling air velocities. In general, temperatures at the surface 2R rise at the same way as at the surface 1R, as shown in Figure 64. The temperature at the highest and lowest temperature point decreases as the cooling air velocity increases. At P19, the cell surface temperature at the end of discharge decrease from 49.8°C to 42.9°C, 39.5°C, 35.2°C and 32.9°C as cooling air velocity increase from 2 m/s to 4 m/s, 6 m/s, 8 m/s and 10 m/s respectively. The difference of temperature between maximum (P19) and minimum (P23) location decreases as the

cooling air velocity increases. At high cooling air velocity of 10 m/s, the cell temperature increases until 300 second discharge time, after that the temperature is nearly constant until the end of discharge while at small cooling air velocity, cell temperature continues to increase until the end of discharge.

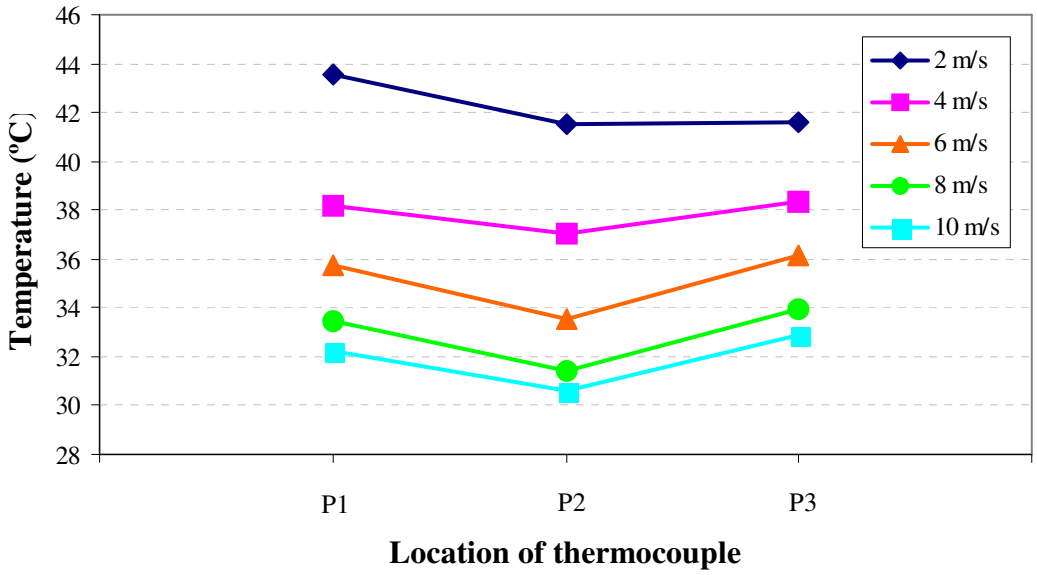

Figure 66. Temperature at P1, P2, and P3 at the end of discharge process for different cooling air velocity at 5C discharge rate.

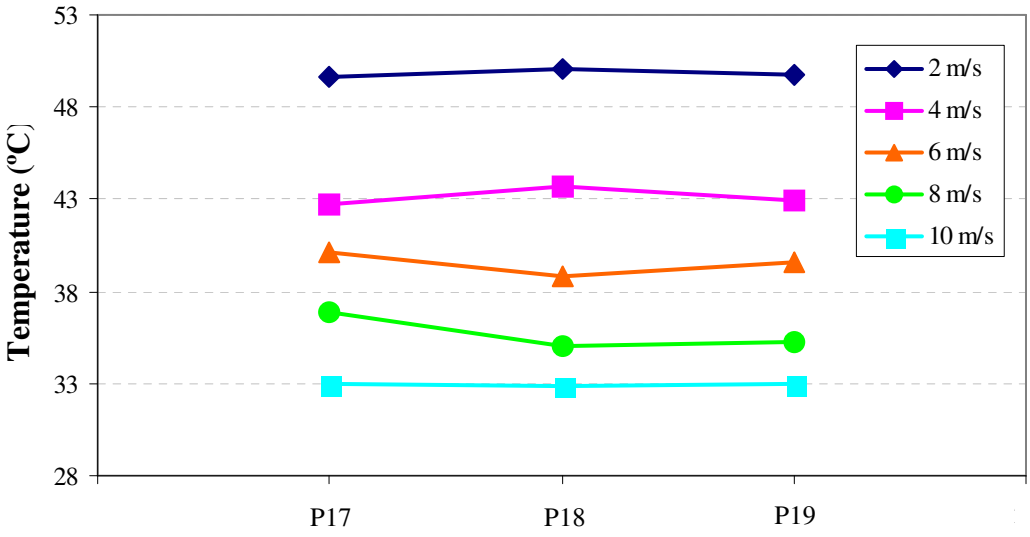

Figure 67. Temperature at P17, P18, and P19 at the end of discharge process for different cooling air velocity at 5C discharge rate.

Figure 66 and Figure 67 summarizes the temperature at the end of discharge process at 5C discharge rate with different cooling air velocities for three highest locations at surface 1R (P1, P2 and P3) and surface 2R (P17, P18, and P19) respectively. Figure 66 shows that at cooling air velocity of 2 m/s, the highest temperature locations are P1, followed by P2 and P3, this trend changes as cooling air velocity increases. At 4 m/s, temperature near positive electrode (P1) is the same as at negative electrode (P3). Starting from 6 m/s and higher, the P3 becomes the hottest point, instead of P1. The cooling air takes more heat from the cell as the air speed increases. P3 is less affected by this condition than P1, because P1 is close to the inlet air with lower cooling air temperature than at P3. In all cases, temperature at P2 is lower than P1 and P3. Figure 67 shows that at cooling air velocity of 2 m/s, and 4 m/s the hottest location is P18, and the temperature at P17 and P19 is equal. At 10 m/s, temperature is the same for all three locations, P17, P18 and P19. At this discharge rate (5C) there is no significant difference of temperature between P17, P18, and P19. But, at lower discharge rate of 1C and 3C, the temperature difference between these three locations is bigger with the highest temperature is recorded at P19 which is near to positive electrode. This phenomenon will be discussed in section 3.5.3.

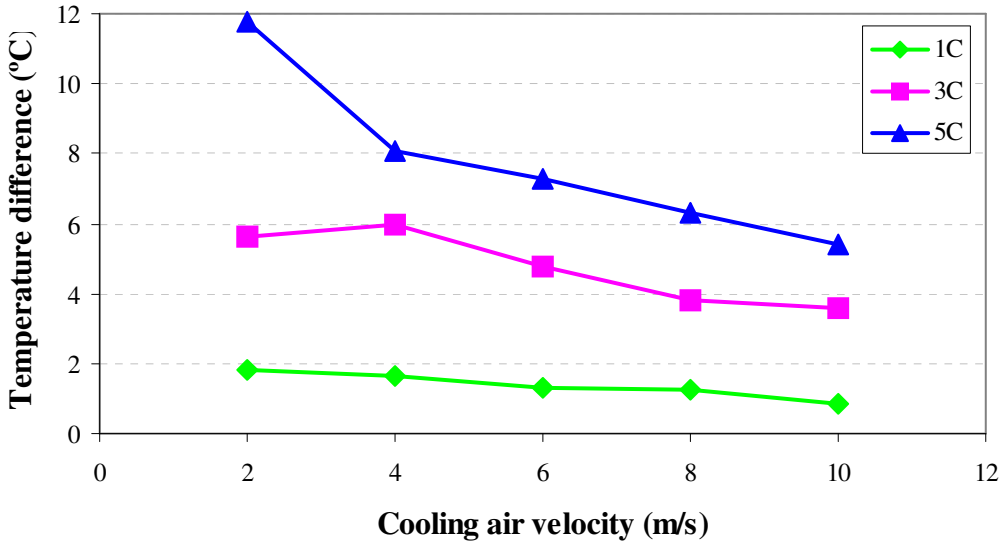

Figure 68. Temperature difference between P1 and P7 at different cooling velocity and different discharge rates.

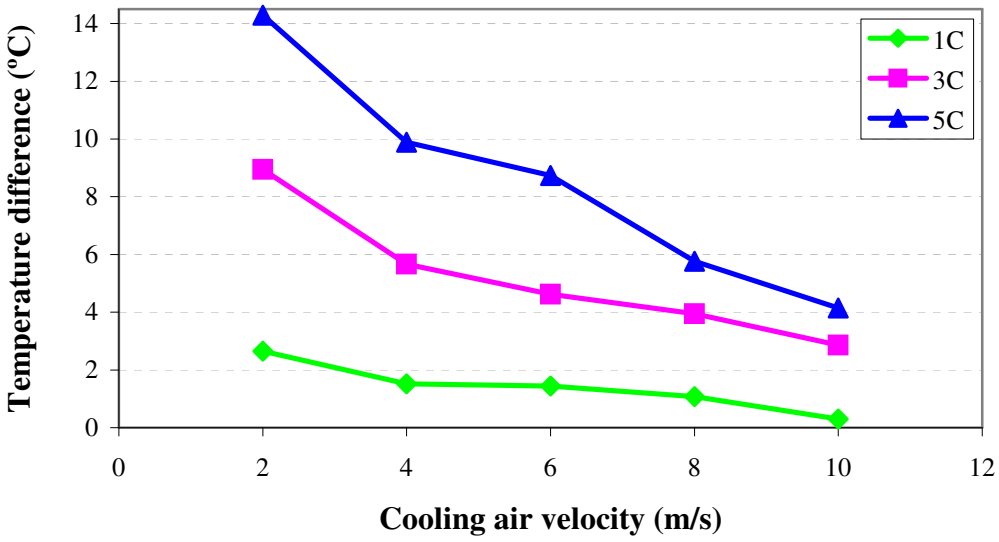

Figure 69. Temperature difference between P19 and P23 at different cooling velocity and different discharge rates.

Figure 68 and Figure 69 shows the temperature difference between the hottest and coolest location at different discharge rates and cooling air velocities for the first cell at surface 1R (P1 and P7) and the second cell at surface 2R (P19 and P23) respectively. In general, the temperature difference decreases as the cooling air velocity increases. At lower cooling air velocity, the temperature difference at surface 2R is higher than at surface 1R for all three discharge rates. But, at higher cooling air velocity (10 m/s) the temperature difference at surface 2R is lower than at surface 1R.

Figure 68 shows that at 5C discharge rate, with 2m/s cooling air velocity, the temperature difference is 11.8ºC, than it decreases to 5.7ºC and 1.8ºC for 3C and 1C discharge rate respectively. The biggest decrease in temperature difference is recorded for cooling air velocity change from 2 m/s to 4 m/s for 5C discharge rate. Then, the temperature difference decreases at a lower but constant rate with the increase of cooling air velocity. At 3C discharge, the temperature difference slightly increases when the cooling air velocity increases from 2 m/s to 4 m/s, then it decreases with further increases of cooling air velocity. At higher cooling air velocity, 8 m/s and 10 m/s, there is nearly no more temperature decrease observed. At 1C discharge rate, in general there are just small temperature differences between hottest and coolest location. Thus,

the cooling air velocities have less effect on the temperature difference. Figure 69 shows that at 5C discharge rate, with 2m/s cooling air velocity, the temperature difference is 14.3ºC, than it decreases to 9.0ºC and 2.7ºC for 3C and 1C discharge rate respectively. The biggest decrease in temperature difference is recorded for cooling air velocity change from 2 m/s to 4 m/s for all three discharge rates. Then, the temperature difference decreases at a lower rate with the increase of cooling air velocity.

3.5 TEMPERATURE BEHAVIOUR FOR ABUSE DISCHARGE CONDITION

3.5.1 Introduction

This section analyses the impact of abuse discharge condition on the cell surface temperature. In the current study, cell discharge down to 10% SOC is considered as an abuse discharge condition. The calculation of the battery cell SOC is explained in section 3.2.2, and the discharge times to reach 20% and 10% SOC for different discharge rates are shown in Table 3 (section 3.2.2). To determine the temperature evolution of the battery cell surface, a series of experiments is conducted. The battery is discharged at 1C, 3C, and 5C discharge rate with a constant cooling air velocity of 2 m/s. The cooling air velocity is maintained constant at 2 m/s from t=0 s until 100 seconds after the end of discharge, to ensure the effective cooling condition after discharge.

Figure 70-Figure 72 show the temperature evolution of the first cell (surface 1R) at P1 to P8 for 1C, 3C, and 5C discharge rate respectively. Figure 73-Figure 75 show the temperature evolution of the second cell (surface 2R) at P17 to P24 for 1C, 3C, and 5C discharge rate respectively. Separator I indicates the discharge time at 20% SOC and separator II is the end of discharge at 10% SOC. In general, the cell surface temperatures increase steadily at the beginning of discharge until 20% SOC for all three discharge rates. After 20% SOC until the end of discharge, there is a sudden increase of temperature for all 8 locations. This phenomenon is explained by Lin et al. [72] by the huge increase of the value of internal resistance between 20% SOC and 10% SOC. This is one of the reasons why it is dangerous to discharge the battery to less then 20% SOC. The description and different values of internal resistance found in literatures are described in section 2.3.4.1. Experimental results to evaluate the internal resistance in the function of temperature and SOC are explained in section 3.6.

3.5.2 First cell at different discharge rates

In general, the temperature evolution at 20% SOC to 10% SOC is similar for all three discharge rates (1C, 3C and 5C) with two distinctive temperatures recorded; one higher temperature for P1, P2, P3, P5, and P8, and one lower temperature for P4 and P7. At 1C discharge rate, the temperature increases to only two distinctive temperatures, 26ºC for P1, P2, P3, P5, P6, and P8, and 24.5ºC for P4 and P7, even though temperature for P1-P8 are different at 20% SOC. From 20% SOC to 10% SOC the value of temperature increase is around 1ºC at P1 to P8. In this condition P1 is no longer the hottest location and P7 is no longer the coolest location. There is no more effect of high current densities at negative and positive electrodes and also the difference of the electrical conductivity on the temperature increases. At 3C the value of temperature increase is 4ºC at P1, P2 and P4, 5ºC at P3 and P6, 6.0ºC at P5 and P7 and 7ºC at P8. Finally, at 5C discharge rate, between 20% SOC to 10% SOC, temperature differences is around 3ºC at P1 and P2, 4ºC at P3 and P4, 6ºC at P5, P6 and P7, and 7ºC at P8. The value of temperatures at the end of discharge at 10% SOC and their differences with the temperature at 20% SOC are listed in Table 4.

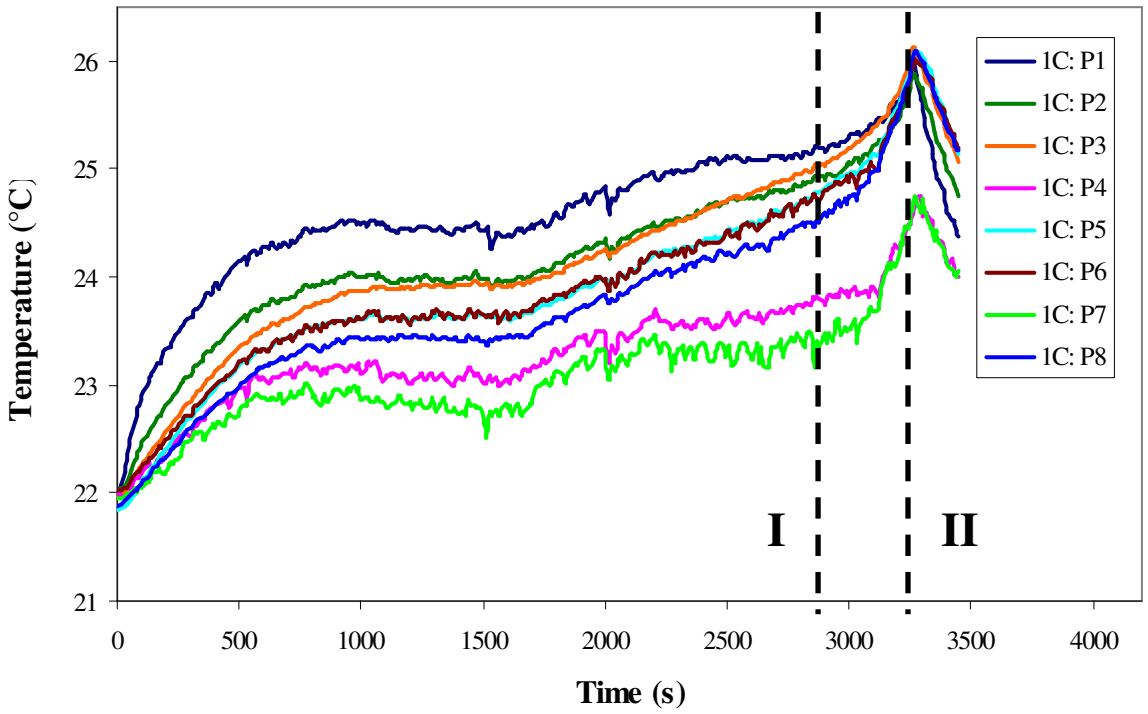

Figure 70. Cell surface temperature evolution under 1C discharge rate at cooling air velocity of 2 m/s for abuse discharge at first cell.

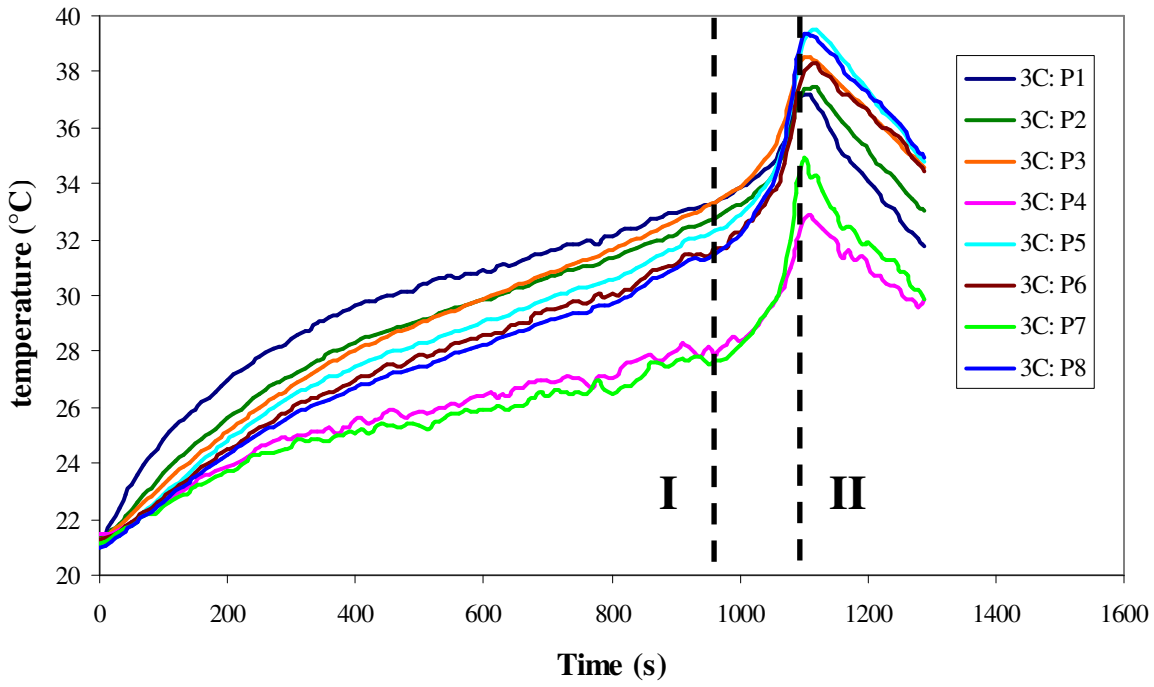

Figure 71. Cell surface temperature evolution under 3C discharge rate at cooling air velocity of 2 m/s for abuse discharge at first cell.

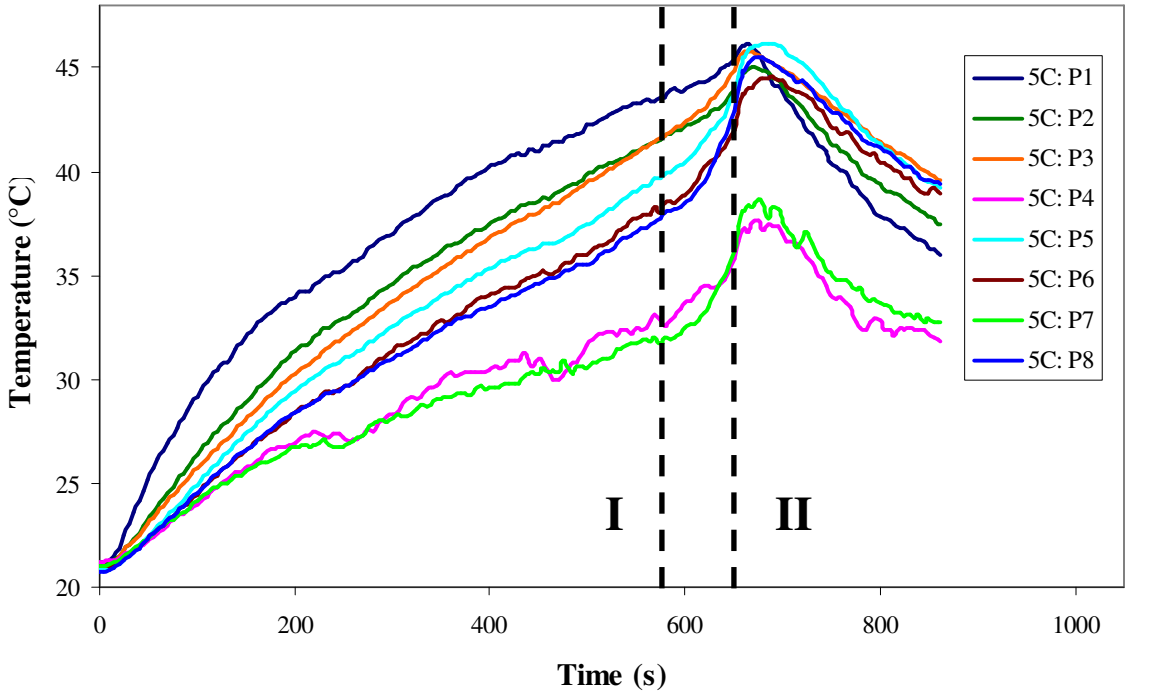

Figure 72. Cell surface temperature evolution under 5C discharge rate at cooling air velocity of 2 m/s for abuse discharge at first cell.

Table 4. Temperature at end of discharge for 20% SOC and 10% SOC at air velocity of 2 m/s for first cell (surface 1R).

Discharge rate	Temperature (°C)	Thermocouple							
		P1	**P2**	**P3**	**P4**	**P5**	**P6**	**P7**	**P8**
1C	At 20% SOC	25.2	24.9	25.0	23.8	24.8	24.7	23.3	24.5
	At 10% SOC	25.9	25.8	26.0	24.5	25.9	25.9	24.6	25.9
	Difference	0.7	0.8	1.0	0.7	1.1	1.2	1.2	1.4
	% increase	***2.9***	***3.3***	***4.0***	***2.9***	***4.6***	***4.8***	***5.2***	***5.7***
3C	At 20% SOC	33.3	32.8	33.3	27.9	32.3	31.7	27.7	31.5
	At 10% SOC	36.8	36.7	38.0	31.8	37.8	36.9	33.7	38.2
	Difference	3.5	3.9	4.7	3.9	5.6	5.3	6.0	6.7
	% increase	***10.6***	***11.9***	***14.1***	***14.0***	***17.2***	***16.7***	***21.7***	***21.2***
5C	At 20% SOC	43.5	41.5	41.6	32.8	39.7	38.0	31.7	37.7
	At 10% SOC	46.1	44.8	45.7	37.3	45.5	43.7	38.1	44.9
	Difference	2.5	3.3	4.2	4.4	5.8	5.7	6.4	7.2
	% increase	***5.8***	***7.8***	***10.0***	***13.5***	***14.6***	***15.0***	***20.1***	***19.0***

For all three discharge rates, the smallest temperature increase is at P1 and the biggest temperature increase is observed at P8. This means that location near the positive electrode will have less temperature increase than other part of battery cell while temperature for location far from positive electrode will increase the most. At 1C discharge rate, temperature from 20% SOC to 10% SOC increase from 3-6%, 11-22% for 3C discharge, and 6-20% for 5C discharge. The highest percentage increase is observed at P8 for 1C discharge and P7 at 3C and 5C discharge. On the other hand, the lowest percentage increase is obtained at P1 for all three cases.

3.5.3 Second cell at different discharge rates

In general, the temperature increases gradually from 100% SOC to 20% SOC for all three discharge rates (1C, 3C and 5C). At the beginning of discharge process, temperature at P17 is the highest for all three discharge rates. Towards the end of discharge process, near 20% SOC, P19 becomes the highest temperature location for 1C and 3C discharge rates. At 5C discharge rate,

there is no significant difference between the temperature at P17, P18 and P19. In all cases, P23 is the lowest temperature location from the beginning until the end of discharge process.

From 20% SOC to 10% SOC, the temperature increases at higher rate compared to the temperature increases from 100% SOC to 20% SOC. Anyhow, the temperature increases from 20% SOC to 10% SOC at second cell is lower than at the first cell. The temperature increases from 20% SOC to 10% SOC is between 0.2ºC to 1.1ºC at 1C discharge, 1.3ºC to 4.1ºC at 3C discharge and 1.4ºC to 5.8ºC at 15C discharge. For all three discharge rates, the highest temperature at 10% SOC is at P19 while the lowest temperature is recorded at P23. The value of temperatures at the end of discharge at 10% SOC and their differences with the temperature at 20% SOC are listed in Table 5.

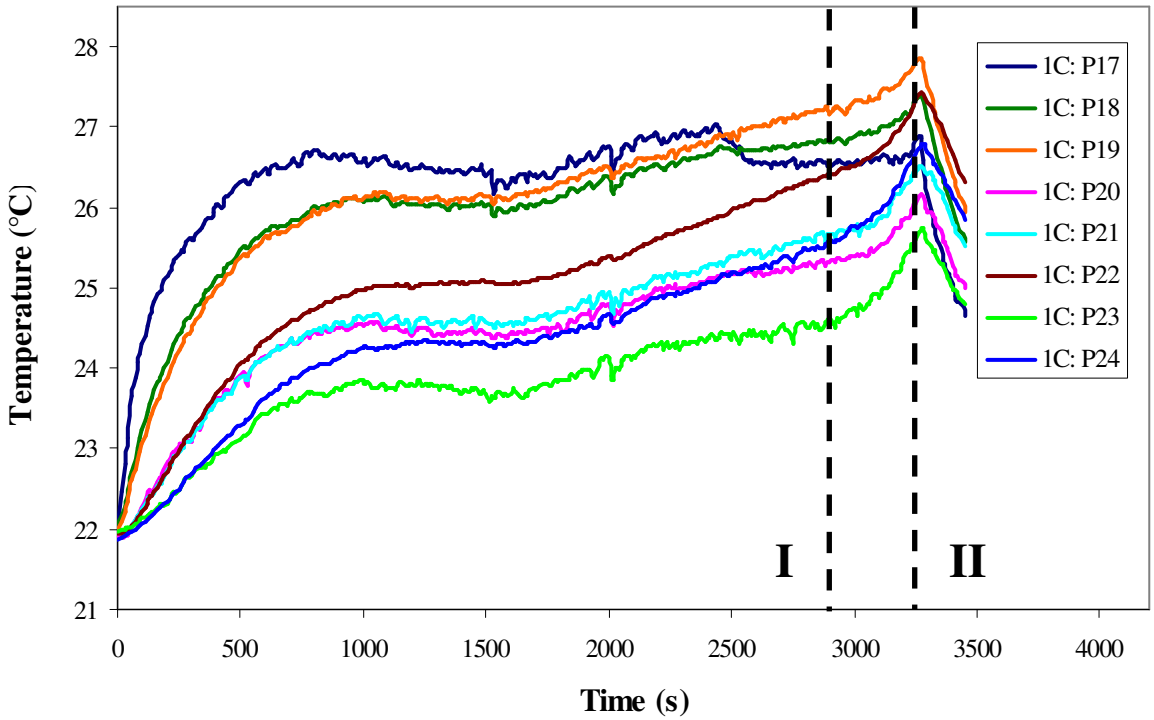

Figure 73. Cell surface temperature evolution under 1C discharge rate at cooling air velocity of 2 m/s for abuse discharge at second cell.

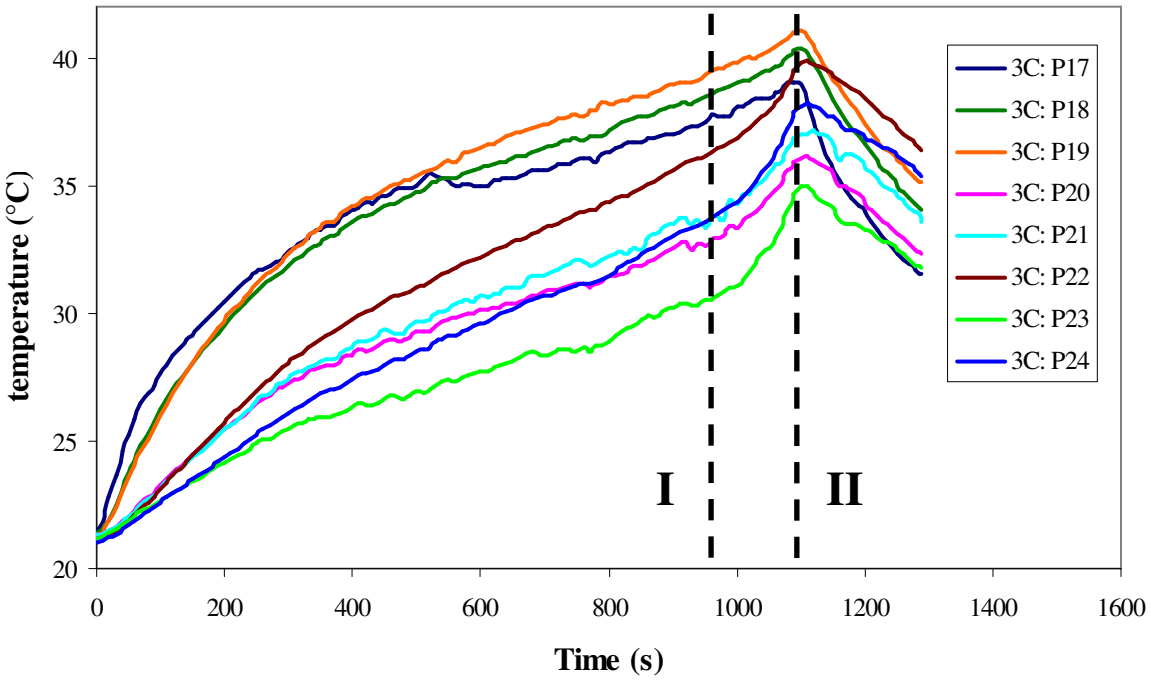

Figure 74. Cell surface temperature evolution under 3C discharge rate at cooling air velocity of 2 m/s for abuse discharge at second cell.

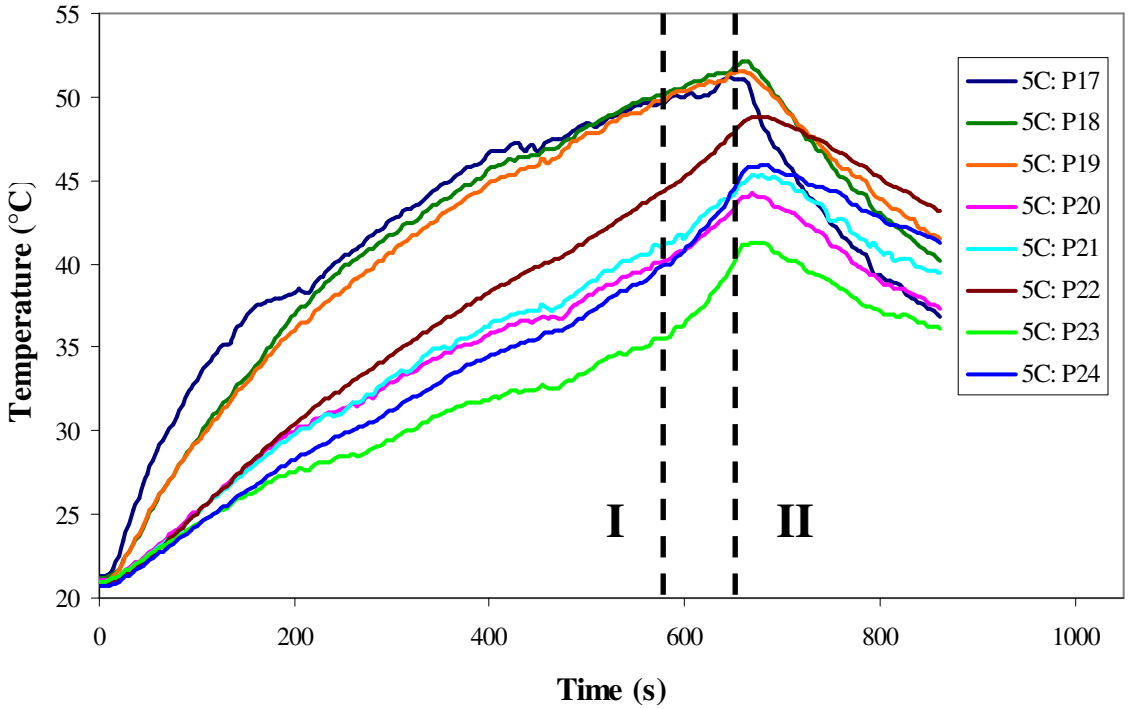

Figure 75. Cell surface temperature evolution under 5C discharge rate at cooling air velocity of 2 m/s for abuse discharge at second cell.

Table 5. Temperature at end of discharge for 20% SOC and 10% SOC at air velocity of 2 m/s for second cell (surface 2R).

Discharge rate	Temperature (ºC)	Thermocouple							
		P17	**P18**	**P19**	**P20**	**P21**	**P22**	**P23**	**P24**
1C	At 20% SOC	26.6	26.8	27.2	25.3	25.6	26.4	24.6	25.5
	At 10% SOC	26.8	27.3	27.8	26.0	26.4	27.3	25.6	26.7
	Difference	0.3	0.5	0.6	0.8	0.9	0.9	1.0	1.1
	% increase	***1.0***	***1.8***	***2.1***	***3.1***	***3.4***	***3.5***	***4.1***	***4.4***
3C	At 20% SOC	37.8	38.6	39.5	32.9	33.7	36.3	30.5	33.7
	At 10% SOC	39.1	40.2	41.0	35.7	36.7	39.4	34.4	37.7
	Difference	1.3	1.6	1.5	2.8	3.0	3.1	3.9	4.1
	% increase	***3.5***	***4.2***	***3.7***	***8.6***	***9.0***	***8.6***	***12.8***	***12.0***
5C	At 20% SOC	49.6	50.1	49.8	40.1	41.1	44.2	35.6	39.8
	At 10% SOC	51.0	52.1	51.6	44.0	44.9	48.5	41.2	45.5
	Difference	1.4	2.0	1.8	3.9	3.8	4.3	5.6	5.8
	% increase	***2.8***	***4.1***	***3.6***	***9.7***	***9.2***	***9.7***	***15.7***	***14.5***

3.6 BATTERY INTERNAL RESISTANCE

Battery internal resistance *R* is an important parameter of a lithium-ion battery that needs to be estimate accurately, especially when modelling the battery thermal behaviour. Most of recent studies consider that the heat generation inside the battery cell is directly proportional to discharge current and the value of internal resistance [31, 36, 38, 55, 76, 96, 101, 103, 105, 107]. Fail to estimate the right value of internal resistance will lead to inaccurate or wrong calculation battery thermal behaviour.

Analysis of literature reveals that the battery internal resistance is normally described in three different ways; as a constant or as a function of battery state of charge (SOC) or temperature as discussed in section 2.3.4.1. In general, battery internal resistance decreases when the temperature increases (from around -20ºC) until certain limits (around 50ºC) due to the electrolyte used in lithium-ion batteries that has an electric conductivity which varies with

temperature [31, 74, 81]. On the other hand, the value of internal resistance is nearly constant with SOC except at small SOC; less than 20% SOC [38, 72, 97]. Even though the fact that the internal resistance changes with SOC and temperature is agreed by most researchers, different values are reported by one researcher to another; 0-2 mΩ in [76], 0.5-3 mΩ in [74], 4-6 mΩ in [95], and 4-15 mΩ in [31], as shown in Figure 27 (section 2.3.4.1). In other words, one cannot easily find the correct value of internal resistance for specific battery type just by using the value found in literature. Experimental study needs to be conducted in order to acquire the correct value of internal resistance. In the current study, two sets of parameter identification experiments are conducted; resistance at different temperatures and resistance at different SOC.

Based on multiphysical model proposed by Watrin et al. [74], the battery resistance can be divided into three components; series resistance R_s, fast branch resistance R_{st}, and slow branch resistance R_{lt} as shown in Figure 45 in section 2. Series resistance is calculated as the ratio of the voltage drop, ΔVs, directly after the current step and the current step amplitude as in equation 28.

$$R_s = \frac{\Delta V_s}{I} \tag{28}$$

where ΔV_s is the voltage drop due to series resistance as shown in Figure 76 and I is the amplitude of current step applied. ΔV_{st} is the voltage drop due to fast branch resistance, and ΔV_{lt} is the voltage drop due to slow branch resistance.

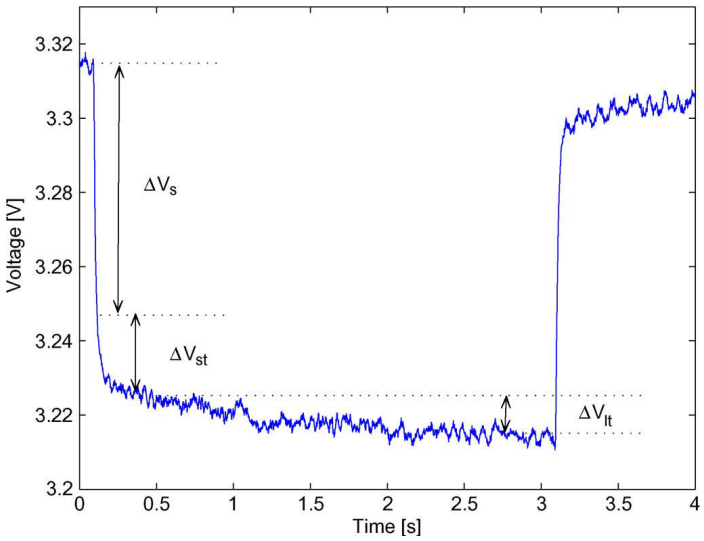

Figure 76. Battery discharge voltage after a current step [74].

3.6.1 Influence of temperature on the battery internal resistance

Temperature has a great influence on the battery internal resistance. This can be explained by the fact that the electrolyte used in lithium-ion batteries, such as LiPF6, LiBF4, or LiCIO4, has an electrical conductivity that varies with temperature [31, 74, 81]. In the present study, experiment is conducted using 0.5C discharge current step at battery temperature between 20ºC to 50ºC. Small discharge current step is used to limit the increase of temperature during current step discharge process and also to ensure that the SOC is higher than 20% throughout the experiment (section 3.6.2). The choice of 0.5C current step use can be observed in several existing works as in [31, 76, 94]. As the cell temperature is different at all cell surface locations, the temperature at hottest location, P1 is chosen as the reference temperature. The experimental procedures are as follow:

1. Experiment starts with the battery cell at full charge, battery initial temperature at P1 is initially at 20ºC.
2. The battery temperature at P1 is recorded.
3. A discharge current step of 0.5C (20 Amps) is applied during 30 seconds.
4. Based on the voltage response to this step, the battery resistance in function of temperature, $R_{s,T}$ is then calculated using equation 29.

$$R_{s,T} = \frac{\Delta V_s}{I} \tag{29}$$

5. Experiment is then conducted with battery temperature at 30ºC. In order to achieve this temperature, the battery cell is discharged at 5C (200 Amps) without cooling system. Using this discharge condition, the battery cell's temperature increases rapidly from 20ºC to 30ºC.
6. When the temperature at P1 achieves 30ºC, the 5C discharge process is stopped, afterwards a relaxation time is allowed for the battery cell temperature to stabilize, then experimental procedure steps 2 to 4 is repeated to calculate the battery internal resistance at 30ºC.
7. Experiment is continued for higher temperature, 40ºC and 50ºC by repeating experimental procedure 2 to 6.

The discharge step applied to the battery cell for overall experimental process, 0.5C and 5C from 20ºC to 50ºC is summarised in Figure 77. Experiment stops at 50ºC for safety reasons. At the end of experiment, the battery SOC drops to 55%.

Figure 78 shows the battery internal resistance in function of temperature. It shows that the resistance decreases over 40% with the increase of temperature from 20ºC to 50ºC. At 20ºC the battery resistance is 2.17 mΩ. The resistance is then decreased to 1.67 mΩ, 1.5 mΩ, and 1.33 mΩ at 30ºC, 40ºC, and 50ºC respectively. Here, the effect of SOC on the resistance is ignored as the battery SOC is kept over 50% SOC throughout the experimental process as the resistance is reported to be approximately constant when operated at SOC higher than 20% [72, 97]. This hypothesis will be verified in the following section.

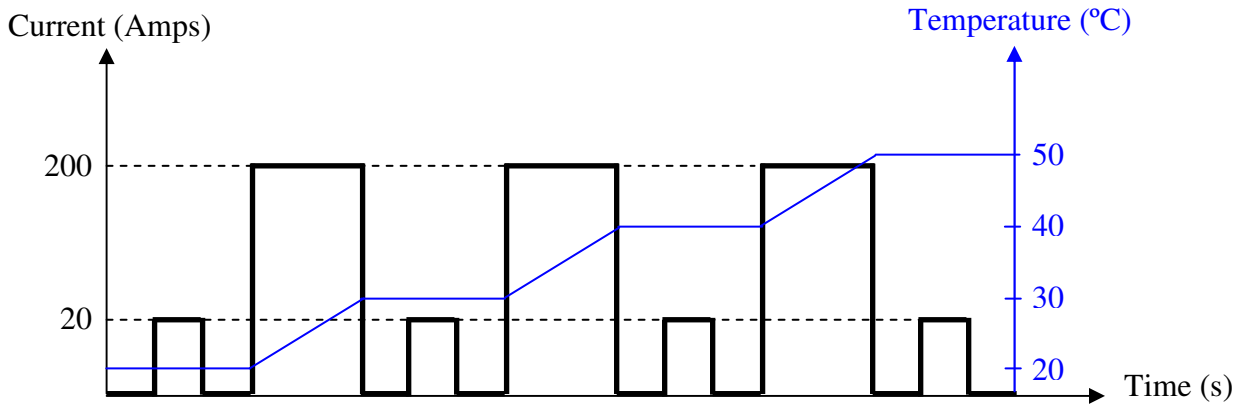

Figure 77. Discharge current steps for different temperature.

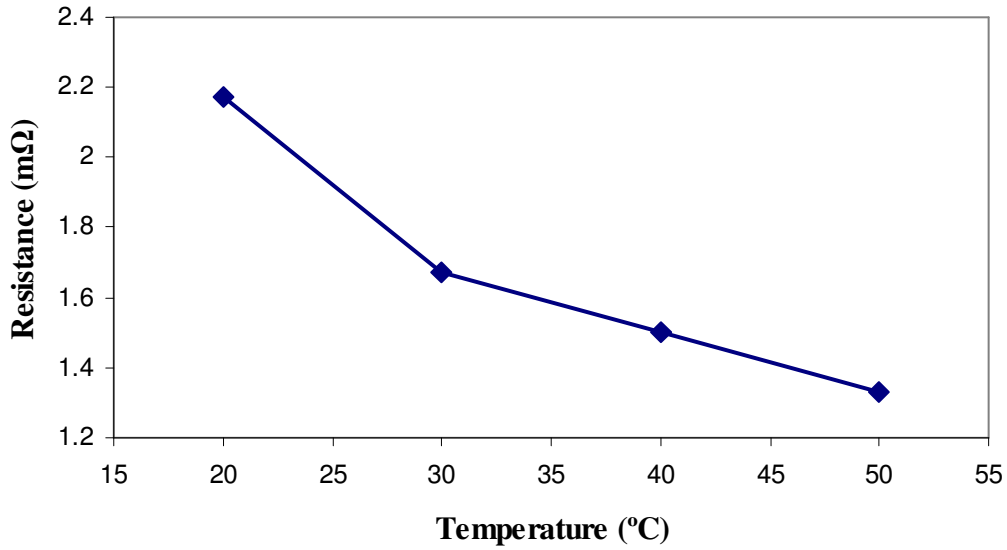

Figure 78. Battery resistance as a function of temperature.

3.6.2 Influence of SOC on the battery internal resistance

In this section, experimental process to estimate the battery internal resistance at different SOC is presented. Experiment is conducted with 0.5C step discharge current, at 22ºC. Throughout the experiment, cooling air at adapted velocity may be used in order to keep the battery cell temperature constant at 22ºC. Experimental procedure follows several steps:

1. Experiment starts with the battery cell at full charge, battery initial temperature at P1 and air velocity is at room temperature, 22ºC during experiment.
2. The battery SOC is considered at 100% SOC at the beginning of experiment.
3. A discharge current step of 0.5C (20 Amps) is applied during 720 seconds as shown in Figure 79. Small discharge rate is used to minimize the increase of temperature during discharge process.
4. Based on the voltage response to this step, the battery resistance as a function of SOC, $R_{s,SOC}$ is then calculated using equation 30.

$$R_{s,SOC} = \frac{\Delta V_s}{I} \tag{30}$$

5. After 720 seconds discharge at 0.5C, the battery SOC drops from 100% to 90%.
6. Experimental procedure steps 3 and 4 are repeated and calculate the battery internal resistance at 90% to 30% SOC.
7. At 20 % SOC, the experimental procedure steps 3 and 4 are repeated with the discharge time set to half, 360 seconds.
8. After 360 seconds discharge at 0.5C, the battery SOC drops from 20% to 15%
9. Experimental procedure step 6 is repeated and calculates the battery internal resistance at 15%, 10% and 5% SOC.

A 30 second relaxation time is given to the battery in between each 0.5C discharge process.

Figure 80 shows the battery internal resistance as a function of SOC at 22ºC. It shows that the resistance is nearly constant at the range 100% to 20% SOC. In this range, the value of internal resistance varies between 1.8-2.17 mΩ. After 20% SOC, there is a sudden jump in the value of internal resistance. At 5 % SOC the value of internal resistance is 3.7 mΩ, which is almost two times the initial value at 100% SOC. These analyses confirm the observation of Baronti at al. [97] and Lin et al. [72].

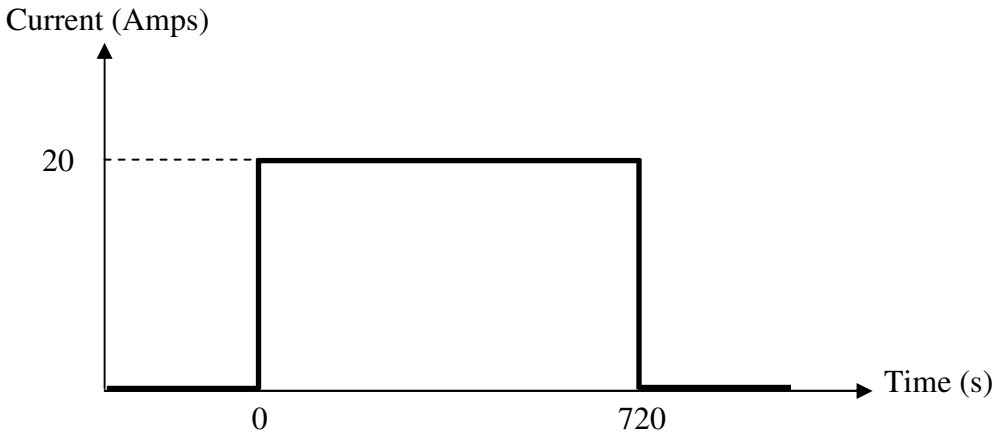

Figure 79. Current step for different SOC.

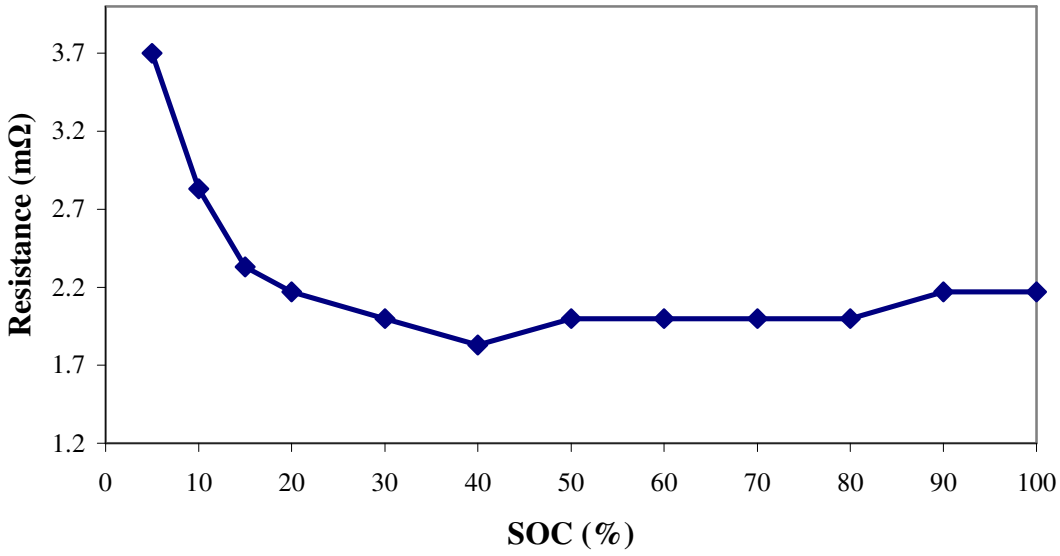

Figure 80. Battery resistance as a function of SOC

3.7 CASE STUDY

In this section, temperature evolution for a battery used under real running conditions of series hybrid electric vehicle is studied. Vehicle specifications used in the present study are given in Table 6. It is based on a series hybrid electric sports car, called Noao. The Noao is designed and build by the *Association des Entreprises du Pole de la Performance Nevers Magny-Cours (PPNMC)* which groups together over 20 companies around the circuit Nevers Magny-Cours that specialise in motorsport and the development of vehicles for the future. This hybrid sport car is

equipped with an electric motor of 90 kW nominal output power, a small 3-cylinder 1 liter ICE engine, and three lithium-ion batteries (144 cells) with a total capacity of 20 kWh. This small innovative hybrid sport car is capable to reach the maximum top speeds of 200 km/h.

Table 6. Vehicle characteristic.

Criteria	***Value***
ICE Power	60 kW
ICE Capacity	1000 cc
Vehicle Weight	1126 kg
Tyre Type	215/35 R18
(Frontal Area) x (Drag coefficient)	0.7
Motor Electric Power	90 kW

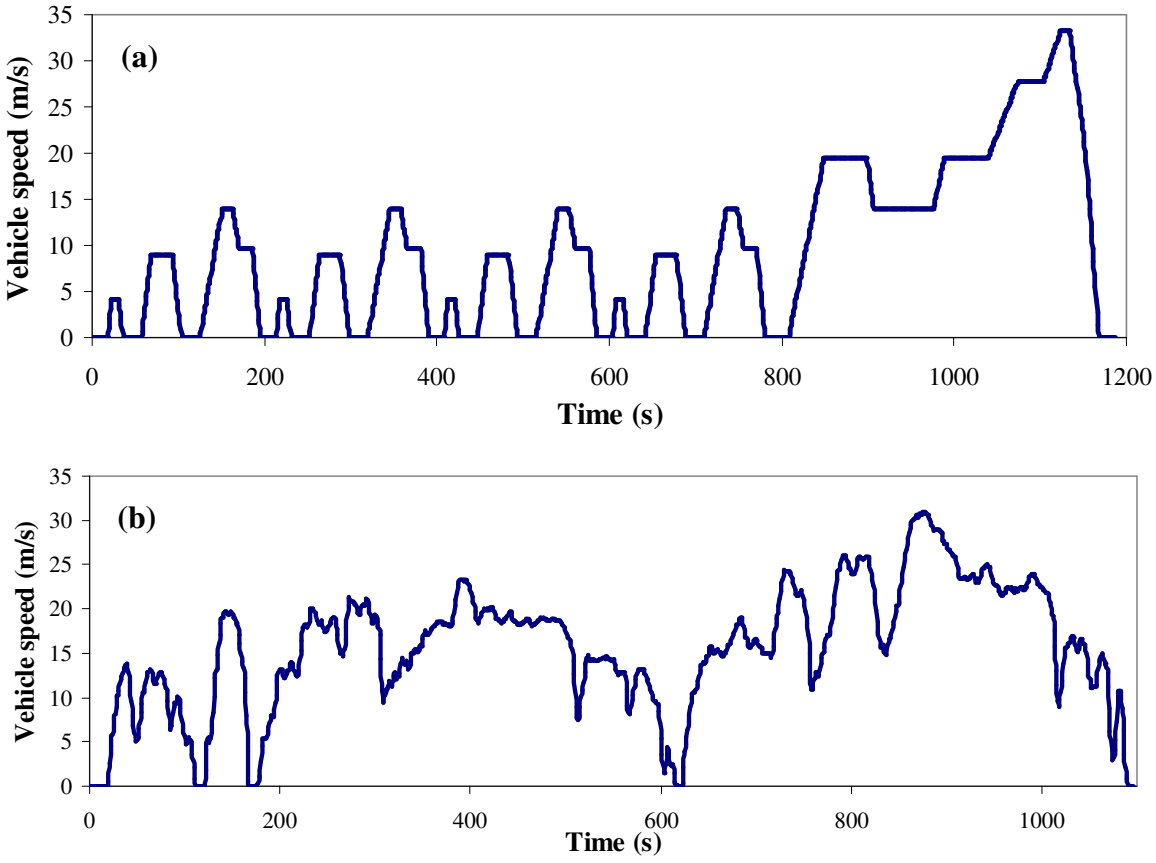

Figure 81. Vehicle speed for (a) NEDC and (b) Artemis rural driving cycle

Two driving cycles are used; NEDC and Artemis rural cycle. Figure 81 shows the NEDC and Artemis rural driving cycle. The NEDC is normally used as reference cycle for vehicle homologation in Europe. Using NEDC cycle, the vehicle needs to undergo a distance of 11 023 meter in 1180 second at the average speed of 9.3 m/s. The Artemis rural is a realistic driving cycle that is based on a statistical study done in Europe within a project called Artemis [109]. During this cycle, the vehicle needs to run a distance of 17 272 meter in 1082 second at the average speed of 16 m/s.

3.7.1 Experimental detail

The experimental procedure is divided into 6 main steps:

1. Calculate power needed to propel the vehicle using information from driving cycle and vehicle model.
2. Calculate electrical power supplied by the battery, based on power needed to propel the vehicle.
3. Calculate the current needed to be discharged from the battery in order to supply electrical power.
4. Apply this calculated discharge current to the battery cells.
5. Apply cooling system using different cooling air velocities; constant cooling air velocity and cooling air velocity as a function of vehicle speed at room temperature.
6. Measure the battery cell surface temperatures.

For procedure 1-3, the calculations are done with Matlab/Simulink software. The explanation and calculation details are given as follow:

1. Power needed to propel the vehicle.

The battery discharge current needed to complete these cycle is calculated using vehicle model and battery model. In the vehicle model, the power needed (P_t) to propel the vehicle with a mass m_v, at a vehicle speed V, and up a slope of angle θ is calculated from the sum of force (F_t) that is used to overcome the vehicle aerodynamic drag (F_a), rolling resistance (F_r), the component of vehicle's weight over a slope (F_g), and vehicle acceleration (F_{acc}) as illustrated in Figure 9 (section 2.1.4). The calculations of F_a, F_r, F_g, F_{acc}, F_t and then P_t are given by equation 1-6 respectively. These equations are adapted from [20, 30, 22].

2. *Battery electrical power supply*

In series hybrid electric vehicle, the power needed to propel the vehicle is supplied by the electric motor by transforming electrical power from battery to mechanical power. The internal combustion engine (ICE) is used to charge the battery when needed. Hybrid electric vehicle can be considered as a fully electric vehicle when the internal combustion engine is turn off and battery provides electrical energy to the electric motor that turns the wheels. The relation between the power needed to propel the vehicle (P_t) with power supplied by the battery (P_{bat}) is given by equation 31.

$$P_{bat} = \eta . P_t \tag{31}$$

where η represents the drive train efficiency and takes into account all losses from the battery to the wheels.

3. *Battery discharge current*

In the battery model, the relation between the power supplied by the battery and the battery discharge current is given by equation 32.

$$I_{bat} = \frac{P_{bat}}{V_{bat}} \tag{32}$$

where I_{bat} is the battery discharge current, and V_{bat} is the battery voltage. Battery voltage, V_{bat} is calculated by equation 11 of section 2.3.4. The battery discharge current to complete the NEDC and Artemis rural driving cycle are illustrated in Figure 82 and Figure 83 respectively. They show the discharge current calculated by the battery model and the discharge current used in the experiment.

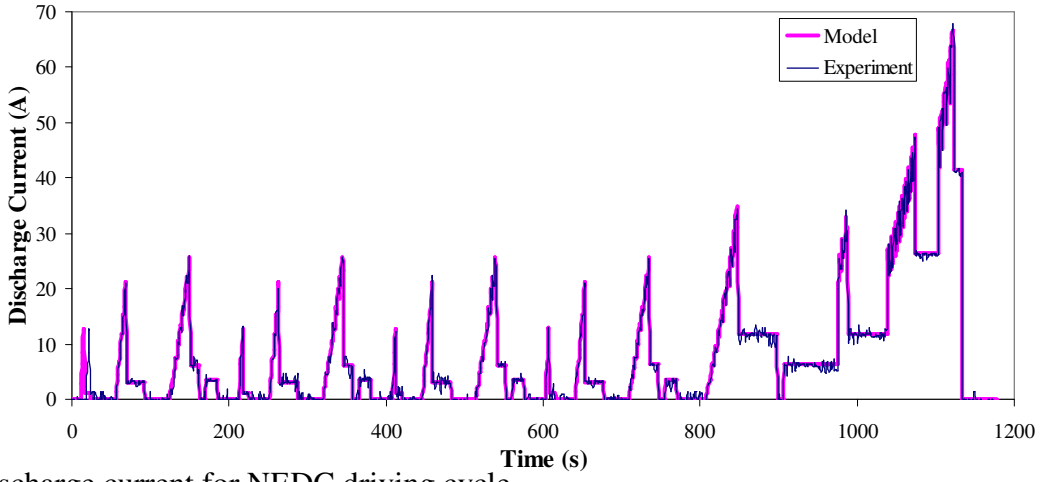

Figure 82. Discharge current for NEDC driving cycle.

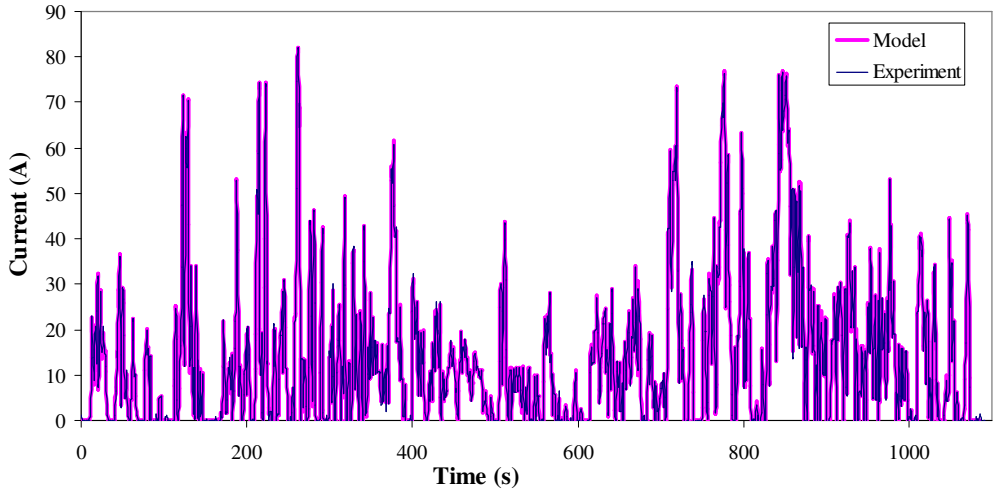

Figure 83. Discharge current for Artemis rural driving cycle.

3.7.2 Temperature evolution for real running conditions used in HEVs

Figure 84 and Figure 85 show the cell surface temperature evolution to complete the NEDC and Artemis rural driving cycle respectively. Figure 84 and Figure 85 (a) are the first case study where a constant air velocity of 2 m/s is used for cooling while figures (b) are the second case study where the air velocity varies as a function of the vehicle speed is used as the cooling system. Authors have considered that the cooling air velocity that is channelled to the battery cells is half of the actual vehicle speed.

As shown in Figure 84 (a) and (b), the cell temperatures for all three points are nearly constant throughout the driving cycle except for P1 in figure (a). At this point, the temperature increases suddenly at the end of the driving cycle. The maximum increase of temperature is 1.5ºC in figure (a) and only 0.8ºC in figure (b). Better temperature distributions are achieved using cooling air velocity in the function of vehicle speed than by using a constant cooling air velocity. This is due to the fact that the cooling air velocity is proportional to the discharge current used to propel the vehicle. To propel the vehicle at higher velocity, higher amount of current is used, thus more heat generates. At the same time, higher cooling air velocity is used, thus higher heat transfer from the battery to atmosphere.

Figure 85 (a) and (b) illustrate the cell temperatures P1, P5 and P7 for Artemis rural driving cycle. Same as in Figure 84 the temperatures are nearly constant throughout the driving cycle with better temperature distribution for the cooling air as a function of the vehicle speed.

The maximum temperature increase in figure (a) is 1.5ºC in and 1ºC in figure (b). The cooling air temperature varied between 20ºC to 21.5ºC during experiments. Base on these results, it is clear that there is no need for auxiliary cooling system in both cases.

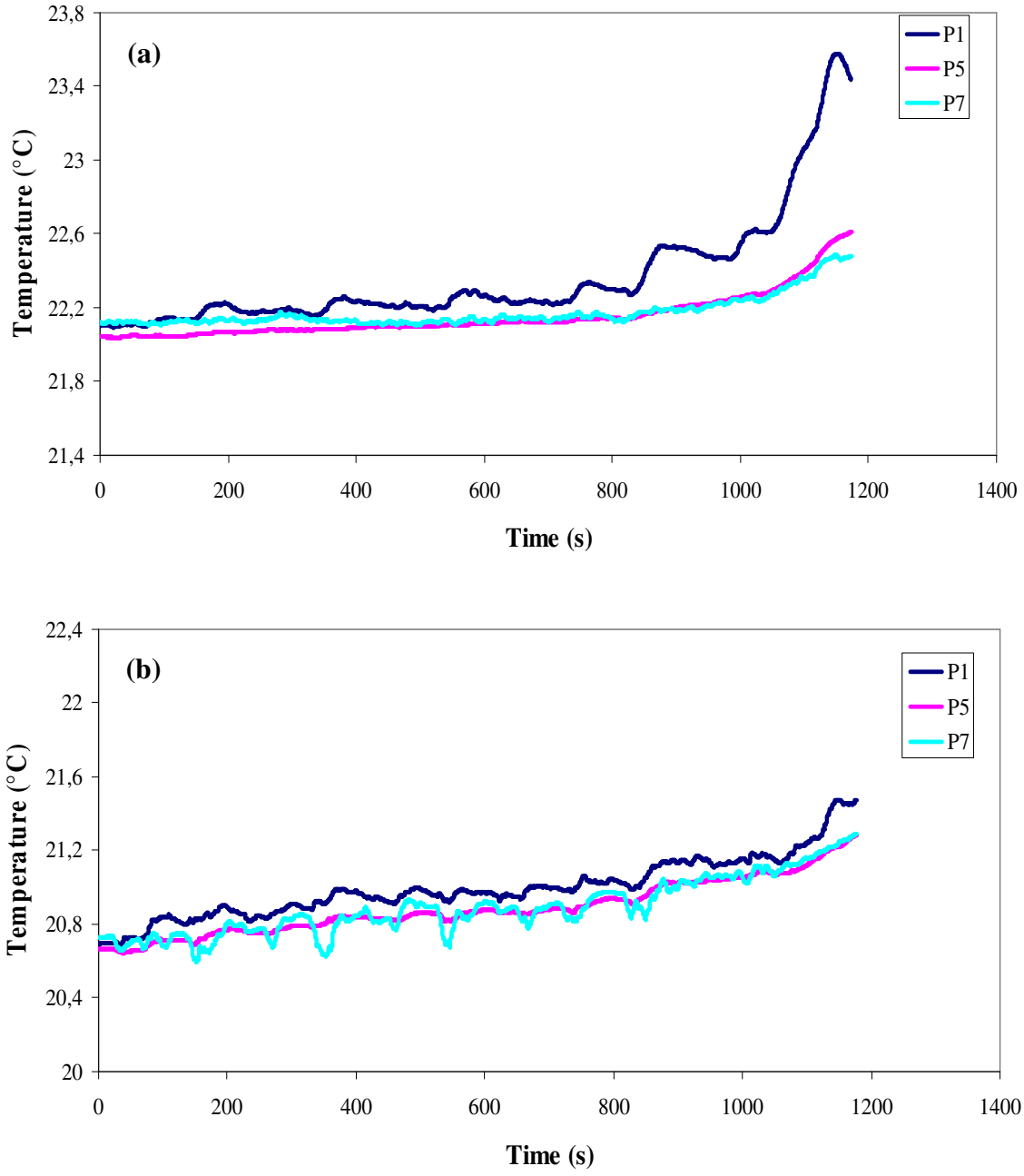

Figure 84. Cell surface temperature for NEDC driving cycle with cooling air velocity of a) 2 m/s and b) half of vehicle speed.

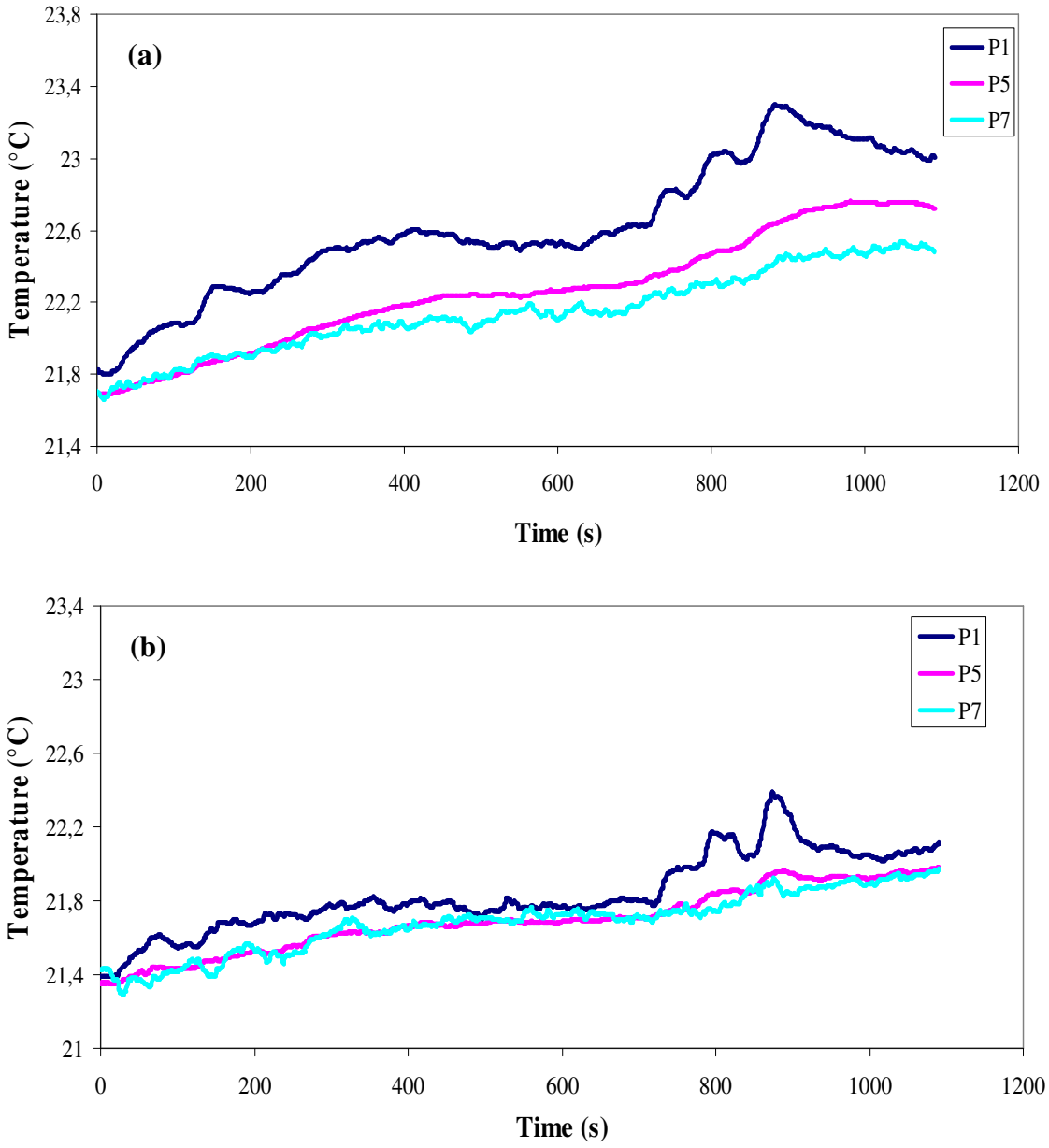

Figure 85. Cell surface temperature for Artemis rural driving cycle with cooling air velocity of a) 2 m/s and b) half of vehicle speed.

3.8 CONCLUSION

This section presents the experimental study on the cell surface temperature behaviour of lithium-ion battery used in automotive applications. Results from constant current discharge and constant cooling air velocity experiments indicate that the temperature on the cell surface is not

homogeneous, with a significant difference between the highest and the lowest temperature. The temperature is higher close to the battery cell positive and negative connectors. In difference with results found in literature, temperature near the positive connector is just slightly higher than at the negative connector.

There is a strong link between the discharge rate and the temperature increase; higher discharge rates meaning higher current circulates in the cell, thus contribute to higher increase of temperature and greater difference between the maximum and minimum temperature. Cooling system is very important in controlling the battery cell temperature. In the present study, the maximum cell surface temperature is reduced by 12°C by using air velocity of 10 m/s compared to 2 m/s. Higher cooling air velocity also helps to decrease the difference between the maximum and minimum temperature. Meaning that, it not just reduces the overall cell temperature, but also regulates the temperature distribution in cell. Discharging the battery at SOC lower than 20% contributes to a radical increase of cell temperature at all battery cell locations. This situation is directly influenced by a sudden increase of internal resistance's value below 20% SOC. This explains why it is dangerous to discharge the battery to less than 20% SOC.

The battery internal resistance decreases with the increase of temperature at certain limit. In the current study, the resistance decreases to nearly half of its initial value at 20ºC as the temperature increases to 50ºC. The value of internal resistance is in the range of 2.17 mΩ to 1.33 mΩ. At a constant temperature, the internal resistance is nearly constant at the range 100% to 20% SOC. In this range, the value of internal resistance varies between 1.8-2.17 mΩ. After 20% SOC, there is a sudden jump in the value of internal resistance to 2.83 mΩ at 10% SOC and 3.7 mΩ at 5% SOC. These observations will be used in the development of an electro-thermal battery model in section 4.

In the case study, there is just a small increase of temperature using constant air cooling velocity and cooling air velocity as a function of vehicle speed for NEDC and Artemis rural driving cycle. Anyhow, better heat distributions are achieved when the battery is cooling using air velocity as a function of vehicle speed. Results suggest that there is no need for auxiliary cooling system in these cases. In the current study, the battery cell thermal behaviour during charging process is not covered. This is because the charging system used in the present study is not capable to recharge the battery at different current rates. Although the heat generation rate during charge is less than that during discharge at the same rated current of the battery [75], the

temperature increase during rapid charge especially for large size battery used in EV and HEVs is quite significant [57]. If the thermal behaviour during charging through regenerative braking is to be considered, the temperature will increase higher and may have some influences on the conclusion of the study.

CHAPTER 4: ELECTRO-THERMAL MODELLING

4.1 INTRODUCTION

Temperature is one of the parameters of a lithium ion battery that has to be carefully controlled, because the battery's working temperature greatly influences efficiency, cell degradation, and the battery's life time. The temperature of each cell inside the battery pack varies, depending on the battery pack's design. Temperature variations may lead to over-charge or over-discharge during cycling which further contribute to premature failure in the battery packs in the form of accelerating capacity fading or thermal runaway. Electro-thermal modelling of battery packs is important, to design better-performing battery management systems (BMS), to prevent battery degradation and extend battery lifetime [39], and also prevent safety risks, such as thermal runaway [35]. Furthermore, an accurate thermal model of battery packs [35] and individual cells is essential to illustrate the real condition of the battery temperature and prevent potential abuse [40, 53]. Moreover, the temperature inside the cell is hard to be measured experimentally, but this is totally possible through modelling.

There exist a lot of articles about battery thermal model, at some degree of complexity and precision. Simple models are only capable to illustrate the battery thermal behaviour in 0D [37, 38, 73, 88, 99, 103, 104, 106], while others are extended to 2D [66, 79, 100, 107] and 3D [31, 36, 76, 96, 101, 102, 108]. In 0D model, the temperature of cell is considered as homogenous. On the other hand, 2D models are capable to illustrate the temperature variation along the cell surface, while 3D models can predict temperature variation at all cell locations. Most modelling works only focused on single cell modelling [31, 38, 72, 73, 74, 79, 92, 103, 104, 105, 106, 107]. There exist though, some models that take into consideration several battery cells in a battery pack [37, 55, 100, 101, 102, 108].

Common battery cooling systems may use air cooling, liquid cooling (water/ oil/refrigerant), phase change materials (PCM), or a combination of these methods [69, 70, 110] as explained in section 2.3.1. Lots of existing models consider air cooling system, as in reality it is the simplest and most efficient way of cooling. The drawback of air cooling system is that the insufficient convection heat dissipation from battery might occur under stressful and abuse conditions [69]. Unfortunately, most of these models are only validated using experiment result

with natural convection. Though, they are then used to simulate battery thermal behaviour in either natural or forced convection or both. These practices may not be a good solution, as the validated model might not represent the real battery cell thermal behaviour under forced convection processes correctly.

This is why, in the current study, an electro-thermal model under forced convection heat transfer is presented. First, this section describes the electro-thermal modelling followed by an introduction to the physical behaviour of a lithium ion battery, and OpenFOAM modelling software that makes it possible to integrate the heat generation resulting from electric current and resistance, into a computational fluid dynamic (CFD) model. The model considers the heat generation from battery current and internal resistance, heat transfer inside the battery cell through conduction and heat transfer from battery cells to environment through convection and radiation. Important attention is given to the battery internal resistance as its value varies with temperature as explained in section 2.3.4 and their value is based on the experimental result presented in section 3.6.1. Then, the simulation results are compared to experimental data in order to validate the model. The model validation is focused on two important aspects, air flow behaviour close to cell surface at different initial cooling air velocities and battery temperature evolutions at various locations on the battery cell surface under different discharge rates and forced convection conditions.

4.2 ELECTRO-THERMAL MODEL DESCRIPTION

The local heat generation inside the battery cells resulting from electrochemical reactions and mass transfer of ions in the electrolyte can be characterized by local internal resistance and current densities [31, 101]. Calculation of the battery cell temperature is based on internal energy balance that can be described as in equation 33. This equation is widely used to calculate the battery cell temperature of lithium-ion battery as in [73, 74, 78, 90]

$$m \cdot C_p \cdot \frac{dT(t)}{dt} = k \cdot \left[R \cdot i^2(t) \right] - (Q_{conv} + Q_{rad}) \tag{33}$$

where m is the cell mass (kg), C_p the specific heat capacity (J kg^{-1} K^{-1}), T the cell temperature (ºC), i the charge/discharge current (A), R the cell internal resistance (Ω), and k is the scale factor that accounts for the difference in electrical conductivity between positive and negative

electrodes. Q_{conv} represents the convection heat energy and Q_{rad} the radiation heat energy. The first term at the right side of the equation represents the heat source inside the cells, while the second and third terms represent the heat transfer from cells to the environment.

Table 7. The value of electrical conductivity for lithium-ion battery as reported in literature

Article	**Electrical conductivity ($S.m^{-1}$)**		Ratio (positive / negative)
	Positive electrode	Negative electrode	
Chacko and Chung [31]	38.3×10^6	63.3×10^6	0.61
Guo et al. [108]	37.8×10^6	59.6×10^6	0.63

During charge and discharge process, the current flows to the positive and negative electrode terminals from the entire electrode plate. Thus, the current densities and consequently the temperatures of the positive and negative terminals are higher than at other parts of the battery cell [79]. The value of electrical conductivity at positive electrode is lower than at negative electrode [31, 108] as shown in Table 7. Therefore, the temperature at the positive electrode is higher than the negative electrode, despite the fact that the current flows in both terminals are similarly high [31]. In the electro-thermal model, a scale factor k is introduced instead of using directly the value of electrical conductivity at positive and negative electrode. The scale factor, k is the ratio of the electrical conductivity between positive and negative electrodes. The aim is to simplify the model without compromising the capability of the model to predict the difference of heat generation at positive and negative electrodes due to the difference of the electrical conductivities. In the current study, the value of k used is 1 at positive electrode and 0.7 at negative electrode. These values are chosen based on the electrical conductivity values found in literatures and battery cell temperatures acquired through experimental works presented in previous chapter. In this way, a lower value of heat source is introduced at negative electrode compared to positive electrode.

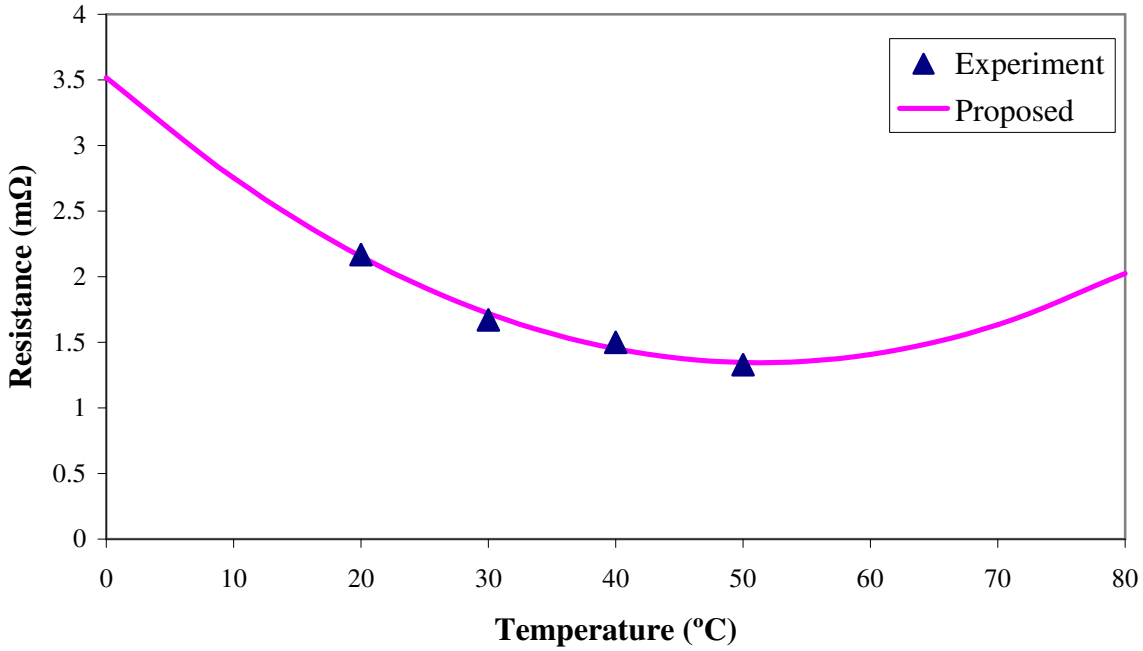

Figure 86. Proposed internal resistance as a function of temperature to be used in OpenFOAM battery modelling.

Generally, the battery internal resistance *R* is described either as a constant [54, 78, 92, 93] or as a function of battery state of charge (SOC) [72, 88, 91, 94] or temperature [31, 40, 76, 95]. In the present study, the value of internal resistance is considered as a function of temperature. The effect of SOC on internal resistance is ignored. This is justified by the fact that the battery normally will not be fully discharged (not less than 20% SOC) to avoid damaging it. Moreover, the resistance is approximately constant over 90% to 20% SOC range, as presented in section 3.6.

Temperature has a huge influence on the value of battery internal resistance as discussed in section 2.3.4. A lack of information exists, though, on the relation of resistance to temperature especially for temperatures above 50ºC. Nevertheless, one can find the information of the battery internal resistance at higher temperature in [40], as shown in Figure 26 (section 2.3.4). It shows that the battery internal resistance decreases with the increase of temperature from 25ºC to 45ºC. At 45ºC, there is a sudden jump of the value of the internal resistance. After 45ºC the value of internal resistance increases with further increase of temperature.

Based on the information gathered through literature and experimental results (section 3.6), the value of internal resistance as a function of temperature is proposed as shown in Figure 86. It shows that the value of internal resistance decreases with the increase of temperature at temperatures below 50ºC, then the internal resistance increases with the further increase of temperature. This relation is given by equation 34.

$$R = 8.25\times10^{-4}\cdot T^{2} - 8.465\times10^{-2}\cdot T + 3.5165 \quad (34)$$

where R is the internal resistance (mΩ), and T is the temperature (ºC). The convection heat transfer, Q_{conv} from the battery cell surface to the environment can be expressed as follows [54, 111]:

$$Q_{conv} = hA(T_s - T_c) \quad (35)$$

where h represents the convective heat transfer coefficient (W m^{-2} K^{-1}), A the cell surface area (m^2), T_s the cell surface temperature (K) and T_c the cooling air temperature (K). The convective heat transfer coefficient depends on the cooling fluid and the type of fluid flow [54]. In the present study, air is used as the cooling fluid. Here the convection type can be considered as forced convection as moving air is introduced into the system. The radiation heat transfer implemented in this model is an adaptation of the P-1 radiation model; the simplest case of P-N model [112], that one can access directly from the OpenFOAM library [113]. The P-1 model offers the advantages of simplicity, high computational efficiency, and relatively good accuracy with little computing effort [113]. Sazhin et al. [112] have discussed in detail the theory of the P-1 model, including its advantages and disadvantages. Other type of radiation model existed in openFOAm is the finite volume discrete ordinates model (fvDOM). This model is capable to produce a high accuracy result, but needs large computing effort.

4.3 MODELLING CONDITIONS

In the present study, a three-cell lithium ion battery pack is modelled using OpenFOAM, which is a free, open source CFD software package produced by OpenCFD Ltd for numerical simulation written in the C++ programming language [113]. OpenFOAM is gaining popularity in both industrial and academic research because of its good capacity to solve complex problems,

offers easy implementation of complex physical models, and allows the customization and extension of existing functionality [114].

The cells are arranged inside a battery box, as shown in Figure 87. The cells arrangement and space between cells is the same as presented and explained in experimental set-up (section 3.2.1). Fan et al. [102] discuss the effect of the different gaps size on cell temperature. As gap size increases, the temperature uniformity is improved, in the studied range. In the present study, a stabilisation length of 100 mm upstream and 100 mm downstream in X direction is used for air flow. These make the computational domain to 415 mm in X direction, 210 mm in Y direction, and 102 mm in Z direction as shown in Figure 88. The cells are numbered 1 to 3 from right to left in Figure 88.

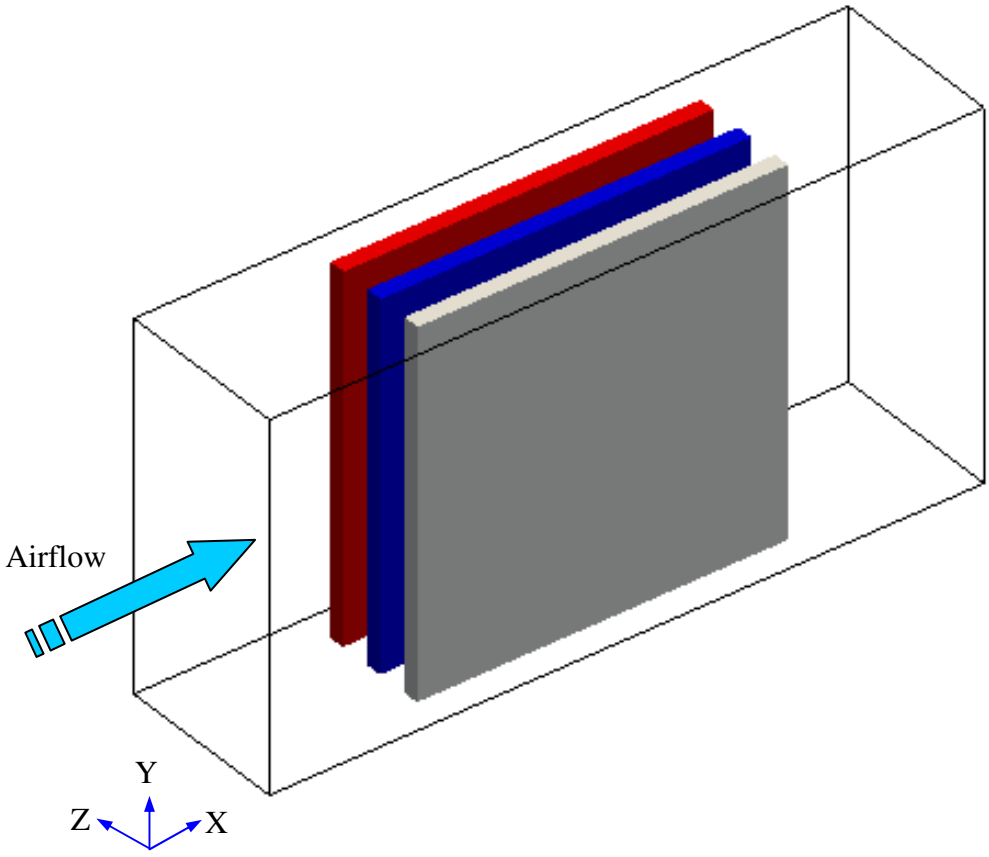

Figure 87. Isometric view OpenFOAM model with 3 battery cells arranged in a box.

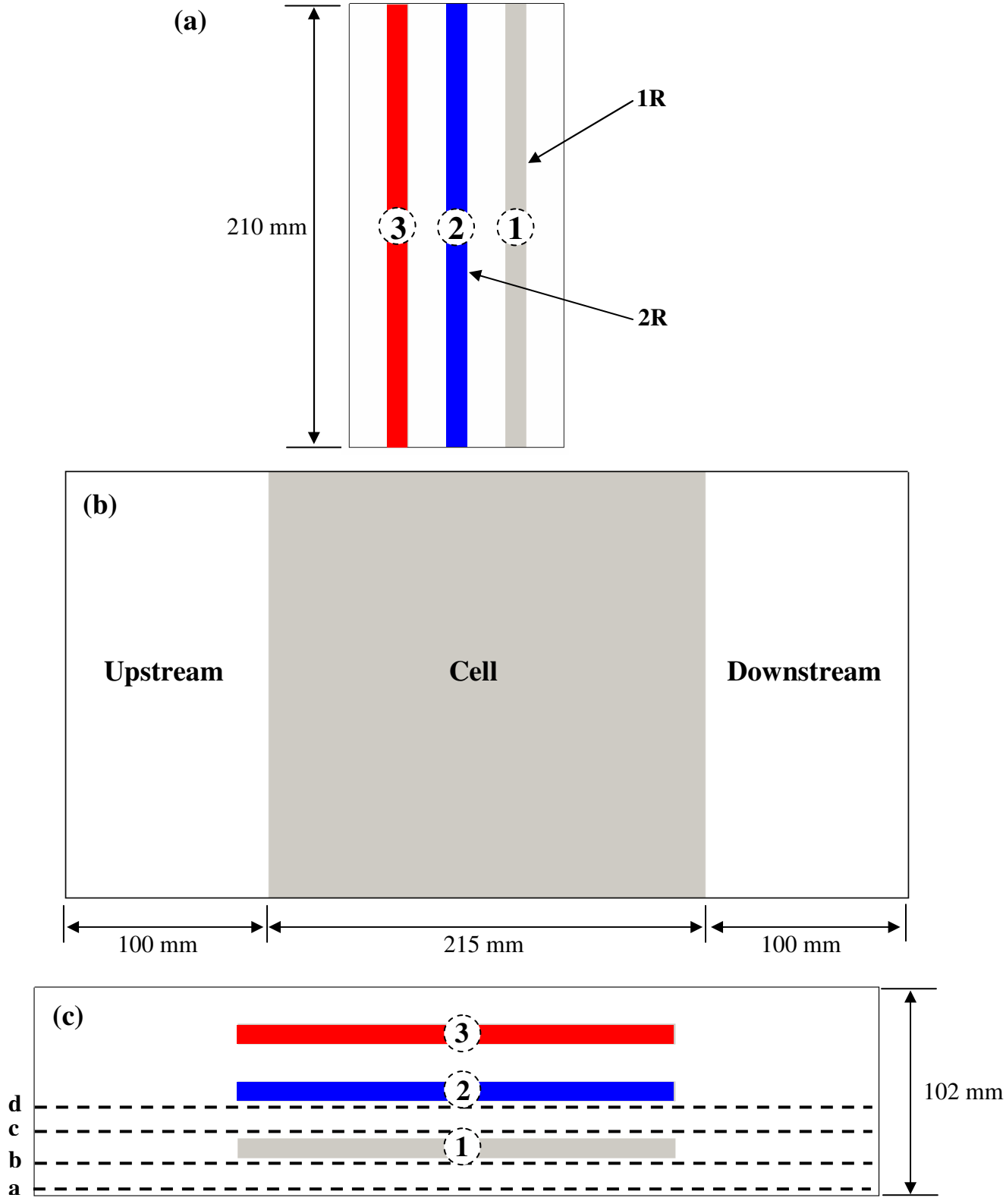

Figure 88. 3 battery cells arranged in a box with (a) represent the Y-Z plane view, (b) the Y-X plane view and (c) the X-Z plane view.

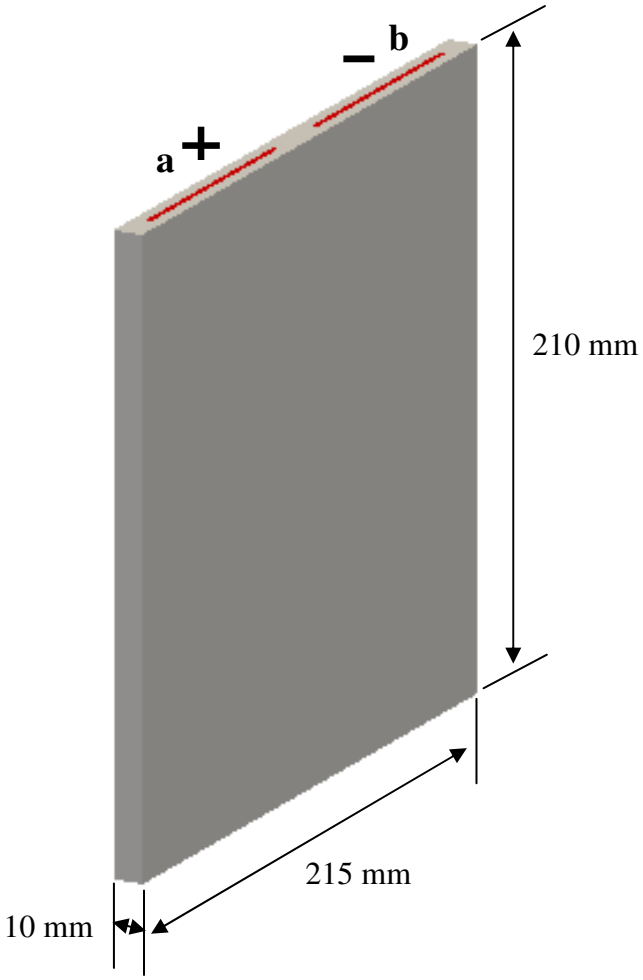

Figure 89. Battery cell parameters

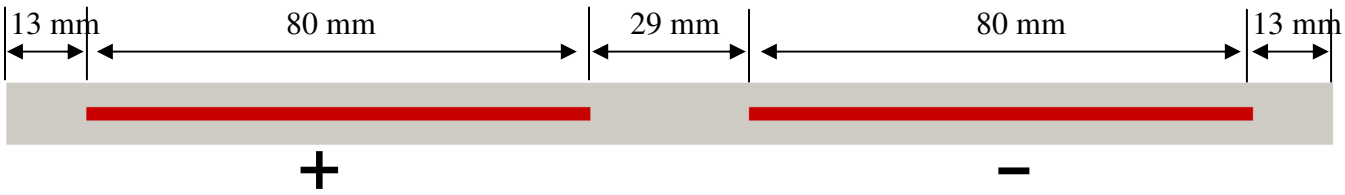

Figure 90. Parameters of the patches used as heat source at positive and negative electrode terminals.

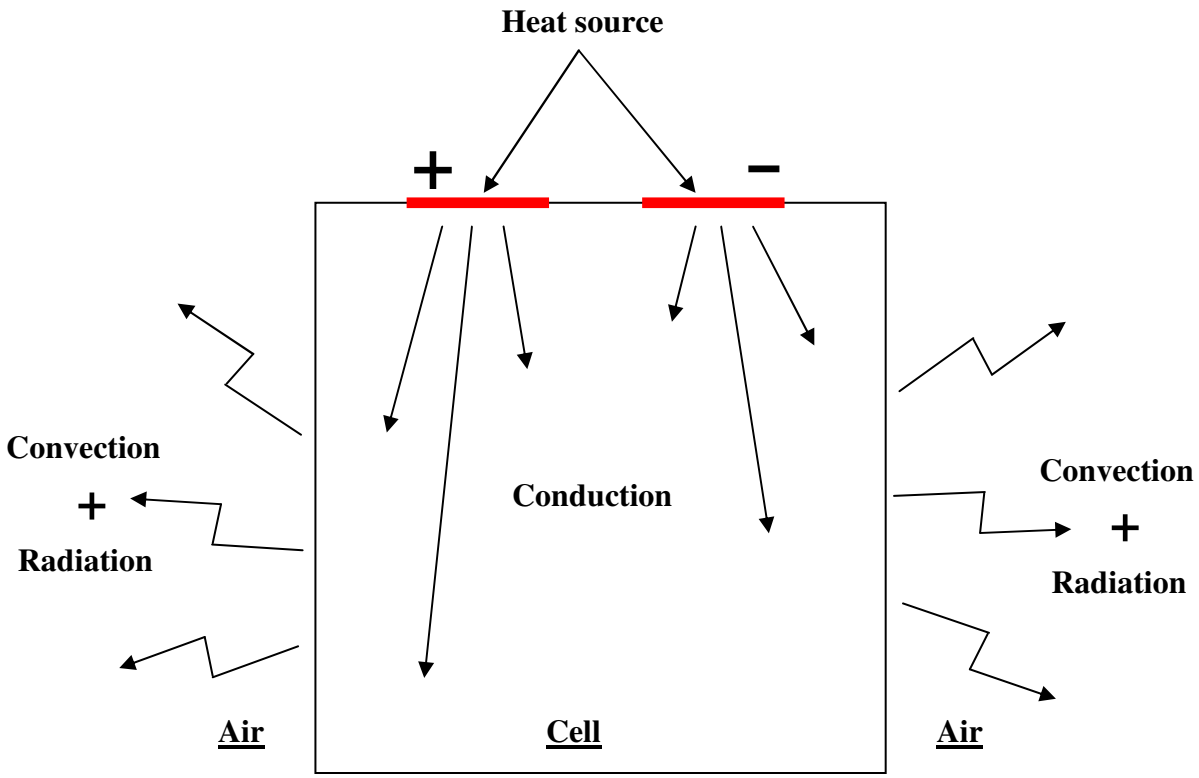

Figure 91. Schematic of thermal modelling with heat sources and heat transfer inside the cell and to the environment.

As explained in section 3.2.1, each battery cell has 10 mm thickness, 215 mm width, and 210 mm length. The battery cell used in this electro-thermal model is shown in Figure 89. Cell properties such as density, thermal conductivity and specific heat capacity are assumed to be uniform throughout the battery and to remain constant within a known range of temperatures. In Figure 89, a and b represent the positive and negative electrode terminal, respectively. They are modelled as patches with zero thickness attached to the cell. These two patches are used as the heat sources. The hypothesis that the heat source comes from these two patches is used in this current study to simplify the model. Each patch has a width of 2 mm and a length of 80 mm as shown in Figure 90. The calculated heat flux is introduced to the cell through these two patches. Then the heat from these patches is transferred to the entire battery cell through conduction process, before dissipating to the environment by convection and radiation heat transfer. These processes are illustrated in Figure 91.

The solver used in this study is chtMultiregionFoam available in the 2.0.1 version of OpenFOAM with some modification to better adapt to our problem. The existing original program using chtMultiregionFoam consists of several functions which are the conduction and convection heat transfer, and heat source using constant temperature. Several functions are added to this existing program including radiation heat transfer and introduced heat flux as the heat source. Radiation heat transfer is the exchange of thermal energy between two or more surfaces as a function of several components including the surface reflectivity, emissivity, surface area, and temperature. To activate and use the radiation model, some changes need to be done in *constant**radiationProperties* file (see appendix A).

The radiation model can be set to be "none" to use *NoRadiation* model, or "P1" for *P-1* model. The model with constant coefficients for absorption and emission is used by selecting the *absorptionEmissionModel*. Also, the *scatterModel* is selected to be *constantScatter*, the only one scatter model available in the current version of OpenFOAM. The *scatterModel* is used for calculating the incident radiation intensity in radiation model. Another modification that needs to be conducted is to add the incident radiation intensity G in the boundary conditions in *system**air**changeDictionaryDict* file. In this model, *MarshakRadiation* boundary condition is used for G. The same conditions are set for all faces of battery box and cells (see appendix B).

Furthermore a modification is made to use the heat flux as the heat source instead of constant temperature heat source *fixedValue* found in original program. The heat source's function is placed in *system**heater**changeDictionaryDict* file. In this model, the heat flux (*heatFlux*) and temperature gradient (*gradT*) are introduced at the positive and negative electrode patches through *groovyBC* function (see appendix C).

The study employs the turbulence k-ε model; the most commonly used in air flow applications. This model uses Reynolds-averaged Navier-Stokes (RANS) equations [115] which are time-averaged equations of motion of fluid flow. The k-ε function can be found in *RASProperties* file. The *RASModel* can be set to "*laminar*" to use laminar model, or "*kEpsilon*" for k-ε model. Along with *RASProperties* file, the *turbulenceProperties* file needs to be set accordingly. The *simulationType* need to be set as "*RASModel*" if the k-ε model is used or "*laminar*" if the *laminar* model is used (see appendix D).

At the inlet, fixed values of boundary conditions are applied to air velocity, temperature and pressure. At the outlet, characteristic conditions are used. At all cell surfaces, the air velocity

is set to zero, zero gradient for temperature and calculated value for pressure. These boundary conditions are situated in *sytem\air\changeDictionaryDict* (see appendix E).

In modelling, mesh size plays an important role in the accuracy of the simulation results. Normally, small mesh size produces accurate numerical results, but small mesh size meaning long computation time is needed. On the other hand, using big mesh size can reduce computation time but produces less accurate results. So, a non-uniform mesh size is the best solution to obtain the accurate result at reasonable computation time. In the current study, non-uniform 3D hexahedral meshes of the measurement section were used. Figure 92 shows the mesh generated by *BlockMesh* with the overall number of cells of 88 000 units. Bigger mesh size is applied to locations which are less critical; far from the battery cells and the battery box surfaces. Smaller mesh is used for the locations closer to the cell surfaces.

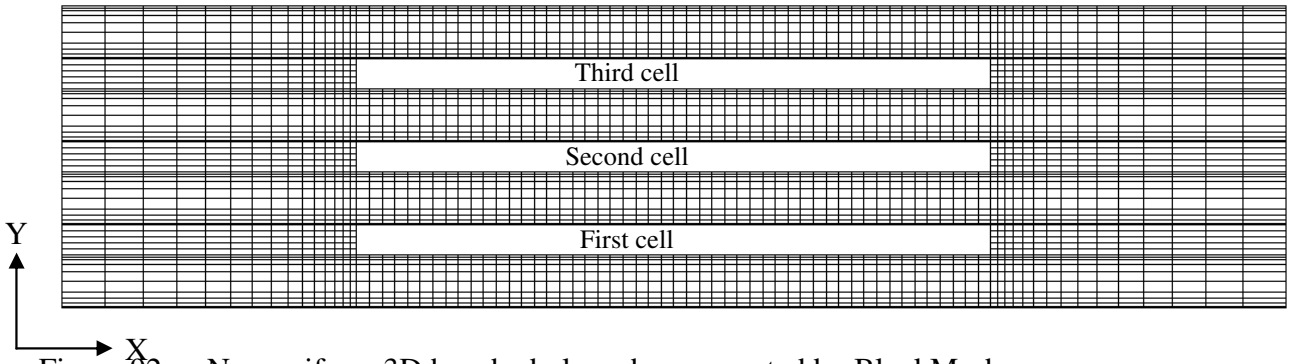

Figure 92. Non-uniform 3D hexahedral meshes generated by BlockMesh.

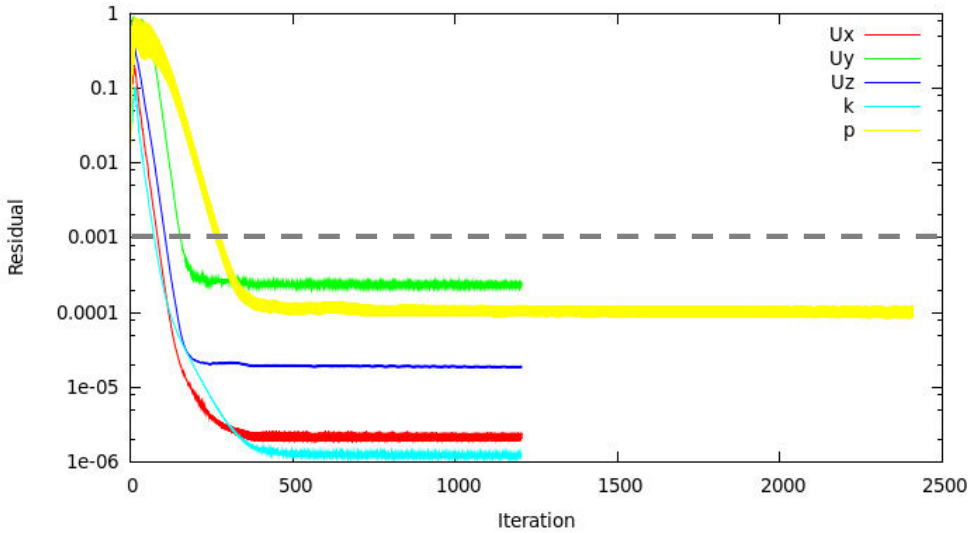

Figure 93. Residual plot for convergence verification.

Checking for convergence is important in order to verify that the simulation is complete and converged. There are several ways to check for convergence. The most general way is to check the residuals (errors) for variables being solved, as used in the current study. The simulation is considered converged if the residual's value reaches below 0.001. Figure 93 shows the residual's value of the U, k, and p. After 300 iterations convergences is reached at acceptable residual's values under 0.001. In general, the number of iteration needed to complete the simulation (until 20% SOC) is around 200 000 for 1C discharge, 65 000 for 3C discharge, and 38 500 for 5C discharge.

4.4 AIR FLOW BEHAVIOUR VALIDATION

4.4.1 Introduction to PIV

Experiments are conducted using particle image velocimetry (PIV) to determine the behaviour of the air flow inside the battery box especially near the cell surface; and validate the simulation results. Key to these experiments is to ensure that the air flow produced by the simulation is correct, as it affects the forced convection process and thus the temperature of the battery cell surface.

PIV is a whole-flow-field technique used to obtain instantaneous velocity measurements and related properties of fluids in a cross section of a flow [116]. The flow is seeded with small tracer particles, and illuminated with a sheet of laser light so that particles are visible [117]. The motion of the seeding particles is used to calculate the fundamental dimensions of the velocity field (speed and direction) of the flow being studied [118].

Researchers have employed PIV widely to measure a large variety of flows [119]. For examples, Willert et al. [119] used PIV to investigate unsteady air velocity fields, Wernert et al. [120] used PIV for air flow characteristics around an airfoil, Miyazaki et al. [121] to measure particle motion in spiral gas-solid two-phase flow, Otsuka and Wolanski [122] to analyse flame propagation in a flat duct, and Weitbrecht et al. [119] to conduct large-scale measurements of the surface of shallow water flows.

4.4.2 Experimental set-up

Experimental setup using PIV is shown in Figure 94. Two cameras (Dantec FlowSence 4M) are used to cover a large area of the battery box. They capture the scattered light with a resolution of

2048 × 2048 pixels (height by width). A DualPower Nd-YAG laser is used to illuminate the seeded particles. The laser wavelength is 532 nm, with pulse energy of 200 mJ per pulse. The battery box wall is transparent so that particles inside the box are visible. In the figure, the arrow indicates the air flow direction. The flow is seeded, thanks to a smoke generator (FOG 2010), that produces small particles, with a mean diameter of approximately 1-2 μm from fluid (SAFEX extra clean fog fluid).

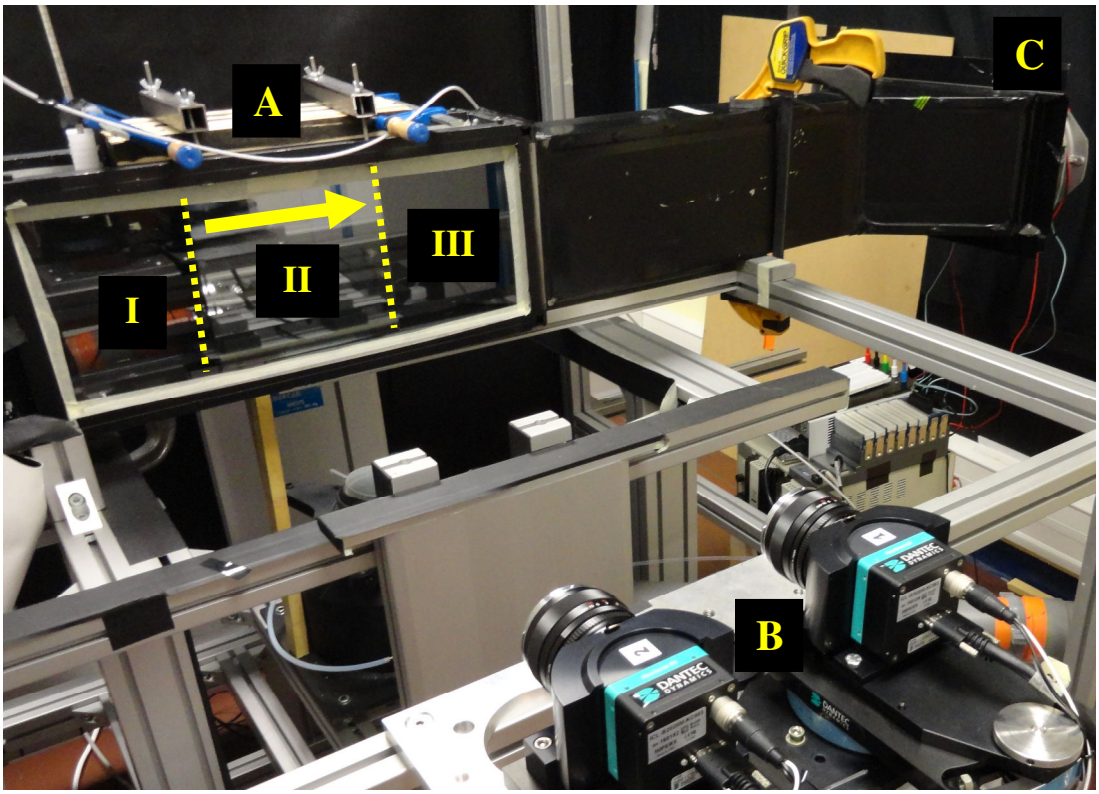

Figure 94. PIV experimental setup (A: battery box, B: camera, C: fan, I: upstream section, II: cell section, and III: downstream section).

The nature of the experiment that uses laser light to illuminate the particles, causes problems with the use of the original battery cell, due to the fact that the battery cells have light reflecting surfaces. The laser light reflected from cell surface will disturb the image captured by the cameras and thus produces inaccurate result. To solve this problem, the original battery cells are replaced with a mock up model with same dimensions. The second and third cells are

replaced by a model painted in black colour to avoid light reflection. The first cell on the other hand is replaced by a transparent glass to acquire result of air characteristic between the first and second cell.

The lines a, b, c, and d in Figure 88 indicate the PIV measurement planes. The plane a, is at 4 mm from the wall of the battery box. The planes b, c, and d are at 4 mm from the cell surface. The 4 mm distance from the surface is chosen by taking into consideration the thickness of the laser light sheet. The laser light should not touch the cell surface but needs to be set as close as possible to the cell surface. 4 mm is though the best distance to fulfil these two conditions.

4.4.3 Comparison and validation of experimental and modelling results

The comparison between simulation and PIV experimental results of the air flow velocity in planes a-d are shown in Figure 95-Figure 98 respectively, at different initial air velocities of 2 m/s, 7 m/s, and 11 m/s. These three different velocities are chosen to represent the low, median and high cooling air velocity to cover full cooling air velocity range produced in the experiment. U ($m\,s^{-1}$) is the air flow velocity component in the X-direction. From now on, ***low velocity*** will be used to indicate air initial velocity at 2 m/s, ***median velocity*** for 7 m/s, and ***high velocity*** for 11 m/s.

As shown in Figure 95-Figure 98, good agreement exists between the simulation and experimental results. In general, findings revealed that the air flow in the beginning of the upstream section is at a nearly constant velocity. The velocity increases as it enters the cell section, where the flow area decreases, occupied by the three battery cells. The air velocity stabilises along the cell section. As air passes from cell section to downstream section, the air velocity decreases until it reaches its initial velocity. At plane a, the air velocity increases and decreases gradually as air enters and leaves the cell section. In contrast, at planes b, c and d, air flow velocity suddenly increases as it enters the cell area. OpenFOAM model is capable to predict air flow velocity behaviour with good conformity as compared to PIV experimental results; the percentage error is only between 1.4% and 5.0%.

Figure 95 shows the air flow velocity at plane a, which is near the wall of the battery box for three different initial air velocity. In the upstream section, simulation predicted well the air velocity as captured in the experiment. A small difference is anyhow detected between

simulation and experiment at the end of upstream section; from X=60 mm to X=90 mm. The model predicted a lower air velocity than acquired in experiment. Along the cell section, there is a good synchronization between simulation and experiment at all three air velocities. The air velocity is stable along the cell section. The velocity at cell section increases by 60% of the initial velocity at upstream section. In the downstream section, the simulation results predict the decrease in air velocity correctly, except a slight difference at low velocity. At this velocity, the model predicted a slightly bigger decrease in air velocity than given by experimental result. The percentage error between predicted model and experiment is 5%, 1.6%, and 1.4% for low, median and high velocity respectively.

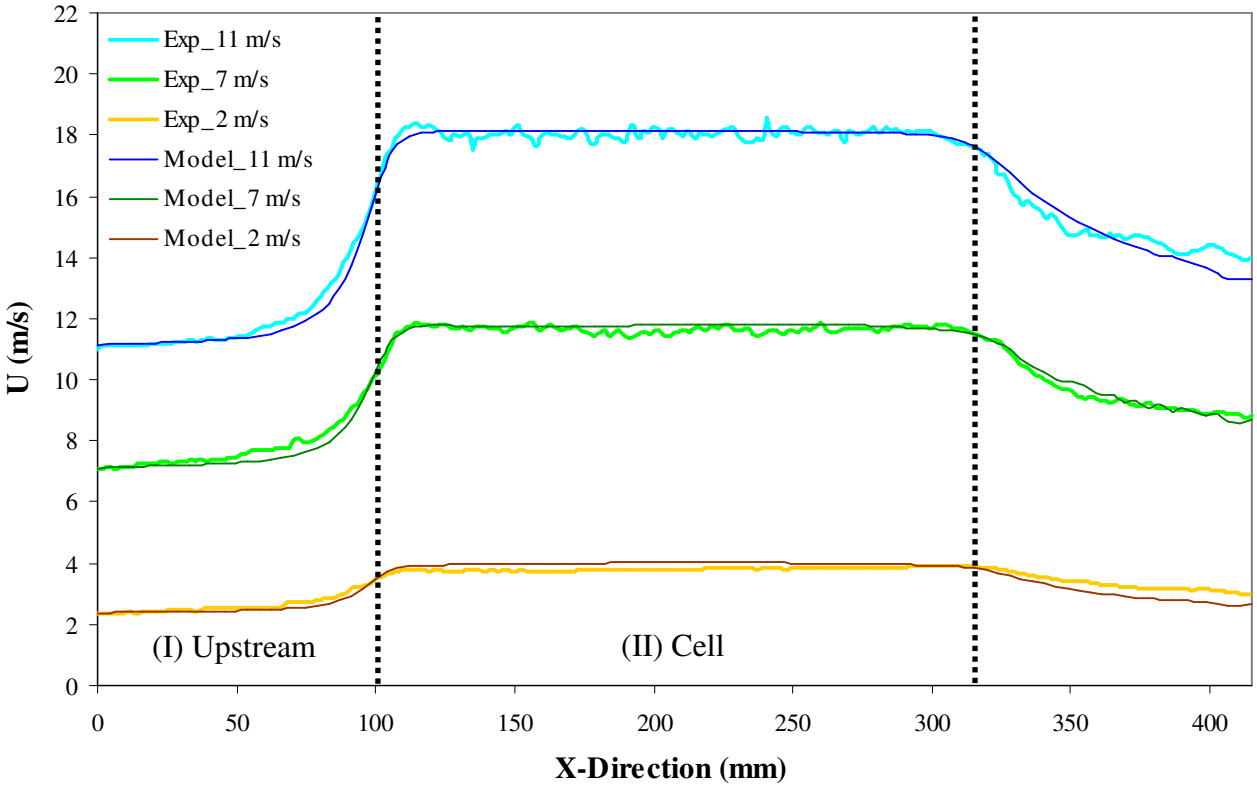

Figure 95. Air flow velocity at plane a for low, median, and high velocity at plane a.

Figure 96 shows the air flow velocity at plane b; near the surface of the first battery cell. In the upstream section, simulation predicted correctly the velocity as acquired in the experiment except small differences at high velocity where a higher air flow velocity is captured through the experiment. In this section, the air velocity is nearly constant from X=0 until end of upstream

section. At the end of the upstream section and the beginning of the cell section, there is a sudden increase in velocities until a peak value is reached before a velocity reduction occurs down to stabilisation throughout cell section. The maximum velocities (at X=110) revealed in the experiment are much higher than predicted by simulation for median and high velocity. The model is capable to predict the phenomenon of the peak velocity as recorded in experiment. But, the peak value predicted by the model is lower than actual value from experiment. This difference is caused by the difference of geometry of the battery edge from the model and actual used in experiment. In the model, the battery edges are perfectly perpendicular while in reality they are slightly curved. In the downstream section, both experiment and model agree that the velocity decreases as the air leaves the cell section. Anyhow, the simulation predicts a more gradual decrease of air velocity compared to the experimental result. This is because the air flow channel used in the experiment (as shown in Figure 56) is not taken into account in the model. The use of air flow channel caused the pressure drops and thus a more significant air velocity drops at downstream section. The percentage error between predicted model and experiment is 2.9%, 4.7%, and 4.5% for low, median and high velocity respectively.

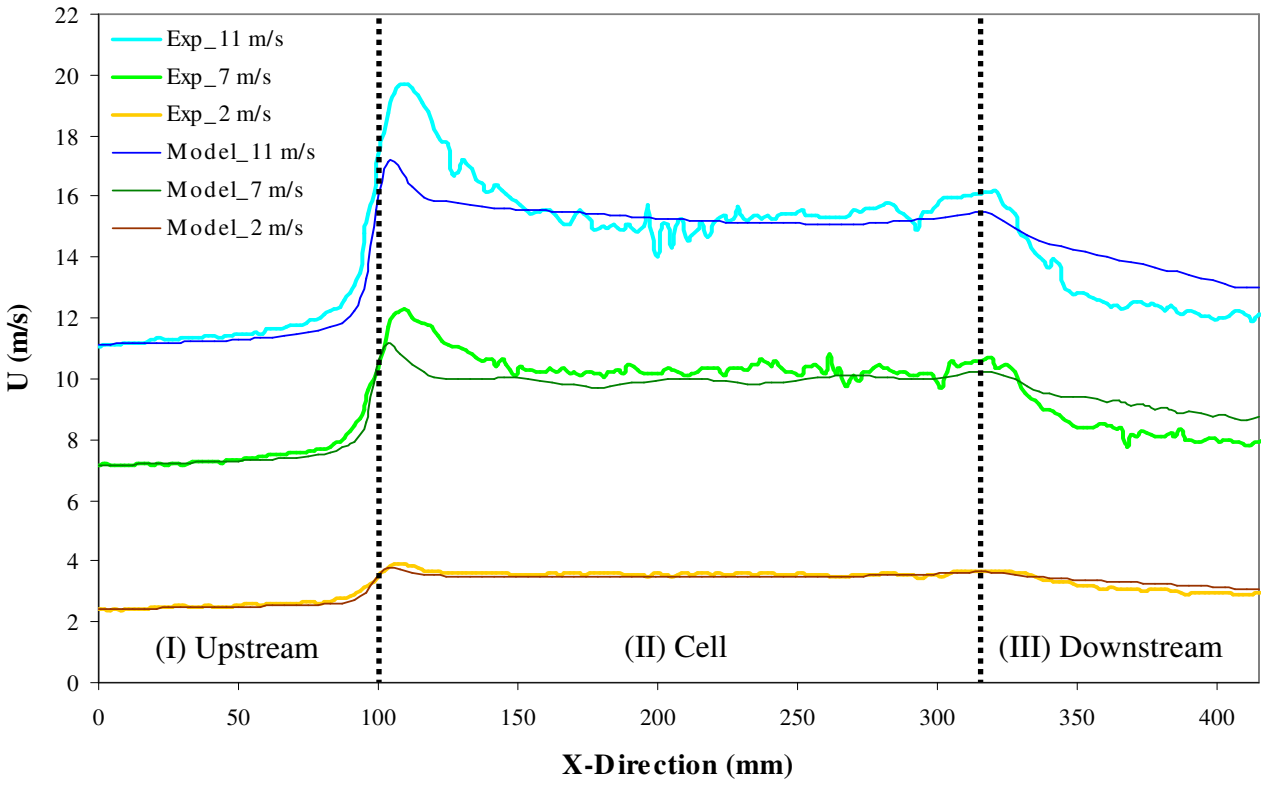

Figure 96. Air flow velocity at plane b for low, median, and high velocity at plane b.

Figure 97 shows the air flow velocity at plane c; near the surface of the first battery cell. In the upstream section, simulation predicts the same velocity as in the experiment for low, median, and high velocity. The velocity in this section is nearly constant. A huge velocity increase occurs at the end of upstream section and beginning of cell section (at X=100). Along the cell section, the experiment shows that the velocity is stable; meanwhile the model predicts some decrease in velocity from beginning to end of cell section. In the downstream section, the simulation results predicted well the decrease in air velocity. The percentage error between predicted model and experiment is 3.0% for low velocity, and 2.5% for median and high velocity.

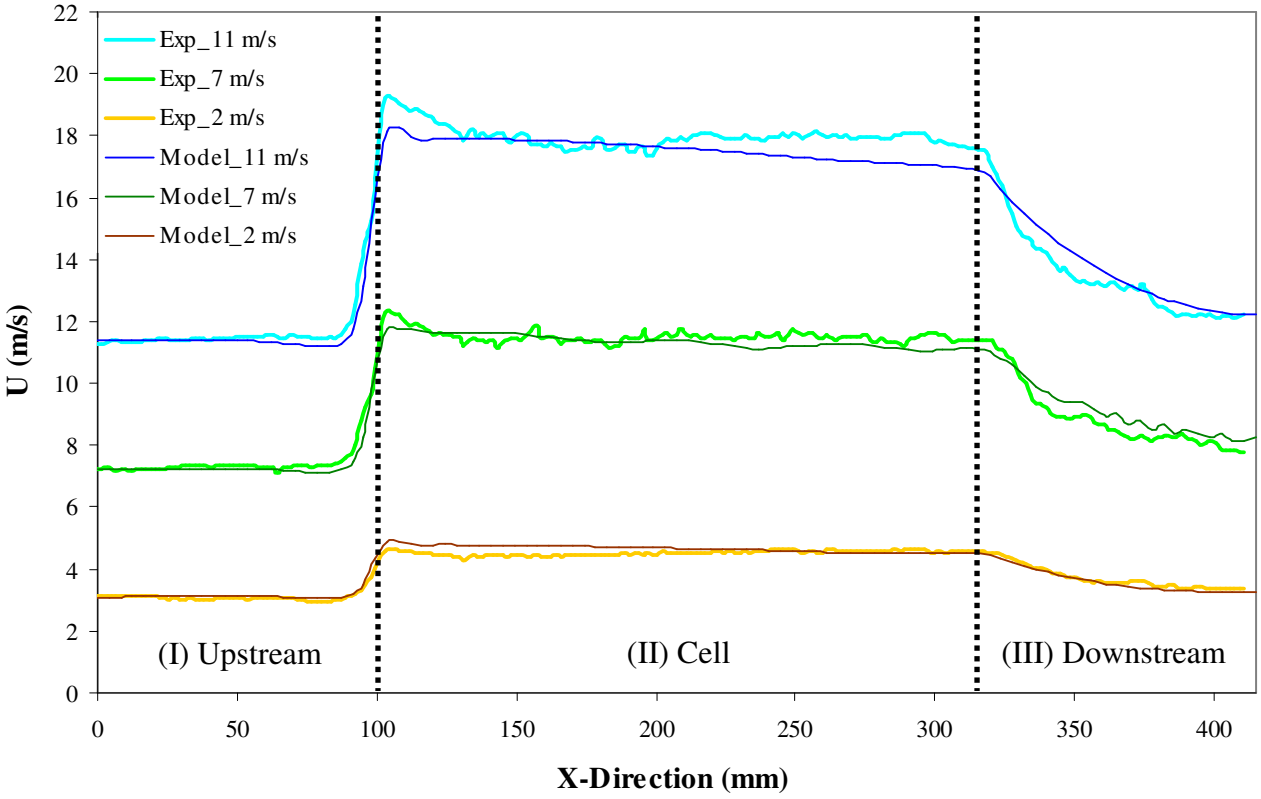

Figure 97. Air flow velocity at plane c for low, median, and high velocity at plane c.

Figure 98 shows the air flow velocity at plane d; near the surface of the second battery cell. For low velocity, a good agreement between experiment result and model prediction is achieved. However, there are some differences between experiment and model for median and high velocity, especially at the end of cell section and downstream section. In the upstream section, the air velocity is stable until the end of upstream section, where a high velocity increase

occurs. The maximum velocity increase recorded through the experiment is higher then predicted by the model, caused by the difference of the geometry of the cell edges from the experiment and the model. At the beginning of cell section (at X=100 mm), the air velocity decreases before stabilising along the cell section. In the downstream section, the simulation results predict a gradual decrease in air velocity, while the experiment showed a sudden decrease in air velocity caused by the use of air flow channel. The percentage error between predicted model and experiment is 3.6%, 4.2%, and 5.0% for low, median and high velocity respectively.

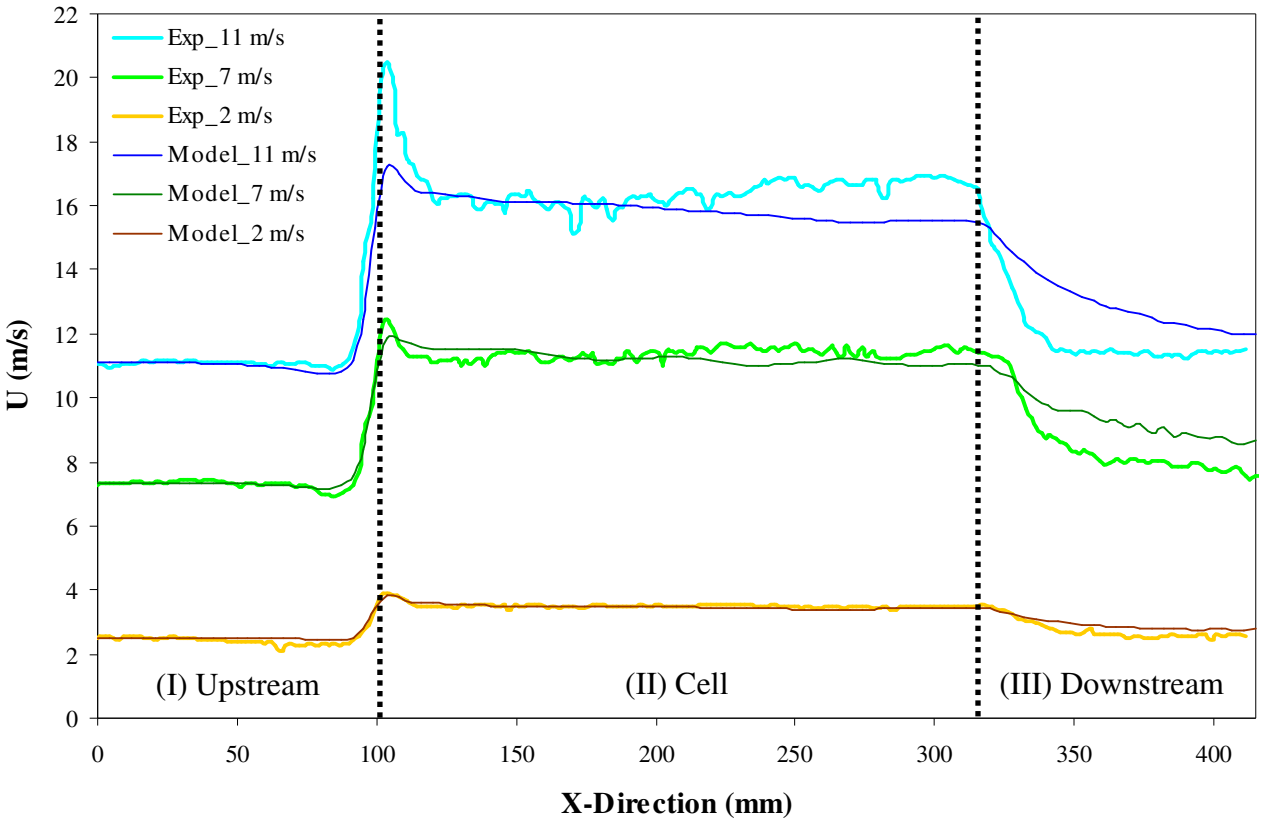

Figure 98. Air flow velocity at plane d for low, median, and high velocityat plane d.

4.5 TEMPERATURE EVOLUTION VALIDATION

4.5.1 Introduction

In this section, cell surface temperature evolution from the OpenFoam electro-thermal model is compared to the experimental results presented in section 3. The main objectives are to validate the model in terms of battery thermal behaviour at different cell surface locations, the reactivity

of the model to predict the temperature when the discharge rates change, and the capacity to simulate the effect of cooling system through forced convection at different cooling air velocities. In order to attain these objectives, the analysis will focus on three main locations; P1, P7, and P19, three discharge rates; 1C, 3C, and 5C, and three different cooling air velocities; 2 m/s, 4 m/s, and 6 m/s. P1, and P7 are chosen to represent the hottest and the coolest locations of the first cell respectively while P19 represents the hottest location of the second cell. By comparing the temperature of P1 and P19, one can validate the capacity of OpenFAOM electro-thermal model to predict the temperature difference for different cells which are arranged at different locations in the battery box.

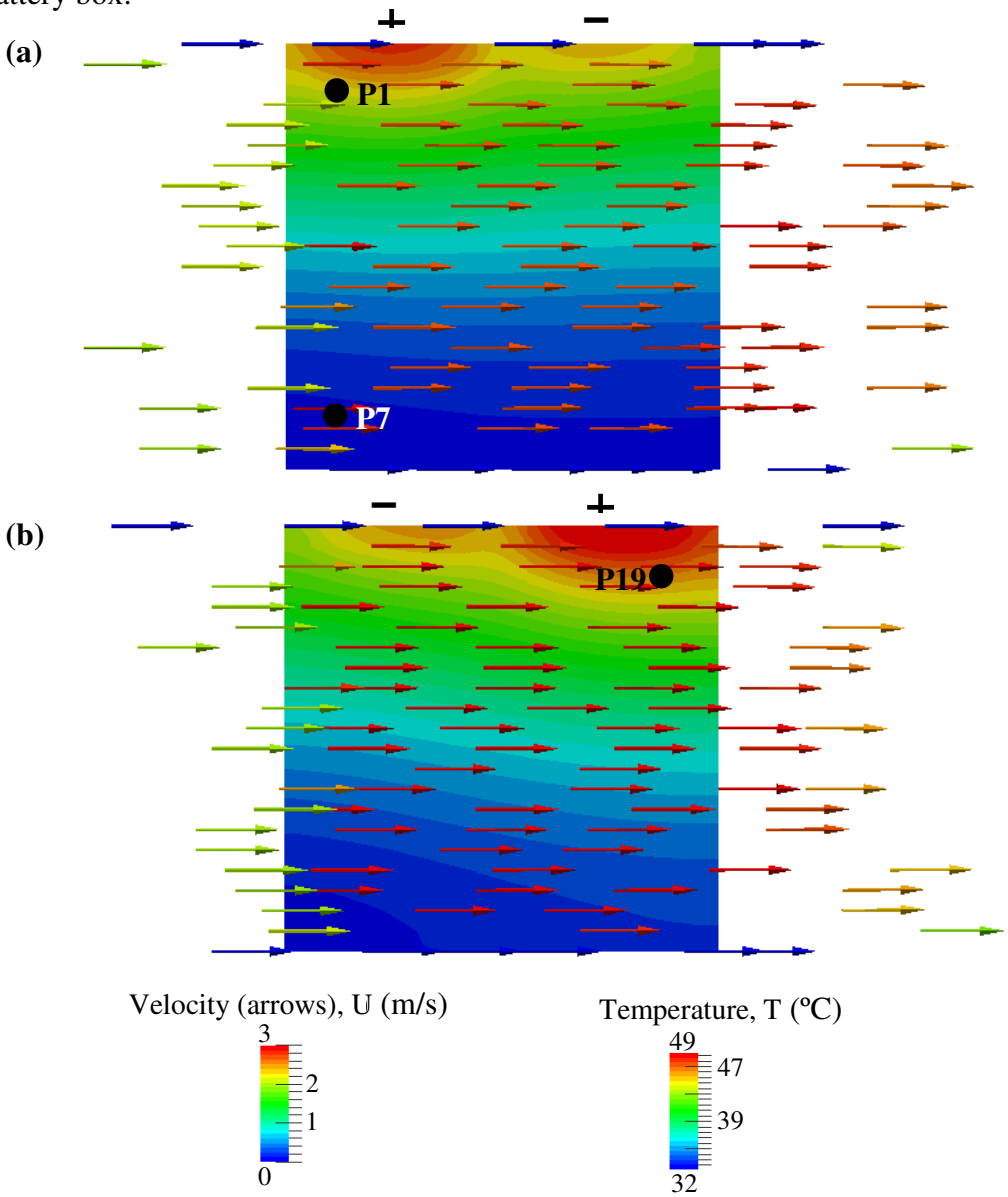

Figure 99. Surface temperature and air flow field of (a) the first cell and (b) the second cell

Figure 99 shows the cell surface temperature and air flow field of (a) the first battery cell (marked 1R in Figure 88) and (b) the second battery cell (marked 2R in Figure 88) at the end of discharge (20% SOC) with 5C discharge rate. A constant air velocity of 2 m/s at inlet and ambient temperature of 21°C is used for cooling. The air velocity at a distance of 4 mm from cell surface is represented by the arrows. Different arrow's colours indicate different cooling air velocities at the upstream section, cell section, and downstream section as validated by PIV experimental result in section 4.4. Both figures illustrate that the temperature near the battery's positive and negative terminal is higher than at other locations on the cell surface due to different current densities at cell terminals. The temperature near the positive terminal is also higher than at the negative terminal because of the difference of electrical conductivity. These simulation results are in good conformity with the results obtained through experiment.

4.5.2 Cell surface temperature of the first cell at different discharge rates

Figure 100, Figure 101, and Figure 102 show the comparison of experimental results and the OpenFOAM simulation results for different discharge rates of 1C, 3C, and 5C of the first cell surface temperature at P1, P3, and P7 respectively. In general the OpenFOAM simulation model produces good results, equivalent to those provided by experiment for the discharge rate of 1C, 3C, and 5C for all three different locations. Anyhow, there is a slight different between predicted results and experimental results. Generally, the difference between these results can be explained by the difference of the boundary conditions used in the model and actual condition during experiment.

In the model, the value of cooling air velocity and temperature at the beginning of the upstream section (X=0 mm) is considered as constant, while in reality, during experiment these values varied slightly from their indicated fixed values. In the experiment, the cooling air velocity produced by the electric fan may increase at the average of 0.5 m/s above or decrease to 0.5 m/s below the stated value. Throughout the experiment, the value of cooling air temperature also varied. The experiment is conducted in a closed room. As the experiment goes on, the heat release from the cell surface causes the ambient air temperature inside the room to increase. The air ambient temperature is controlled by letting air from outside enter the room through window. Thus, the window is open and closed if needed. By doing this, the cooling air temperature inside

the room is managed to be set near the desired temperature with the average temperature variation of 0.5ºC above or below the stated value.

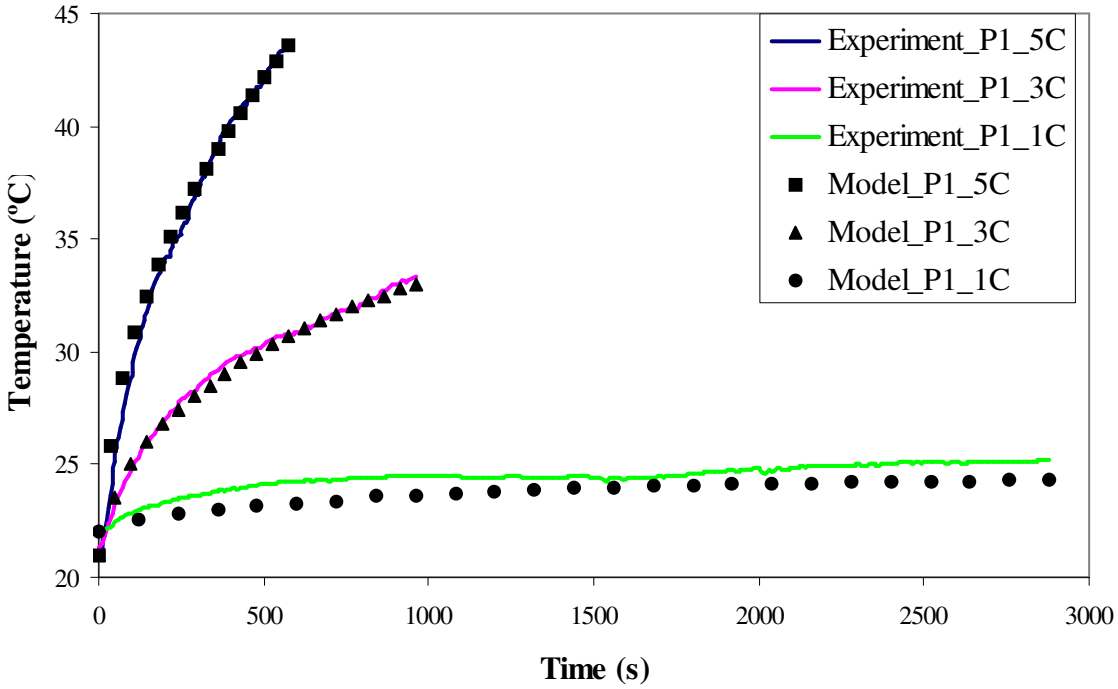

Figure 100. Comparison of the temperature at P1 from experiment and the OpenFOAM simulation model at discharge rate of 1C, 3C, and 5C with cooling air velocity of 2 m/s.

Figure 100 shows the comparison of temperature evolution at P1; near the cell positive electrode. The OpenFOAM simulation model predicts with good precision the temperature evolution for 5C and 3C discharge rates. At 5C discharge, the model simulates a barely higher temperature at the beginning of discharge. At the end of discharge, the same temperature is recorded by experiment and predicted by simulation, this end of discharge temperature is 43.6ºC for both experiment and simulation. Temperature at end of discharge for 3C discharge rate is 33.3ºC given by the experiment and 33.0ºC predicted by the model. At 1C discharge rate, the temperature acquired from the experiment is slightly higher than predicted by the model. The temperature at the end of discharge is 25.2ºC recorded through experiment and 24.3ºC predicted by OpenFOAM model. This is because the heat generation through electrochemical reaction inside the battery is not considered in the model. This heat generation is less important than the heat generation by current density and internal resistant at a high value of discharge rate, but it

become more significant when small discharge rate is used. The percentage errors between predicted OpenFOAM model and experiment are 2.0%, 0.7%, and 2.7% for 5C, 3C, and 1C discharge rates respectively.

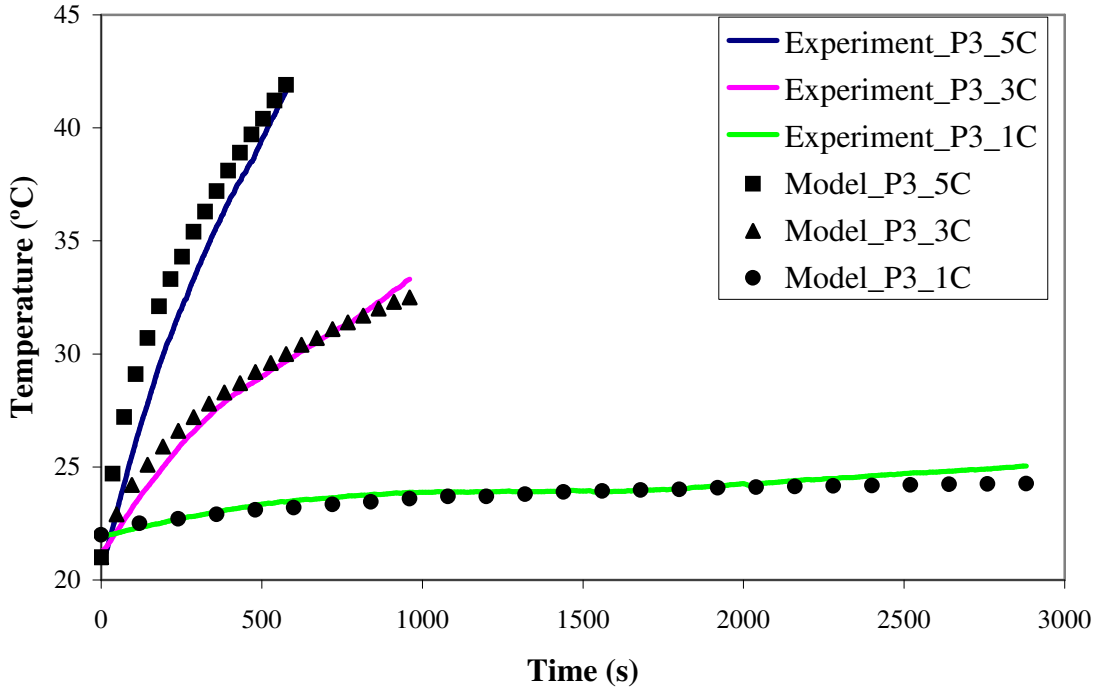

Figure 101. Comparison of the temperature at P3 from experiment and the OpenFOAM simulation model at discharge rate of 1C, 3C, and 5C with cooling air velocity of 2 m/s.

Figure 101 shows the comparison of experimental results and the OpenFOAM simulation results for different discharge rates of 1C, 3C, and 5C of the first cell surface temperature at P3 which is near the cell negative electrode. At 5C discharge rate, the model predicted a much higher temperature than given by experiment. This temperature difference decreases as the discharge process goes on until it reaches nearly the same temperature at the end of discharge. End of discharge temperature is 41.6ºC from experiment and 41.9ºC from simulation. At 3C discharge rate, the OpenFOAM model predicts a little higher temperature at the beginning of the discharge process. After 700 seconds, temperature obtained from experiment continues to increase at a slightly higher rate than the temperature predicted by the model. The end of discharge temperature is 33.3ºC obtained from experiment and 32.5ºC from simulation. At 1C discharge rate, there is a good agreement between experiment and simulation results especially at the beginning of discharge until 2000 seconds. Then, temperature calculated by the model is

stable while temperature given by experiment is slightly increased. This difference is caused by slight increase of ambient air temperature used for cooling, during experiment, while cooling air temperature in the model is maintained constant from throughout the simulation process. The end of discharge temperature is 25.0ºC gained from experiment and 24.3ºC from simulation. The percentage errors between predicted OpenFOAM model and experiment are 5.9%, 1.8%, and 3.0% for 5C, 3C, and 1C discharge rates respectively.

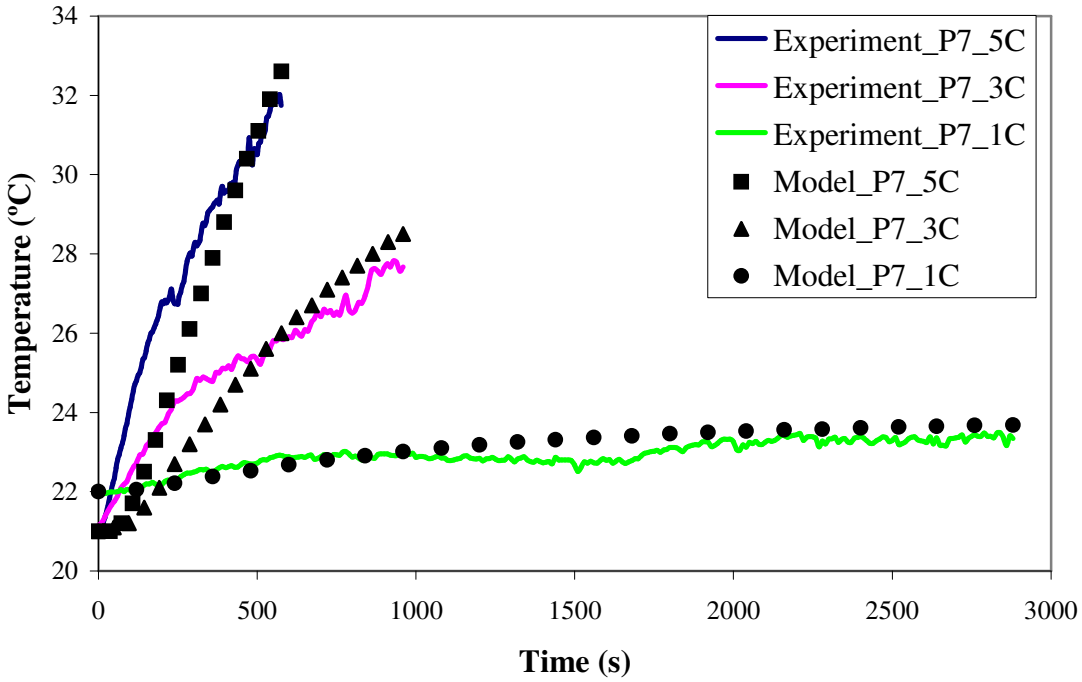

Figure 102. Comparison of the temperature at P7 from experiment and the OpenFOAM simulation model at discharge rate of 1C, 3C, and 5C with cooling air velocity of 2 m/s.

Figure 102 demonstrates the comparison of experimental results and the OpenFOAM simulation results for surface temperature of the first cell at P7 which is the lowest temperature location. In general, there are some temperature differences at the beginning of discharge process for 5C and 3C discharge rate. The OpenFOAM model predicts the temperature lower than that obtained from experiment. Nevertheless, a more precise prediction is attained towards the end of discharge process. This difference is due to the way of the heat sources is modelled in the simulation. The calculated heat comes from positive and negative electrodes which are at the top of the battery cell. The heat is then transferred to the rest of the battery cell trough conduction process. The fact that the location P7 is far from negative and positive electrode causing the heat

to take some time before reaching this location. On the other hand, at 1C discharge rate, a good synchronization is achieved between experimental and predicted results with a slightly higher temperature observed through the predicted result. End of discharge temperature at 5C is 31.8ºC for experiment and 32.6ºC for model, at 3C discharge this value goes to 27.7ºC for experiment and 28.5 for model and finally at 1C discharge model predicts 23.7ºC while experiment recorded 23.3ºC. The percentage errors between predicted OpenFOAM model and experiment are 5.2%, 3.1%, and 1.2% for 5C, 3C, and 1C discharge rates correspondingly.

Figure 103-Figure 105 show the cell surface temperature of the first battery cell (marked 1R in Figure 88) at the end of discharge process (20% SOC) with cooling air velocity of 2 m/s at ambient temperature of 21°C. Figure 103 shows the cell surface temperature under 1C discharge rate at t=2880 seconds, Figure 104 for 3C discharge rate at t=960 seconds, and Figure 105 for 5C discharge rate at t=576 seconds. Different colours indicate the temperature difference at the battery cell surface, with red indicates the highest temperature and blue indicates the lowest temperature. As discussed in previous section, the temperature near the battery's positive and negative terminal is higher than at other locations on the cell surface and the temperature near the positive terminal higher than at the negative terminal. At 1C discharge, only small temperature difference occurs between the hottest and coolest location. In continuation, higher temperature difference is observed at higher discharge rates.

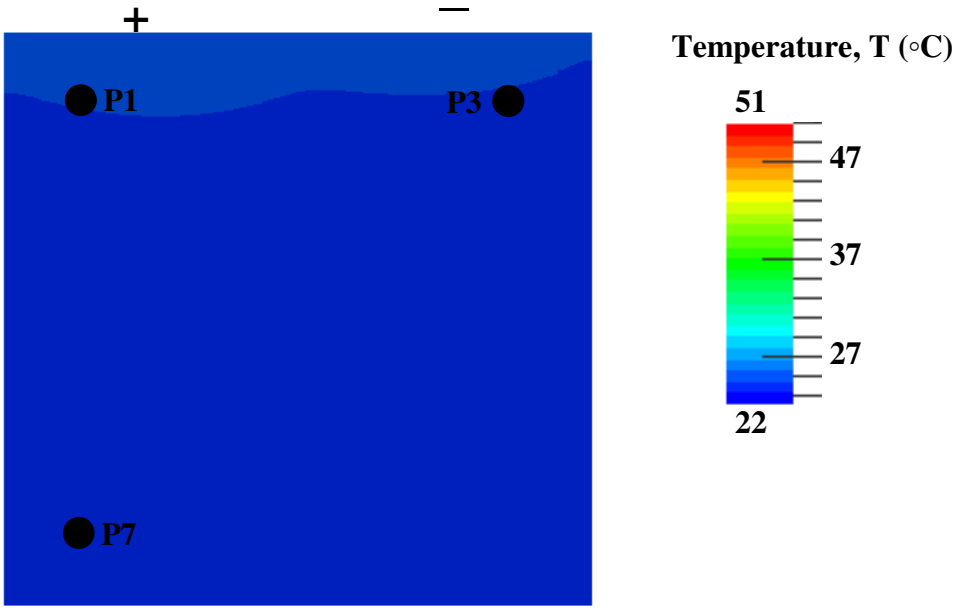

Figure 103. Surface temperature of the first cell (1R) at the end of discharge (20% SOC) with 1C discharge rate.

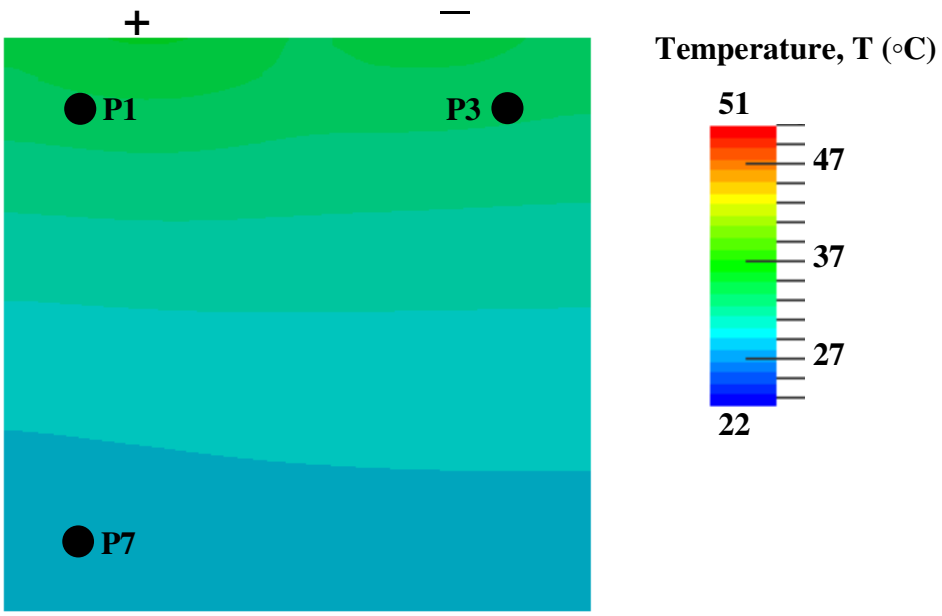

Figure 104. Surface temperature of the first cell (1R) at the end of discharge (20% SOC) with 3C discharge rate.

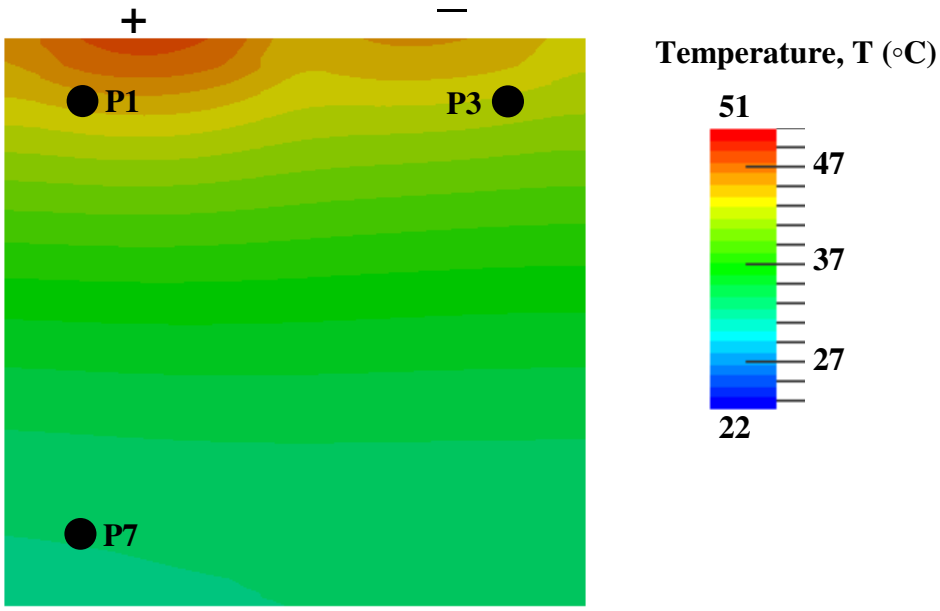

Figure 105. Surface temperature of the first cell (1R) at the end of discharge (20% SOC) with 5C discharge rate.

4.5.3 Cell surface temperature of the second cell at different discharge rates

Figure 106 shows the comparison of the cell surface temperature evolution of the second cell at P19 which is near the highest temperature location. In general, at this point the temperature

obtained from experiment is higher than the one calculated by the OpenFOAM model for all three different discharge rates. Actually, the model is capable to predict the effect of arrangement of the battery cells in the box, the temperature for the cell at the centre of the box (second cell) is higher than the temperature of the first cell. Anyhow the temperature differences between P19 and P1 calculated by the model are smaller than those acquired through experiment.

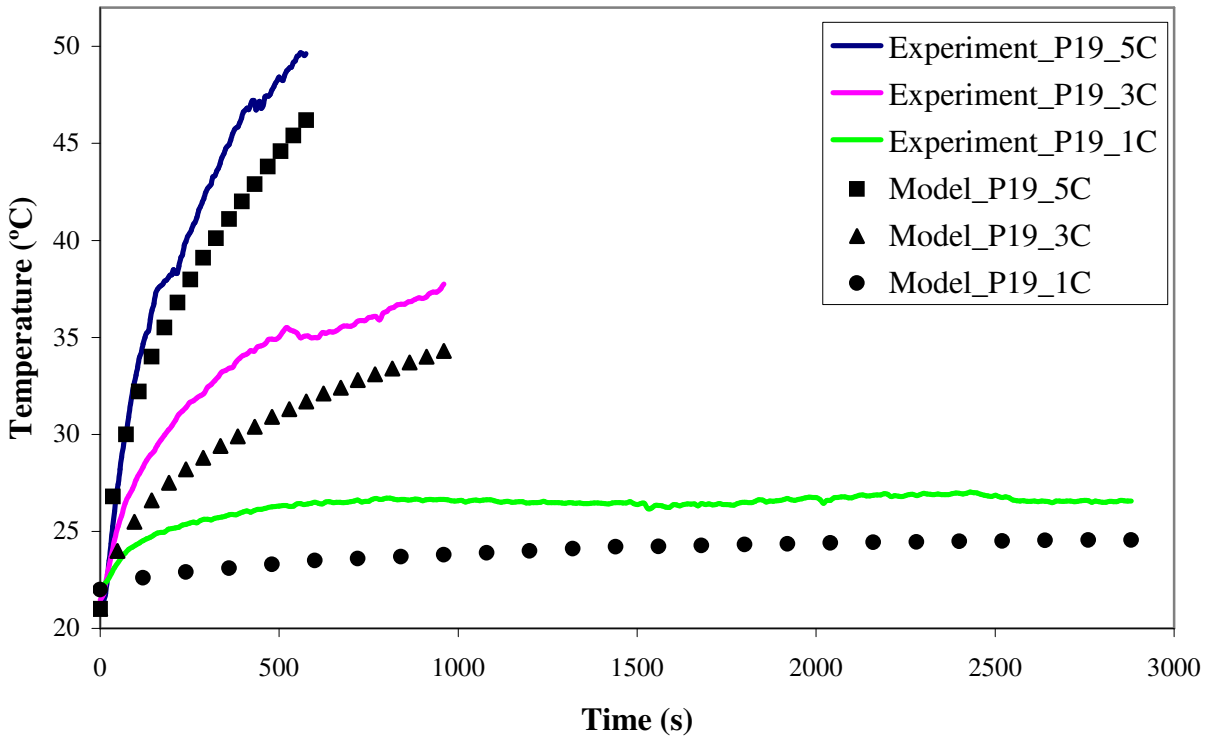

Figure 106. Comparison of the temperature at P19 from experiment and the OpenFOAM simulation model at discharge rate of 1C, 3C, and 5C with cooling air velocity of 2 m/s.

Temperature difference between P19 and P1 captured in experiment is 6.2ºC for both 5C and 3C, and 2ºC for 1C while model calculates the temperature difference of 2.6ºC for 5C, 1.3ºC for 3C, and 0.3ºC for 1C. The average temperature difference between experiment and predicted by the model is 2.0ºC at 5C, 3.5ºC at 3C, and 1.9ºC at 1C discharge rate. End of discharge temperature is 49.8°C at 5C, 39.5°C at 3C, and 27.24°C at 1C recorded through experiment. On the other hand, end of discharge temperature is 46.2°C at 5C, 34.3°C at 3C, and 24.6°C at 1C predicted by the model**.** This difference can be explained by the use of thermocouples to measure the cell surface temperature in experiment. Even though the thermocouples are very thin, they

might anyhow slightly disturb the cooling air circulation between the cells. This effect is not taken into consideration during modelling, as cell surfaces with no obstacles are used. Thus, there will be some difference in heat transfer calculated by the model and obtained in the experiment. The percentage errors between predicted OpenFOAM model and experiment are 7.4 %, 9.9 %, and 5.4 % for 1C, 3C, and 5C respectively.

Figure 107-Figure 109 show the cell surface temperature of the second battery cell (marked 2R in Figure 88) at the end of discharge process at t=2880 seconds for 1C discharge, t=960 seconds for 3C discharge and t=576 seconds for 5C discharge. Figure 107 shows the temperature at 1C discharge, Figure 108 at 3C discharge and Figure 109 at 5C discharge. In general, the cell surface temperature of the second cell is higher than the first cell under equivalent discharge rate. Furthermore, the temperature differences between positive and negative electrode are more significant at second cell compared to the first cell.

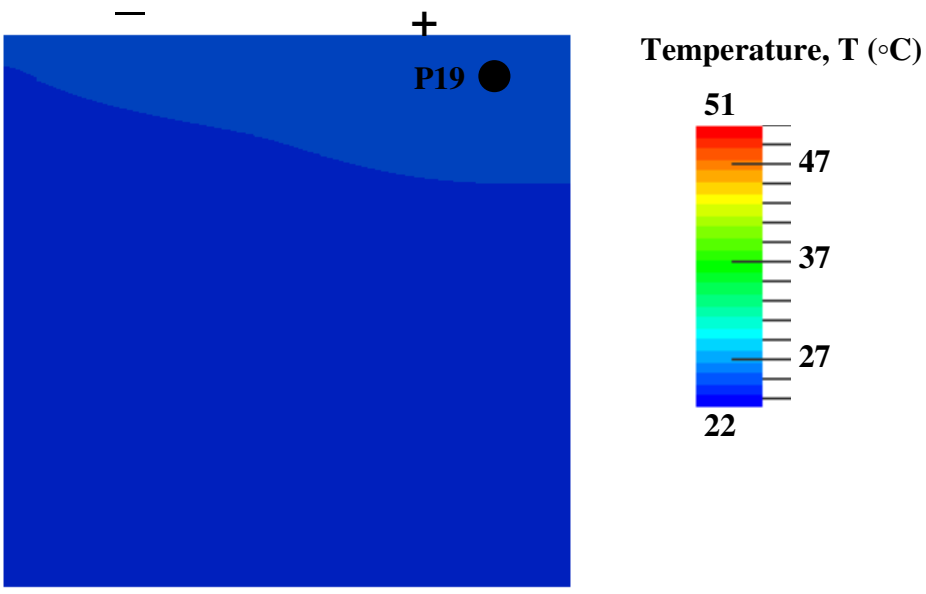

Figure 107. Surface temperature of the second cell (2R) at the end of discharge (20% SOC) with 1C discharge rate.

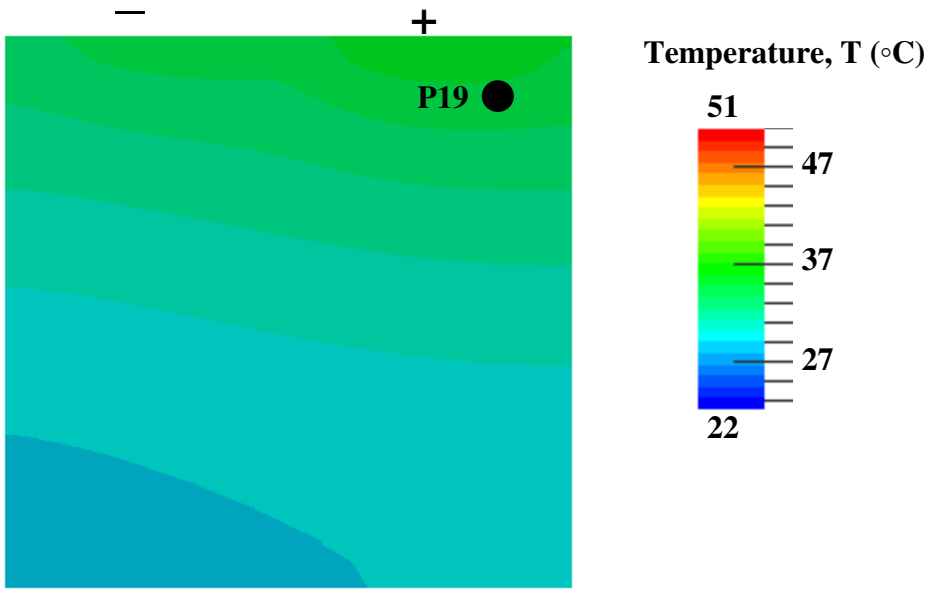

Figure 108. Surface temperature of the second cell (2R) at the end of discharge (20% SOC) with 3C discharge rate.

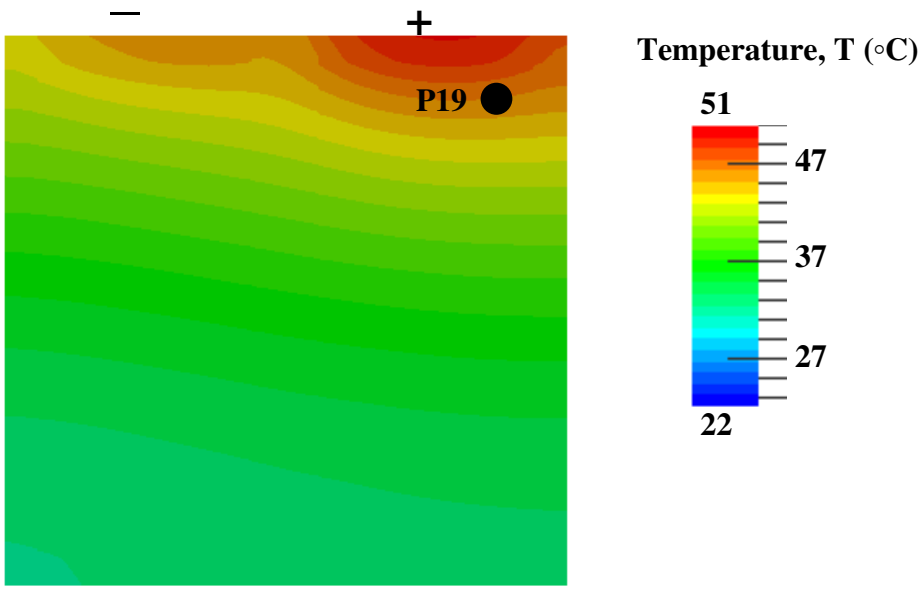

Figure 109. Surface temperature of the second cell (2R) at the end of discharge (20% SOC) with 5C discharge rate.

4.5.4 Cell surface temperature at different cooling air velocities

To make sure that the OpenFOAM model is capable to predict the cell surface under different forced convection conditions, marked by the difference in cooling air velocities, the model is compared to the experimental result at higher air velocity, 4 m/s and 6 m/s. Figure 110 and Figure 113 illustrates the cell surface temperature evolution from experiment and model under 5C discharge rate at cooling air velocities of 4 m/s and 6 m/s respectively. Both figures show the comparison for the temperature evolution of the first cell; P1 and P7, and the second cell; P19.

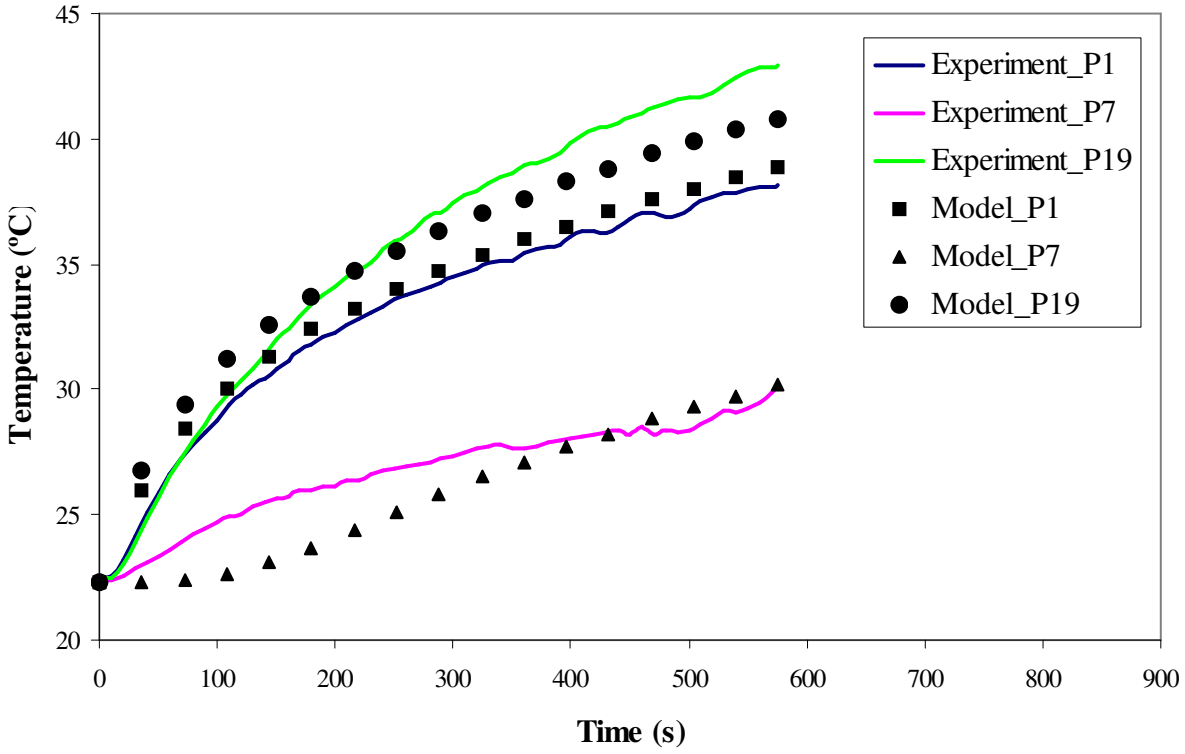

Figure 110. Comparison of the experiment and the OpenFOAM simulation model at 5C discharge rate of with cooling air velocity of 4 m/s for P1, P7, and P19.

In Figure 110, at P1, the OpenFOAM model predicted a slightly higher temperature from the beginning to the end of discharge process. In average, the temperature calculated by the model is 0.6°C higher than captured in the experiment. End of discharge temperature is 38.2°C obtained from experiment and 38.9°C calculated by model. At P7, at the beginning of discharge process, the temperature predicted by the model is much lower than the experimental result. As the discharge process goes on, better temperature prediction is achieved by the model. It can be

observed that after 400 seconds, the simulation shows a good conformity with the experiment result until the end of discharge process. End of discharge temperature is 30.2°C for both results captured through experiment and predicted by the model.

For the second cell, at P19 there are some differences between the results shown by experiment and predicted by the model. The model is capable to predict the temperature difference between first and second cell even though the temperature at the end of discharge process obtained from experiment is higher than predicted by the model. The model foresees a temperature at P19 slightly higher than obtained from experiment at the beginning of discharge process. After 200 seconds, the temperature captured through experiment is higher than calculated by the model. End of discharge temperature is 42.9°C recorded through experiment and 40.8°C predicted by the model. The percentage error between predicted OpenFOAM model and experiment are 2.0%, 4.2%, and 3.6% for P1, P7, and P19 respectively.

Figure 111 and Figure 112 summarise the cell surface temperature at the end of discharge process under 5C discharge for the first (1R) and second (2R) cell respectively at cooling air velocity of 4 m/s. In general, using higher cooling air velocity (4 m/s) reduces the overall cell surface temperatures for both first and second cell compared to the cell temperatures presented in previous section under air velocity of 2 m/s.

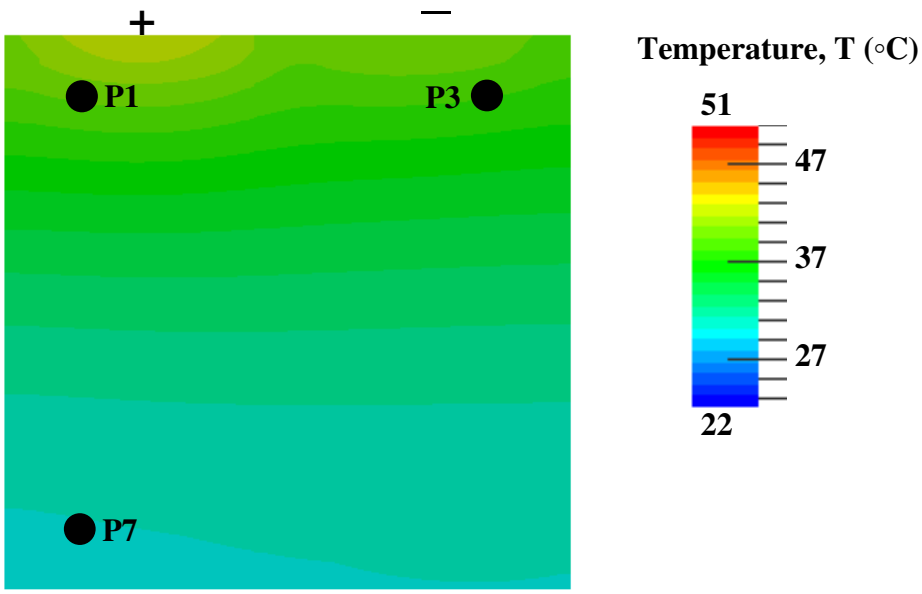

Figure 111. Surface temperature of the first cell (1R) at the end of discharge (20% SOC) with 5C discharge rate at cooling air velocity of 4 m/s .

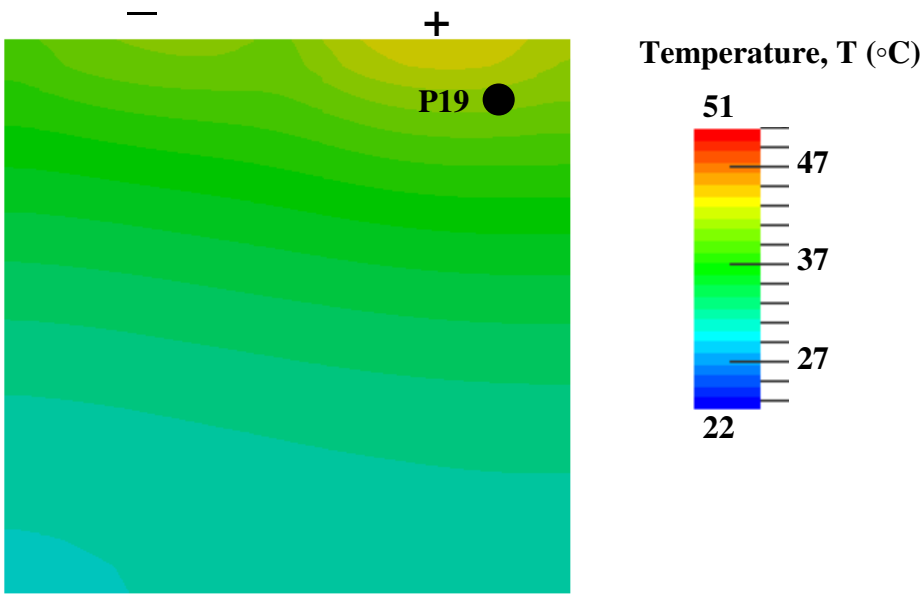

Figure 112. Surface temperature of the second cell (2R) at the end of discharge (20% SOC) with 5C discharge rate at cooling air velocity of 4 m/s .

Figure 113 shows the comparison of the cell surface temperature for cooling air velocity of 6 m/s. In general results shown in Figure 113 have the same trend as in Figure 110. OpenFOAM model predicts a slightly higher temperature than acquired in experiment at P1. End of discharge temperature is 35.8°C obtained from experiment and 36.3°C calculated by the model. At P7, the model predicts lower value of temperature than recorded by the experimental result at the beginning of discharge process. Then, good temperature prediction is achieved from 300 seconds towards the end of discharge process. End of discharge temperature is 28.5°C predicted by the model and 28.8°C captured through experiment. At P19, model calculates slightly higher temperature obtained from experiment at the beginning of discharge process. After 180 seconds, the temperature captured through experiment increases at higher rate than predicted by the model. End of discharge temperature is 39.5°C recorded through experiment and 38.0°C predicted by the model. The percentage error between predicted OpenFOAM model and experiment are 2.0%, 2.5%, and 2.9% for P1, P7, and P19 respectively. These cell surface temperatures are summarised in Figure 114 and Figure 115 for the first (1R) and second (2R) cell respectively.

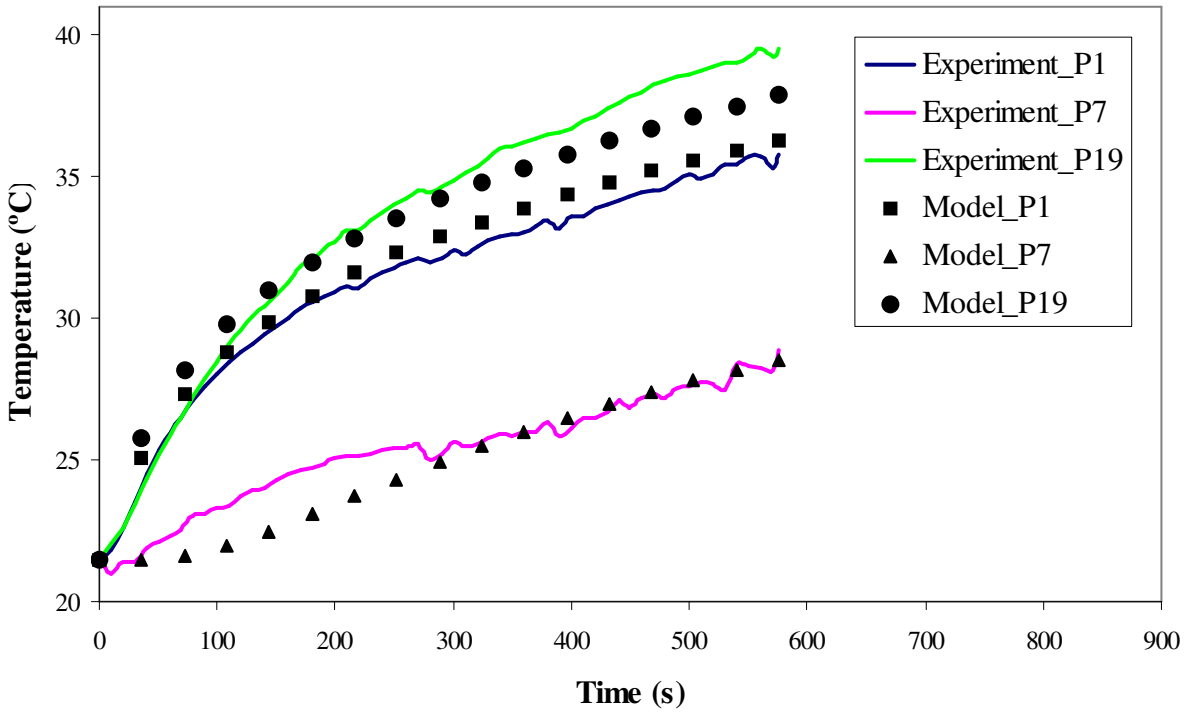

Figure 113. Comparison of the experiment and the OpenFOAM simulation model at 5C discharge rate of with cooling air velocity of 6 m/s for P1, P7, and P19.

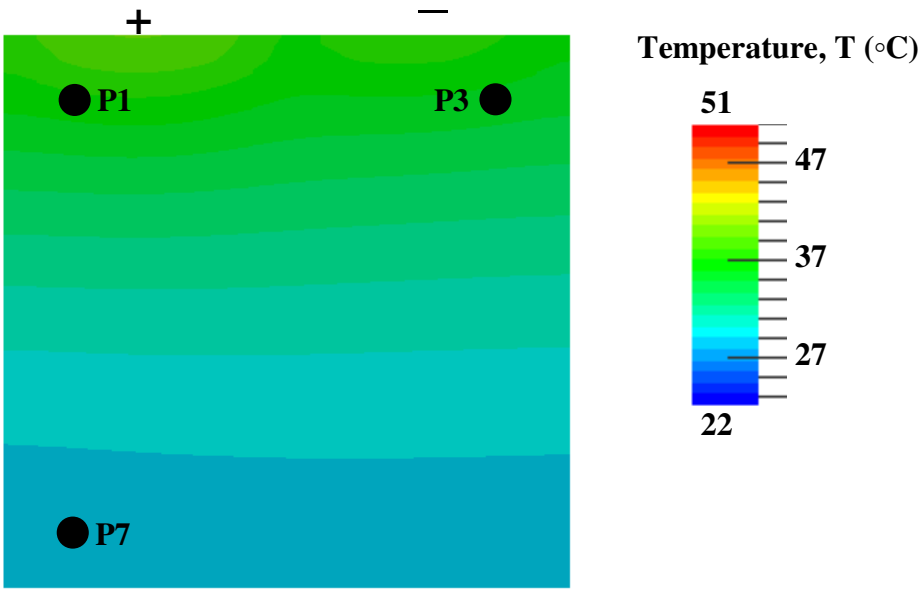

Figure 114. Surface temperature of the first cell (1R) at the end of discharge (20% SOC) with 5C discharge rate at cooling air velocity of 6 m/s .

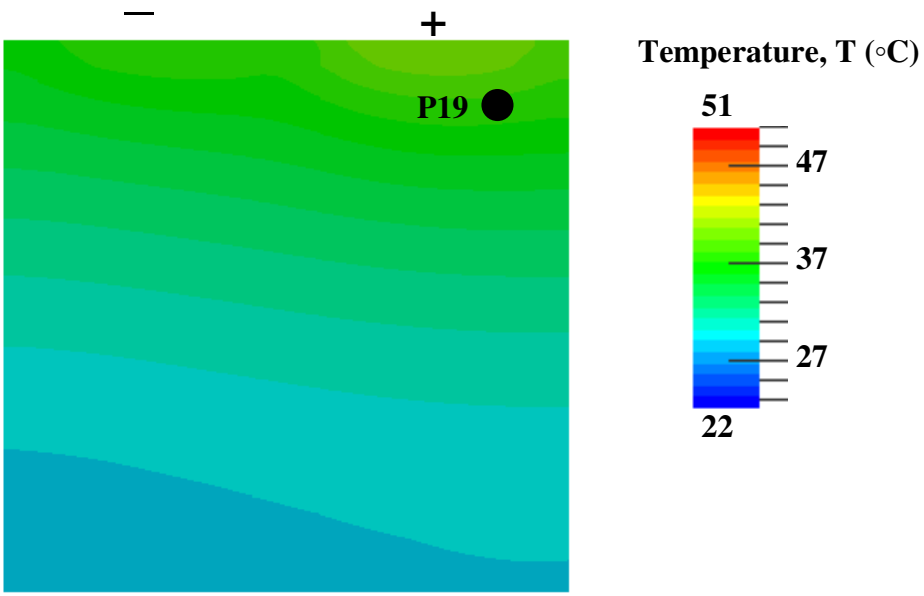

Figure 115. Surface temperature of the second cell (2R) at the end of discharge (20% SOC) with 5C discharge rate at cooling air velocity of 6 m/s .

4.6 CONCLUSION

An electro-thermal model of a lithium ion battery for automotive applications is presented and validated. This model is implemented in OpenFOAM software, providing the possibility to link heat generation from thermal losses inside battery cells to radiation and forced convection of an air stream. The heat source is calculated as a function of the battery discharge current and the internal resistance. A scale factor that takes account of the difference in electrical conductivity between positive and negative electrodes is used to differentiate the amount of heat generated at positive and negative electrodes. The battery internal resistance as a function of temperature is proposed and used in this current study. The calculated heat source is introduced to the cell through two patches located at positive and negative electrodes at the top of the battery cell. Then the heat from these patches is transferred to the entire battery cell through conduction process, before dissipating to the environment by radiation and force convection heat transfer.

The openFOAM simulation results are validated by experimental results in two main aspects; cooling air flow field characteristic and thermal behaviour of the cell surface. The comparison of OpenFOAM simulation and PIV experimental results in the present study shows that the simulation is capable of producing good results of air flow field characteristics inside the battery box for different initial air velocities. The air flow is at constant velocity at the beginning

of the upstream section. Then, the air flow velocity increases at the cell section as the area decreases, and finally the air flow velocity gradually decreases as it leaves the cell section.

In terms of thermal behaviour, good agreement is obtained from the predicted simulation results and the acquired experimental results. The simulation results confirm observations from experimental results that the temperature is higher close to the connectors and there is a strong link between the discharge rate and the temperature increase. The model is able to predict the cell surface temperature at different locations on a cell surface, and for different cells, especially the difference of temperature of the first and second cell. The proposed model is also capable of simulating the effect of different discharge rates and different cooling air velocities on the cell surface temperatures. Good precision results are obtained for the temperature of the cell surface near the positive and negative electrodes. A slight difference between calculated and experimental result can be observed for the battery cell surface temperature at the location far from the cell electrodes; near the lowest cell temperature location at the beginning of discharge process, then good result synchronization is achieved towards the end of discharge process. The model is capable to predict the effect of stacking the battery cell inside the battery the box. Anyhow, some differences exist between experiment and simulation for the temperature of the cell in the middle of the stack (second cell), the model predicted a slightly lower temperature than obtained through experiment.

Generally, the difference between results predicted by the model and acquired from experiment is caused by the difference of the initial value of cooling air velocity and temperature imposed in the model and the real value during experiment. In the model, the value of cooling air velocity and temperature is set as a constant, while in reality, during experiment these values varied slightly from their indicated fixed values. Other factors that contribute to the difference of the results comes from the way the heat sources are introduced through patches at the top of the cell in the proposed model and the use of thermocouples in the experiment that slightly interrupted the air flow velocity near the cell surface, which is not taken into account in the model.

CHAPTER 5: CONCLUSION AND PERSPECTIVES

5.1 CONCLUDING REMARKS

The main purpose of the study presented in this thesis is to investigate the thermal behaviour of the lithium ion battery cells in packs through experimental work. Along with the experimental work, the current study focuses on the development and validation of 3D electro-thermal CFD model of lithium-ion battery cells and pack. The experimental study is focused on the distribution of temperature at various points on the battery cell surface, impact of abuse discharge condition, impact of different constant discharge rates, and also the importance of cooling system (different cooling air velocities) on the battery cell surface temperature. In addition, a case study is conducted to evaluate the thermal behaviour for battery used in electric vehicle to complete driving cycles.

Based on the experimental results, one can conclude that the temperature on the cell surface is non-homogeneous, with a significant difference between the highest and the lowest temperature. Furthermore, the temperature is higher close to the battery cell positive and negative electrodes, with a slightly higher temperature near the positive electrode observed compared to the negative electrode. It was found that the battery discharge rate has a huge influence on the battery thermal behaviour; higher discharge rates meaning higher amount of current circulates inside the cell, more heat is generated and thus higher temperature increases. As for example, at constant cooling air velocity of 2 m/s, the highest temperature of the first cell at P1 increase from 25.2°C at 1C discharge rate to 33.3°C , and 43.6°C at 3C and 5C discharge rates respectively.

Cooling system plays an important role in controlling the battery cell temperature. In the present study, the maximum cell surface temperature is reduced by 12°C by using air velocity of 10 m/s instead of 2 m/s. Moreover, higher cooling air velocity also helps to decrease the temperature variation of the cell surface. At air velocity of 2 m/s, the difference between maximum (P1) and minimum (P7) temperature of the first cell is 11.8°C, and this value decreases to 4.8°C using cooling air velocity of 10 m/s.

Discharging the battery at SOC lower than 20% reveals a sudden huge increase of cell temperature at all battery cell locations. This situation is directly influenced by the change of the value of internal resistance at different SOC. Experiments show that at a constant temperature,

the variation of internal resistance is small from 100% to 20% SOC. Anyhow, after 20% SOC there is a sudden jump in the value of internal resistance. On the other hand, the battery internal resistance is greatly influenced by the temperature. In the current study, the resistance decreases to nearly half its initial value as the temperature increasess from 20ºC to 50ºC. The value of internal resistance is between 2.17 mΩ and 1.33 mΩ. In the case study, there is just a small increase of the battery cell surface temperature for both cases, which is using constant air cooling velocity and cooling air velocity in function of vehicle speed for NEDC and Artemis rural driving cycle. Anyhow better heat distributions are achieved when the cooling air velocity as function of vehicle speed is used.

The second part of the work presented in this thesis consists of the battery electro-thermal modelling through OpenFOAM software. The model considered the heat generation from battery current and internal resistance, heat transfer inside the battery cell through conduction and heat transfer from battery cells to environment through forced convection and radiation. The proposed model used battery internal resistance as a function of temperature based on the result found in experiment. The calculated heat source is introduced into the cell through two thin patches located at positive and negative electrodes at the top of the battery cell. Then, the heat from these patches is transferred to the entire battery cell through conduction process, before dissipating to the environment by radiation and forced convection heat transfer.

The model is validated by comparing to experimental results through two main aspects; air flow behaviour close to cell surface at different initial cooling air velocities and battery temperature evolutions at various locations on the battery cell surface under different discharge rates and forced convection conditions. The comparison of OpenFOAM simulation and PIV experimental results in the present study shows that the simulation is capable of producing good results of air flow field characteristics inside the battery box; near the battery cell surface, for different initial air velocities. In terms of thermal behaviour, good agreement between predicted simulation results and the acquired experimental results is obtained. The simulation results confirm observations from experimental results that the temperature is higher close to the connectors and there is a strong link between the discharge rate and the temperature decrease. The model is able to predict the cell surface temperature at different locations on a cell, and for different cells. Furthermore, the proposed model is capable to simulate the effect of different cooling air velocities on the cell surface temperatures. Good precision results are obtained for the

temperature of the cell surface near the positive and negative electrodes. A slight difference between calculated and experimental results can be observed for the battery cell surface temperature at the location far from the cell electrodes; near the lowest cell temperature location principally at the beginning of discharge process, then good results synchronization is achieved towards the end of discharge process. The model is capable to predict the effect of stacking the battery cell inside the battery the box. Anyhow, some differences exist between experiment and simulation for the temperature of the cell in the middle of the stack (second cell), the model predicted a slightly lower temperature than obtained through experiment.

In general, the difference between the predicted result and experiment result can be described as the difference of the boundary conditions between the proposed model and experiment. In the model, the value of cooling air velocity and temperature at the beginning of the upstream section (X=0 mm) is constant, while in experiment these values varied slightly from their indicated fixed value. Other factors that contribute to the difference of results are the way the heat sources are introduced through patches at the top of the cell in the proposed model, the use of thermocouples in the experiment that slightly interrupted the air flow near the cell surface and the air flow channel in the experimental work that is not taken into account in the modelling.

As a conclusion, the electro-thermal model proposed in this current study is capable to predict the cell surface temperature behaviour and air flow characteristics near cell surfaces with a good accuracy. Furthermore, this model is relatively simple that needs a reasonable computation source to obtain good results. This electro-thermal model that is implemented in free, open source CFD software (OpenFOAM) is easy to access, manipulate and use by other researchers for further battery cell analysis.

5.1 SUGGESTIONS FOR FUTURE WORK

As a continuation from the works presented in this thesis, it is first suggested that the experimental study is conducted for battery during charging process and also using higher number of battery cells and different spaces between cells. This is to better understand the heat generation during charging, the effect of stacking the battery cells in battery box, and different spacing between cells to the battery thermal behaviour. These results can then be used to validate the electro-thermal OpenFOAM model. In this way, the model's capability to predict the thermal

behaviour of the battery cells at various aspects; different charge-discharge rates, different cooling air velocities, different cell surface locations, different cell numbers, and spaces between cells will be confirmed. The goal is that in the future, the proposed model can be used to predict the battery cell thermal behaviour for any battery configurations as required in hybrid and electric vehicles.

For the future it will be important to improve the heat generation inside the battery cell in the electro-thermal model. The first approach used through this current study is by using small and thin patches attached at the top of the cell at positive and negative electrodes. This approach has some weaknesses, especially for the battery cell location far from the heat source patches. As the distance from these patches increases, the result calculated by the model becomes less accurate, particularly at the beginning of discharge process. In addition with the current method it is suggested to create a thin surface inside the battery cell to be used as heat source. This thin surface should be placed in the middle of the cell, and should cover the length and height of the cell. Using this method, a better heat distribution at all cell locations can be achieved.

In continuity with the current work, it is suggested to improve the value of internal resistance used in the electro-thermal model, for more accurate results. In the current study, the battery internal resistance proposed is based on the experimental result. It is a polynomial curve that best fit the experimental result. This proposed internal resistance is then used in the battery thermal behaviour calculation. Anyhow, the model tends to predict a slightly higher temperature (for the locations near the heat source) especially at the beginning of discharge process, where the temperature is relatively low, thus high value of internal resistance. In the future, the improvement of the value of internal resistance can be achieved by using the temperature acquired through experiment to calculate the internal resistance. Applying calculated internal resistance through this method may result in better cell surface temperature prediction.

APPENDIX A: OPENFOAM CODE – RADIATION PROPERTIES

```
// ************************************************************************//

        radiation           on;
        radiationModel      P1;

        noRadiation
        {           }

        P1Coeffs
        {           }

        absorptionEmissionModel             constantAbsorptionEmission;
        constantAbsorptionEmissionCoeffs
        {           a           a [ 0 -1 0 0 0 0 0 ] 0.5;
                    e           e [ 0 -1 0 0 0 0 0 ] 0.5;
                    E           E [ 1 -1 -3 0 0 0 0 ] 0;            }

        scatterModel                        constantScatter;
        constantScatterCoeffs
        {           sigma       sigma [ 0 -1 0 0 0 0 0 ] 0;
                    C           C [ 0 0 0 0 0 0 0 ] 0;              }


// ************************************************************************* //
```

APPENDIX B: OPENFOAM CODE – RADIATION INTENSITY

```
// ************************************************************************//

        G
        {
        dimensions      [1 0 -3 0 0 0 0];
        internalField   uniform 0;
        boundaryField

        ".*"
        {       type                    MarshakRadiation;
                T                       T;
                emissivityMode          lookup;
                emissivity              uniform 1.0;
                value                   uniform 0;          }

        maxY
        {       type                    MarshakRadiation;
                T                       T;
                emissivityMode          lookup;
                emissivity              uniform 1.0;
                value                   uniform 0;;         }

       maxZ …
       minY…
       minZ…

// ************************************************************************//
```

APPENDIX C: OPENFOAM CODE – HEAT FLUX

```
// ************************************************************************//


T
  {
    internalField   uniform 294;
    boundaryField
    {
      ".*"
      {             type          zeroGradient;
                    value         uniform 294;             }

      "heater_to_.*"
      {             type                        compressible::turbulentTemperatureCoupledBaffleMixed;
                    neighbourFieldName          T;
                    K                           solidThermo;
                    KName                       none;
                    value                       uniform 294;       }

      maxY  (Positive electrode patch)
      {             type                        groovyBC;
                    value                       uniform 294;
                    valueExpression   "294";
                    gradientExpression          "gradT";
                    fractionExpression          "0";
                    variables                   "Cp0=2300;rho0=2436;
                    heatFlux=1*((2.5e8)*(0.088112375+((8.25e-7)*T*T)-((5.351e-4)*T)));
                    gradT=heatFlux/(alphaEff*Cp0*rho0);" timelines ( );             }


// ************************************************************************//
```

APPENDIX D: OPENFOAM CODE – TURBULENCE MODEL

```
// ************************************************************************//

RASProperties
        RASModel        kEpsilon;
        turbulence      on;
        printCoeffs     on;

// ************************************************************************//

// ************************************************************************//

RASModel
        simulationType  RASModel;

// ************************************************************************//
```

APPENDIX E: OPENFOAM CODE – BOUNDARY CONDITIONS

```
// ************************************************************************//

U (Air velocity)
{       internalField       uniform (0 0 0);
        boundaryField
   {

       ".*" (box and cell surfaces)
      {           type            fixedValue;
                  value           uniform (0 0 0);          }

       minx (inlet)
      {           type            fixedValue;
                  value           uniform ( 2 0 0 );        }

       maxX (outlet)
      {           type            inletOutlet;
                  inletValue      uniform ( 0 0 0 );
                  value           uniform ( 0 0 0 );        } } }


T (Temperature)
{
   internalField          uniform 294;
   boundaryField
   {
      ".*" (box and cell surfaces)
      {           type            zeroGradient;             }

       minx (inlet)
      {           type            fixedValue;
                  value           uniform 294;              }

       maxX (outlet)
      {           type            inletOutlet;
                  inletValue      uniform 294;
                  value           uniform 294;              }

       "Air_to_.*"
      {           type                    compressible::turbulentTemperatureCoupledBaffleMixed;
                  neighbourFieldName      T;
                  K                       basicThermo;
                  KName                   none;
                  value                   uniform 294;      } } }
```

```
P (Pressure)
{
   internalField           uniform 1e5;
   boundaryField
   {
      ".*" (box and cell surfaces)
      {           type            calculated;
                  value           uniform 1e5;            }

        maxX (outlet)
      {           type            calculated;
                  value           uniform 1e5;            } } }


// ********************************************************************************//
```

REFERENCES

[1] B. G. Pollet, I. Staffell, and J. L. Shang. Current status of hybrid, battery and fuel cell electric vehicles: From electrochemistry to market prospects. *Journal of Electrochimica Acta*, 84:235–249, 2012.

[2] J. Sousanis. World vehicle population tops 1 billion units. Ward AutoWorld. http://wardsauto.com, Retrieved April 2014.

[3] J. Voelcker. 80 million vehicles built globally last year - a new record. Green Car Reports. http://www.greencarreports.com, Retrieved April 2014.

[4] D.Doerffel and S. Abu Sharkh. System modeling and simulation as a tool for developing a vision for future hybrid electric vehicle drivetrain configurations. *Vehicle Power and Propulsion Conference (VPPC)*, pages 1–6, 2006.

[5] A. Rousseau, F. Badin, M. Redelbach, N. Kim, A. Da Coata, D. Santini, A. Vyas, F. Le Berr, and H. Friedrich. Comparison of energy consumption and costs of different hevs and phevs in european and american context. In *EEVC*, pages 19–22, Brussels, Belgium, November 2012.

[6] I.Taymaz and M. Benli. Emissions and fuel economy for a hybrid vehicle. *Fuel*, 115:812–817, 2014.

[7] S. J. Gerssen-Gondelach and A. P.C. Faaij. Performance of batteries for electric vehicles on short and longer term. *Journal of Power Sources*, 212:111–129, 2012.

[8] M. Khan and N. C. Kar. Hybrid electric vehicles for sustainable transportation: A Canadian perspective. *World electric vehicle journal*, 3:2032–6653, 2009.

[9] A.Peterson and J. Rohrer. Cause and effect for global warming. Time for change. http://timeforchange.org, Retrieved October 2014.

[10] A. P. M. Baede and P. Van Der Linden. IPPC AR4 SYR Appendix Glossary. http://www.ipcc.ch/pdf/assessment-report/ar4/syr/ar4_syr_appendix.pdf, Retrieved October 2014.

[11] M. Lallanilla. Effects of global warming. Live Science. http://www.livescience.com, Retrieved October 2014.

[12] H. Selin. Global warming. Encyclopaedia Britannica. http://global.britannica.com, Retrieved October 2014.

[13] D. Markham. Global warming effects and causes: A top 10 list. planetsave. http://planetsave.com, Retrieved October 2014.

[14] Q. Schiermeir. The cost of global warming. *Nature*, 439:374–375, January 2006.

[15] I. S. Nashawi, A. Malallah, and M. Al-Bisharah. Forecasting world crude oil production using multicyclic hubbert model. *Energy Fuels*, 24:1788–1800, 2010.

[16] W. Zittel, J. Zerhusen, and M. Zerta. Fossil and nuclear fuels – the supply outlook. Technical report, Energy Watch Group (EWG), March 2013.

[17] D. Chrenko, L. Le Moyne, E. H. Aglzim, D. Bouquain, and A. Miraoui. High temperature pem fuel cell system for small mobile applications. In *X Congreso Internacional de la Sociedad Mexicana del Hidrogeno: "Energias Renouvables"*, pages 1–6, Teluca, Mexico, September 2010.

[18] T. Hutchinson, S. Burgess, and G. Herrmann. Current hybrid-electric powertrain architectures: Applying empirical design data to life cycle assessment and whole-life cost analysis. *Applied Energy*, 119:314–329, 2014.

[19] D. H. Phuc, P. Raksincharoensak, n. Masao, and S. Masahiro. Control strategy for hybrid electric vehicles based on driver vehicle following model. In *SICE-ICASE International Joint Conference*, pages 555 – 560, October 2006.

[20] M. Ehsani, Y. Gao, S. E. Gay, and A. Emadi. *Modern Electric,Hybrid Electric, and Fuel Cell Vehicles*. CRC Press, USA, 2005.

[21] A. Kéromnès, B. Delaporte, G. Schmitz, and L. Le Moyne. Development and validation of a 5 stroke engine for range extenders application. *Energy Conversion and Management*, 82:259–267, 2014.

[22] J. Larminie and J. Lowry. *Electric Vehicle Technology Explained*. John Wiley & Sons Ltd,, West Sussex, England, 1 edition, 2003.

[23] K. Oh, D. Kim, T. Kim, C. Kim, and H. Kim. Operation algorithm for a parallel hybrid electric vehicle with a relatively small electric motor. *KSME International Journal*, 18(1):30 – 36, 2004.

[24] M. Ehsani, Y. Gao, and J. M. Miller. Hybrid electric vehicles: Architecture and motor drives. *Proceedings of the IEEE*, 95:719 – 728, 2007.

[25] F. L. Mapelli, D. Tarsitano, and M. Mauri. Plug-in hybrid electric vehicle: Modeling, prototype realization, and inverter losses reduction analysis. *IEEE Transactions on Industrial Electronics*, 57(2):598 – 607, February 2010.

[26] S. Amjad, S Neelakrishnan, and R Rudramoorthy. Review of design considerations and technological challenges for successful development and deployment of plug-in hybrid electric vehicles. *Renewable and Sustainable Energy Reviews*, 14:1104–1110, 2010.

[27] K. Ç. Bayindir, M. A. Gözüküçük, and A. Teke. A comprehensive overview of hybrid electric vehicle: Powertrain configurations, powertrain control techniques and electronic control units. *Energy Conversion and Management*, 52:1305–1313, 2011.

[28] M. Ducusin, S. Gargies, and C. Mi. Modeling of a series hybrid electric high-mobility multipurpose wheeled vehicle. *IEEE Transactions on Vehicular Technology*, 56:557 – 565, 2007.

[29] J. Gover. Do we need federal government policies to promote the adoption of electric vehicles? IEEE Transportation Electrification. http://electricvehicle.ieee.org, Retrieved October 2014.

[30] L. Guzzella and A. Sciarretta. *Vehicle Propulsion systems (Introduction to Modelling and Optimization)*. Springer, New York, second edition edition, 2007.

[31] S. Chacko and Y. M. Chung. Thermal modelling of li-ion polymer battery for electric vehicle drive cycles. *Journal of Power Sources*, 213:296–303, 2012.

[32] M.A. Hannan, F.A. Azidin, and A. Mohamed. Hybrid electric vehicles and their challenges: a review. *RenewableandSustainableEnergyReviews*, 29:135–150, 2014.

[33] M. Urbain, S. Raël, and B. Davat. Energetical modelling of lithium-ion batteries. In *IEEE Conference on Industry Applications*, number 42, pages 714 – 721, New Orleans (Louisiana, USA), September 23-27 2007.

[34] Q. Wang, P. Ping, X. Zhao, G. Chu, J. Sun, and C. Chen. Thermal runaway caused fire and explosion of lithium ion battery. *Journal of Power Sources*, 208:210–224, 2012.

[35] A. Shafiei, A. Momeni, and S. S. Williamson. Battery modeling approaches and management techniques for plug-in hybrid electric vehicles. In *Vehicle Power and Propulsion Conference (VPPC)*, Chicago, USA, September 6-9 2011.

[36] Y. Abdul-Quadir, P. Heikkila, T. Lehmuspelto, J. Karppinen, T. Laurila, and M. Paulasto-Krockel. Thermal investigation of a battery module for work machines. In *Thermal,*

Mechanical and Multi-Physics Simulation and Experiments in Microelectronics and Microsystems Conference (EuroSimE), pages 1–6, Palais Kaufmannischer Verein, Linz, Austria, 18-22 April 2011.

[37] S. Al-Hallaj and J. R. Selman. Thermal modeling of secondary lithium batteries for electric vehicle/hybrid electric vehicle applications. *Journal of Power Sources*, 110:341–348, 2002.

[38] F. Baronti, G. Fantechi, E. Leonardi, R. Roncella, and R. Saletti. Effective modeling of temperature effects on lithium polymer cells. In *International Conference on Electronics, Circuits, and Systems (ICECS)*, 17, pages 990 – 993, Athens, Greece, 12-15 December 2010.

[39] F. Martel, Y. Dube, L. Boulon, and K. Agbossou. Hybrid electric vehicle power management strategy including battery lifecycle and degradation model. In *Vehicle Power and Propulsion Conference (VPPC)*, pages 1–8, Chicago, USA, September 6-9 2011.

[40] C. Sen and N. C. Kar. Battery pack modeling for the analysis of battery management system of a hybrid electric vehicle. In *Vehicle Power and Propulsion Conferences (VPPC)*, pages 207 – 212, Dearborn, MI, September 7-11 2009.

[41] C. Zhou, H. Liu, and K. Liu. The simulation research of parallel hybrid electric vehicle based on virtual prototype technique. *IEEE Conference on Power and Energy Engineering (APPEEC)*, pages 1–6, 2009.

[42] S. Sadeghi, J. Milimonfared, and M. Mirsalim. Dynamic modeling and simulation of a series hybrid electric vehicle using a switched reluctance motor. In *Proceeding of International Conference on Electrical Machines and Systems 2007, Oct. 8 11, Seoul, Korea*, pages 2017 –2022, October 2007.

[43] W. Jiaxue, W. Qingnian, L. Jishun, and Z. Xiaohua. Forward simulation model precision study for hybrid electric vehicle. In *International Conference on Mechatronics and Automation*, pages 2457 – 2461, Changchun, China, August 2009.

[44] X. He, T. Maxwell, M. Parten, and P. Shurlok. Modeling and validation of a hydrogen engine powered hybrid electric vehicle. In *Vehicle Power and Propulsion Conference (VPPC)*, pages 506 –510, 2007.

[45] C.C. Chan, A. Bouscayrol, and K. Chen. Electric, hybrid, and fuel-cell vehicles: Architectures and modeling. *IEEE Transactions on Vehicular Technology*, 59(2):589 – 598, February 2010.

[46] A. Emadi, K. Rajashekara, S. S. Williamson, and S. M. Lukic. Topological overview of hybrid electric and fuel cell vehicular power system architectures and configurations. *IEEE Transactions on Vehicular Technology*, 54(3):763 – 770, May 2005.

[47] J. Scordia, R. Trigui, M. Desbois-Renaudin, B. Jeanneret, and F. Badin. Global approach for hybrid vehicle optimal control. *Journal of Asian Electric Vehicles*, 7:1221–1230, 2009.

[48] C. E. S. Thomas. How green are electric vehicles? *International Journal of Hydrogen Energy*, 37:6053–6062, 2012.

[49] K.T. Chau and Y.S. Wong. Overview of power management in hybrid electric vehicles. *Energy Conversion and Management*, 43:1953–1968, 2002.

[50] S. F. Tie and C. W. Tan. A review of energy sources and energy management system in electric vehicles. *Renewable and Sustainable Energy Reviews 20 (2013) 82–102*, 20:82–102, 2013.

[51] B. Powell, X. Xianjie, and R. Baraszu. Computer model for a parallel hybrid electric vehicle (phev) with cvt. In *Proceedings of the American Control Conference*, pages 1011 – 1015, June 2000.

[52] M. Kuchita, T. Kitada, and K. Kido. Development of virtual powertrain model. *Mitsubishi Motors Technical review*, 14:16–23, 2002.

[53] A. Väyrynen and J. Salminen. Lithium ion battery production. *The Journal of Chemical Thermodynamics*, 46:80–85, 2012.

[54] Y. K. Tan, J. C Mao, and K. J. Tseng. Modelling of battery temperature effect on electrical characteristics of li-ion battery in hybrid electric vehicle. In *International Conference on Power Electronics and Drive Systems (PEDS)*, 9, pages 637 – 642, Singapore, December 5-8 2011.

[55] S. Bhide and T. Shim. Novel predictive electric li-ion battery model incorporating thermal and rate factor effects. *IEEE Transactions on Vehicular Technology*, 60:819 – 829, March 2011.

[56] K. M. Tsang, L Sun, and Chan W. L. Identification and modelling of lithium ion battery. *Journal of Energy Conversion and Management*, 51:2857–2862, June 2010.

[57] R. Spotnitz. Simulation of capacity fade in lithium-ion batteries. *Journal of Power Sources*, 113:72–80, September 2003.

[58] S. Bourlot, P. Blanchard, and S. Robert. Investigation of aging mechanisms of high power li-ion cells used for hybrid electric vehicles. *Journal of Power Sources*, 196:6841–6846, 2011.

[59] A. Eddahech, O. Briat, H. Henry, J.-Y. Delétage, E. Woirgard, and J.-M. Vinassa. Ageing monitoring of lithium-ion cell during power cycling tests original research article. *Microelectronics Reliability*, 51:1968–1971, 2011.

[60] A. Hoke, A. Brissette, A. Pratt, and K. Smith. Electric vehicle charge optimization including effects of lithium-ion battery degradation. In *Vehicle Power and Propulsion Conference (VPPC)*, pages 1 – 8, Chicago USA, Sept 2011.

[61] Z. Li, L. Lu, M. Ouyang, and Y. Xiao. Modeling the capacity degradation of lifepo4/graphite batteries based on stress coupling analysis. *Journal of Power Sources*, 196:9757– 9766, 2011.

[62] W. LIU, C. DELACOURT, C. FORGEZ, and S. PELISSIER. Study of graphite/nca li-ion cell degradation during accelerated aging tests - data analysis of the simstock project. In *Vehicle Power and Propulsion Conference (VPPC)*, pages 1 – 6, Chicago, USA, Sept 2011.

[63] P. Ramadass, B. Haran, R. White, and B. N. Popov. Mathematical modeling of the capacity fade of li-ion cells. *Journal of Power Sources*, 123:230 – 240, March 2003.

[64] Y. Zhang, C. Y. Wang, and X. Tang. Cycling degradation of an automotive lifepo4 lithium-ion battery. *Journal of Power Sources*, 196:1513–1520, February 2011.

[65] S. B. Peterson, J. Apt, and J.F. Whitacre. Lithium-ion battery cell degradation resulting from realistic vehicle and vehicle-to-grid utilization. *Journal of Power Sources*, 195:2385 – 2392, October 2010.

[66] A. Smyshlyaev, M. Krstic, N. Chaturvedi, J. Ahmed, and A. Kojic. Pde model for thermal dynamics of a large li-ion battery pack. In *American Control Conference (ACC)*, pages 959 – 964, O'Farrell Street, San Francisco, CA, USA, June 2011.

[67] Y. S. Choi and D. M. Kang. Prediction of thermal behaviors of an air-cooled lithium-ion battery system for hybrid electric vehicles. *Journal of Power Sources*, 270:273–280, 2014.

[68] M. R. Giuliano, A. K. Prasad, and S. G. Advani. Experimental study of an air-cooled thermal management system for high capacity lithiumetitanate batteries. *Journal of Power Sources*, 216:345–352, 2012.

[69] T. H. Tran, S. Harmand, and B. Sahut. Experimental investigation on heat pipe cooling for hybrid electric vehicle and electric vehicle lithium-ion battery. *Journal of Power Sources*, 265:262–272, 2014.

[70] C. V. Hemery, F. Pra, J. F. Robin, and P. Marty. Experimental performances of a battery thermal management system using a phase change material. *Journal of Power Sources*, 270:349–358, 2014.

[71] A. Ritchie and W. Howard. Recent developments and likely advances in lithium-ion batteries. *Journal of Power Sources*, 162:809–812, 2006.

[72] C. Lin, K. Chen, F. Sun, P. Tang, and H. Zhao. Research on thermo-physical properties identification and thermal analysis of ev li-ion battery. In *Vehicle Power and Propulsion Conference (VPPC)*, pages 1643–1648, Dearborn, September 7-11 2009.

[73] M. S. Rad, D. L. Danilov, M. Baghalha, M. Kazemeini, and P. H. L. Notten. Adaptive thermal modeling of li-ion batteries. *Electrochimica acta*, 102:183–195, 2013.

[74] N. Watrin, R. Roche, H. Ostermann, B. Blunier, and A. Miraoui. Multiphysical lithium-based battery model for use in state-of-charge determination. *IEEE Transactions on Vehicular Technology*, 61(8):3420–3429, October 2012.

[75] U. S. Kim, J. Yi, C. B. Shin, T. Han, and S. Park. Modelling the thermal behaviour of a lithium-ion battery during charge. *Journal of Power Sources*, 196:5115–5121, January 2011.

[76] A. Awarke, M. Jaeger, O. Oezdemir, and S. Pischinger. Thermal analysis of a li-ion battery module under realistic ev operating conditions. *International Journal of Energy Research*, 37:617–630, 2013.

[77] M. R. Giuliano, S. G. Advani, and A. Prasad. Thermal analysis and management of lithium–titanate batteries. *Journal of Power Sources*, 196:6517–6524, 2011.

[78] U. S. Kim, C. B. Shin, and C. S. Kim. Effect of electrode configuration on the thermal behavior of a lithium-polymer battery. *Journal of Power Sources*, 180(2):909–916, 2008.

[79] U. S. Kim, C. B. Shin, and C. S. Kim. Modeling for the scale-up of a lithium-ion polymer battery. *Journal of Power Sources*, 189(1):841–846, 2009.

[80] A. A. Pesaran and M. Keyser. Thermal characteristics of selected ev and hev batteries. In *Annual Battery Conference: Advances and Applications*, pages 1–7, Long Beach, California, January 2001.

[81] N. Sato. Thermal behavior analysis of lithium-ion batteries for electric and hybrid vehicles. *Journal of Power Sources*, 99:70–77, August 2001.

[82] E. Okamoto, Y. inoue, Y. Akasaka, S. Okada, T. Ebina, T. Kasai, S. Murata, Y. Abe, T. Chinzei, I. Saito, T. Isoyama, S. Mochizuki, K. Imachi, and Y. Mitamura. Evaluation of temperature rise of lithium ion secondary battery used in implantable battery system of uv-vad. In *Internal Federation for Medical and Biological Engineering (IFMBE) proceeding*, volume 14, pages 4142–4145. Springer Berlin Heidelberg, 2007.

[83] J. Patten, N. Christensen, G. Nola, and S. Srivastava. The impact of temperature on plug-in hybrid electric vehicle battery performance. In *Vehicle Power and Propulsion Conference (VPPC)*, Chicago USA, 6-9 sept 2011.

[84] D. XU, L. Wang, and J. Yang. Research on li-ion battery management system. In *International Conference on Electrical and Control Engineering*, pages 4106–4109, 2010.

[85] D. Szente-Varga, G. Horváth, and M. Rencz. Thermal characterization and modelling of lithium-based batteries at low ambient temperature. In *International Workshop on Thermal Inveatigation of ICs and Systems, THERMINIC*, 14, pages 128 – 131, 2008.

[86] M. W. Yatsui and H. Bai. Kalman filter based state-of-charge estimation for lithium-ion batteries in hybrid electric vehicles using pulse charging. In *Vehicle Power and Propulsion Conference (VPPC)*, pages 1–5, Chicago , USA, 6-9 Sept 2011.

[87] S. Cho, H. Jeong, C. Han, S. Jin, J. H. Lim, and J. Oh. State-of-charge estimation for lithium-ion batteries under various operating conditions using an equivalent circuit model. *Computers and Chemical Engineering*, 41:1– 9, 2012.

[88] M. Chen and G. A. Rincon-Mora. Accurate electrical battery model capable of predicting runtime and i-v performance. *IEEE Transactions on Energy Conversion*, 21(2):504–511, June 2006.

[89] O. Erdinc, B. Vural, and M. Uzunoglu. A dynamic lithium-ion battery model considering the effects of temperature and capacity fading. In *International Conference on Clean Electrical Power*, pages 383–386, June 2009.

[90] L. Gao, S. Liu, and R. A. Dougal. Dynamic lithium-ion battery model for system simulation. *IEEE Transactions on Components and Packaging Technologies*, 25(3):495 – 505, September 2002.

[91] R. C. Kroeze and P. T. Krein. Electrical battery model for use in dynamic electric vehicle simulations. In *Power Electronics Specialists Conference(PESC)*, pages 1336 – 1342, Rhodes, Greece, June 15-19 2008.

[92] Y. Ye, Y. Shi, N. Cai, J. Lee, and X. He. Electro-thermal modeling and experimental validation for lithium ion battery. *Journal of Power Sources*, 199:227– 238, 2012.

[93] J. Yi, U. S. Kim, C. B. Shin, T. Han, and S. Park. Modeling the temperature dependence of the discharge behavior of a lithium-ion battery in low environmental temperature. *Journal of Power Sources*, pages 1–6, 2013.

[94] F. Sun, R. Xiong, H. He, W. Li, and J. E. E. Aussems. Model-based dynamic multi-parameter method for peak power estimation of lithium–ion batteries. *Applied Energy*, 96:378–386, 2012.

[95] J. P. Schmidt, S. Arnold, A. Loges, D. Werner, T. Wetzel, and E. Ivers-Tiffée. Measurement of the internal cell temperature via impedance: Evaluation and application of a new method. *Journal of Power Sources*, 243:110–117, 2013.

[96] H. Sun, X. Wang, B. Tossan, and R. Dixon. Three-dimensional thermal modeling of a lithium-ion battery pack. *Journal of Power Sources*, 206:349–356, 2012.

[97] F. Baronti, G. Fantechi, E. Leonardi, R. Roncella, and R. Saletti. Enhanced model for lithium-polymer cells including temperature effects. In *Industrial Electronics Society Conference (IECON)*, pages 2329 – 2333, 2010.

[98] S. A. Khateeb, M. M. Farid, J. R. Selman, and S. Al-Hallaj. Design and simulation of a lithium-ion battery with a phase change material thermal management system for an electric scooter. *Journal of Power Sources*, 128:292–307, 2004.

[99] X. Hu, S. Lin, and S. Stanton. A novel thermal model for hev/ev battery modeling based on cfd calculation. In *IEEE Conference on Energy Conversion Congress and Exposition (ECCE)*, pages 893 – 900, 2010.

[100] C. Mi, B. Li, D. Buck, and N. Ota. Advanced electro-thermal modeling of lithium-ion battery system for hybrid electric vehicle applications. In *Vehicle Power and Propulsion Conference (VPPC)*, pages 107–111, 2007.

[101] A. A. Pesaran. Battery thermal models for hybrid vehicle simulations. *Journal of Power Sources*, 110:377–382, 2002.
[102] L. Fan, J. M. Khodadadi, and A. A. Pesaran. A parametric study on thermal management of an air-cooled lithium-ion battery module for plug-in hybrid electric vehicles. *Journal of Power Sources*, 238:301–312, 2013.
[103] A. Thanheiser, T. P. Kohler, C. Bertram, and H. G. Herzog. Battery emulation considering thermal behavior. In *Vehicle Power and Propulsion Conference (VPPC)*, pages 1–5, Chicago 2011, sept 2011.
[104] K. Smith and C. Y. Wang. Power and thermal characterization of a lithium-ion battery pack for hybrid-electric vehicles. *Journal of Power Sources*, 160:662–673, September 2006.
[105] W. Fang, O. J. Kwon, and C. Y. Wang. Electrochemical–thermal modeling of automotive li-ion batteries and experimental validation using a three-electrode cell. *Internal Journal of Energy Research*, 34:107–115, november 2009.
[106] S. Bhide and T. Shim. Development of improved li-ion battery model incorporating thermal and rate factor effects. In *Vehicle Power and Propulsion Conference (VPPC)*, pages 544–550, 2009.
[107] D. Simic. Thermal modelling, simulation and evaluation of a high power battery cell for automotive applications. In *IEEE conference on Vehicle Power and Propulsion Conference (VPPC)*, pages 1–4, 2010.
[108] M. Guo, G. H. Kim, and R. E. White. A three-dimensional multi-physics model for a li-ion battery. *Journal of Power Sources*, 240:80–94, 2013.
[109] M. Andre. The artemis european driving cycles for measuring car pollutant emissions. *Science of the Total Environment*, 334:73–84, 2004.
[110] H. Park. A design of air flow configuration for cooling lithium ion battery in hybrid electric vehicles. *Journal of Power Sources*, 239:30–36, 2013.
[111] M. Mousavi, S. Hoque, S. Rahnamayan, I. Dincer, and G. F. Naterer. Optimal design of an air-cooling system for a li-ion battery pack in electric vehicles with a genetic algorithm. In *IEEE Congress on Evolutionary Computation (CEC)*, pages 1848 – 1855, New Orleans, LA, USA, June 5-8 2011.
[112] S. S. Sazhin, E. M. Sazhina, O. Faltsi-Saravelou, and P. Wild. The p-1 model for thermal radiation transfer: advantages and limitations. *FUEL*, 75:289–294, 1996.
[113] Openfoam. OpenCFD Ltd, http://www.openfoam.org, Retrieved April 2014.
[114] H. Jasak, A. Jemcov, and Z. Tukovic. Openfoam: A c++ library for complex physics simulations. In *International Workshop on Coupled Methods in Numerical Dynamics*, pages 1–20, Dubrovnik, Croatia, 19-21 September 2007.
[115] A. Mack and M.P.N. Spruijt. Validation of openfoam for heavy gas dispersion applications. *Journal of Hazardous Materials*, 262:504– 516, 2013.
[116] F. Xiao, X. Li, K. Lam, and D. Wang. Investigation of the hydrodynamic behavior of diatom aggregates using particle image velocimetry. *Journal of Environmental Sciences*, 24:1157–1164, July 2012.
[117] S. K. Chung and S. K. Kim. Digital particle image velocimetry studies of nasal airflow. *Respiratory Physiology & Neurobiology*, 163:111–120, November 2008.
[118] K. Reinhold-Lópeza, A. Braeuera, A. Schmitta, N. Popovska-Leipertz, and A. Leipertz. Flow field characterization in a vertically oriented cold wall ccvd reactor by particle image velocimetry. *Chemical Engineering Journal*, 184:315–325, March 2012.

[119] V. Weitbrecht, G. Kuhn, and G. H. Jirka. Large scale piv-measurements at the surface of shallow water flows. *Flow Measurement and Instrumentation*, 13:237–245, 2002.

[120] P. Wernert, G. Koerber, F. Wietrich, M. Raffel, and J. Kompenhans. Demonstration by piv of the non-reproducibility of the flow field around an airfoil pitching under deep dynamic stall conditions and consequences thereof. *Aerospace Science and Technology*, 2:125–135, 1997.

[121] K. Miyazaki, G. Chen, F. Yamamoto, J. I. Ohta, Y. Murai, and K. Horii. Piv measurement of particle motion in spiral gas-solid two-phase flow. *Experimental Thermal and Fluid Science*, 19:194–203, 1999.

[122] T. Otsuka and P. Wolanski. Particle image velocimetry (piv) analysis of flame structure. *Journal of Loss Prevention in the Process Industries*, 14:503–507, 2001.

Contribution to Thermal Behaviour Study of Lithium-ion Battery for Electric and Hybrid Electric Vehicle

The main objectives of this study are to provide the essential information on the thermal behaviour of the battery cells for automotive purpose especially for EVs and HEVs through experimental work in order to develop an effective 3D electro-thermal model for lithium-ion battery cells and pack. The experimental study is focusing on the distribution of temperature at various points of the battery cell surface, impact of different constant discharge rates, and also the importance of cooling system on the battery temperature behaviour. This thesis highlights the battery cell temperature under abuse discharge condition and the impact of stacking the battery cells inside the battery pack. Impact of different temperature and SOC on the battery cell internal resistance and a case study on the battery cell thermal behaviour used in a series HEV to complete driving cycles using different cooling strategies are also studied. Furthermore, the experimental study is extended to the characteristic of the cooling air flow behaviour inside the battery pack, using particulate image velocimetry (PIV) system. The 3D electro-thermal CFD model is implemented in a free, open source CFD software package called OpenFOAM. The target is to have a relatively simple but accurate model with reasonable computation time. This proposed model considers the heat generation from battery current and internal resistance as a function of temperature, heat transfer through conduction, forced convection and radiation.

Keywords: thermal behaviour, lithium-ion battery, experimental study, particle image velocimetry (PIV), electric and hybrid electric vehicles, electro-thermal model, 3D CFD model

Contribution à l'Etude du Comportement Thermique de la Batterie Lithium-ion pour Véhicules Electriques et Hybrides

Les principaux objectifs de cette étude est de fournir les informations essentielles sur le comportement thermique des cellules de batterie pour une application automobile, en particulier pour les véhicules électriques et hybrides. Cette application est notre cadre de travail expérimental afin de développer un modèle électro-thermique 3D efficace pour les cellules lithium-ion et du pack batterie. L'étude expérimentale se concentre sur la distribution de température en différents points de la surface de la cellule, de l'impact de différents débits constants, et également l'importance du système de refroidissement sur le comportement en température de la batterie. Cette thèse met en évidence le comportement de température de la cellule dans des conditions de décharge agressive et de l'impact de l'empilement de plusieurs cellules à l'intérieur de la batterie. Une étude de cas sur le comportement thermique de la cellule dans une application véhicule électrique hybride série est proposée pour compléter les cycles de conduite en utilisant différentes stratégies de refroidissement. En outre, l'étude expérimentale est étendue à la caractéristique du comportement de refroidissement par flux d'air à l'intérieur de la batterie, en utilisant le système d'image de particules (PIV). Le modèle électro-thermique CFD 3D est développé sous un logiciel Open Source OpenFOAM. L'objectif principal est d'obtenir un modèle relativement simple mais précis avec un temps de calcul raisonnable. Le modèle proposé, estime la production de chaleur, à partir du courant de la batterie et la résistance interne en fonction de la température, le transfert de chaleur par conduction, convection forcée et rayonnement.

Mots clés: comportement thermique, batterie lithium-ion, étude expérimental, vélocimétrie par imagerie de particules (PIV), véhicules électriques et hybrides, modèle électro-thermique, modèle CFD 3D